



UNIVERSITAT POLITÈCNICA
DE CATALUNYA
BARCELONATECH

Advanced image analysis techniques for laboratory experiments on soils

Author

Ferran Parera Morales

Thesis Advisors

Eduardo Alonso Pérez de Ágreda

Núria Pinyol Puigmartí

A Thesis submitted to the Universitat Politècnica de Catalunya (UPC)

in partial fulfillment of the requirements for the degree of

DOCTOR OF PHILOSOPHY

Ph.D. program on Geotechnical Engineering and Geo-Sciences

Department of Civil and Environmental Engineering

Barcelona, September 2019

Thesis written by Ferran Parera

This work has been supported by FI Research Fellowship Program, and the funding from the project **LOOK** under the Explora Ciencia Program.

Acknowledgments

En primer lloc m'agradaria agrair els meus tutors Eduardo Alonso i Núria Pinyol per el seu guiatge durant tota la Tesi. Gràcies per acompanyar-me durant el camí de la Tesi, oberts a noves propostes i ajudant-me a evolucionar.

Eduardo, tu mirada más allá de lo evidente que permite discernir las buenas ideas me ha dado la confianza.

Núria, la teva decisió per anar més lluny però sense perdre el rigor científic m'ha donat l'empenta.

I want to extend my gratitude to the professors Greg Siemens and Andy Take for their guidance during my stage in Kingston, Canada. Thank you for sharing with me your passion for science.

Vull donar les gràcies als professors del departament de Enginyeria del Terreny que m'han ajudat. En especial voldria agrair al professor Toni Lloret per dedicar desinteressadament part del seu temps i compartir el seu coneixement en el camp experimental. Tambien quisiera agradecer la colaboración del departamento de Teoria del senyal i comunicacions, en especial al profesor Sergio Ruiz y su equipo por abrirme las puertas de su laboratorio e introducirme en el campo del análisis de la luz.

Agradezco a todo el equipo que conforma el laboratorio de Ingeniería del Terreno, en especial a Mercedes Sondon y Tomás Martínez por su apoyo en la creación de ensayos de laboratorio; así como a Enrique Romero y Rodrigo Gómez.

Agraeixo al personal de secretaria del Departament d'Enginyeria del Terreny per gestionar els tràmits administratius.

Aquesta Tesi s'ha pogut realitzar, principalment, gràcies al suport econòmic de la Generalitat de Catalunya a través de la beca FI, durant els tres primers anys. L'últim any de Tesi, s'ha obtingut el finançament a través del projecte LOOK en el programa Explora Ciencia del Ministerio de Ciencia e Innovación.

Me gustaría agradecer a los amigos con los que he compartido tiempo, charlas y experiencias durante estos años. Arisleidy Mesa, Gaia di Carluccio, Riccardo Rorato, Gerard Matas, Ningning Zhang, Lu He, Lluís Saló, Miquel de Francisco y Raül Oorthuis. Quiero hacer extensivo este agradecimiento a mis compañeros de despacho y universidad.

Voldria agrair als meus professors de l'ETPClot i de Enginyeria Geològica per ensenyar-me amb dedicació i invertir el seu temps en regar la llavor del coneixement.

Vorrei ringraziare l'intera famiglia Quarta - Pascali. Rosalba, Fabrizio, Anna Maria, Valeria e Paolo per avermi accolto nella loro famiglia. Soprattutto per aver reso piacevole la scrittura della mia Tesi nel meraviglioso Salento.

I deixo pel final als més importants, la meva família i la meva parella, pel seu amor incondicional, que sempre m'ha donat les ales per arribar on fos. Vosaltres sou la veritable llum que il·lumina el món, o si més no, el meu món.

Abstract

The understanding of soil behavior is the foundation where the geotechnical engineering is built on. Experimentation is essential to improve this comprehension, and then to be able to translate it into models, theories, or laws. In a proper scientific method, experimentation is present in all phases of model development from conception to validation.

Experimentation comprises two different types of data: field and laboratory data. Both approaches are essential and complementary, considering their weaknesses and strengths. This Thesis focuses on laboratory experimentation. The experiments are interesting because they are an abstraction of reality, focusing on the objective of the investigation. The main advantage of laboratory experiments is the high reproducibility, which, together with the control of the initial and contour conditions, enables to analyze the effects of different variables on the soil behavior.

This Thesis focuses on the development and improvement of methodologies and techniques to provide more and better information from the laboratory experiments in a massive and non-invasive way. The developed methodologies are based on the analysis of sequential images of experiments which are able to provide the spatial distribution through the domain of the analyzed variables.

The first technique presented and validated is the Particle Image Velocimetry - Numerical Particle (PIV-NP). This is a post-process to enhance the image correlation methods (PIV). The technique is able to transform the instantaneous displacements measured by PIV between two consecutive images on fixed points in the space into accumulated displacements and strains on points (Numerical Particles) which represent portions of the moving soil analyzed. The technique is especially suitable for the analysis of large displacements and strains in experiments and combines the advantages of Eulerian and Lagrangian scheme. The validation of the technique is done by means of synthetic examples and laboratory tests.

For application on unsaturated soils, the Thesis presents a technique to measure the degree of saturation (S_r) using Short-Wave InfraRed images (SWIR). The methodology is based

on the relatively high absorbance of light by water in specific wavelengths of the SWIR spectrum (1400 -1550 nm and 1900 - 2000 nm) respect to the solid particles of soils. The technique is created to be applied in a sequence of images to analyze the spatial distribution of degree of saturation and its evolution in time. The average Pixel Intensity is measured in a grid of points in each image. The Pixel Intensity is normalized and translated into its correspondent degree of saturation using the calibration curve previously calibrated.

Both techniques, PIV-NP and Sr measurements from SWIR images, are combined into an integrated methodology. The result provides the position, velocity, acceleration, strains, and degree of saturation in time of the analyzed moving soil discretized into numerical particles. This allows to compare and correlate directly all the variables. The methodology offers different options to display the results: surface (2D), line (1D), and particle (0D). The information that provides each display dimension is complementary and useful for a complete understanding of the soil behavior.

Finally, the integrated methodology is also applied combining the PIV-NP with a more mature technique developed in Canada to measure the degree of saturation in transparent soils. The study of the dry footprints on the seashore is the chosen case to show the capability of the combined techniques on the analysis of soil behavior. The three different options of results display are crucial to understanding the correlation between the degree of saturation and the velocity of failure.

The methodology and techniques developed can be used in any geotechnical laboratory and conform a base to extend the volume of data that can be obtained from the experiments, but especially enhancing the utility of the information deduced from the data.

Resum

La comprensió del comportament del sòl és el fonament sobre el qual es construeix l'enginyeria geotècnica. L'experimentació és essencial per millorar aquesta comprensió, i després poder traduir-la en models, teories o lleis. En un mètode científic adequat, l'experimentació està present en totes les fases del desenvolupament del model, des de la concepció fins a la validació.

L'experimentació comprèn dos tipus diferents de dades: dades de camp i de laboratori. Tots dos enfocaments són essencials i complementaris, considerant les seves debilitats i fortaleces. Aquesta tesi se centra en l'experimentació de laboratori. Els experiments són interessants perquè són una abstracció de la realitat, centrant-se en l'objectiu de la investigació. El principal avantatge dels experiments de laboratori és l'alta reproductibilitat, que, juntament amb el control de les condicions inicials i de contorn, permet analitzar els efectes de diferents variables en el comportament del sòl.

Aquesta tesi se centra en el desenvolupament i la millora de metodologies i tècniques per a proporcionar més i millor informació dels experiments de laboratori de forma massiva i no invasiva. Les metodologies desenvolupades es basen en l'anàlisi d'imatges seqüencials d'experiments que poden proporcionar la distribució espacial de les variables analitzades en tot el domini.

La primera tècnica presentada i validada és el Particle Image Velocimetry - Numerical Particle (PIV-NP). Aquest és un post-procés per millorar els mètodes de correlació d'imatges (PIV). El mètode és capaç de transformar els desplaçaments instantanis mesurats per PIV entre dues imatges consecutives en punts fixos en l'espai en desplaçaments acumulats i deformacions en punts (Partícules Numèriques) que representen parts del sòl analitzat en moviment. El mètode és especialment adequat per a l'anàlisi de grans desplaçaments i experiments de deformació, combina els avantatges dels esquemes eulerià i lagrangià. La validació del mètode es realitza mitjançant casos sintètics i experiments de laboratori.

Per aplicacions en sòls no saturats, la Tesi presenta una tècnica per mesurar el grau de saturació (S_r) utilitzant imatges infraroges d'ona curta (SWIR). La metodologia es basa en l'alta absorció de la llum per l'aigua comparativament a les partícules sòlides dels sòls, en longituds d'ona específiques de l'espectre SWIR (1400-1550 nm i 1900-2000 nm). La tècnica es crea per ser aplicada a una seqüència d'imatges, per analitzar la distribució espacial del grau de saturació i la seva evolució en el temps. La intensitat de píxel mitjana es mesura en una quadrícula de punts en cada imatge. La intensitat del píxel es normalitza i es tradueix en el seu corresponent grau de saturació utilitzant la corba de calibratge prèviament calibrada.

Les dues tècniques, els mesuraments PIV-NP i S_r a partir d'imatges SWIR, es combinen en una metodologia integrada. El resultat proporciona l'evolució en el temps de la posició, la velocitat, l'acceleració, les deformacions i el grau de saturació del sòl analitzat en moviment, discretitzat en partícules numèriques. Això permet comparar i correlacionar directament totes les variables. La metodologia ofereix diferents opcions per mostrar els resultats: superfície (2D), línia (1D) i partícula (0D). La informació que proporciona cada dimensió de visualització és complementària i útil per a una comprensió completa del comportament del sòl.

Finalment, la metodologia integrada també s'aplica combinant el PIV-NP amb una tècnica més madura desenvolupada al Canadà per mesurar el grau de saturació en sòls transparents. L'estudi de les petjades seques a la vora de la platja és el cas triat per mostrar la capacitat de les tècniques combinades en l'anàlisi del comportament del sòl. Les tres diferents opcions de visualització de resultats són crucials per comprendre la correlació entre el grau de saturació i la velocitat de trencament.

La metodologia i les tècniques desenvolupades es poden utilitzar en qualsevol laboratori geotècnic i conformen una base per ampliar el volum de dades que es poden obtenir dels experiments, però especialment millorant la utilitat de la informació deduïda de les dades.

Resumen

La comprensión del comportamiento del suelo es el cimiento sobre el cual se construye la ingeniería geotécnica. La experimentación es esencial para mejorar esta comprensión, y luego poder traducirla en modelos, teorías o leyes. En un método científico adecuado, la experimentación está presente en todas las fases del desarrollo del modelo, desde la concepción hasta la validación.

La experimentación comprende dos tipos diferentes de datos: datos de campo y de laboratorio. Ambos enfoques son esenciales y complementarios, considerando sus debilidades y fortalezas. Esta tesis se centra en la experimentación de laboratorio. Los experimentos son interesantes porque son una abstracción de la realidad, centrándose en el objetivo de la investigación. La principal ventaja de los experimentos de laboratorio es la alta reproducibilidad, que, junto con el control de las condiciones iniciales y de contorno, permite analizar los efectos de diferentes variables en el comportamiento del suelo.

Esta tesis se centra en el desarrollo y la mejora de metodologías y técnicas para proporcionar más y mejor información de los experimentos de laboratorio de forma masiva y no invasiva. Las metodologías desarrolladas se basan en el análisis de imágenes secuenciales de experimentos que pueden proporcionar la distribución espacial a través del dominio de las variables analizadas.

La primera técnica presentada y validada es la Particle Image Velocimetry - Numerical Particle (PIV-NP). Este es un postproceso para mejorar los métodos de correlación de imágenes (PIV). El método es capaz de transformar los desplazamientos instantáneos medidos por PIV entre dos imágenes consecutivas en puntos fijos en el espacio en desplazamientos acumulados y deformaciones en puntos (Partículas Numéricas) que representan partes del suelo analizado en movimiento. El método es especialmente adecuado para el análisis de grandes desplazamientos y experimentos de deformación, combina las ventajas del esquema euleriano y lagrangiano. La validación del método se realiza mediante ejemplos sintéticos y pruebas de laboratorio.

Para aplicaciones en suelos no saturados, la Tesis presenta una metodología para medir el grado de saturación (S_r) utilizando imágenes infrarrojas de onda corta (SWIR). La metodología se basa en la alta absorción de la luz por el agua con respecto a las partículas sólidas de los suelos, en longitudes de onda específicas del espectro SWIR (1400-1550 nm y 1900-2000 nm). La metodología se crea para ser aplicada en una secuencia de imágenes, para analizar la distribución espacial del grado de saturación y su evolución en el tiempo. La intensidad de píxel promedio se mide en una cuadrícula de puntos en cada imagen. La intensidad del píxel se normaliza y se traduce en su correspondiente grado de saturación utilizando la curva de calibración previamente calibrada.

Ambas técnicas, las mediciones PIV-NP y S_r a partir de imágenes SWIR, se combinan en una metodología integrada. El resultado proporciona la evolución en el tiempo de la posición, la velocidad, la aceleración, las deformaciones y el grado de saturación del suelo analizado en movimiento, discretizado en partículas numéricas. Esto permite comparar y correlacionar directamente todas las variables. La metodología ofrece diferentes opciones para mostrar los resultados: superficie (2D), línea (1D) y partícula (0D). La información que proporciona cada dimensión de visualización es complementaria y útil para una comprensión completa del comportamiento del suelo.

Finalmente, la metodología integrada también se aplica combinando el PIV-NP con una técnica más madura desarrollada en Canadá para medir el grado de saturación en suelos transparentes. El estudio de las pisadas secas en la orilla de la playa es el caso elegido para mostrar la capacidad de las técnicas combinadas en el análisis del comportamiento del suelo. Las tres opciones diferentes de visualización de resultados son cruciales para comprender la correlación entre el grado de saturación y la velocidad de rotura.

La metodología y las técnicas desarrolladas se pueden utilizar en cualquier laboratorio geotécnico y conforman una base para ampliar el volumen de datos que se pueden obtener de los experimentos, pero especialmente mejorando la utilidad de la información deducida de los datos.

Contents

| | | |
|-------|--|----|
| 1 | Introduction | 1 |
| 1.1 | Motivation | 1 |
| 1.2 | Objectives | 3 |
| 1.3 | Thesis layout | 4 |
| 2 | Soil behavior analysis based on images | 6 |
| 2.1 | Experimental data | 7 |
| 2.2 | Image correlation methods | 9 |
| 2.2.1 | Evolution of the image correlation methods | 9 |
| 2.2.2 | Basis of Image Correlation Methods..... | 11 |
| 2.3 | Eulerian vs Lagrangian | 13 |
| 2.3.1 | Eulerian approach | 13 |
| 2.3.2 | Lagrangian approach | 16 |
| 2.4 | Conclusions..... | 18 |
| 3 | Light principles for image analysis | 19 |
| 3.1 | Physical principles of light..... | 19 |
| 3.1.1 | The wave-particle duality | 20 |
| 3.1.2 | Electromagnetic wave description | 21 |
| 3.1.3 | Electromagnetic spectrum | 22 |
| 3.2 | Interactions between light and matter | 24 |
| 3.3 | Interactions between light and water..... | 30 |
| 3.3.1 | Refraction and Reflection | 30 |
| 3.3.2 | Light absorbance on the wavelength spectrum..... | 32 |
| 3.4 | Conclusions..... | 34 |
| 4 | Development of apparatus and sensors..... | 35 |
| 4.1 | Transparent tank for 1G experiments | 36 |

| | | |
|-------|--|-----|
| 4.2 | Low-cost moisture sensors | 40 |
| 4.2.1 | Calibration procedure for the sensors | 41 |
| 4.3 | Direct shear apparatus for low-stress tests | 43 |
| 4.3.1 | Initial tests in the standard direct shear apparatus..... | 43 |
| 4.3.2 | Literature review | 43 |
| 4.3.3 | Design and materials | 44 |
| 4.4 | Conclusions..... | 53 |
| 5 | Analysis of scale experiments by PIV-NP | 54 |
| 5.1 | PIV-NP description..... | 54 |
| 5.1.1 | Introduction..... | 54 |
| 5.1.2 | Input data structure | 56 |
| 5.1.3 | Algorithm..... | 58 |
| 5.2 | Validation of PIV-NP..... | 65 |
| 5.2.1 | Synthetic data..... | 66 |
| 5.2.2 | Synthetic images | 78 |
| 5.2.3 | Real images | 86 |
| 5.3 | PIV-NP analysis of experiments | 91 |
| 5.3.1 | Experimental setup..... | 91 |
| 5.3.2 | Input data and preliminary steps..... | 92 |
| 5.3.3 | Results..... | 94 |
| 5.4 | Conclusions..... | 99 |
| 6 | Non-invasive surface measurement of the degree of saturation by ShortWave InfraRed images | 100 |
| 6.1 | Introduction | 101 |
| 6.2 | Physical principles..... | 102 |
| 6.3 | Experimental setup | 106 |
| 6.3.1 | Camera | 106 |
| 6.3.2 | Material..... | 107 |

| | | |
|-------|--|-----|
| 6.3.3 | Measuring the reflectance (gray value) | 108 |
| 6.4 | Calibration..... | 110 |
| 6.5 | Analysis | 113 |
| 6.6 | Validation and evaluation..... | 115 |
| 6.6.1 | Experimental setup..... | 115 |
| 6.6.2 | Results..... | 117 |
| 6.7 | Numerical model | 121 |
| 6.8 | Discussion | 125 |
| 6.8.1 | Effect of void ratio | 125 |
| 6.8.2 | Limitations of the method..... | 128 |
| 6.9 | Conclusions..... | 130 |
| 7 | Measurement of the degree of saturation by SWIR images on soils in motion..... | 131 |
| 7.1 | Introduction | 131 |
| 7.2 | Algorithm | 132 |
| 7.2.1 | Steps..... | 132 |
| 7.3 | Validation and evaluation..... | 134 |
| 7.3.1 | Camera | 134 |
| 7.3.2 | Material..... | 135 |
| 7.3.3 | Results..... | 138 |
| 7.4 | Conclusions..... | 145 |
| 8 | Footprints in the beach - Analysis using PIV-NP and transparent soil..... | 146 |
| 8.1 | Introduction | 147 |
| 8.2 | Techniques description..... | 150 |
| 8.2.1 | Transparent soil..... | 150 |
| 8.2.2 | PIV-NP in transparent soils measurements | 153 |
| 8.3 | Experimental setup | 154 |
| 8.3.1 | Ultrahigh-speed camera and lighting. | 154 |

| | | |
|-------|--|-----|
| 8.3.2 | Tank, pneumatic load system and sensors | 156 |
| 8.3.3 | Experiment performance | 157 |
| 8.4 | Results on three representative cases | 158 |
| 8.4.1 | Dry case | 159 |
| 8.4.2 | Submerged case | 163 |
| 8.4.3 | Saturated case | 166 |
| 8.5 | The effect of the phreatic level on the bearing capacity. | 178 |
| 8.5.1 | Difficulties on the comparison of the shallow foundation experiments.... | 179 |
| 8.5.2 | Effect of the inclination and eccentricity | 180 |
| 8.6 | Conclusions..... | 184 |
| 9 | Conclusions and future work..... | 185 |
| 9.1 | Final conclusions and contributions | 185 |
| 9.2 | Future work..... | 188 |
| | Bibliography..... | 189 |
| | List of figures..... | 198 |
| | List of tables | 207 |

1

Chapter 1

Introduction

This Chapter presents the motivation for the work carried out. Then, the main and the specific objectives to reach it are stated. Finally, the organization of the document is outlined.

1.1 Motivation

The knowledge developed in recent years in the field of geotechnics is reflected in the emergence or modifications of theories and models that explain the observed soil response. The observation of the experimental results is where the fundamental ideas and concepts arise to evolve the paradigms of current knowledge. The finding of results or patterns that are not well explained with existing models is the first step in the development of new theories. In the same way, experimentation is vital to translate correctly these concepts into mathematical formulas. It is essential to combine synergistically the theoretical branch with the experimental branch; so that the abstractions necessary to synthesize ideas in equations do not depart too much from the reality they want to represent. And finally, the experimental results are basic for the validation of any method or model developed.

Given the intrinsic purpose of the experimental studies, the importance of the type and quality of results that can be extracted from the experiments is revealed. Focusing on the laboratory geotechnical tests, many of the results are based on data extracted from installed sensors. There is a wide range of sensors to measure variables of interest. These data may be reliable and robust due to the long experience in their use. However, conventional sensors usually present some limitation: (a) They provide the value of the variable measured at localized volumes of the sample or the average value of a larger volume; (b) The sensors

placement has to be decided beforehand. The interesting points to measure is often unknown before the experiment performance (c) The sensors are commonly not suitable for measuring large displacements. These limitations are particularly evident in the field of landslides. The Thesis focuses on covering and solving these limitations, particularly in the study of rainfall triggered collapses and landslides, where the variables as the degree of saturation have a critical role.

To obtain a more comprehensive visualization, techniques that use sequences of images in time to analyze experiments have been developed. These techniques have been proved very useful for understanding soil behavior during an experiment. The different image techniques are able to measure different variables: the displacement, the degree of saturation, the flow of a fluid, the content of specific components, or the temperature. The measure of the evolution in time and the distribution in the space of a variable allows for a more global conception of its behavior. This visualization can be complemented and corroborated by the singular data of the sensors. The development of new techniques to measure variables through images is useful to extend the knowledge generated by the different existing or new apparatus.

The image analysis techniques generate a massive volume of data. The proper display of the results is crucial to exploit the potential of the data. The image analysis results use to be presented in bidimensional visualizations; the most common example is the 2D contour plot. This 2D display is useful to study the spatial distribution of one variable in a single instant of time. The evolution in time, can be visualized as a sequence of 2D plots or as an animation, that provides a qualitative idea of the tendencies but is unsuitable for quantitative analysis. However, the linear graphs are more adequate for quantitative analysis of the data and offer a direct comparison between variables. The proper use of the different options of results display is critical for an effective data analysis.

The combination of the different techniques of image analysis with the different options of results display could offer a new range of analysis opportunities. This integrated analysis might promote the emergence of new concepts and ideas, facilitate synergy in the development of theories, and create an in-depth validation system for models.

1.2 Objectives

The Thesis main objective is to have an integrated methodology to obtain the spatial evolution of the degree of saturation, the displacements, and the deformations. The measurements focus on laboratory experiments on soils with small and large deformations. Different image analysis techniques were used and developed to measure and calculate the evolution during the time of these variables in all the points of the soil sample surface.

The following specific objectives were defined to achieve this main objective.

- To develop and validate a technique to calculate the movement of each part of the soil with particular interest in the accumulative values: accumulated displacement and strains particularly interesting for the geotechnical field. A technique consisting of a lagrangian post-process of the measurements from the eulerian image analysis correlation techniques.
- To develop and validate an image analysis technique to measure the degree of saturation in laboratory soil experiments. A flexible technique able to be used in already existing experiments inside the common geotechnical laboratory facilities.
- To generate a methodology that integrates the results from the developed or already existing techniques to facilitate the comprehensive analysis of the results. To explore and evaluate the potential of the result display options that the methodology can offer.

1.3 Thesis layout

The Thesis is organized in 9 Chapters. The main arguments presented in the Chapters are introduced here:

In Chapter 2, a general review of the concepts of the image analysis in soil experiments is presented. The focus is on the image correlation methods which are used in the Thesis. These methods are divided into Eulerian and Lagrangian, and the main advantages and disadvantages to be used for geotechnical purposes of each scheme are discussed.

In Chapter 3, an introduction of the physical description of light is presented. The fundamental concepts of the interaction between light and matter are detailed for a better understanding of Chapters 6 and 8.

In Chapter 4 the main apparatus specially designed and built for the Thesis purposes are described, a transparent tank to perform the experiments and a low-stress direct shear test with suction control. The calibration of low-cost alternative moisture sensors is also described.

In Chapter 5, the PIV-NP post-process bases are explained, and the algorithm is described step by step with visual representations. An in-depth validation of the results is performed using a set of tests at different levels of abstraction. The capabilities of the method are finally applied to the analysis of a small scale landslide in which the position of several particles is known.

Chapter 6 presents the developed technique to measure the degree of saturation in the soil surface of laboratory experiments using SWIR images. The fundamentals of the method are discussed based on state of the art. The algorithm and calibration are described in detail. The methodology is applied to the wetting process of an initially unsaturated soil column. The results are validated with the comparison of moisture sensors data and with a numerical simulation using Code-Bright.

In Chapter 7, the previous methodologies developed to evaluate the motion and the degree of saturation in experiments are integrated. The results of both techniques are coupled in

a single file. The Chapter explains the modifications in the PIV-NP algorithm to introduce other image analysis results. The possibilities of result display using the new format of combined data are explored in a column collapse due to the changes in the degree of saturation.

Chapter 8 includes the measure of the degree of saturation using transparent soils. This technique, combined with PIV-NP, is used to analyze the dry footprint effect close to the seashore. The potential of the results combination and the different options of result display is emphasized in this analysis.

Finally, general conclusions are summarized in Chapter 9. The Chapter also suggests future research lines following the scope of the Thesis.

2

Chapter 2

Soil behavior analysis based on images

The use of images to extract information from experimental cases is widespread in all the science fields. This comprises from the satellite images of the earth and space to the microscopic images of unicellular organisms. The power of the images is to offer two-dimensional information (sometimes even three-dimensional) of the object of study through the time. This provides a complete and exhaustive idea of the status and evolution of different variables of interest through the all domain, without the need for interpolations between punctual data.

This Thesis is based on two types of methods for image analysis:

- The first method is the measure of relative movement through the comparison of pairs of images. These methods, known as Image Correlation Methods, are discussed straightaway on this Chapter.
- The second method is the correlation between pixel intensity and the state of one of the object's properties on its surface. The pixel intensity corresponds to the light received on each pixel of the image. The key aspect of this method is the interaction between light and matter. This topic will be discussed later in Chapter 3.

2.1 Experimental data

The geotechnical field, as the majority of the science fields, requires the experimental data to develop and validate theories, laws and models (Cleland, 2001). The most basic classification for the experimental data divides them into two types: field data and laboratory data. Both types are important and complement each other considering their strengths and weaknesses.

The field data is useful because it is extracted from real cases in nature. They represent the complexity of nature and encompass the full interaction between the elements. However, these real cases are rare, the occurrence is low linked to particular natural conditions. These cases happen sporadically in scattered places, for that reason the cases that are fully well-instrumented or slightly instrumented are even more scarce. Therefore, the field data is somehow incomplete; like pieces of a puzzle that require the full picture to be placed in the correct place (Matheson, 1989; Elkateb, Chalaturnyk and Robertson, 2003). In order to get the field data without waiting to naturally occur, artificial cases are prepared and triggered. The high economic cost makes them scarce and complicated to repeat (Moriwaki *et al.*, 2004; Ochiai, Sammori and Okada, 2007). The type and amount of information that is available in both cases makes them particularly difficult to analyze. The reality is heterogeneous and difficult to outline, determining the initial conditions and contour is often as important and complex as developing a theory itself.

The laboratory data is extracted from experiments carried out within the facilities of a laboratory, so their size is limited to the space available. The dimensions usually are on the order of decimeters to a couple of meters, except in a few exceptions. This type of tests has a relatively low cost of execution compared with full-scale tests. So, once the device is built, multiple cases can be carried out without increasing the costs derived from it. Its small dimensions allow good maneuverability, in most cases, do not require more than one researcher to perform the test. An important aspect of the tests in the laboratory is the control of the initial and boundary conditions. The control of these parameters reduces the number of uncertainties, that facilitates a more accurate numerical simulation (van Genuchten and Parker, 1984; Baker and Hillel, 1990). The geotechnical properties of the material used in a test can be measured. Due to the reduced amount of soil used, it is assumed that these properties are generalizable for the entire trial. It is feasible to perform

the preparation and disposition of the material with a procedure that allows calculating the initial test conditions, such as density, porosity or stress (Germaine and Germaine, 2009). The control of the boundary conditions implies not only the limitation of uncertainties for better numerical modeling. Furthermore, the variation of these boundary conditions allows the creation of similar cases with the exception of some controlled variables. These cases are perfect to understand the effect, independent or combined, of various parameters in the soil behavior (Berger *et al.*, 2010). The reproducibility of the test also allows the comparison of results to understand the origin of unexpected results or errors. The main disadvantage of this type of test is the scale effect. The behavior of the soil in the scale test is not directly extrapolated to real cases. The conclusions extracted from the test with small tensions might not be directly applicable to the reality, because the soil behavior is not linearly correlated with the dimension of the cases (De Beer, 1963; Garnier *et al.*, 2007). This Thesis is focused on going one step further in the analysis of these experiments.

2.2 Image correlation methods

The Image Correlation is the field that comprises different non-intrusive optical methods based on the observation and measurement of changes in sequential images. The images of the object of study are captured in regular time intervals, recording its movement and or deformation. These methods are used to measure and evaluate full-field displacement, velocities and strains. The most well known among them are the Particle Image Velocimetry (Raffel *et al.*, 2018) and the Digital Image Correlation (Yoneyama and Murasawa, 2009).

The images are matrixes of pixels: one matrix in greyscale images, and three matrixes in color images (RGB). Every pixel is defined by its position and its pixel intensity value. The pixel intensity value is a number, from 0 to 255, that represents the amount of light received in that position of the camera matrix sensor.

2.2.1 Evolution of the image correlation methods

The first examples that could be considered precursors of the image correlation methods date from the end of the 19th century. These techniques appear with the possibility of recording and saving sequences of photos. (Marey, 1874; Ahlborn, 1896; Prandtl, 1953) are some of the outstanding names of this early stage in the use of image correlation for the evaluation of movement. The work of these precursors focuses on animal movement and fluid dynamics. This original technique was based on the traditional photograph using flashes and special apparatus to capture sequences of images of the object of study. The correlation between images was done manually in an analogical way. With the advances in computing power, this correlation between images was carried out digitally.

In the last two decades of the twentieth century, several research groups develop algorithms for the computational correlation of images. These groups competed with each other for better performance of the optical and digital methods in the evaluation of image correlation methods. The two most outstanding techniques developed are the Particle Image of Velocimetry (PIV) and the Digital Image Correlation (DIC).

The Particle Image Velocimetry was developed to be used in the fields of fluid dynamics and aerodynamics (Meynart, 1983; Lauterborn and Vogel, 1984; Adrian, 1991; Hinsch, 1995; Westerweel, 1997). Their techniques were based on images captured using a laser flash on a fluid flow with artificial targets. The correlation between images permits the observation and measurement of the flow and turbulence lines.

The Digital Image Correlation was developed to be used on the experimental solid mechanics (Peters and Ranson, 1982; Sutton *et al.*, 1983). Their techniques permit measure strains at the surface of pieces caused by mechanical stresses.

After being applied to the fields of fluid and solid mechanics, these methods were extended to other areas as diverse as microbiology, astronomy or geotechnics. These new applications require adaptations of the methods to meet their particular needs and adapt to the specific objectives of each field.

Some authors on the field of geotechnics found these techniques especially interesting for geotechnical testing. Different methods were developed to full-fill the specialties and requirements of the soil experimentation that differentiate them from the uses that could be given in the analysis of fluids or solids. Geotechnical tests do not require artificial targets or prints. The natural texture of the soil (colors and shades of the grains) usually creates a traceable pattern that identifies each area of the soil for a proper correlation. Unlike fluids, the evolution ("history") of each part of the soil is important to understand its behavior. It is not only important to observe the velocity of deformation in all the points of the soil, but the accumulated deformation of each part of the soil.

The most important code developed especially for geotechnical testing is GeoPIV (White, Take and Bolton, 2003) and the improved version GeoPIV-RG (Stanier *et al.*, 2016). This code is based on the DIC theory adapted for the larger displacements that occur in soil experiments. Other authors proposed codes with more specific objectives. (Sadek, Iskander and Liu, 2003) developed a digital image correlation technique to analyze experiments with transparent soils. (Rechenmacher and Finno, 2004) developed a technique focused on the measure of shear-bands and the dilatation.

2.2.2 Basis of Image Correlation Methods

The procedure described below is a conceptual abstraction of an image correlation method, a general overview without inquiring into the peculiarities and particular equations of the different existing techniques and algorithms. The image correlation methods are based on the analysis of pairs of images, measuring the displacement of each part of the original image with respect to its corresponding pair (Figure 1).

Consider the application of the method on to two images captured with a certain interval of time. The basic procedure for their correlation, common in most of the methods, is based on the following steps:

- i. The images A and B are captured with an *interval of time* Δt .
- ii. The area of interest, where the analysis is going to be made, is defined in image A. The points outside the area of interest are not going to be analyzed.
- iii. The area of interest in the image A is discretized by a grid.
- iv. A *patch* is created on each node of the grid. A patch is a parcel of the image around the node that represents it, a small matrix of pixel intensity values. Its size depends on the heterogeneity of the medium; the number of pixels required to characterize the patch and distinguish it from the rest of the image.
- v. The *searching area* is defined around each node with the expected maximum movement that might occur.
- vi. The analysis consists of finding the correspondent location every patch of image A on the image B. This is the keystone of each image correlation method. The most used algorithms are based on the cross-correlation (CC) and the sum of squared differences (SSD).

For each *patch*, the algorithm search in image B for the pixel intensity values matrix that is more similar to the original patch. The search is limited to the *searching area* around the original location. The rotation and deformation of the patch add complexity to the search. Some algorithms use a refining step to improve the precision of the correlation. The most used algorithms are summarized on (Pan *et al.*, 2009).

- vii. The *vector of displacement* of each node is measured comparing the new location with the original. The displacement of every node is calculated on pixels.
- viii. The vector of displacement is expressed in metric units using a *calibration distance* introduced by the user. The velocity is calculated dividing the measured displacement between the time interval between images.

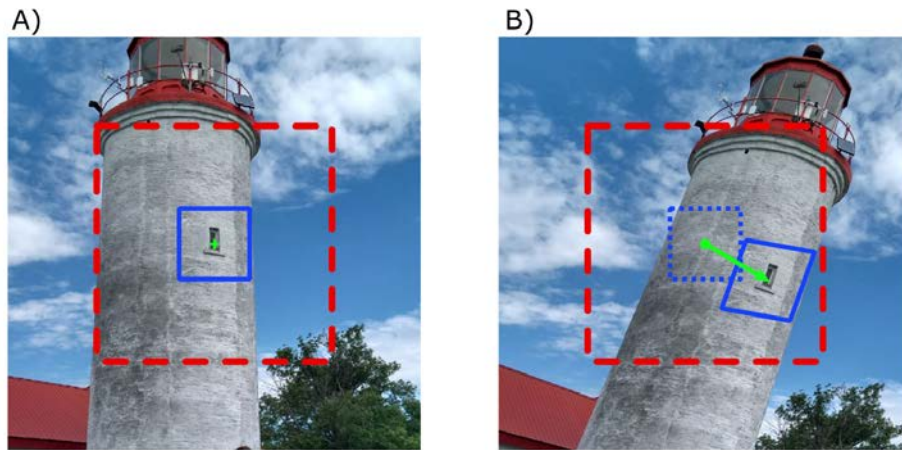


Figure 1. Example of a generic image analysis focused on one single node. The patch is defined on the picture A (blue square). The location of the patch is found on picture B inside the searching area (red dashed square). The original location and the new location of the patch are connected by a green vector to represent the measured displacement.

2.3 Eulerian vs Lagrangian

In the image correlation field, there are two main approaches to analyze the changes in image sequences: Eulerian and Lagrangian. The two techniques coexist to cover different types of necessities, depending on the nature of the analyzed material and the performed experiment. Both approaches are similar considering the analysis of a single pair of images. The differences emerge in the analysis of sequences of multiple images.

2.3.1 Eulerian approach

The Eulerian approach is based on the changes that occur on fixed coordinates of the space (Christensen and Adrian, 2002; Thielicke and Stamhuis, 2014). The coordinates of the reference patches defined on the first image remain constant through all the analysis. The reference mesh is reset on every image analysis. The result is the evolution of the velocity or displacement as a field. The vectors maintain constant their initial coordinates. Figure 2 is an idealized representation of 3 time steps of the Eulerian approach image correlation. Table 1 summarizes the evolution of the reference and displaced coordinates of the patches for each time step.

Time step 1: image A and B are correlated.

A regular grid of reference patches is defined on image A. These are the patches searched in image B to evaluate the displacements between A and B images.

Time step 2: images B and C are correlated.

The coordinates of the regular grid of patches defined on the image A are reset to be the coordinates of the reference patches on image B. Therefore, these searched patches might be completely different than the patches searched on the time step 1, but the coordinates of the origin of each relation vector in time step 2 are the same than in time step 1.

Time step 3: images C and D are correlated.

As in the previous time steps, the regular grid of reference patches defined on the image A is used again on image C. These patches might be different than in the previous time steps, as it can be observed looking at the evolution of the upper-right patch. In the time step 1 the searched patch was a sky with clouds, while in the time step 3 the searched patch is the upper part of a lighthouse.

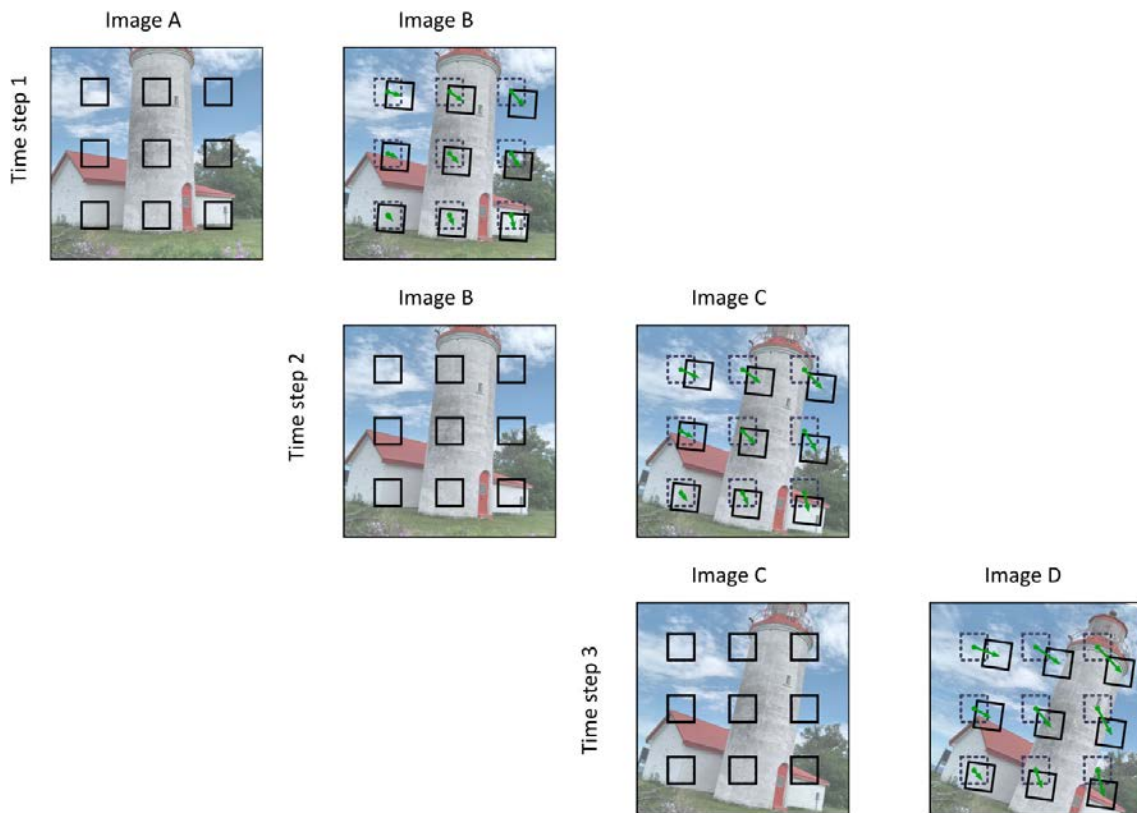


Figure 2. Eulerian image correlation

Table 1: Coordinates of the reference and compared patches in the Eulerian approach.

| | Reference | | Compared | |
|-------------|-----------|-------------------|----------|-------------------|
| | Image | Patch coordinates | Image | Patch coordinates |
| Time step 1 | A | XY | B | X'Y' |
| Time step 2 | B | XY | C | X''Y'' |
| Time step 3 | C | XY | D | X'''Y''' |

This technique is commonly used in fluid dynamics. An example of the use on this field is the analysis on the boat keel hydrodynamics by (Aloisio and Di Felice, 2006). The analysis

is focused on the turbulence that occurs when a flux of water interacts with the keel of the boat. The interest is on the speeds that the water reaches right next to the boat that could produce extra friction. Therefore, it is important to evaluate and track the changes in the displacement (or velocity) on that particular coordinates. It is not important the path that each molecule of water has followed during the experiment.

Advantages and disadvantages of the Eulerian approach for geotechnical testing

The Eulerian type of image correlation methods has been developed to fulfill the needs and characteristics of fluid dynamics. On that type of cases, the measurements of displacements and velocities could be independent of the previous states. Whereas, in the geotechnical testing, the importance is focused on the accumulative values, the strains that a soil suffer modify its properties and behavior. The non-accumulative velocities and displacements, that is the key point of those methods, use to be insufficient for several geotechnical purposes.

The positive point is based on the same aspect, the independence between time steps. The results from Eulerian methods can be easily modified because the results of a time step are not related to the next time steps. The miss-matched patch correlation between images, known as wild vectors, can be eliminated and interpolated from the correct surrounding result vectors. Besides, any filter can be applied to smooth the data or remove the background noise. These characteristics make the eulerian approach a robust technique to analyze any type of deformation.

2.3.2 Lagrangian approach

The Lagrangian type of Image Correlation methods is based on the track of the movement of the specific points of the object of study. The analysis of the set of images can follow two different schemes, leapfrog or sequential. In the leapfrog scheme, the initial image is set as a reference which each subsequent image is compared (1-2, 1-3, 1-4...). The difficulties in correlation the patches after large deformations cause the creation of systems to update the reference image. The limit to update the reference image can be set manually or related to the correlation quality. The limit set as one results to the sequential scheme. The sequential scheme, the reference image is actualized on each time-step (1-2, 2-3, 3-4...) similarly to the eulerian approach. The main difference between the sequential lagrangian approach and the eulerian approach lays on the actualization of the patch coordinates. In the sequential lagrangian approach, the coordinates of the reference patches are updated taking as a reference the result of the previous two-image analysis. (Blaber, Adair and Antoniou, 2015). Figure 3 is an idealized representation of 3 time steps of the sequential Lagrangian approach image correlation. Table 2 summarizes the evolution of the reference and displaced coordinates of the patches for each time step.

Time step 1: images A and B are correlated.

A regular grid of reference patches is defined on the image A. These are the patches searched in image B to evaluate the displacements between A and B images.

Time step 2: images B and C are correlated.

The new final coordinates of the displaced patches from the time step 1 are set to be the coordinates of the reference patches on image B. The searched patches keep being the same as in the time step 1. The vectors attached to each other describe the track that each part of the object has followed.

Time step 3: images C and D are correlated.

The new final coordinates of the displaced patches from the time step 2 are set to be the coordinates of the reference patches on image C. The searched patches keep being

the same as in the time step 1 and 2. The track of the wall next to the window can be followed by looking at the upper-middle patch.

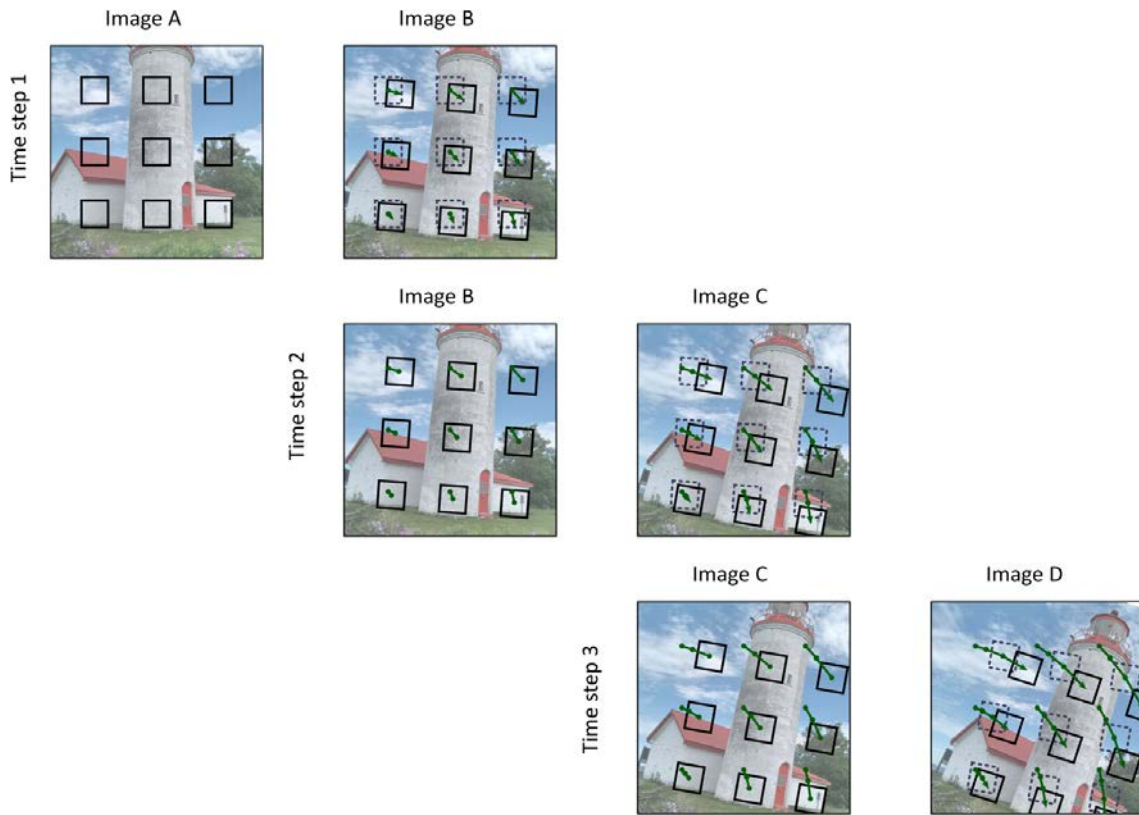


Figure 3. Lagrangian Image Correlation

Table 2: Coordinates of the reference and compared patches in the Lagrangian approach.

| | Reference | | Compared | |
|-------------|-----------|-------------------|----------|-------------------|
| | Image | Patch coordinates | Image | Patch coordinates |
| Time step 1 | A | XY | B | X'Y' |
| Time step 2 | B | X''Y'' | C | X'''Y''' |
| Time step 3 | C | X''''Y'''' | D | X''''''Y'''''' |

This technique is commonly used in mechanical engineering. An example of the use on this field is the analysis based on the deformation that occurs on a railway when a train passes on it (Murray, Take and Hout, 2015). The interest is on the total amount of deformation that is absorbed by each point of the railway and ballast to see when it could reach the fatigue. Therefore, it is important to evaluate and track the changes that occur at each point of the railway.

Advantages and disadvantages of the Lagrangian approach for geotechnical testing.

The Lagrangian type of image correlation is useful for geotechnical purposes. The accumulative displacement measurement facilitates the calculation of strains and other parameters of the soil. The main complexity is the rectification of the errors, known as wild vectors. As the final coordinates resulting from one time step of image correlation are the initial reference coordinates form the next time step, any error on the correlation is carried on the subsequent time steps. This problem is attacked, by the different methods, developing algorithms to detect these wild vectors and correct them before the next time step.

2.4 Conclusions

The Image Correlation methods are a powerful tool to measure displacements and strains in experiments. These methods were initially developed for the fluid dynamics and solid mechanics fields. The application of the image correlation methods for geotechnical purposes implies two main challenges: the large and complex displacements that are not common in solid mechanics and the interest on calculating historical dependent variables that is not important in fluid dynamics.

There are two main approaches to the analysis of image sequences, Eulerian and Lagrangian:

- The Eulerian approach is based on independent analysis of each time step. The non-accumulative errors and the facility to modify them make this approach robust for any type of displacement. However, the calculation of the historical dependent variables is complicated.
- The Lagrangian approach, based on accumulative analysis of the time steps. This approach is able to calculate historical dependent variables. However, there are some difficulties to deal with the errors on correlation.

3

Chapter 3

Light principles for image analysis

Understanding the physical principles that rule the light behavior is fundamental to improve and develop the image analysis techniques. Light is the main element in the use of images for the analysis of tests. Light is the element that extracts information from the state of the soil, but also the communication channel through which this information is transported to the receiver. For this reason, it is key to know and understand the nature of light, as well as its interaction with matter.

The Chapter is divided into three Sections:

- The fundamental concepts and the physical parameters of light are introduced.
- The different types of interaction between light and matter are described.
- The interaction between light and water, relevant for the techniques developed or used in this Thesis, are detailed.

3.1 Physical principles of light

Understanding the nature of light has been a challenge since humanity has started wondering about the world that is around us. Light is omnipresent and affects every one of the human actions, regardless it does not behave like any other mater. The following articles represent the historical evolution and paradigm changes in the light nature conception (Descartes, 1637; Huygens, 1678; Newton, 1730; Young, 1802; Maxwell, 1868; Hertz, 1888; Einstein, 1905; Bohr, Kramers and Slater, 1924; Dirac, 1927).

3.1.1 The wave-particle duality

The *particle* and the *wave* interpretation are the two most successful theories to explain the nature of light, and historically, they have been under scientific debate. The basic ideas of each interpretation are: the particle theories describe the light as a flux of particles, while the wave theories describe the light as an energy wave.

The debate is well explained and summarized by Dimitrova and Weis on the introduction of its article *The wave-particle duality of light: A demonstration experiment* (Dimitrova and Weis, 2008):

“The historical debate on the particle versus wave interpretation of light is well known. The debate between Newton and Huygens seemed definitely settled in favor of the wave nature by the work of Young, Fresnel, Maxwell, Hertz, and others. The discussion was revived by Einstein’s interpretation of the photoelectric effect in terms of light being a stream of particles, later called photons. The wave and particle aspects were unified by Bohr and Heisenberg who introduced the concept of complementarity, which was later identified as a distinguishing characteristic of quantum mechanics: contradictory properties of a physical system, here particles and waves, are interpreted as complementary properties, and a complete description of the system is obtained only when considering both properties (duality). Later the wave-particle duality was given a simple interpretation by stating that light propagation is described by a quantum mechanical wave function with the same superposition and interference properties as a classical wave. The particle nature is revealed at the moment of detection when the wave function collapses. Put simply, light behaves as a wave when it propagates and like a particle when it is detected.”

This Thesis is more focused on the wave interpretation of light because this model is more useful to explain the basis of the developed methodology. However, in the theoretical introduction of the light-matter interaction concepts of quantum physics are used.

For a compressible explanation of the concepts and to avoid the misinterpretation of the term light; the light will be understood as the whole spectrum of electromagnetic radiation which covers further than just visible light.

3.1.2 Electromagnetic wave description

The electromagnetic radiation (*EM radiation*) is energy propagating through space at the speed of light in the form of electromagnetic waves, composed of perpendicularly arranged electric and magnetic fields (Kerle, 2013). The electromagnetic wave is a periodic wave described by these parameters (Figure 4):

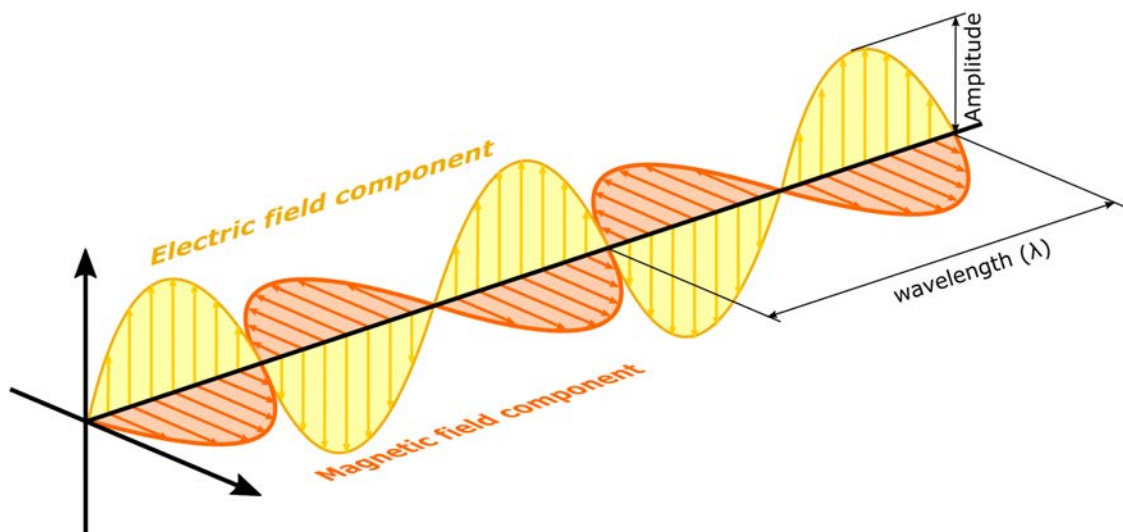


Figure 4. Example of the electromagnetic wave.

Speed of light (c): Velocity of the light in the vacuum is a universal physical constant, and it can be approximated to 300,000 km/s.

Amplitude: Distance between the maximum point and the central axis of the wave. It is expressed in $\text{W/m}^2/\mu\text{meter}$. The wave's energy (intensity) is proportional to the amplitude squared.

Wavelength (λ): Spatial distance between two corresponding points, two consecutive points that have completed the same fraction of the periodic cycle (from crest to crest or from trough to trough). It is expressed with a wide range of distance units (\AA m-nm).

Frequency (ν): Number of cycles that pass a fixed point per unit of time. It is expressed with Hz, which is equal to $1/\text{s}$.

The wavelength and frequency are the central parameters to characterize the different forms of electromagnetic radiation. These two parameters are intrinsically bound; the frequency is inversely proportional to wavelength following Equation 1.

Equation 1

$$c = \lambda\nu$$

On the next paragraphs, the concepts of wavelength and frequency will appear, to explain the behavior of the interaction between electromagnetic waves and mater. Depending on the context it would be more useful to express in terms of wavelength and others in terms of frequency, but it is important to keep in mind that both parameters are intrinsically related by Equation 1.

3.1.3 Electromagnetic spectrum

The electromagnetic spectrum comprises the full range of wavelengths (or frequencies) that the electromagnetic waves can be. El range of wavelength goes from 1 Å (10^{-10} m) to more than 1 Km. The frequency of each EM radiation determines its properties. The full range of frequencies and wavelengths are summarized in Figure 5.

Each frequency corresponds to an amount of energy that each photon has. This value of energy is unique and characteristic for each frequency; the amount of energy is proportional to the frequency and inversely proportional to its wavelength.

The image analysis methods and techniques developed or used on this Thesis are:

- Image correlation methods (Chapter 2)
- Particle Image Velocimetry - Numerical Particle (Chapter 5)
- Degree of saturation measurements by SWIR images (Chapter 6)
- Degree of saturation measurements with transparent soils (Chapter 8).

All these methodologies use images on the visible and Short-Wave InfraRed bands of the EM spectrum. The energy of these bands is unharful for the biological tissues. Therefore, the methodologies do not require especial protection in that aspect.

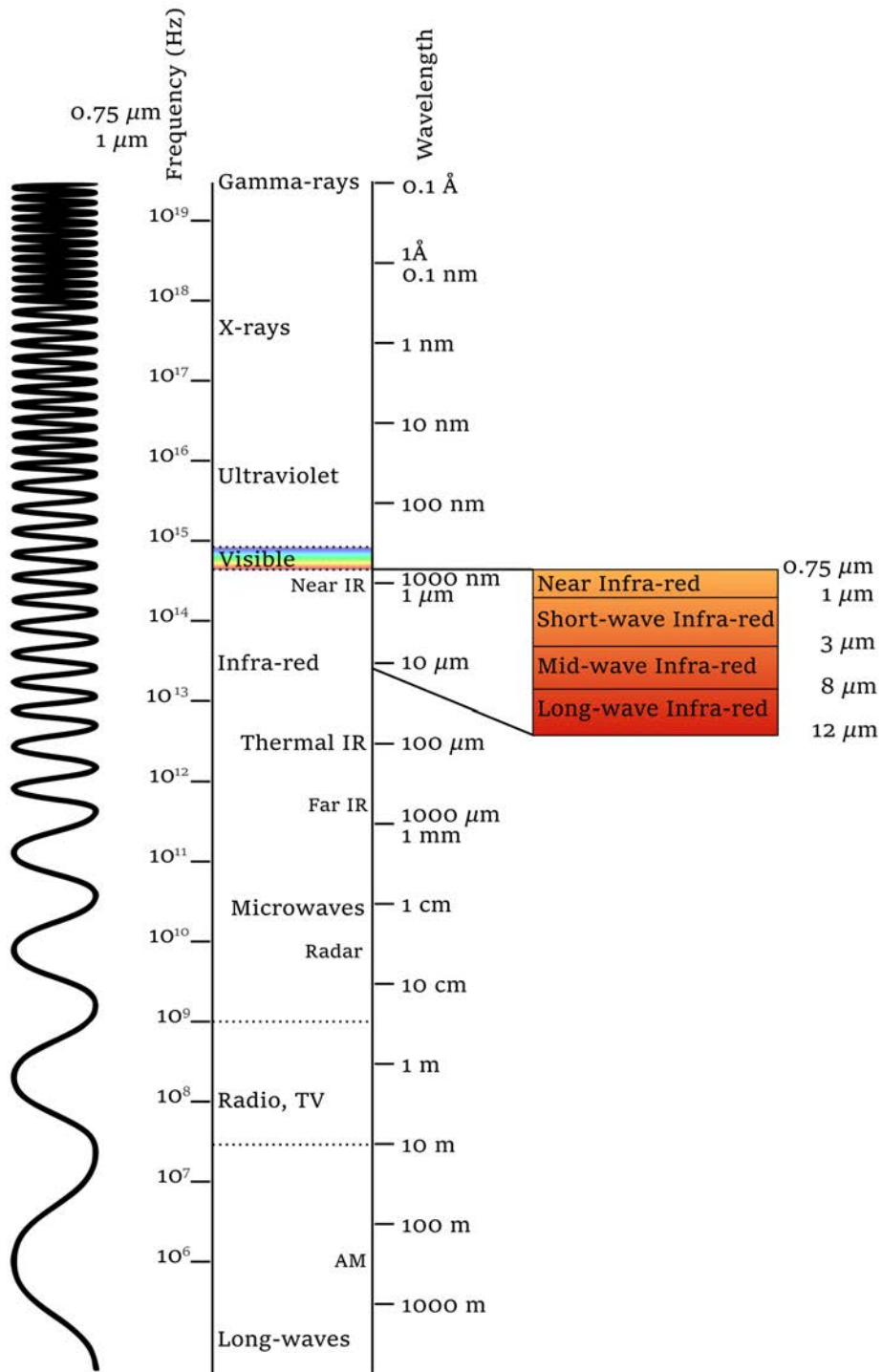


Figure 5. Electromagnetic spectrum.

3.2 Interactions between light and matter

The electromagnetic waves (*EM waves*) across the spectrum interacts with the matter depending on the EM wave frequency and the composition of the object. The nature of the different type of interaction lays on the atomic and molecular levels explained by the quantum theory (Planck, 1914; Weisskopf, 1968).

The quantum theory explains how the quantum changes in the atomic and molecular energies determine the interactions between light and matter. Quantum changes are variation between energetically higher or lower stable states.

- In the atoms, the quantum changes occur when the electron switch between orbitals.
- In the molecules, the quantum changes occur on three energy states:
 - The energy of rotation around the axes of symmetry (J).
 - The vibrational energy of the atoms around its equilibrium position (v).
 - The energy of its electrons (Λ).

Two fundamental processes are involved in the interactions:

- A) An EM wave provides part of its energy to increase an atom or molecule energy.
- B) An atom or molecule declines its energy and radiates an EM wave.

Depending on these phenomena, there are different types of interactions, that can be classified into three groups: Absorption, Reflection, and Refraction.

I. Absorption (Figure 6):

The absorption of a photon of energy by a molecule requires that the photon provides the exact amount of energy to produce the transition from one quantum state (J, v, Λ) to another valid quantum state (J', v', Λ'), changing one, two, or all three energy states. The absorption of a photon of energy by an atom requires that the photon provide the exact amount of energy to make an electron switch from its original orbital (ground level) to a higher orbital (excited level).

According to that, the energy of an electromagnetic wave is absorbed by the atoms or the molecules if its frequency corresponds to one of these quantum energetic changes. Then it is said that the frequency is in resonance.

Normally the adsorbed photon is dispersed through the time in small portions into lattice vibrations of the material molecules. The absorbed energy is transformed into heat. For this reason, inside the white houses, typical in the Mediterranean area, is cooler than inside other color houses. The whitewashed walls absorb less percentage of light, therefore less is transformed into heat.



Figure 6. a) Ideal representation of the absorption of the light. b) Whitewashed house example.

II. Reflection:

The reflection occurs when the EM wave interacts with the atoms or molecules, but the frequency of the wave does not match with one of the atom or molecule quantum changes. The photon of energy is transmitted to the atom or molecule, inducing it to a higher energy state. As the frequency does not make the atom or molecule change into another stable quantum state, the result is that the atom or molecule emits an electromagnetic wave with the same frequency. The direction of the re-emission of the EM wave indicates the type of reflection.

Diffuse Reflection (Figure 7):

In the diffuse reflection, the EM wave is reemitted with the same frequency in a random direction. The summary of this effect on a group of atoms or molecules is a dispersion in all directions of the EM waves of that frequency (schematically represented in Figure 7a). Normally the diffuse reflection happens on the surface of the matter. In Figure 7b the range of the light spectrum that corresponds to the green light is reflected diffusely by the leaf. That green color of the leaf is perceived regardless of the angle of observation, because the leaf surface is reflecting the incident light in all directions.

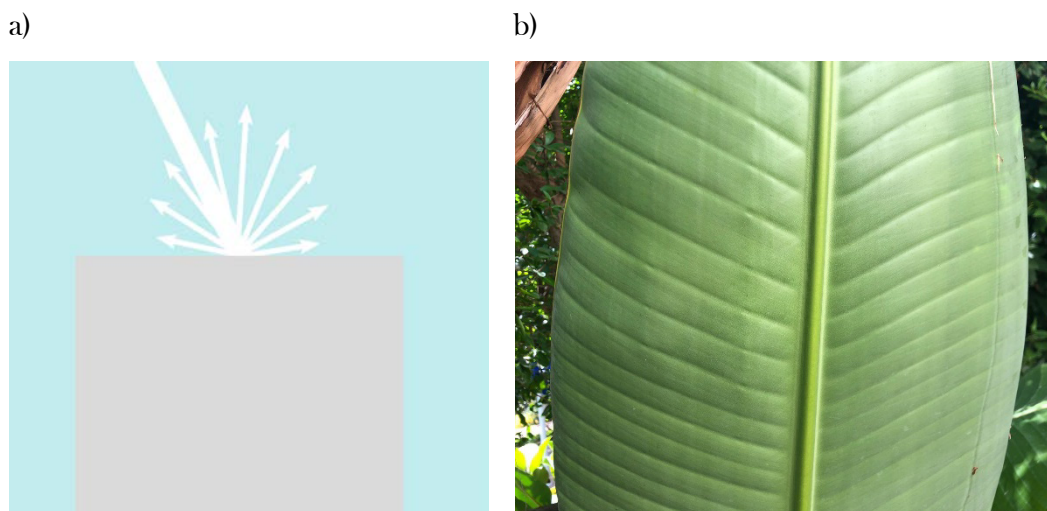


Figure 7. a) Ideal representation of the diffuse reflection of the light. b) Green leaf example.

Scattering (Figure 8):

In some cases, the surface does not reflect the wavelength; and the diffuse reflection occurs inside the matter. That interaction is called scattering (schematically represented in Figure 8a).

Figure 8b shows the classic example of scattering, the blue color of the sky. The O₂ and N₂ molecules of the air scatter the sunlight, especially the EM waves which the frequency corresponds to blue. If that scattering did not exist, the sky would be black, and the light would be just focused on the sun; as occurs in the pictures from the moon surface.

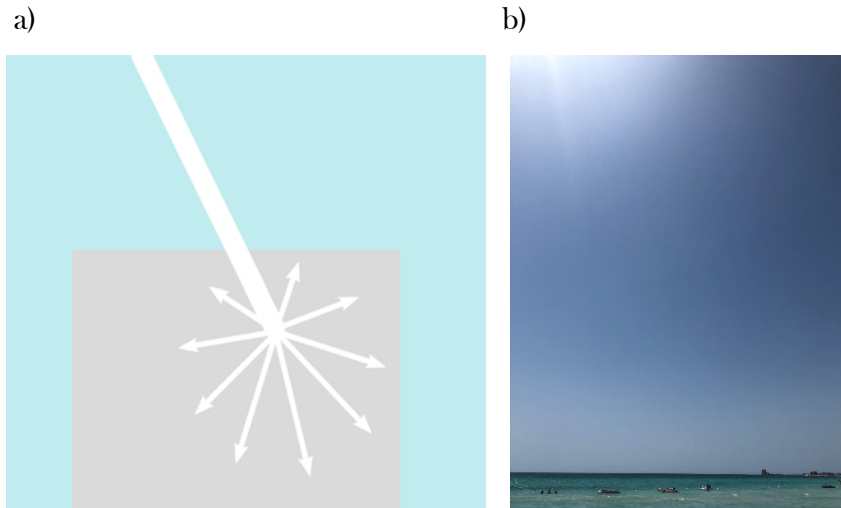


Figure 8. a) Ideal representation of the scattering of the light. b) Blue sky example.

Specular reflection (Figure 9):

The specular reflection occurs when the beam of EM waves interacts with a smooth surface of ordered molecules or atoms. The reemitted waves interfere with each other following a definite pattern. In one single direction, the inference is constructive, and the reflection in all the other direction tend to cancel each other (schematically represented in Figure 9a).

Figure 9b shows the specular reflection on the surface of the coffeepot. The light reflected by the blanket is reflected secularly by the coffeepot conserving the direction and distribution of the light, which allows observing the blanket draws reversed.

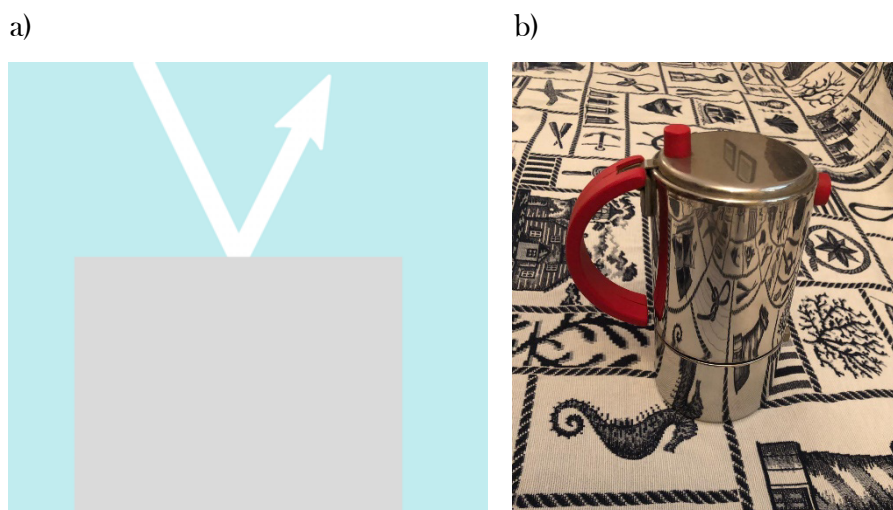


Figure 9. a) Ideal representation the specular reflection of the light. b) Metallic surface example.

III Refraction (Figure 10):

The refraction phenomenon is similar to the specular reflection, the interaction between the EM wave and the atoms and molecules gives. As a result, a definite pattern of EM waves: a constructive interference in the forward direction (the direction of the EM wave path) and destructive interferences in all the other directions (schematically represented in Figure 10a).

Figure 10b shows the effect of the refraction of the light entering into the water, that creates the effect that the spoon is crooked and split.

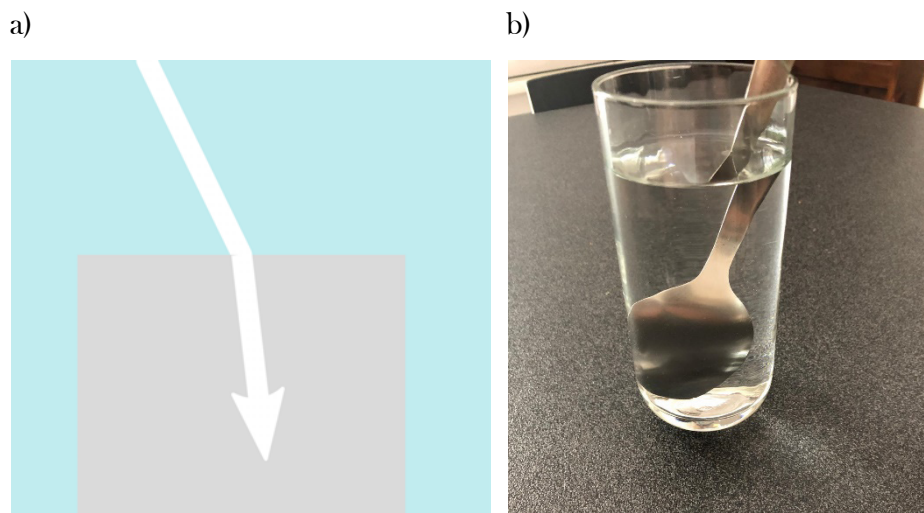


Figure 10. a) Ideal representation of the refraction of the light. b) Spoon in a glass of water example.

The interaction reduces the speed of the EM waves. When an EM wave changes the medium where it propagates, its frequency remains invariable. If the light speed is lower in the new medium, then according to Equation 2 the wavelength is reduced. The only possible continuous transition at the interface is changing the direction angle of the EM wave. (Figure 11) α and β are the angles of the rays with respect to the surface normal.

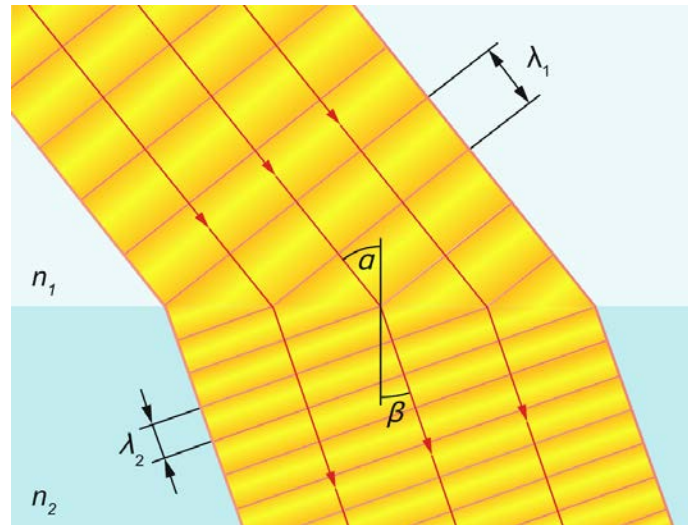


Figure 11. Effect of the refraction on a beam of light. α and β are the angles of the rays with respect to the surface normal. (based on the figure from the book *Basic Sciences in Ophthalmology* (Flammer, Mozaffarich and Bebie, 2013)).

Equation 2, developed at the same time by Snell and Descartes describes the relation between the angle of incidence (α) and the angle of refraction (β) depending on the relation between the refractive index of each medium (n_1, n_2) (Snell, 1621; Descartes, 1637). The refractive index of a medium is the relation between the speed of light in the vacuum and the speed of light in the medium.

$$\frac{\sin \alpha}{\sin \beta} = \frac{n_2}{n_1} \quad \text{Equation 2}$$

3.3 Interactions between light and water

The interaction between light and water is especially interesting for this Thesis to understand the different potential approaches to measure the degree of saturation in soils through image analysis.

3.3.1 Refraction and Reflection

In the previous Section, the general concepts of refraction and reflection have been defined. Considering the case of the interaction of a beam of light that propagates through the air (characterized by a refractive index $n_a = 1.000277$) and changes of medium to water (characterized by a refractive index $n_w = 1.330$). According to the theory, the beam of light should be refracted completely into the new medium modifying the propagation angle following Snell-Descartes law (Equation 2). However, when a beam reaches the interface between air and water, part of the light is reflected specularly. This can be observed by looking at the surface of a calm lake, as the water reflects the surrounding landscape as if it was a mirror (Figure 12).



Figure 12. Mirror effect on the calm water of the Charleston lake, Canada.

The explanation of this phenomenon is intrinsic in the definition of the refraction mechanism. As described above in the refraction process, the interferences between the light re-emitted by the different molecules tend to cancel each other in all directions except in the direction of refraction. However, near the water surface (Figure 13), the interferences between the light reflected by the first lines of water molecules do not cancel out in the direction complementary to the angle of incidence, thus forming a specular reflection.

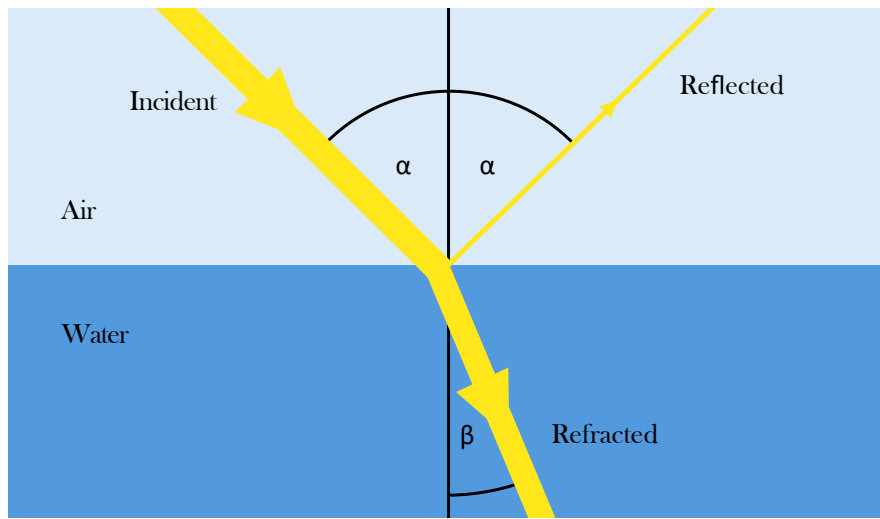


Figure 13. Refraction and reflection of a beam of light in the air-water interface.

This phenomenon occurs in general when the beam of light changes between mediums with different refractive index. Following the Fresnel equations (Fresnel, 1818) (Equation 3), when the incident angle (α) equals 0° , the amount of light reflected due to this effect can be calculated as:

Equation 3

$$R = \left(\frac{n_2 - n_1}{n_2 + n_1} \right)^2$$

The fraction of light reflected (R) is a correlation between n_1 and n_2 , the refractive indices of the initial medium and the second medium. The fraction of reflected light increases with the incident angle (α), until α reaches the angle of total internal reflection in which case all the incident light is reflected. On the mirror effect explained above, if the light was perpendicular to the lake surface, the percentage of reflected light would be 2% of the incident light. On the contrary, when a beam of light travels through an object submerged in a liquid with the same index of refraction, the combination behaves like a completely homogeneous medium to the light propagation, and no fraction of light is reflected. This light-matter interaction is the base of the degree of saturation measurement in transparent soils. The technique was developed in the Royal Military College of Canada and the Queen's University (Peters, Siemens and Take, 2011). The technique is explained and used in Chapter 8.

3.3.2 Light absorbance on the wavelength spectrum

As explained in the previous Section, the absorption of light by matter is determined by stable quantum changes in atomic and molecular energies: the rotational energy (J), the vibrational energy (u), and the electronic energy (L). The energy required for these quantum changes depends on the molecule that is excited.

In the specific case of the water molecule, the areas of the electromagnetic spectrum that coincide with stable quantum changes would generally correspond to:

- Ultraviolet (x and γ radiation): Changes in the electronic levels of atoms (L).
- Infrared: Changes in the vibrational state of the molecule (u).
- Microwaves: Changes in the vibrational and rotational state of the molecule (u, J).

These bands of the electromagnetic spectrum in which water is more absorbent to light can be used to determine the degree of saturation of soil. The choice of which spectrum band use depends on the resolution that is required in absolute units. The wavelength of each band of the spectrum determines the minimum pixel size that can be obtained. For example, bands corresponding to microwaves have a minimum pixel size of 1 dm. A minimum resolution adequate for measures of the degree of saturation in the field, but insufficient for the laboratory. As a clarification, the final resolution depends on the sensors used, the resolution defined above is the most accurate that can be reached by the limits of the physics of electromagnetic waves (Wozniak and Dera, 2006).

At the level of geotechnical testing in the laboratory, the most suitable bands are visible and infrared. Therefore, the explanation is focused on this part of the electromagnetic spectrum.

The light absorbance by water on these bands is controlled by the vibrational states of the water molecule. The water molecule has three vibration modes, which correspond to the quantum numbers ν_1, ν_2, ν_3 . The mode ν_1 corresponds to symmetric stretch vibrations. The mode ν_2 corresponds to bending deformation vibrations. The mode ν_3 corresponds to asymmetric stretch vibrations (Figure 14).

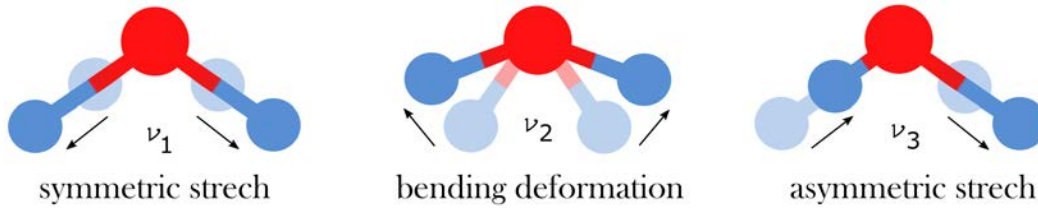


Figure 14. Vibration modes of the water molecule.

Stable vibration excited states correspond to specific combinations of these three modes of vibration. Wavelengths that its energy coincides with one of these stable excited vibration states tend to be absorbed and retained by the water molecule with which they interact (Table 3).

Table 3: Bands of the wavelength with light absorbance by water, beside the correspondent vibrational state of the excited water molecule.

| Symbol | Wavelength | Assignment |
|--------------------|------------|--------------------------------------|
| α | 739 nm | $a\nu_1 + b\nu_3; a + b = 4$ |
| μ | 836 nm | $a\nu_1 + \nu_2 + b\nu_3; a + b = 3$ |
| $\rho \sigma \tau$ | 970 nm | $a\nu_1 + b\nu_3; a + b = 3$ |
| φ | 1200 nm | $a\nu_1 + \nu_2 + b\nu_3; a + b = 2$ |
| ψ | 1470 nm | $a\nu_1 + b\nu_3; a + b = 2$ |
| Ω | 1900 nm | $a\nu_1 + \nu_2 + b\nu_3; a + b = 1$ |
| χ | 2870 nm | ν_3 |

Figure 15 plots the bands of light absorbance, defined in Table 3, respect to its wavelength. Notice that the most absorbent bands lay on the Short-Wave InfraRed part of the electromagnetic spectrum, while in the visible part the absorbance is almost negligible.

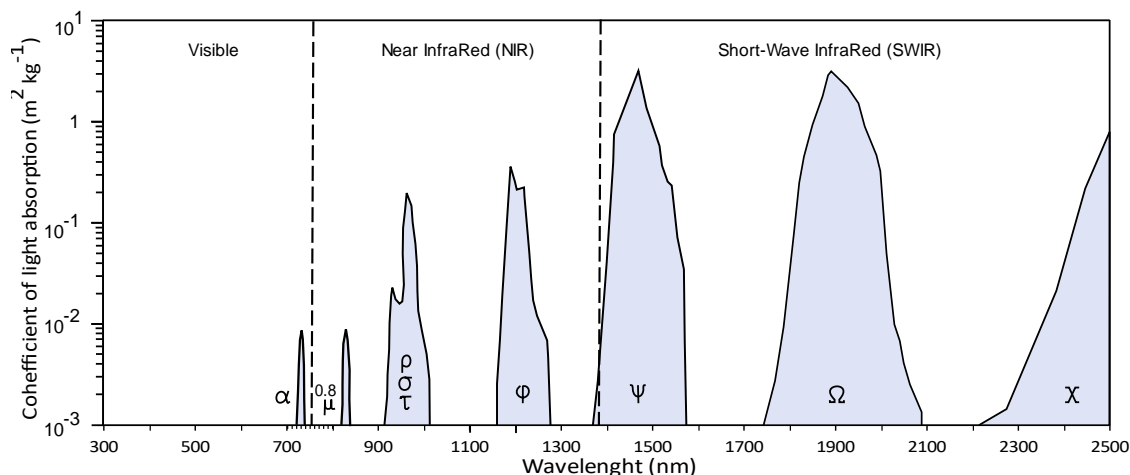


Figure 15. Coefficient of light absorption by water depending on the light wavelength (visible, NIR and SWIR). Based on the figure from the book *Light absorption in seawater* (Wozniak and Dera, 2006).

This light-matter interaction is the base of the developed technique to measure the degree of saturation using Short-Wave InfraRed images. The technique is presented, calibrated, and validated in Chapter 6.

3.4 Conclusions

The physical principles of light are the base of some techniques introduced in the Thesis. Light behaves as a wave when it propagates and like a particle when it is detected. The electromagnetic wave is the general term for light. Each EM wave is characterized by its amplitude, wavelength, and frequency. The electromagnetic spectrum classifies the EM waves depending on their frequency/wavelength. These two parameters are intrinsically tied and define the physical properties and the energy of the electromagnetic wave.

The interaction between light and matter is ruled by quantum theory.

- The absorption of light occurs when the energy of the EM wave coincides with a stable quantum change in the atomic and molecular energies of the matter. Else, different types of reflection or refraction occur depending on the molecule arrangement.
- The refraction of light occurs when it changes the medium where it propagates to another medium with different index of refraction. However, the mirror effect takes place in the surface of the second medium: a percentage of the light is reflected specularly.

4

Chapter 4

Development of apparatus and sensors

The techniques presented in this Thesis are applied to experiments performed inside the geotechnical laboratory facilities. The performance of the experiments requires the design and construction of specialized apparatus. The most relevant apparatus development and improvement realized during the Thesis are detailed in this Chapter.

- **4.1** The transparent tank to perform the 1G experiments with control of different boundary conditions. The design and construction were assisted by the UPC laboratory technician Tomás Perez.
- **4.2** The low budgeted alternative moisture sensors using an Arduino shield.
- **4.3** The direct shear test for unsaturated soil samples at low stress. The design and construction were assisted by the UPC laboratory technician Mercedes Sondon.

4.1 Transparent tank for 1G experiments

The tank was designed and built, especially for the purpose of this Thesis. Its most important features are versatility, to perform a different type of experiments on the soil at 1G, and transparency, to different ranges of the light spectrum to record and analyze the experiments. The characteristics of each one of the parts that form the tank are detailed below.

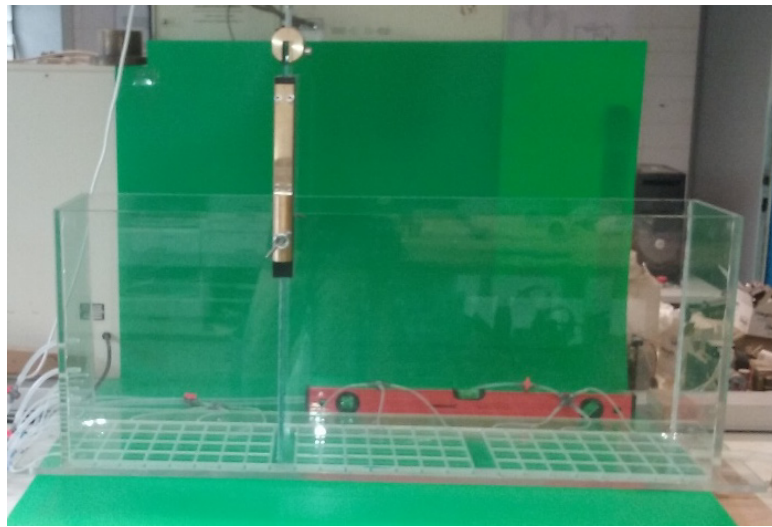


Figure 16. Overview of the tank from the main face.

Dimensions and materials

The tank dimensions are 1000mm long, 200mm wide, and 412mm high (Figure 17). The material of the entire box is transparent methacrylate, except the main face made of laminated glass (10mm thick) to avoid scratches from sand experiments affect the image quality of following experiments.

The lateral and back walls have a thickness of 12mm. A horizontal line of 5mm holes was drilled in the lower part of the walls to inject water. A vertical line of three 50mm holes was drilled, where three rubber plugs were fit to install moisture sensors.

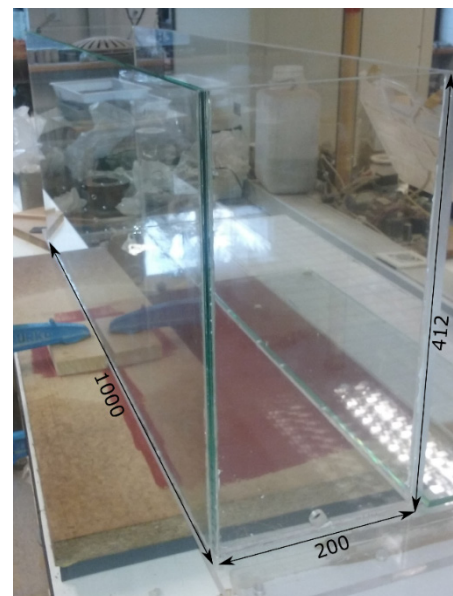


Figure 17 Dimensions of the tank.

Lower and lateral water injection

Lower water injection system (Figure 18). A methacrylate plate was mechanized to create a system of channels and holes. These channels distribute the water injected from the sides to a grid of pores. There is a pore in each intersection of the channels; the grid of pores ensure that the water is equally injected on the lower surface of the soil. Two divisions of the channels create three independent zones of lower water injection. The keys of passage allow controlling the area of wetting.



Figure 18 Lower water injection system, at the initial moment of injection.

After some experiments, an alternative lower water injection system was implemented (Figure 19). The mechanized methacrylate plate was substituted by a layer of gravel, to simulate a high permeable aquifer. This alternative system, combined with a hanging water column system, allows to define and keep a water level while the water raises by capillarity through the sample soil. A similar system of lateral water injection is implemented to simulate variation on the upstream level.

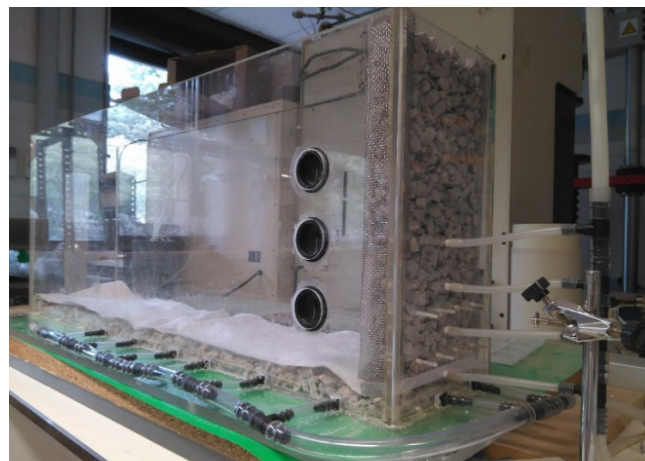


Figure 19. Modified lower and lateral water injection system.

Upper water application

A drip system with a regular matrix of nozzles separated 10 mm has been created to simulate rainfall (Figure 20). The system allows graduating the intensity of rain until a maximum flow rate of 0.0257 l/s (equivalent to precipitation of 0.6425 mm/s on a 200x200 mm area).



Figure 20. Upper water system.

Guillotine

A guillotine has been designed to set and release lateral confinement (Figure 21).

The basic guillotine consists of a laminated glass sheet of 10mm thick with a system to attach it to the tank that allows its vertical movement. This system can be loosened to move the guillotine laterally and change its location. The slip release system is removing the guillotine vertically with a pulley system. When the guillotine is entirely vertical, the release is not instantaneous but in less than 0.1 seconds.

Subsequently, a system with a second glass has been added, which allows giving an initial angle to the slope. The system consists of screws to modify the angle and set it at will. The conjunction of the two systems allows the immediate release of the slope, as required.



Figure 21 Guillotine with the system to fix the initial angle.

Ambient humidity

A CoolMist type humidifier has been acquired from the TaoTronics company. This allows elevating the environmental humidity to a level close to 100% using cold steam at a speed of 5mL / min. It has been adapted so that the steam is focused on the tank without changing the humidity of the laboratory (Figure 22).

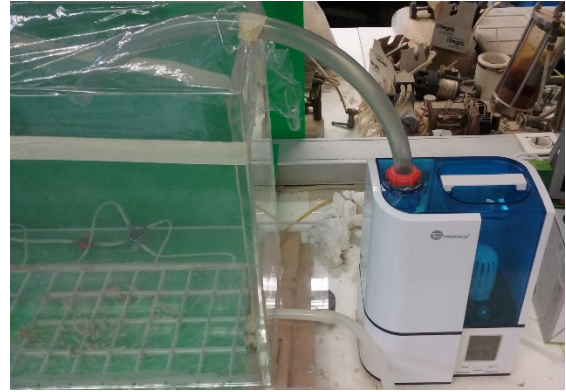


Figure 22 Humidifier adapted to the tank.

Illumination and camera holding structure

The structure is build using metallic slotted angle bars, and it is attached to the tank base (Figure 23). The purpose of the structure is to predefine the cameras distance and the light distance and angle respect to the main wall of the tank. The importance of the fixed distances of cameras and lighting is explained in Sections 5.4 and 5.5.

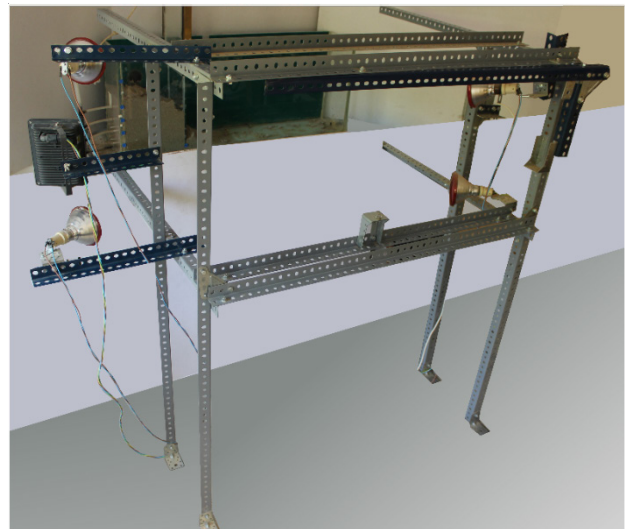


Figure 23 Illumination and camera holding structure.

4.2 Low-cost moisture sensors

The moisture sensors used on the unsaturated experiments are SEN0193. These sensors are controlled by an Arduino board. Arduino is a platform for the electronic creations, which is based on open-source hardware and software, flexible and easy to use for nonelectronic engineers.

Arduino was developed by Hernando Barragán, Massimo Banzi et al. in Interaction Design Institute Ivrea, Italy (Barragán, 2004; Banzi and Shiloh, 2014). The Arduino moisture sensors are an affordable option compared to the classic laboratory moisture sensors from the market. Besides, the programming of the sensors is simple and do not require specialized data logger.

The SEN0193 sensor measures the soil moisture levels by capacitive sensing. This procedure of sensing does not cause the corrosion of the sensor, in comparison with the classic resistivity sensing that causes the rusting of the sensor. This is important because the rusting of the sensor makes the data unreliable after a few measurements, which is the problem that suffers most of the other moisture sensors controlled with Arduino.

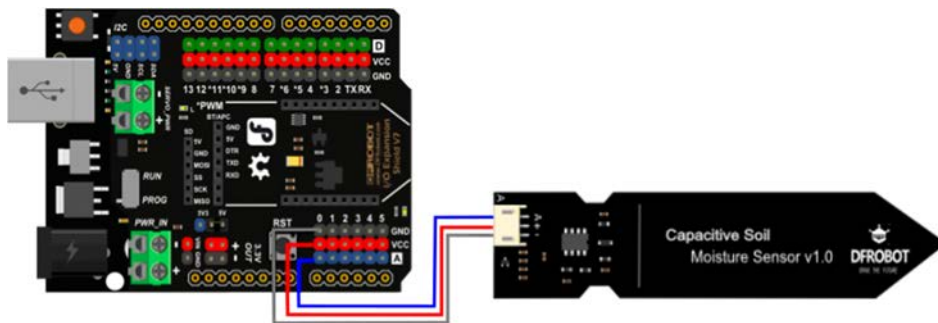


Figure 24. Instructions to connect the SEN0193 moisture sensor to an Arduino shield (DFRobot, 2018).

A code was programmed to control 4 sensors, store the results on an excel file using a macro while plotting a reference number on an LCD screen to correlate the results with the images. A Gravity I/O expansion shield was used to firmly connect the 4 sensors and the LCD screen to the Arduino board.

4.2.1 Calibration procedure for the sensors

The calibration of the SEN0193 sensors was performed to correlate the value that Arduino read with the degree of saturation of the sand where it is placed. The initial calibration procedures were performed individually to evaluate the consistency of the values obtained by the sensors. The surrounding elements attached to the sensors might affect to the values measured. Afterward, the measurements were performed with multiple sensors measuring at different time-lapses. The distance between the sensors might cause interferences on the measurements between the sensors. These two conditions determine that the calibration procedure had to be performed replicating the placement of the sensors in the tank. A methacrylate sheet was drilled to fit three rubber plugs at the same distances as in the tank. The sheet was placed on the soil surface, and the sensors were thrust on slot of the rubber plugs. The final calibration procedure disposition is shown in Figure 25.

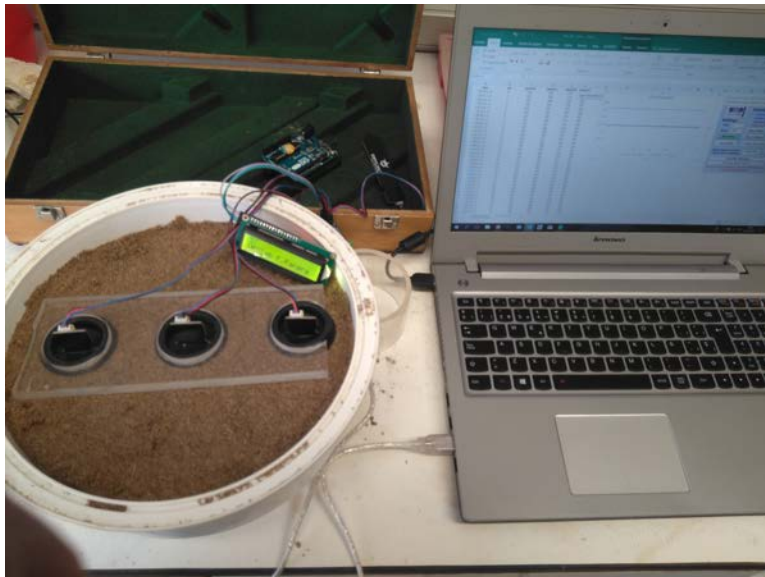


Figure 25. Disposition of 3 sensors for the calibration. The disposition recreates the tank arrangement to consider possible interferences between the sensors and the effect of the rubber plug.

Figure 26 presents the calibration curve (purple) that correlates the sensor value with the degree of saturation of the sand that is measuring. The calibration curve is specifically calculated for the beach sand from Castelldefels, used on most of the experiments on this Thesis. Figure 26 also shows the percentile 90 and 10 to express the deviation on the measurements that the sensor might have. The sensor is highly accurate on the low degree of saturation. On the high saturated soils, the measurements are not precise because of different degree of saturation shear a similar sensor value.

In conclusion, the SEN0193 sensor is a good alternative to the classic laboratory sensing for low budget projects where the high accuracy of the sensor is not mandatory.

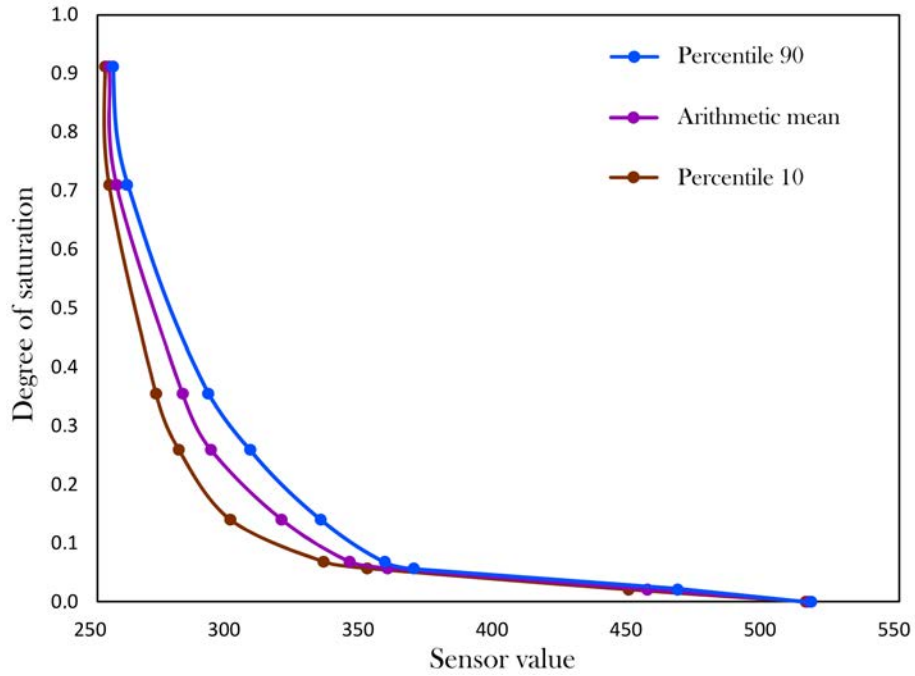


Figure 26. Calibration curve of the SEN0193 moisture sensors.

4.3 Direct shear apparatus for low-stress tests

The experiments presented in this Thesis are carried out in the laboratory facilities. This limits the soil sample size to the decametric level. The experiments are performed in 1G. That characteristics imply that the stresses are on the range of the kPa. That range of stresses and pressures are not used on the standard laboratory test, designed to perform the conditions several meters below the soil surface.

4.3.1 Initial tests in the standard direct shear apparatus

That problem was evident on the measure of the friction and dilatancy angles of the studied soil under low stresses. Initially, the measures of the properties were performed in the standard direct shear test available in the UPC geomechanical laboratory. The vertical load that the mechanism enables to apply was too high compared with the aimed pressures. The standard vertical load mechanism was removed, and the vertical load was imposed by placing the weight directly on the soil sample. That proceeding seemed to be sufficient to perform the direct shear test under the needed range of stress. The comparison of the results of several tests at different vertical loads and shearing velocities exposed some problems to understand the soil behavior. The results did not show any correspondence between the friction angle and the vertical load. The behavior of the soil extracted from the results was erratic and without consistency. That unexpected behavior of showed on the results was caused by the improper shear apparatus used. The inherent friction between the pieces of the apparatus, which was negligible in high vertical loads, was causing noise on the results that conceal the soil behavior. This first experimentation concludes with the necessity to design and build a new direct shear apparatus specially suited for low stresses.

4.3.2 Literature review

Before the design of the direct shear apparatus, a literature review was performed to implement the ideas developed previously. The direct shear apparatus for unsaturated soils developed by Likos et al. provides the ideas of the suction system (Likos *et al.*, 2010). These ideas were confirmed with the other studies of direct shear test on unsaturated soils (Purwana *et al.*, 2012)

Lings and Dietz did a review and proposed their own modification of the direct shear apparatus to ensure the normal vertical load (Lings and Dietz, 2004). The Thesis written by Amarasinghe provides an interesting review of the direct shear test parts (Amarasinghe, 2013).

4.3.3 Design and materials

The direct shear apparatus was designed to be performed in the range of stresses used in the Thesis experiments, from 0 to 10 kPa. The apparatus characteristics are prepared to test soil samples in unsaturated conditions. The disposition of the pieces enables the observation of the shear band during the test. An initial overview of the designed apparatus is exposed in Figure 27 and Figure 28. The detailed description is arranged below.

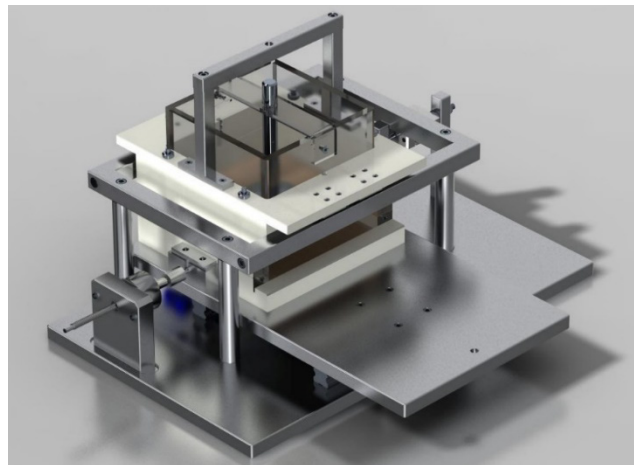


Figure 27. Frontal view of the designed direct shear apparatus for low-stress tests.

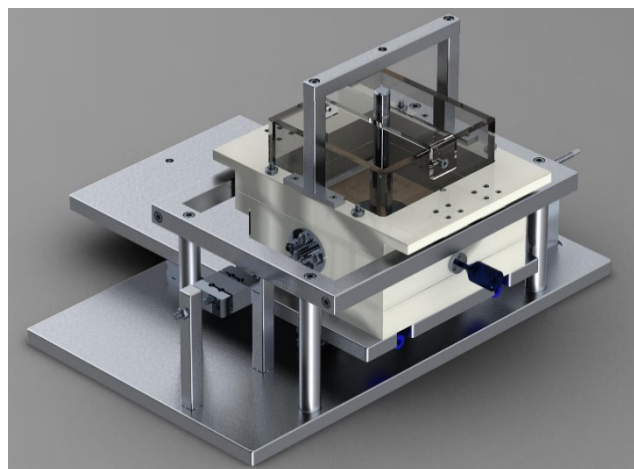


Figure 28. Posterior view of the designed direct shear apparatus for low-stress tests.

Figure 29 displays an expanded view of the direct shear apparatus, where all the main pieces can be observed individually. The apparatus pieces are classified into six categories for a better description: shear box, holding structure, vertical load system, suction system, motor, and load cell. The descriptions of the material, dimensions, and characteristics of each part are detailed below.

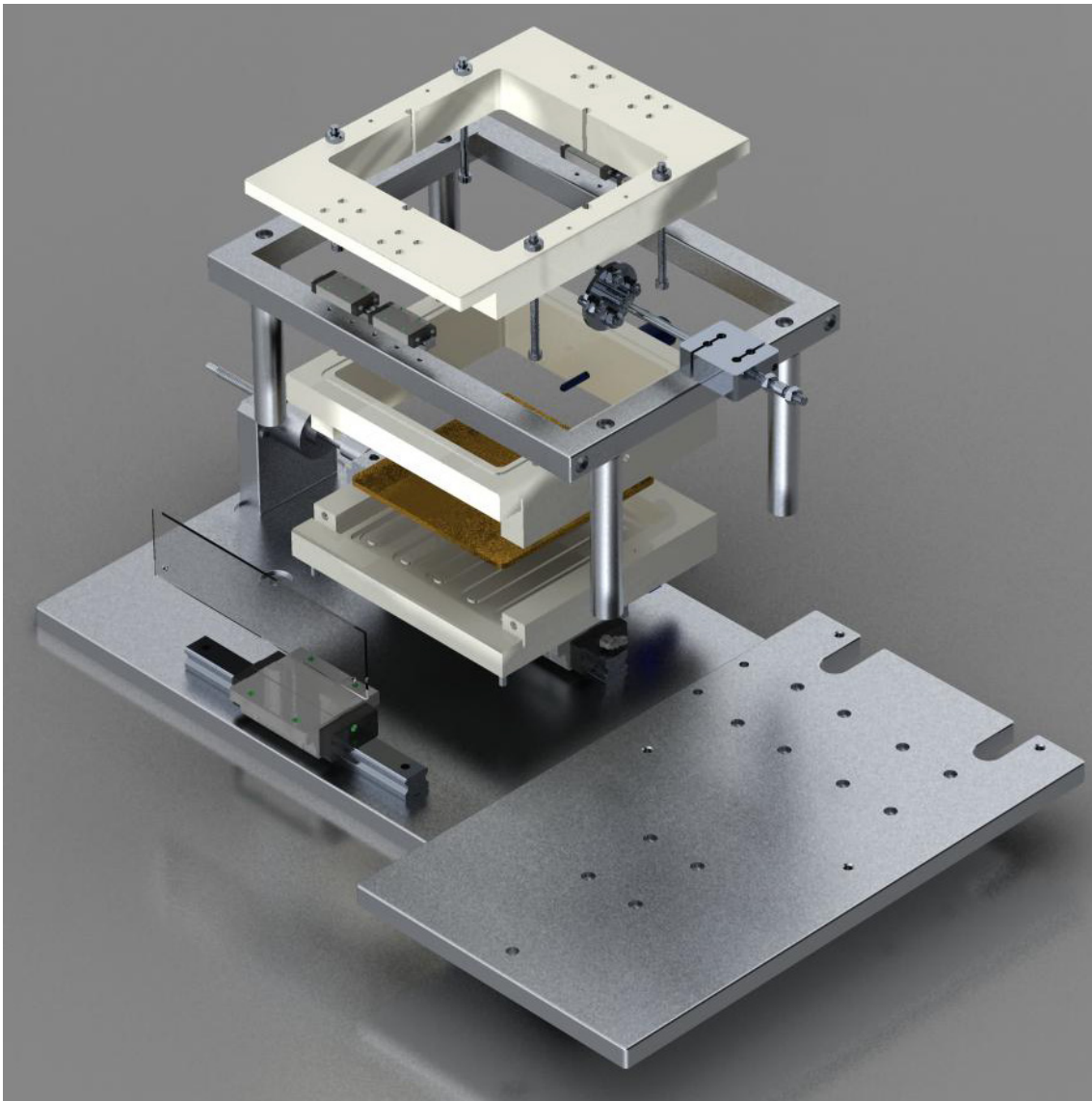


Figure 29. Expanded view of the direct shear apparatus pieces.

Shear box

The shear box is made of polyacetal (POM), also known as polyoxymethylene, acetal, polyformaldehyde, and Delrin. The POM is a synthetic polymer with optimal characteristics for this project; the properties are summarized in Table 4 and commented below.

Table 4 Polyacetal physical properties

| Property | Value | Units |
|--|-------|-------------------|
| Density | 1410 | kg/m ³ |
| Friction coefficient | 0.21 | |
| Wear resistance | 0.75 | u/km |
| Tensile elastic modulus | 3100 | MPa |
| Tensile strength | 70 | MPa |
| Compressive strength | 110 | MPa |
| Flexural elastic modulus | 2900 | MPa |
| Flexural strength | 110 | MPa |
| Poisson coefficient | 0.35 | |
| Water absorption (immersion 24 hours) | 0.2 | % |

The low density (compared to steel [7850 kg/m³] and aluminum [2700 kg/m³]) and the low friction coefficient are the most critical properties to reduce the noise in the results created by the friction between pieces. The high mechanical strength ensures the negligible strain due to the tensile and compressive stresses that are applied during the test. The low water absorption makes it suitable for unsaturated and saturated tests. Moreover, the POM is a thermoplastic easy to machine to create the shapes that fit the pieces together.

The shear box external dimensions are 190x190x110 mm with two wings on the top. The internal dimensions are 150x150x100 mm. The box is divided in three parts:

- Upper: 190x250x30 mm
- Middle: 190x190x50 mm
- Lower: 190x190x30 mm

The lower and middle parts form the sample box. This part of the box can be extracted to place the soil sample inside. The soil sample admitted dimensions are 150x150x40mm.

The lower part is the active side of the shear box that moves at a constant velocity. It is supported and moves attached to the moving baseplate made of aluminum (Figure 30). The internal base of the box has a serpentine carved on, with a sintered sheet on it to provide the suction (explained in the suction system section).

The middle and upper parts are the passive side of the shear box that remains fixed and experiments the effects of the soil friction. The middle part is attached to the upper part with four threaded rods (Figure 29). The upper part is supported by two sliding blocks mounted on their linear guides (Figure 30). This allows the passive side to move freely as a reaction of the soil friction.

The upper and lower parts height are fixed, as they are attached directly to the holding structure (Figure 30). The height of the middle part is regulable using the threaded rods. The regulation of the middle part height is important to obtain the desired distance of the shearing surface (between the lower and middle part). This distance is essential to be minimal to ensure that any soil grain slips between the two parts; but, at the same time, the interface between the lower and middle parts should have the minimal vertical stress to avoid the friction between the pieces affect the results.

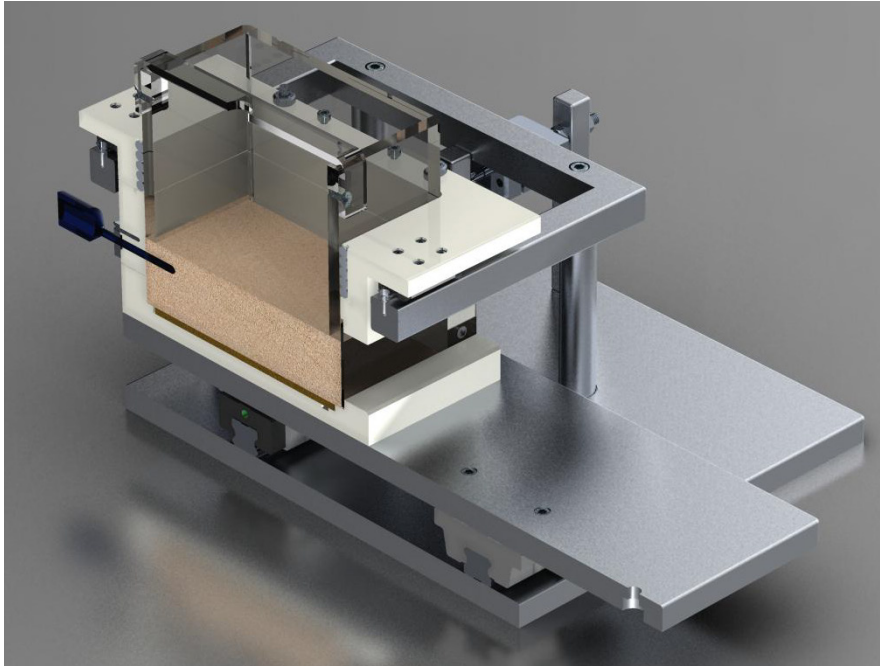


Figure 30. Half slice of the apparatus. The arrange between the shear box, and the holding structure is visible.

The visor is a rectangular glass plate (190x50x2 mm) fixed to the lower part. The visor covers the entire lateral surface of the soil sample, perpendicular to the shear surface. That enables to observe and record the displacements of the soil grains. The images are analyzed using the image correlation techniques, the PIV-NP post-process (Chapter 5), and degree of saturation measurement by SWIR images (Chapter 6). The contact line between the lower and middle parts in the middle of the shear surface would be inconvenient for proper image analysis. For that reason, the visor is a single glass plate that covers the area of the lower and the middle parts (Figure 33). The middle part slides along the top of the visor without covering it.

Holding structure

The holding structure is made aluminum. Aluminum was the chosen metal for its stiffness and the low density. The holding structure is divided into three main parts (Figure 29):

- Stable baseplate: 300x480x15 mm
- Moving baseplate: 400x230x15 mm
- Perimeter structure: 280x275x20 mm

The sable baseplate function is to hold all the parts at a fixed distance. The parts screwed to it are: the perimeter structure bars, the motor holding piece, the load cell holding piece and the two main linear guides. The moving baseplate is screwed on four sliding blocks that move along the two main linear guides (Figure 31). A camera might be placed and screwed to the moving baseplate to record the soil sample through the visor during the full shear test.

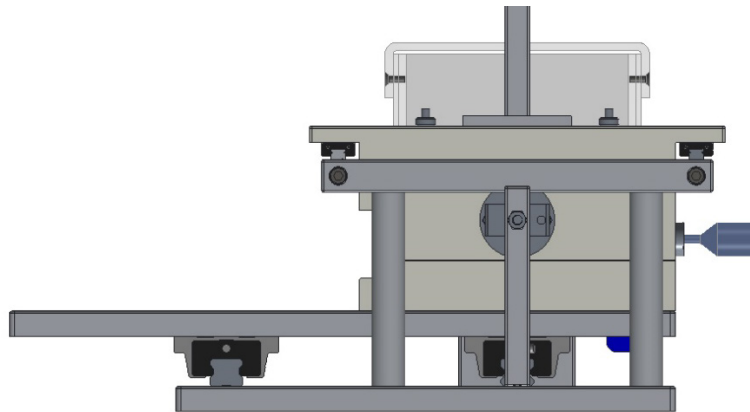


Figure 31. Design plan - lateral view. The linear guides and sliding blocks engagements are visible.

The perimeter structure is made by prismatic bars (Section 20x20 mm). The structure leaves an internal space of 260x255mm, where the shearing box is placed (Figure 29). Two linear guides are screwed on the bars parallel to the movement. These bars serve as a holding to the upper and middle parts of the shearing box (Figure 31). An arc to hold the vertical LVDT is screwed on the top of the perimeter structure (Figure 32).

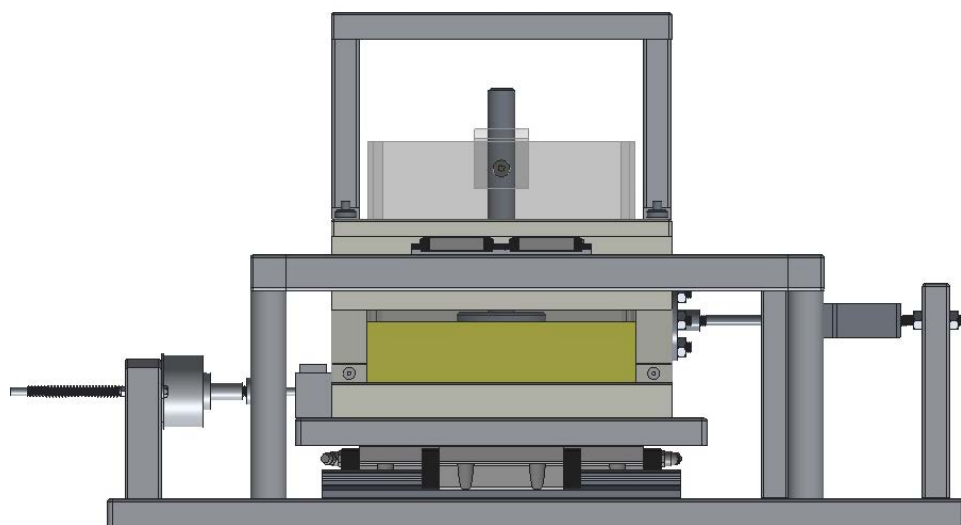


Figure 32. Design plan - frontal view. The arc to hold the vertical LVDT is visible.

Vertical load system

The vertical load system is based on a box made of polymethyl methacrylate (PMMA), also known as acrylic or plexiglass. The dimensions of the box are 149x149x100 mm. The superior side of the box is opened, and the inferior side is covered by a thin rubber membrane. Attached to the membrane a bar transfer to the LVDT, the vertical displacements produced by the compaction or dilatancy of the soil sample.

The load is produced by a set of lead or iron balls placed inside the box. The flexibility of the combination between the membrane and the weight balls permits the vertical application of the load, avoiding the tilting problem of rigid weights.

The load box slides inside the upper part of the shear box using rotation ball rows installed inside the shear box (Figure 33). That system permits the pure vertical displacement of the load box without adding friction between the parts.

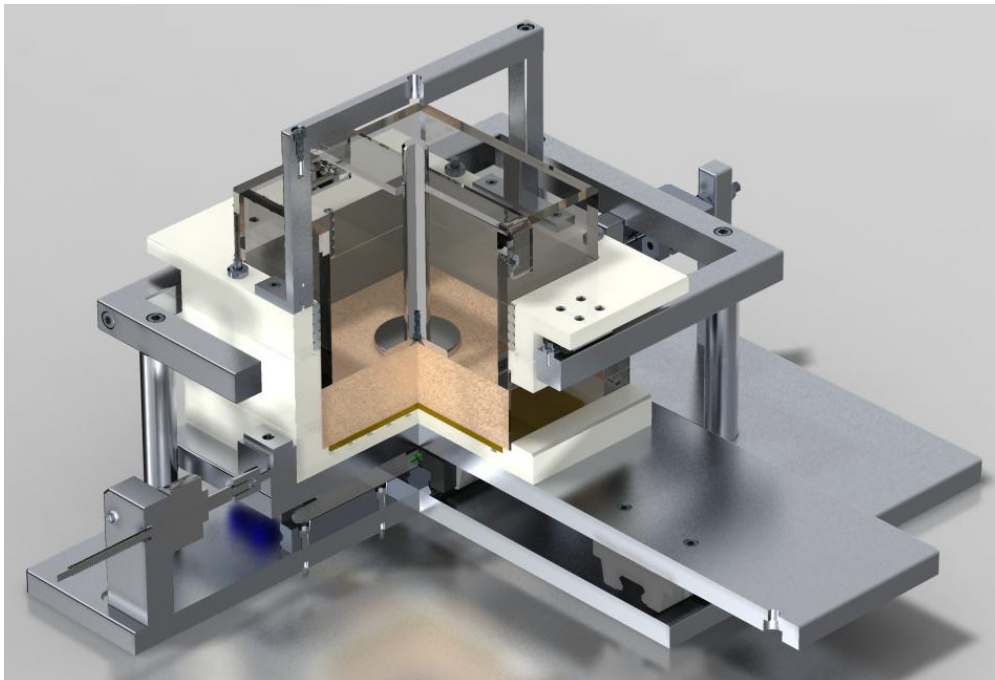


Figure 33. Interior view of the direct shear apparatus with a soil sample inside. The vertical load system is visible.

Suction system

The suction system is built in the lower part of the shearing box. A serpentine channel is carved on the superior face of the box base (Figure 34). The initial and final points of the channel are connected to a standard hanging column assembly, which provides a predefined suction.

The face of the box with the incised channel is fully covered by a sintered metal sheet (Figure 29). The sintered sheet is a plaque created by the partial fusion of small metallic balls. Through this process, the balls get merged, creating a pore medium. The function of this sheet is to transmit the suction distributed by the serpentine channel to the soil sample, without letting the grains soils enter into the channel. The properties of the sintered sheet are summarized in Table 5.

Table 5 Sintered metal sheet properties

| Property | Value | Units |
|--------------------------|--------------------|---------------|
| Grade | B8 | |
| Porosity | 0.32 | |
| Maximum pore size | 23.4 | μm |
| Permeability coefficient | $2 \cdot 10^{-12}$ | m^2 |
| Bobble point pressure | 3.93 | kPa |
| Shear strength | 130 | MPa |

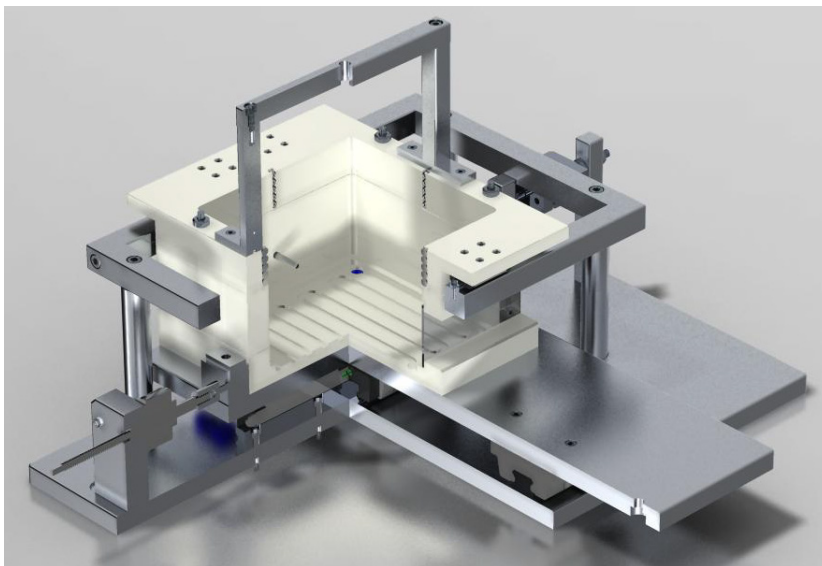


Figure 34. Interior view of the apparatus without soil sample, vertical load system nor sintered filter.

Motor

The chosen motor to move the lower part of the shearing box is an RS Pro 100N Electric Linear Actuator. The motor body is fixed to the stable baseplate. This model is a stepper motor. A stepper motor is an electric motor where the full rotation is divided into an equal number the steps (in this model 300). The motor is controlled by an electronic shield that sends sequential input pulses to the motor electromagnets. Each pulse creates a fraction of the full rotation. The velocity of the motor is controlled, modifying the velocity of pulses. This property of the stepper enables to impose a constant or gradual increasing velocity in a high range of speeds. The velocity is unaffected by the resistance (in this model up to 100 N).

This model of motor is particular because it is also a linear actuator. The motor axis is a leadscrew with a longitude of 61 mm. Therefore, for each fraction of rotation of the motor, the leadscrew advances a certain distance. The end of the leadscrew is attached to the lower part of the shear box (left side of Figure 35). The attachment allows the free rotation of the leadscrew while moving forwards or backward with it. This combination between the stepper motor and the linear actuator simplifies the control of the linear velocity imposed in the shear box.

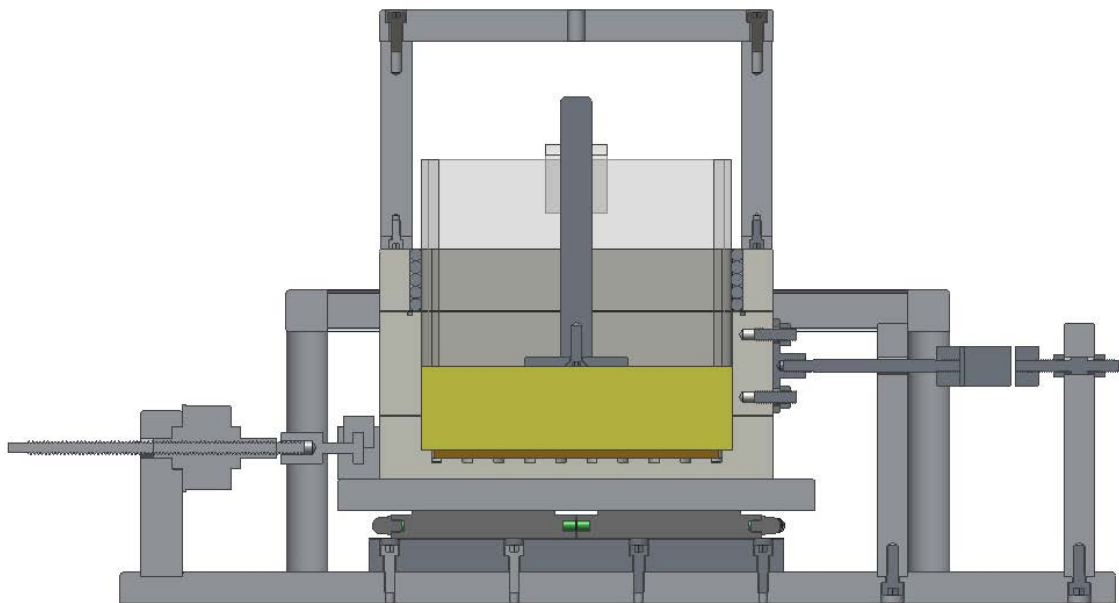


Figure 35. Design plan - parallel cut. The attachment pieces for the motor and the load cell are visible.

Load cell

The load cell used in the designed shear apparatus is CTCM load cell with 10 Kg range. The disposition of the load cell follows the traditional arrangement: the cell is screwed in the back to a threaded rod that fixes it to the stable baseplate. The front part of the cell is screwed to a bar that is attached to the middle part of the shear box (passive side). The arrangement is visible in the right part of Figure 35.

4.4 Conclusions

- **Transparent tank:**

The transparent tank was designed and built to perform scale experiments at 1G. The contour conditions of the soil inside the tank that can be modified are: upper, lower and lateral water injection, angle of the lateral confinement (removable), and ambient humidity. The holding structure to place the light system and cameras is attached to the tank.
- **Moisture sensors:**

A low-cost moisture sensor alternative was calibrated. The sensor control and the data acquisition system is Arduino based.
- **Direct shear apparatus for low-stress tests:**

The traditional direct shear apparatus intrinsic noise make them unsuitable for low-stress tests. The direct shear apparatus with low friction was designed focused on the range of stress found in 1G scale experiments. A suction system in the base of the shear box enables the unsaturated soil tests. The full test might be recorded through a glass window in the lateral of the shear box. The window is not divided, there are no interferences in the shear band vision.

5

Chapter 5

Analysis of scale experiments by PIV-NP

This Chapter focusses on the Particle Image Velocimetry - Numerical Particle (PIV-NP) post-process code developed together with Núria Pinyol and Mauricio Alvarado. The Chapter is divided into three sections.

- Section 5.1 the PIV-NP method is described from the conceptual idea to the algorithm.
- Section 5.2 shows the evaluation and validation of the method by means of tests based on synthetic data, synthetic images, and real images.
- Section 5.3 presents the application of the method PIV-NP in a small scale laboratory test.

5.1 PIV-NP description

5.1.1 Introduction

The idea of the PIV-NP arises from the need for a method that combines the useful characteristics of the two types of image correlation methods (Eulerian and Lagrangian) for geotechnical purposes. The aim is to combine the robustness and the flexibility to correct errors of the Eulerian method (Section 2.3.1), with the Lagrangian conception of the medium that is more useful for the analysis of soil behavior (Section 2.3.2).

The most effective procedure for this objective has been to develop a post-process code that uses the results of a Eulerian image correlation as input data. The post-process transforms them into the Lagrangian paradigm to calculate and store the evolution of the parameters of each part of the soil. The use of already existing image correlation codes takes advantage of the great advances that have been made on that field and facilitates to keep updated with the improvements.

The fundamental concept of the post-process has its origin on the Material Point Method (MPM) procedure. The MPM is a numerical method, alternative to FEM and DEM, especially useful to model large displacements (Sulsky, Chen and Schreyer, 1994). Our investigation group in Universitat Politècnica de Catalunya is widely involved in the MPM code development (Alonso, Pinyol and Yerro, 2014; Yerro Colom, 2015; Yerro, Alonso and Pinyol, 2015; Alvarado Bueno, 2018; Pinyol *et al.*, 2018).

On the Material Point Method, the media is discretized in two different frames, one Lagrangian and other Eulerian. The Lagrangian discretization consists of the division of the continuum into a set of material points; each one represents a portion of the domain. The material point moves attached to its represented subdomain and carries all its information (mass, velocities, strains, and stresses).

The Eulerian discretization consists of a computational mesh, similar to one the used in FEM, covering the full problem domain. The governing equations are solved on the mesh nodes.

The sequence of a time step on Material Point Method is:

1. The variables carried on the material points are transferred to the nodes using shape functions.
2. These variable values are used to solve the discrete governing equations in the nodes.
3. The variables carried on the material points are updated, mapping the mesh results, using the same shape functions.
4. The material points move to their new calculated location.
5. The mesh is reinitialized, and its associated information discarded.

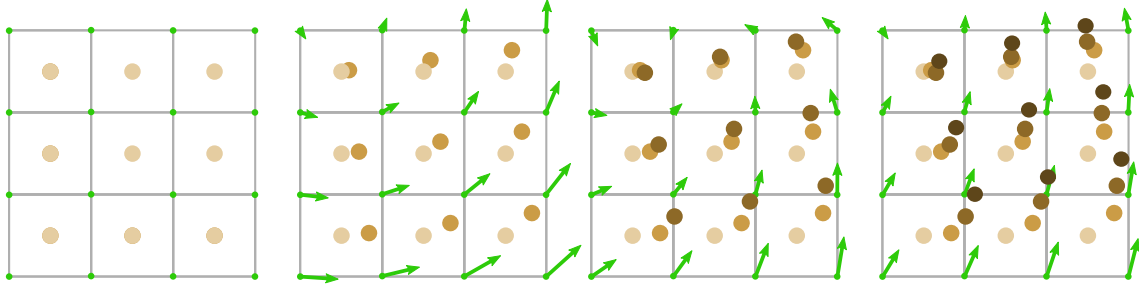


Figure 36. Graphical representation of the MPM scheme used by PIV-NP

The PIV-NP is based on the MPM double discretization. The media is discretized in two different frames, Lagrangian and Eulerian. The Lagrangian discretization consists of the division of the area of interest into a set of numerical particles (NP). Each NP carries the information of the subarea that represents and moves attached to it. The Eulerian discretization consists of the grid extracted from the previous Eulerian Image Correlation analysis.

The sequence of the PIV-NP algorithm is based on the 2D MPM but without solving governing equations on the nodes. Instead, the results mapped on the numerical particles are the displacements measured in Eulerian Image Correlation. The PIV-NP algorithm is detailed in the following sections.

5.1.2 Input data structure

The input data of the PIV-NP is the output data of the Eulerian Image Correlation Analysis. The most widely extended type is the Particle Image Velocimetry. The input data in each time, t_k , with k from 1 to the total number of frames, is the following:

- a) The time interval between the analyzed frames (Δt_k).

The image correlation analysis is performed in pairs of frames. The time interval between each pair of frames analyzed is fixed throughout the analysis.

- b) The coordinates of the nodes of the mesh.

The analysis mesh is a regular grid (blue data in Table 6 and Figure 37), in this particular case is a rectangular grid.

The coordinates of the mesh nodes remain invariant throughout the analysis, following the Eulerian scheme. The grid extends beyond the initial soil configuration,

to cover the entire area of soil movement. Normally the mesh is generated in the entire extension of the image. Mesh nodes can be active or inactive, depending on if they belong or not to the defined area of interest.

c) The instantaneous displacements $u(t_k)$ measured at the nodes.

For each time step, the displacements are measured in the active nodes of the grid (green data in Table 6 and Figure 37). The general image correlation procedure is outlined in Chapter 2 . If the node is inactive, the displacement values appear as *Not a Number* (NaN) (red data in Table 6 and Figure 37).

Exist Image Correlation methods that the data is the calculated velocity of displacement in the nodes. In these cases, the velocity is converted into displacements multiplying by the time interval (Δt).

Table 6 Example of the structure of the input data from Eulerian Image Correlation analysis for one time step for PIV-NP.

| Coordinates | | Displacements | |
|-------------|------|---------------|-------|
| x | y | u_x | u_y |
| 0.00 | 0.00 | NaN | NaN |
| 0.00 | 0.05 | 0.006 | 0.023 |
| 0.00 | 0.10 | 0.014 | 0.021 |
| 0.00 | 0.15 | 0.024 | 0.021 |
| 0.05 | 0.00 | NaN | NaN |
| 0.05 | 0.05 | 0.006 | 0.014 |
| 0.05 | 0.10 | 0.014 | 0.012 |
| 0.05 | 0.15 | 0.024 | 0.010 |

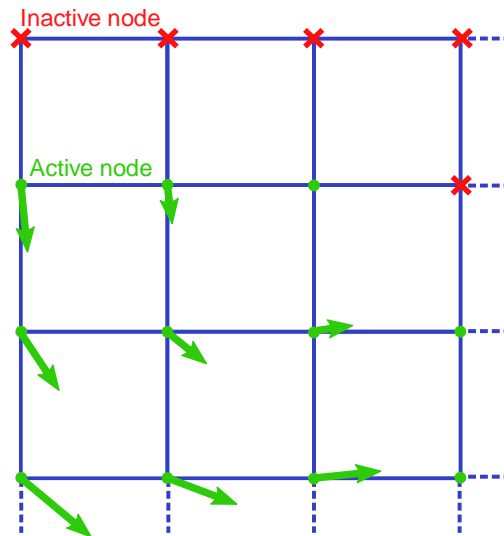


Figure 37 Visual representation of the input data from Eulerian Image Correlation analysis for one time step.

5.1.3 Algorithm

The algorithm of the PIV-NP post-process is schematized in the following flowchart (Figure 38). The steps marked in the flowchart are described above in order of appearance. Each step has a graphic representation to facilitate the understanding of the process.

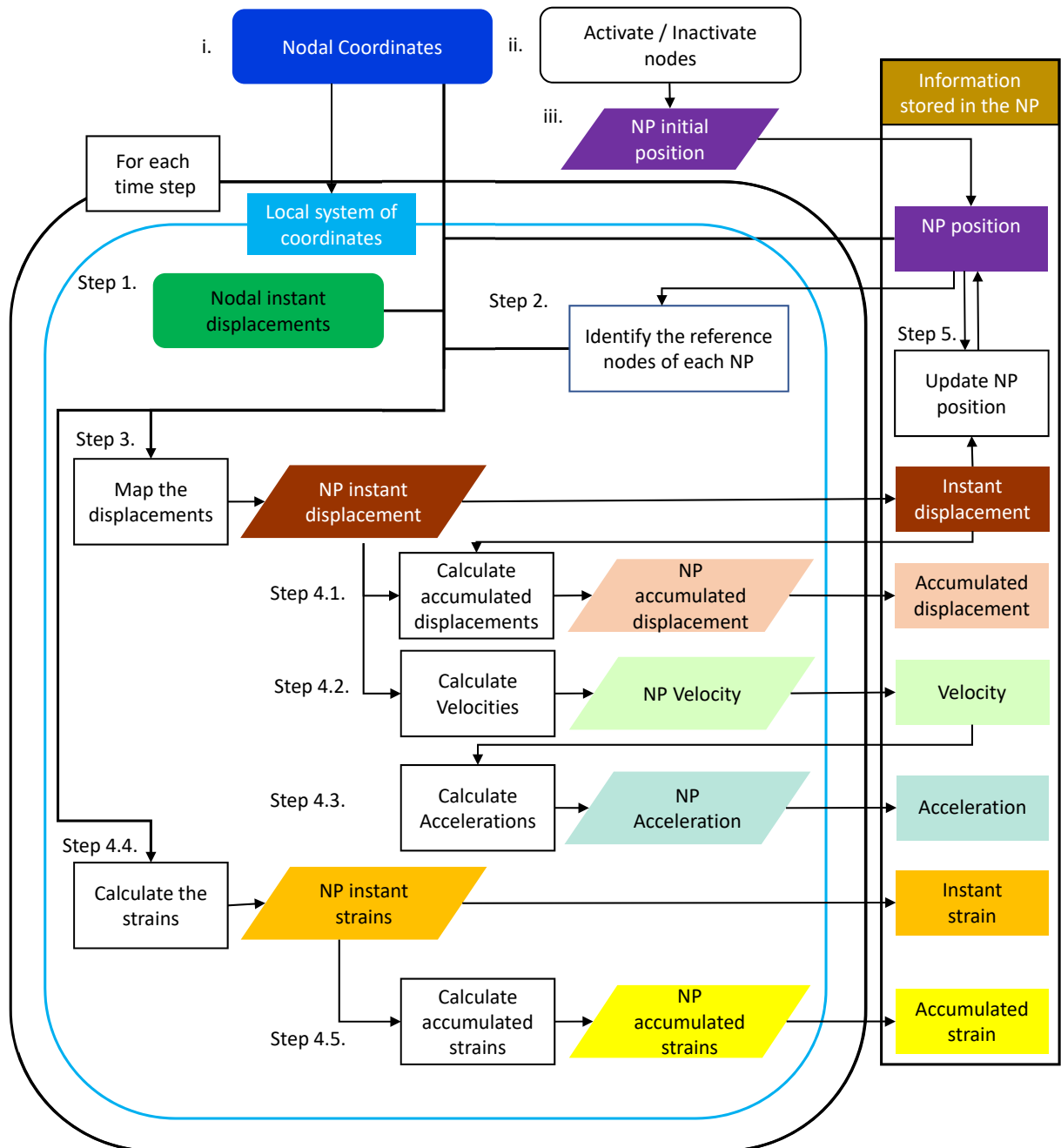


Figure 38 Flowchart of the PIV-NP.

Algorithm steps

The equations presented in this Section are described using the visualization method proposed by Stuart Riffle (Riffle, 2011) and extended by Kalid Azad (Azad, 2017). The visualization method is called “colorized math equation”. The equation is displayed associating a color to each element. Below, the equation is explained in a sentence coloring each concept with the same associated color. The equation and the sentence form themselves a diagram that facilitates the understanding.

On this case the associated colors are also used on the image representation of each step, and also in the flowchart (Figure 38). The elements of the equations that conform the input data and the calculation parameters are written in colors. While the variables that are stored into the numerical particles during that time step are written in black and surrounded by colors.

Preparatory steps:

The preparatory steps are carried out with the information of the first time step input data.

- **Preliminary step i.** Read the coordinates of the nodes of the grid where displacements are measured by PIV.

Equation 4

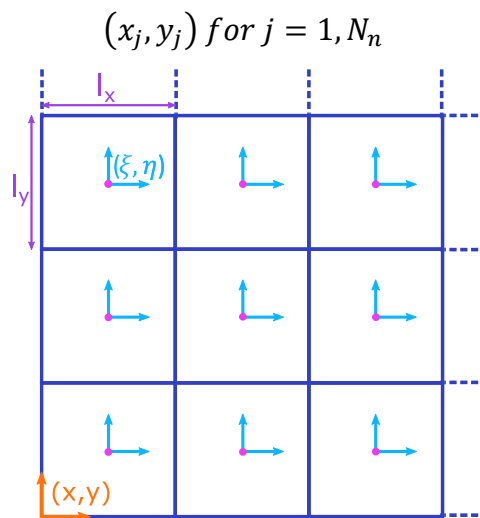


Figure 39 Visual representation of the preliminary step i.

$$\xi = \frac{x - x_c}{l_x/2} ; \quad \eta = \frac{y - y_c}{l_y/2}$$

Based on the **general system of coordinates**, a **local system of coordinates** (ξ, η) is defined and located at the **center of each element** to facilitate the calculations.

- **Preliminary step ii.** Identify the elements of the mesh whose nodes are active, the nodes with instantaneous displacement information. Inactive nodes would contain a NaN.

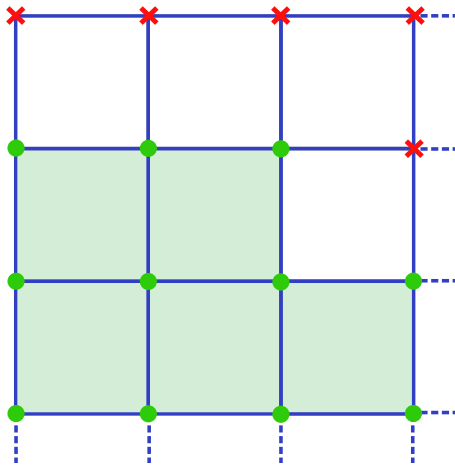
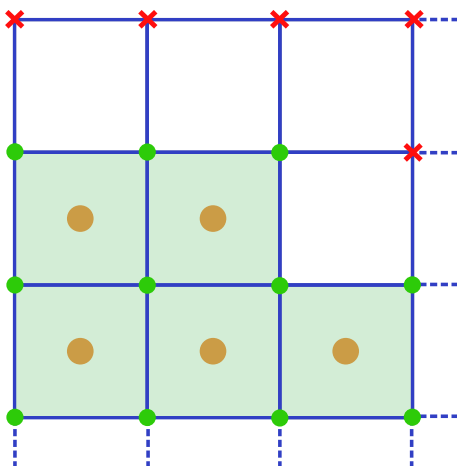


Figure 40 Visual representation of the preliminary step ii.

- **Preliminary step iii.** Place the numerical particles in the active elements.

The number of numerical particles per element is user-defined. The most common options are 1 or 4 particles per element.

a)



b)

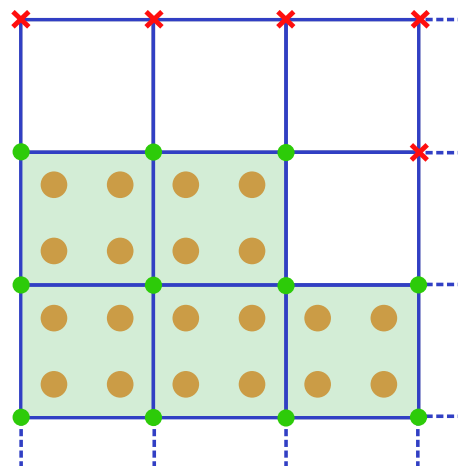


Figure 41 Visual representation of the preliminary step iii. a) 1 numerical particle per element. b) 4 numerical particles per element.

For each time step (t_{k+1}), going from 1 to the total number of steps analyzed.

- **Step 1:** Read the **instantaneous displacements** of **each node** from the input data. The nodes go from 1 to N_n (total number of nodes).

Equation 6

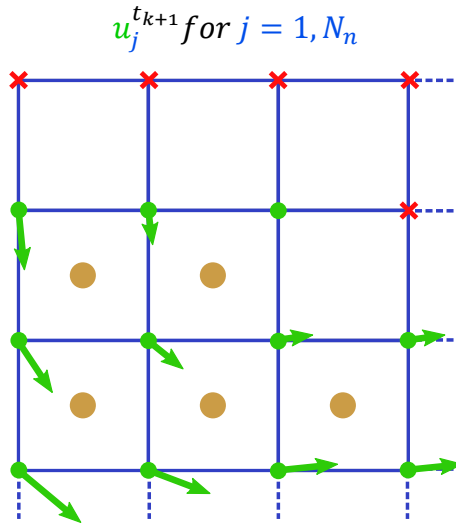


Figure 42 Visual representation of step 1.

- **Step 2:** Identify the nodes of each particle according to the element in which it is located.

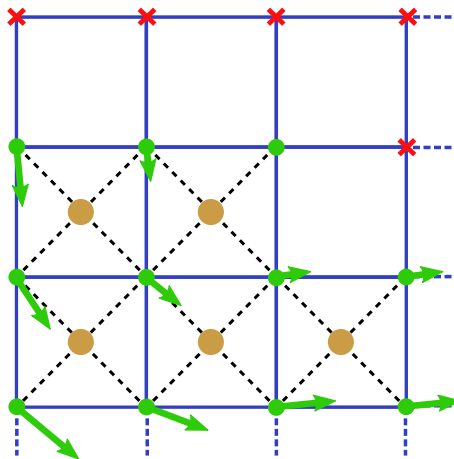


Figure 43 Visual representation of step 2.

- **Step 3:** Map the instantaneous displacement to each numerical particle.

Equation 7

$$\mathbf{u}_p^{t_{k+1}} = \left[\sum_{j=1}^{N_n} \mathbf{u}_j^{t_{k+1}} N_j(x_p^{t_k}) \right]^e$$

The **instantaneous displacement** of each **numerical particle** is the **summation** of the **instantaneous displacement** of its **reference nodes** weighted with the **shape function** depending on the **particle position** calculated at the **element level**. Lineal shape functions are used.

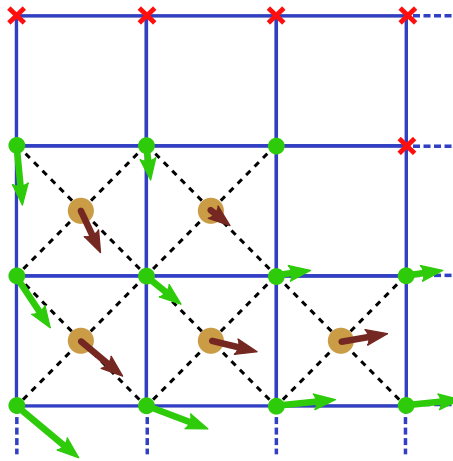


Figure 44 Visual representation of step 3.

- **Step 4:** Calculate the variables of interest stored in each numerical particle.
 - **Step 4.1:** Calculate the accumulated displacements.

Equation 8

$$\mathbf{U}_p^{t_{k+1}} = \mathbf{U}_p^{t_k} + \mathbf{u}_p^{t_{k+1}}$$

The **accumulated displacement** of a **numerical particle** is calculated adding the **instantaneous displacement** to the **accumulated displacement** of the previous time step.

- **Step 4.2:** Calculate the velocity.

Equation 9

$$v_p^{t_{k+1}} = \frac{u_p^{t_{k+1}}}{\Delta t_k}$$

The velocity of a numerical particle is the instantaneous displacement divided by the time interval.

- **Step 4.3:** Calculate the acceleration.

Equation 10

$$a_p^{t_{k+1}} = \frac{v_p^{t_{k+1}} - v_p^{t_k}}{\Delta t_k}$$

The acceleration of a numerical particle is the difference between actual velocity and previous velocity of divided by the time interval.

- **Step 4.4:** Calculate the strain increment.

Equation 11

$$\Delta \varepsilon_p^{t_{k+1}} = \left[\sum_{j=1}^4 B_j^{t_{k+1}}(x_p^{t_k}) u_j^{t_{k+1}} \right]^e$$

The strain increment of each numerical particle is the summation of the instantaneous displacement of its reference nodes pondered with the strain shape function matrix depending on the particle position calculated at the element level.

Equation 12

$$B_j^{t_{k+1}} = \begin{bmatrix} \frac{\partial N_j}{\partial \xi} \frac{\partial \xi}{\partial x} & 0 \\ 0 & \frac{\partial N_j}{\partial \eta} \frac{\partial \eta}{\partial y} \\ \frac{\partial N_j}{\partial \eta} \frac{\partial \eta}{\partial y} & \frac{\partial N_j}{\partial \eta} \frac{\partial \eta}{\partial y} \end{bmatrix}^{t_{k+1}}$$

- **Step 4.5:** Calculate the accumulated strain.

Equation 13

$$\boldsymbol{\varepsilon}_p^{t_{k+1}} = \boldsymbol{\varepsilon}_p^{t_k} + \Delta\boldsymbol{\varepsilon}_p^{t_{k+1}}$$

The **accumulated strains** of a **numerical particle** are calculated adding the **strain increment** to the **accumulated strains of the previous time step**.

Step 5: Update the position of the numerical particle

Equation 14

$$\boldsymbol{x}_p^{t_{k+1}} = \boldsymbol{x}_p^{t_k} + \boldsymbol{u}_p^{t_{k+1}}$$

The **actualized position** of a **numerical particle** at **this time** is calculated adding the calculated **instantaneous displacement** to the **position** on the **previous time**.

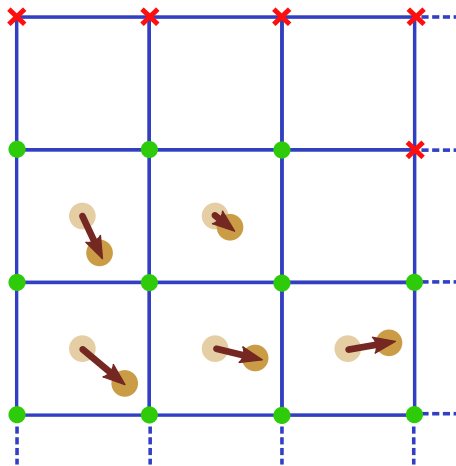


Figure 45 Visual representation of step 5.

5.2 Validation of PIV-NP

The evaluation of the PIV-NP code was performed using three methods. The PIV-NP, as a post-process, is always tight to the performance of the Image Correlation program that generates the input data. The methods to evaluate the performance of the PIV-NP itself are designed to cover the full range of degree of interaction, from the most abstract to the most realistic.

Synthetic data: The input data for the PIV-NP code is written manually. Therefore, in this evaluation case, errors and limitations that depend only on the post-processing method are detailed.

Synthetic images: The input data for the PIV-NP code is the output data from the analysis of synthetic images by means of an Eulerian Image Correlation program [PIVlab (Thielicke and Stamhuis, 2014)]. The analysis of synthetic images is the classic method for the evaluation of Image Correlation programs (Gui and Merzkirch, 2000; Kähler, Scharnowski and Cierpka, 2012). In this case, the accuracy of the Image Correlation program is not being evaluated, but rather the effect that the tolerable errors of the input data have on the post-processing results. For this reason, the analyzed cases of this Section are equal to the synthetic data cases, but with the “noise” caused by the Image Correlation.

Real images: The input data for the PIV-NP code is the output data of the image analysis of a real case carried out in the laboratory by a Eulerian Image Correlation program (PIVlab). In this case, three blue particles were introduced into the soil in order to know the position of some particles which can be compared with the measured position by means of PIV-NP. The capability of the PIV-NP code to track the path of the three particles is evaluated. This analysis considers the errors coming from the Image Correlation program when dealing with real images.

5.2.1 Synthetic data

5.2.1.1 Linear displacement

The first case of analysis is a linear displacement of a rigid body. The input data is organized as a regular grid of 17 x 17 nodes; the separation between the nodes is 8 px. The input data in each node is a displacement vector of (5,2) for all time steps. The initial disposition of the particles takes the input data of the first time step as a reference (Figure 46 - Initial disposition). The area of interest is defined in this first input data distinguishing between internal nodes, which have assigned displacement, and the external nodes, which have NaN value (defined in the figure with a red cross). The numerical particles (NP) are created in the elements inside the area of interest, which have displacement data in all their nodes.

Commonly, the eulerian type of image correlation methods require defining the area of interest in each time step to avoid the background results contamination. In the analysis of soil experiments (like a landslide), the area of interest changes for each time step. The delimitation of the area of interest for each time step manually highly time-consuming.

The PIV-NP eliminates the requirement to delimitate the area of interest for each time step. The area of interest is defined in the first time step to place the NP. Afterward, the Numerical Particles are who define the area of interest. Each NP reads the information from its reference nodes, the nodes of the element where the NP is located at each moment. Therefore, just the elements with NPs inside delimit the area of interest, the input data of the rest of the nodes are irrelevant. That self-defining area of interest facilitates the eulerian image correlation procedure.

Figure 35 shows how the NPs were originally placed inside the initial area of interest. The particles move through the grid changing the reference nodes without alterations on its movement. From time step 2 onwards, there is no area of interest defined; all the nodes have displacement information. The nodes in contact with particles provide their information to the particle. The information in the rest of the nodes is not used. Therefore, the displacement information of these unused nodes could be any value without affecting the displacement of the NPs.

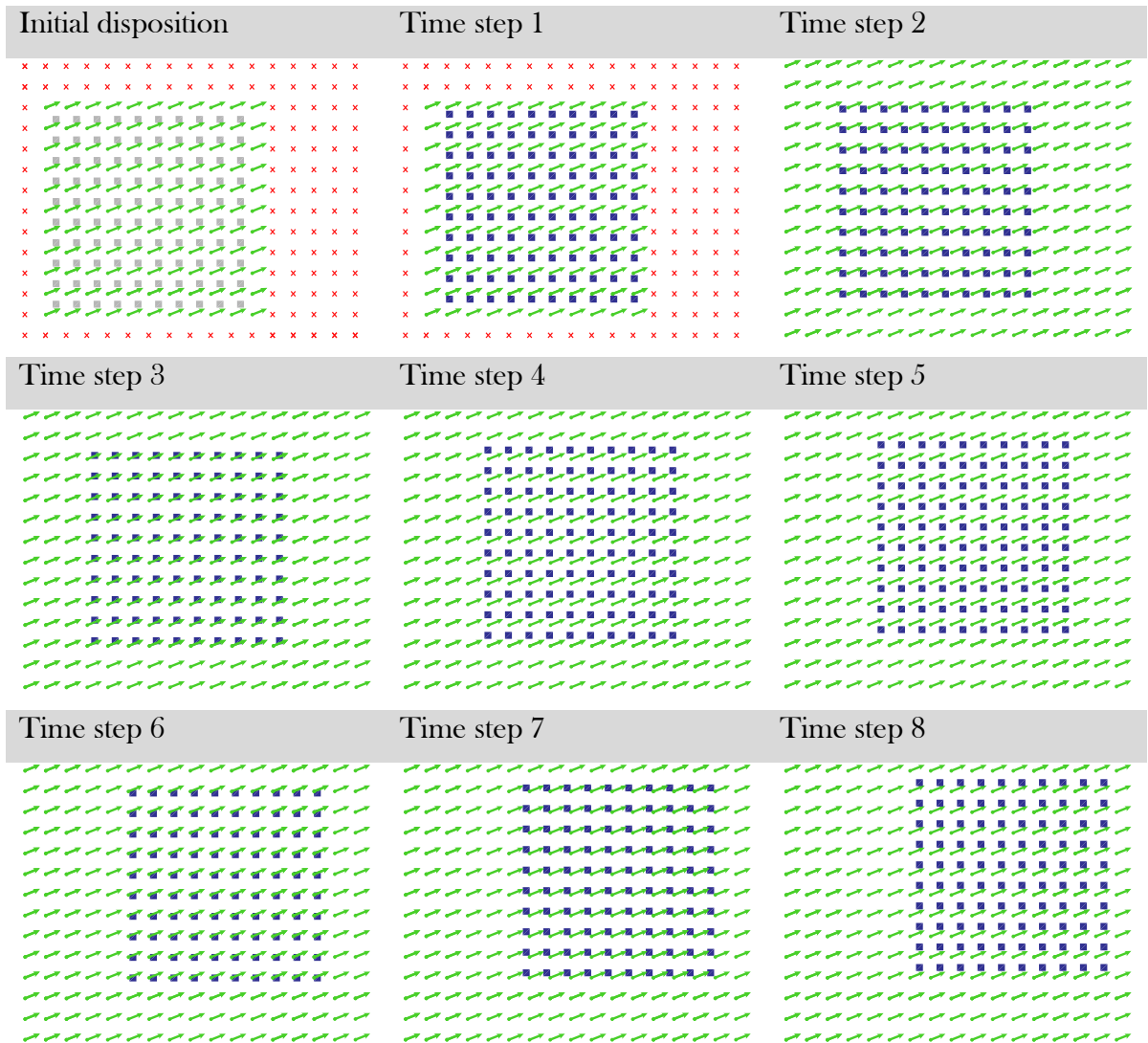


Figure 46. Numerical Particle location on the linear displacement case with synthetic data.

Figure 47 shows the instantaneous displacement vector (horizontal and vertical component and module) of all particles. The mapping of the displacements is correct in all the particles regardless of their relative distance to the nodes. The cases with 1 and 4 numerical particles per element have been analyzed, and there are no errors in the mapping of the displacements of the particle movements.

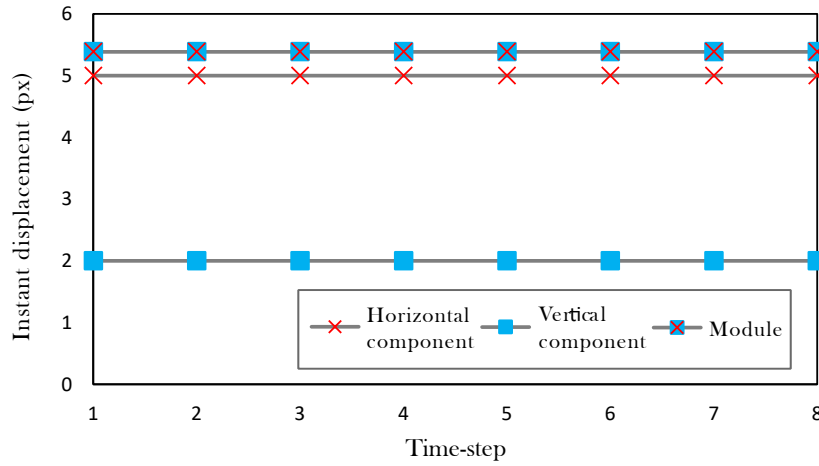


Figure 47. Instantaneous displacement of the numerical particles. Case of synthetic data with linear displacement.

Figure 48 shows the accumulated displacement of all the particles. As in the previous figure, the mapping of the displacement does not introduce errors; the accumulated displacement is precisely the expected one.

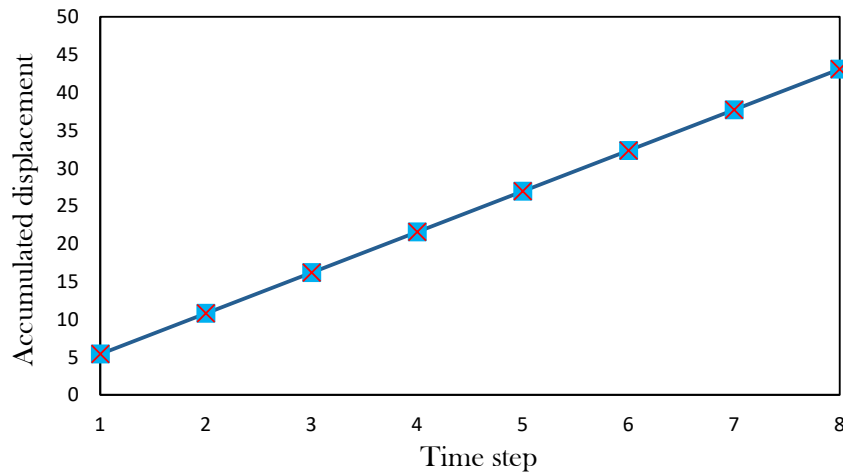


Figure 48. Accumulated displacement of the numerical particles. Case of synthetic data with linear displacement.

5.2.1.2 Horizontal shear

The method is evaluated with input data simulating a shearing test. In the first case, the relative displacement is horizontal. The area is divided by a horizontal shear band, parallel to the arrangement of the reference nodes in the grid. The area is divided into two blocks, the nodes on the upper block a horizontal displacement of 10 is imposed in the input data, while the nodes on the lower block a null displacement is imposed.

The input data represents a theoretical case with a zero thickness shear band. The discretization in nodes transforms the zero thickness into 1 element thickness. The elements that conform the shear band have the upper nodes with an imposed displacement of 10 and the lower nodes with an imposed displacement of 0.

Figure 49 shows the displacement of the numerical particles in the eight time steps. The represented case was defined with an initial arrangement of 1 numerical particle per element. The colors indicate the instantaneous displacement for each time step. The numerical particles of the lower block remain static, and the displacement of the upper block ones is 10, as evaluated in the previous section there are no problems on mapping the displacement in the NP.

The evaluation of the PIV-NP focuses on the displacement of the particles inside the shear band elements. The information obtained by these particles by its four reference vectors is 10 for the two upper vectors and 0 for the two lower vectors. The displacement of each the particle, following the shape functions, depends on the distance from each vector. In this particular case of a horizontal shear band, that could be summarized as the vertical position of the particle.

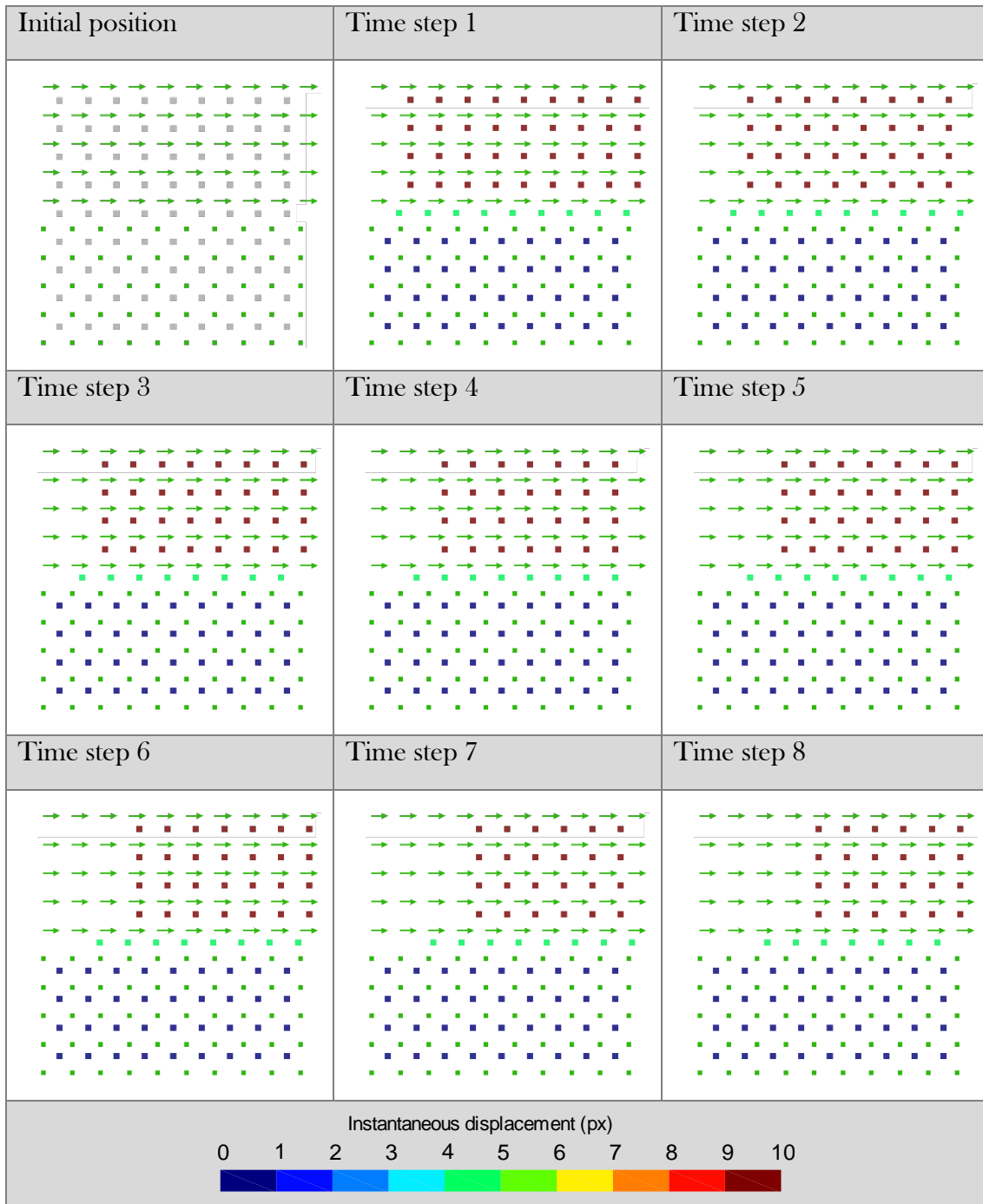


Figure 49. Numerical Particle location and instantaneous displacement on the horizontal shear case with synthetic data. The numerical particles can be grouped in three zones depending on its instantaneous displacement: upper block (red particles = 10 px/time step), shear band (green particles = 5 px/time step), and lower block (blue particles = 0 px/time step).

Figure 50 shows the instantaneous displacement of all the NPs (1 particle per element). The instantaneous displacement of the NPs inside the shear band is constant despite the movement of the particle. The movement of the particle implies the change on the nodes taken as reference and the variation of the node-particle distance. This constant

instantaneous displacement of the particles inside the shear band is due to the purely horizontal displacement of the particle, which makes the sum of the distances between the particle and the higher nodes always equal the sum of the distances between the particle and the lower nodes.

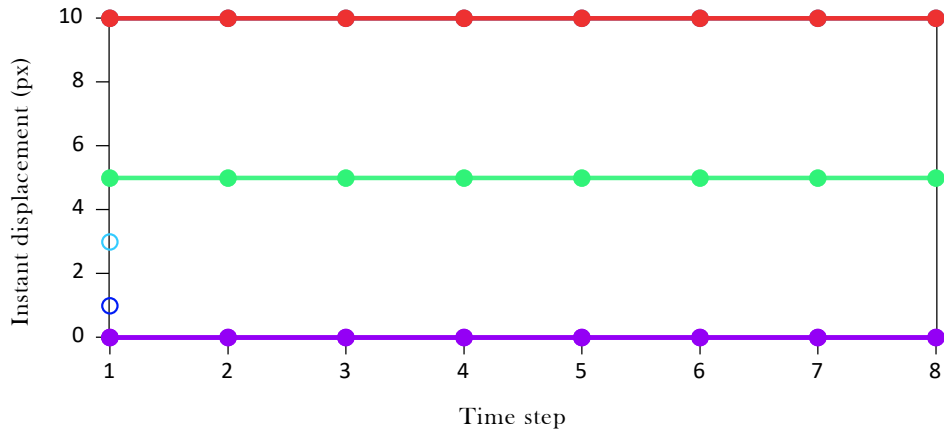


Figure 50. Instantaneous displacement of the numerical particles. Case of synthetic data with horizontal shear band (1 numerical particle per element).

Figure 51 is a graph of the instantaneous displacement of the NPs in the case with an initial arrangement of 4 particles per element. On this case the particles inside the elements that conform the shear band

This case shows that the particles affected by the shear band are classified in two, NPs with a displacement of 7.5 and NPs with a displacement of 2.5. These are the particles that are the particles placed in the elements on the shear band.

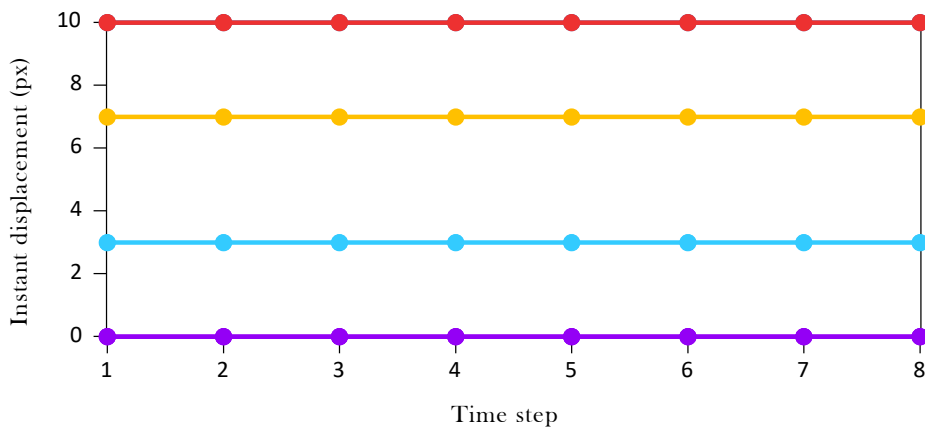


Figure 51. Instantaneous displacement of the numerical particles. Case of synthetic data with horizontal shear band (4 numerical particles per element).

As conclusions, this case input data represents a relative displacement with a shear band of one element thickness and parallel to the arrangement of the nodes. The NPs affected by the shear band are the particles inside the elements that form it. This is independent of the number of particles per element. The localization of the shear band is limited by the discretization of the input data extracted from the previous image correlation analysis. The PIV-NP maximum resolution is determined by the resolution of its input data. The use of a higher number of particles per element might smooth the transitions, but the refinement must be provided by the input data.

A second horizontal shear case is analyzed, this case represents a refinement on the shear band. Therefore, the shear band is discretized in five elements instead of one element, the displacement input data is a transition from 0 to 10, (0, 2, 4, 6, 8, 10). Figure 52 plots the particle location in the input data grid of vectors in both cases.

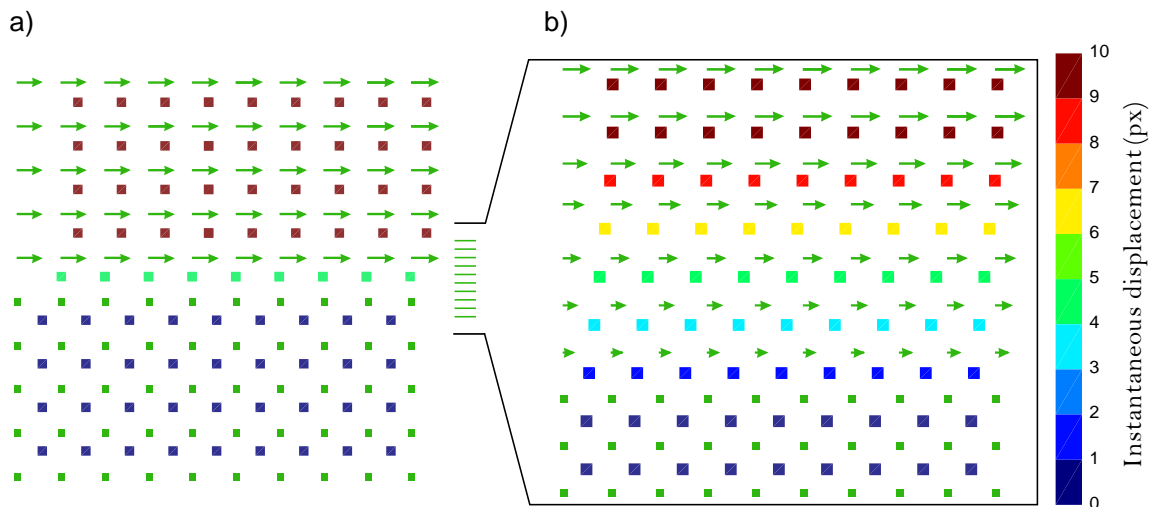


Figure 52. Numerical Particle location and instantaneous displacement. a) Shear band one element thickness. b) Shear band five elements thickness.

The dimensions of the shear band are restrained to the 5 elements of the input data. Figure 53 shows the evolution of the instantaneous displacement of the numerical particles. The instantaneous displacements of the particles in the shear band are the mean of the input displacement value of its referent elements (1, 3, 5, 7, 9), and remain constant through the time.

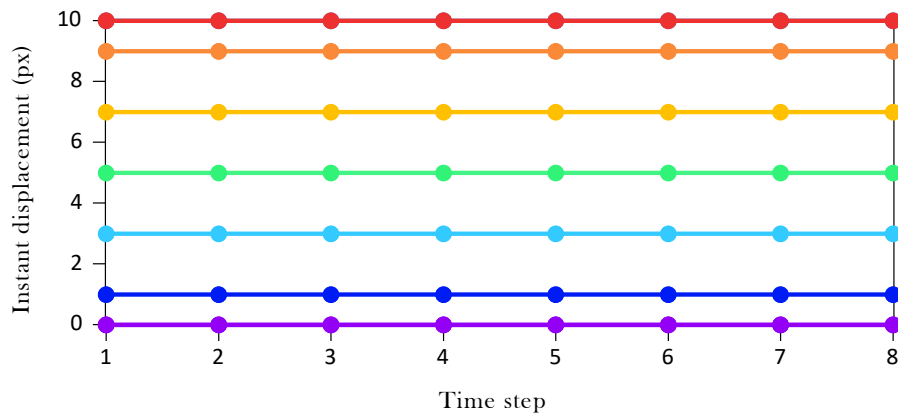


Figure 53. Instantaneous displacement of the numerical particles. Case of synthetic data with horizontal shear band.

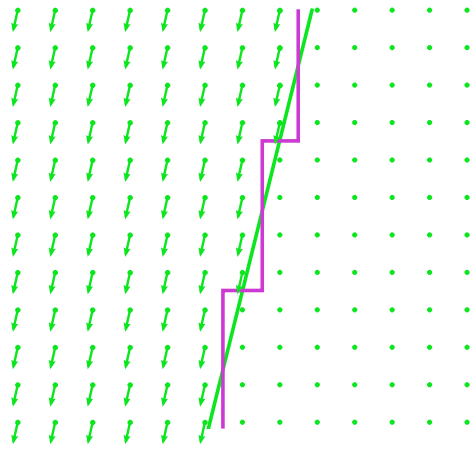
As a conclusion, the horizontal shear band size is defined by the input data discretization. The transition between the two extreme displacement value might be controlled by a refinement on the input data discretization or by the addition of more numerical particles per element. In both cases, the shear band is restrained to the thickness defined in the input data. These horizontal shear example can be extrapolated to the cases where the shear band is parallel to the input data arrangement.

5.2.1.3 Oblique shear

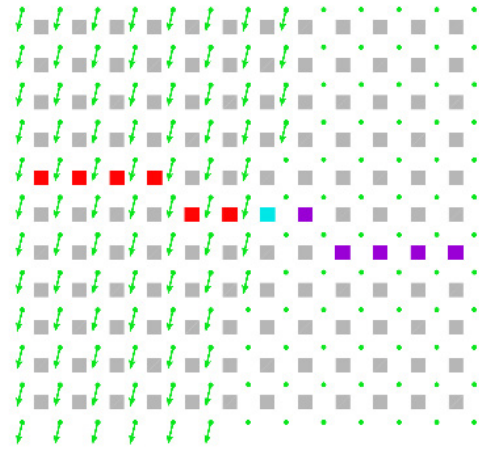
The second case of relative displacement is similar to the previous one, but the shear band is oblique (76°). Therefore, the shear band does not match the arrangement of the grid of reference vectors set as input data. The area is divided into two blocks, the upper left block has a displacement parallel to the shear band $(-2.5, 10)$, while the lower right block has a zero displacement.

Figure 54 shows the displacement of the NPs (one per element) in the 8 time steps. The highlighted NP line (red-blue-purple) is normal to the shear band direction. Figure 55 shows the instantaneous displacements along this normal line.

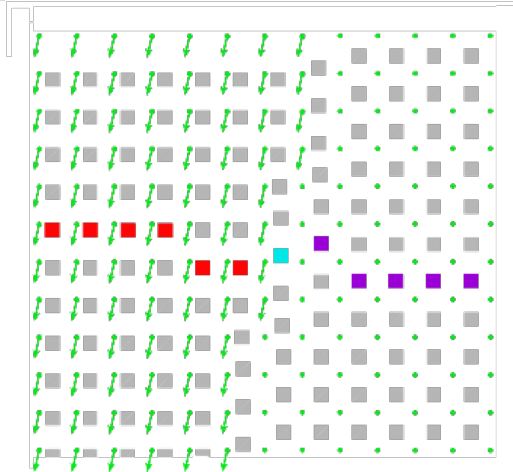
Input Data



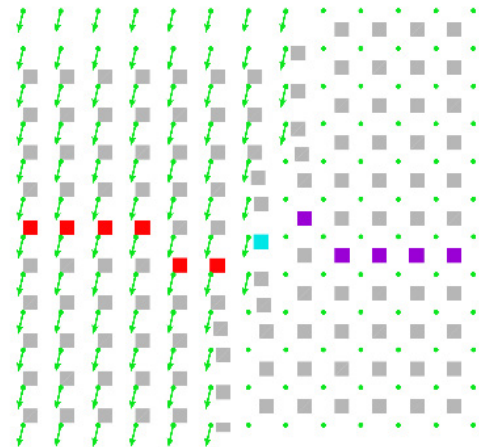
Initial NP arrangement



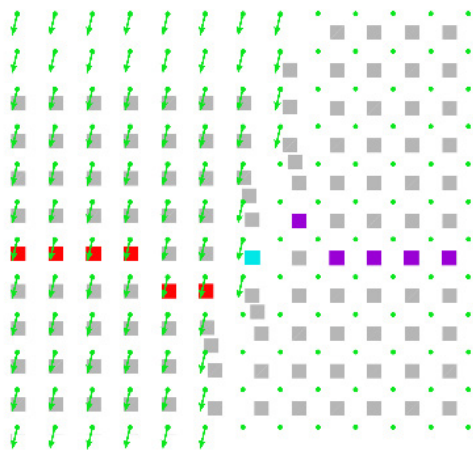
Time step 1



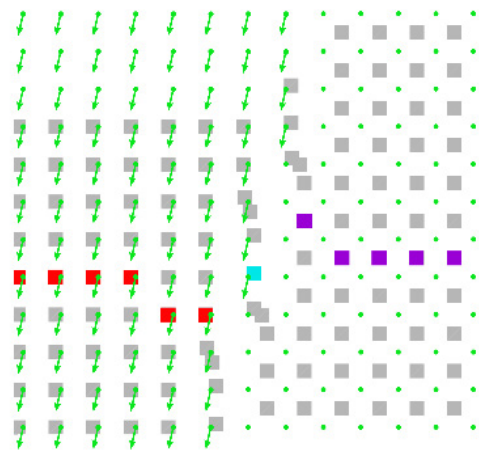
Time step 2



Time step 3



Time step 4



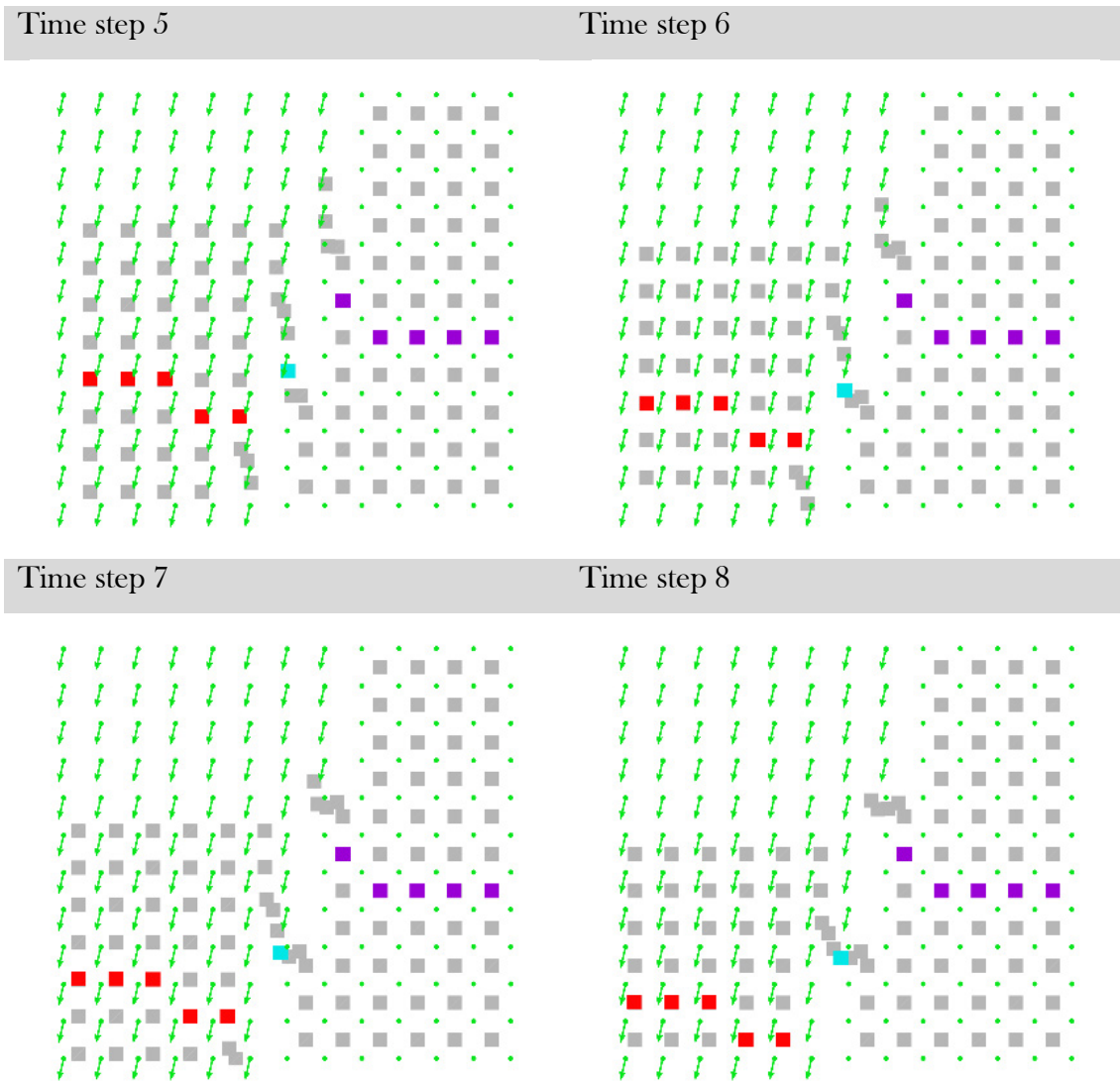


Figure 54. Numerical Particle location on the oblique shear case with synthetic data. A line of NP is highlighted in red, blue, and purple to be analyzed in Figure 55.

Figure 55 and Figure 56 show that the shear band has a width of one and two particles respectively, which corresponds to the size of an element of the input data vector grid. The peculiarity of this case is that the displacement of the NPs in the shear band varies in each time step. This variation in the displacement is governed by the discretization of the medium in a grid of nodes. In this case, the shear band in the input data is no longer a straight line, but rather a staircase that follows the trend $(-1, 4)$ corresponding to the 76° (input data - Figure 54).

The trajectory (Figure 54) and the instantaneous displacement (Figure 55) of the blue NP are described as an example. This NP moves in a straight line at 76° , parallel to the theoretical shear band. The discretization of the shear band in the input data grid implies that the trajectory of the NP passes through areas more influenced by the vectors that provide movement and other areas more influenced by vectors with zero displacement.

In time step 1, the displacement is 5.15 since it is at an intermediate point between the vectors that provide displacement and the vectors that provide zero displacement. In the following time steps, the particle progressively enters in an area where the influence of the vectors with displacement is greater. Arriving at time step 5, where it is located close to one of the vectors with displacement. After that, it enters in an area where the influence of vectors with displacement is lower.

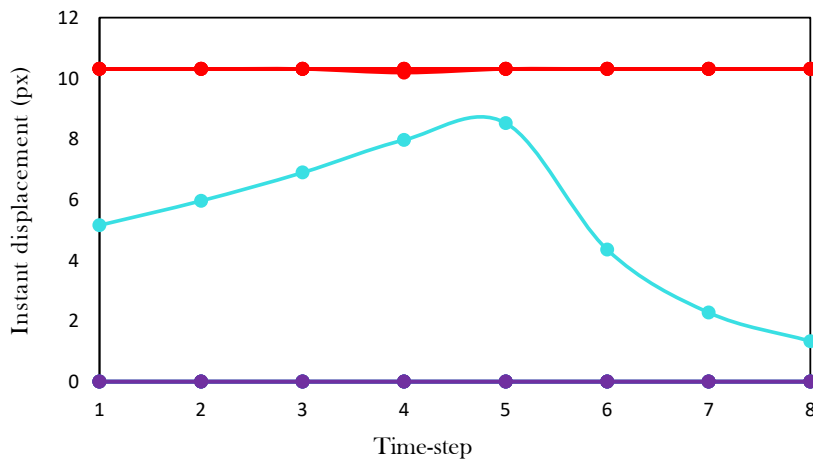


Figure 55. Instantaneous displacement graph of a line of particles normal to the shear band. Case of synthetic data with oblique shear band (1 numerical particle per element).

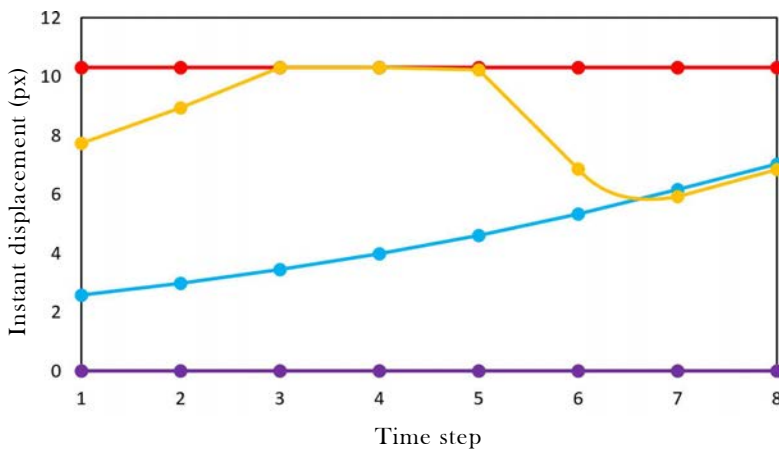


Figure 56. Instantaneous displacement graph of a line of particles perpendicular to the shear band. Case of synthetic data with oblique shear band (4 numerical particles per element).

5.2.2 Synthetic images

The analysis of images using any type of Image Correlation code introduces a certain level of error in the input data used by the PIV-NP. As these Image Correlation codes improve their cross-correlation algorithms, the amount and size of errors decrease. In the case of the Eulerian Image Correlation codes, the wrong cross-correlations (known as wild vectors) can be easily detected and corrected. The displacement value at this mismatched point is calculated by interpolating the data from the surrounding nodes. However, this Section is not focused on this type of errors. The input data of the following cases have already been cleared from punctual wild vectors. The errors that this Section focuses on are the background noise implicit in the analysis of images, acceptable errors within the tolerance marked by the Image Correlation code. This Section analyzes how these acceptable errors in the input data affect the result of the PIV-NP post process.

The Eulerian Image Correlation code used is the PIVlab developed by William Thielicke ((Thielicke and Buma, 2014; Thielicke and Stamhuis, 2014). The PIVlab works as a Matlab tool and applies several built-in features, which requires the image processing toolbox. The initial aim of the code was to visualize and measure flow with tracer particles, but it does not require modifications to analyze synthetic or real soil images.

On this Section, a set of synthetic images are generated and correlated using PIVlab. The results are used as input data for PIV-NP. The post-process results are compared with their homologs in the previous Section (5.2.1)

5.2.2.1 Linear displacement

The first case of analysis is a linear displacement of a rigid body. The input data is organized as a regular grid of 17 x 17 nodes; the separation between the nodes is 8 px. The linear displacement with synthetic data on Section 5.2.1.1 is the ideal version of this case. Therefore, the results from that Section are used to evaluate the current Section results.

In Figure 58, as in its numerical analog, the area of interest is defined only in the input data of time step 1. The numerical particles move like a rigid body, even though the instantaneous displacements are not exactly identical. These differences in the

instantaneous displacements are observed in the colors of the particles and are due to the background noise of the input data. The errors, in this case, are not relevant enough to deviate an NP from the general trajectory.

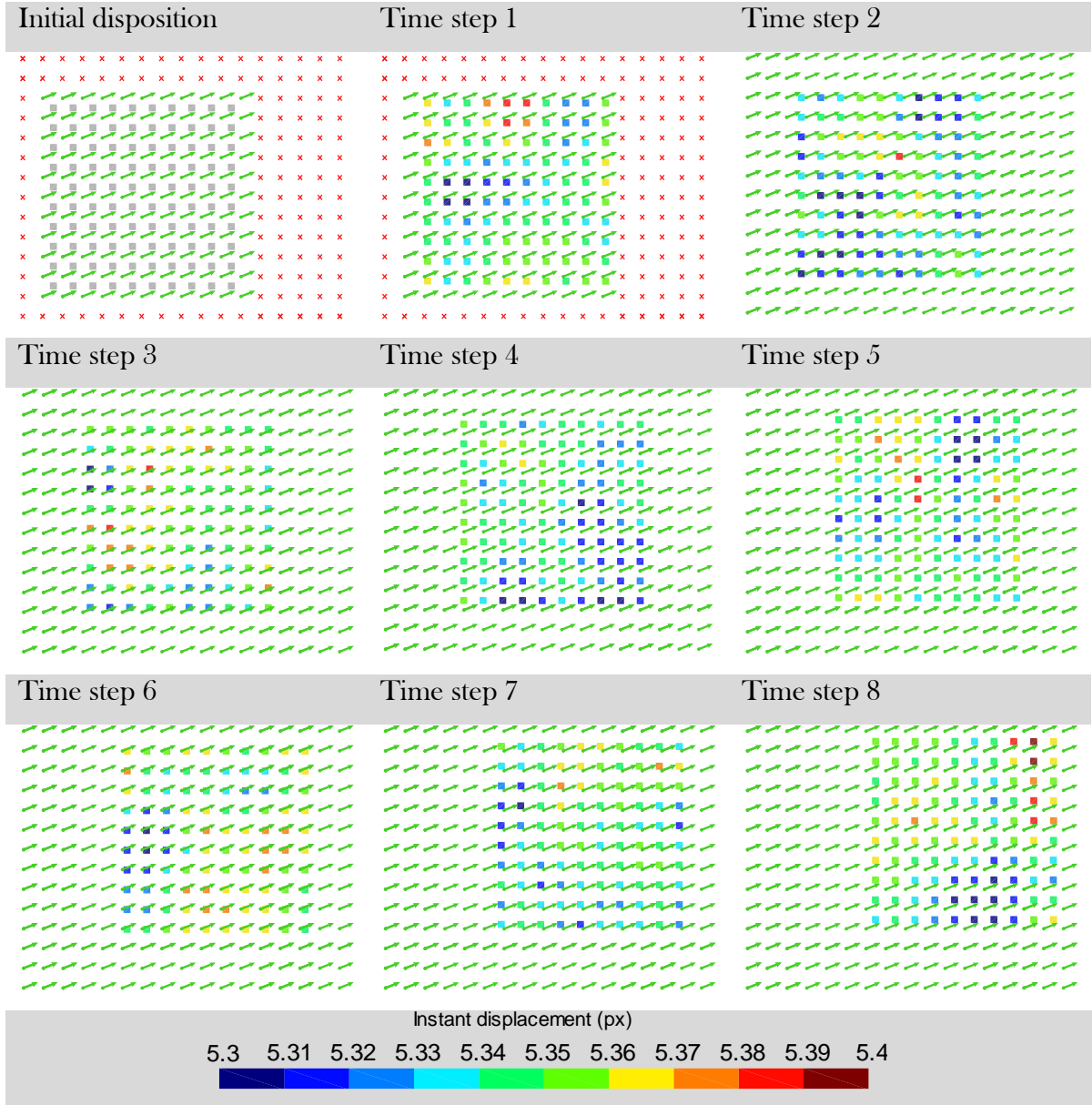


Figure 58. Numerical Particle location and instantaneous displacement on the linear displacement case with synthetic images.

Figure 59 and Figure 60 represent respectively the x, y and total instantaneous displacement of all the numerical particles. A line with the expected real values obtained in the analog Section with synthetic data is added.

In all three cases, the values of the numerical particles tend to be lower than the expected value. The green line marks the average instantaneous displacement of the PNs for each time step. The average value of instantaneous displacement in X is around 4.97 px, -0.03 px respect to the expected value of 5 px. In Y it is located around 1.973 px, -0.027 px respect to the expected value of 2 px. The combination of these, the value of instantaneous displacement is located at 5.3476, - 0.0376 px respect to the expected value of 5.3852. These error values by themselves are negligible. The problem is that the PIVlab is underestimating the displacements systematically. The noise introduced by the image analysis gives values lower than the real ones in almost all the input values.

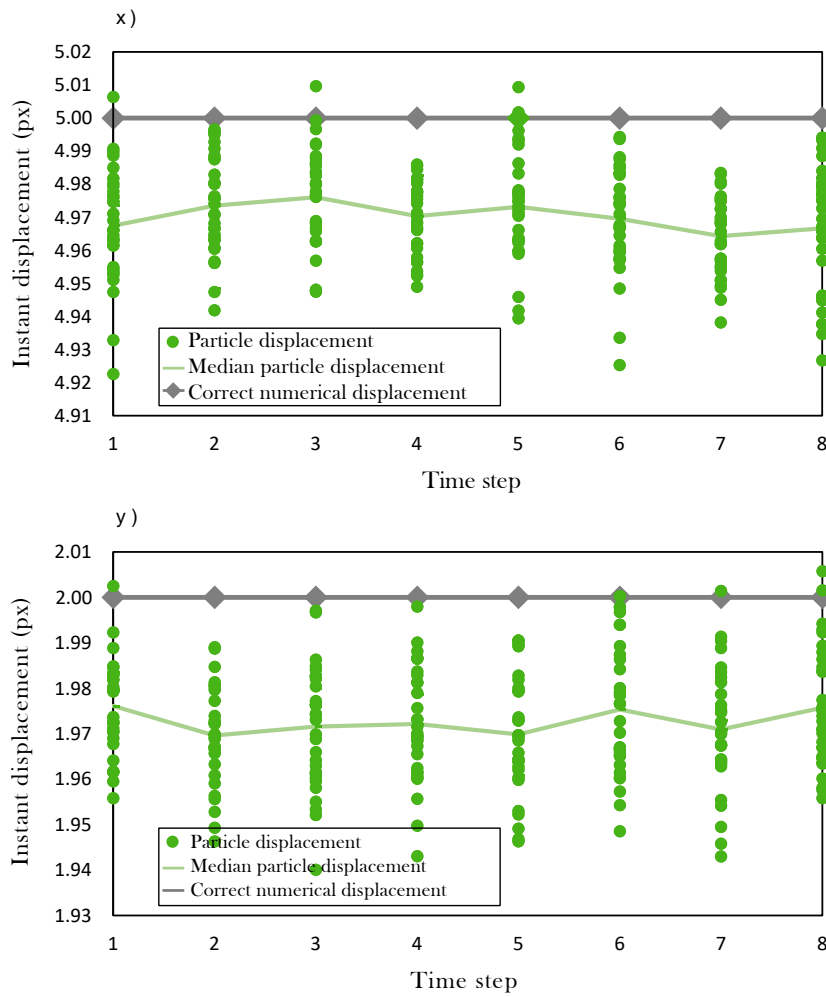


Figure 59. Instantaneous displacement (x,y) of the particles respect to the correct expected displacement. Case of synthetic images with linear displacement (1 numerical particle per element).

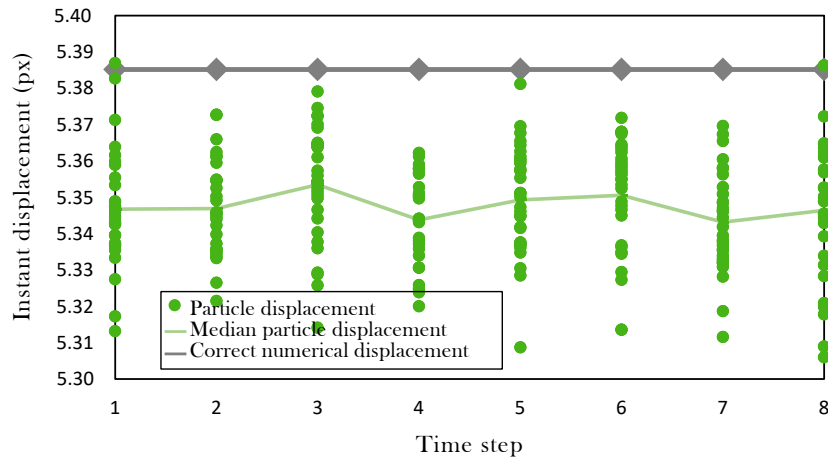


Figure 60. Total instantaneous displacement of the particles respect to the correct expected total displacement. Case of synthetic images with linear displacement (1 numerical particle per element).

This is a problem when these errors accumulate in the numerical particles. Figure 61 shows the error in the accumulated displacement in all the particles. The error, being systematically negative, is not compensated but accumulates in each time step. If the case is long and the number of time steps is high, this could be a problem.

This is a weakness of the PIV-NP code, and it should be considered when evaluating the suitability of the input data introduced. On the other hand, we must assess the importance of these background noise errors in the analysis of synthetic images comparatively with the errors in the analysis of real images. This assessment is done in Section 5.2.3 - Real Images.

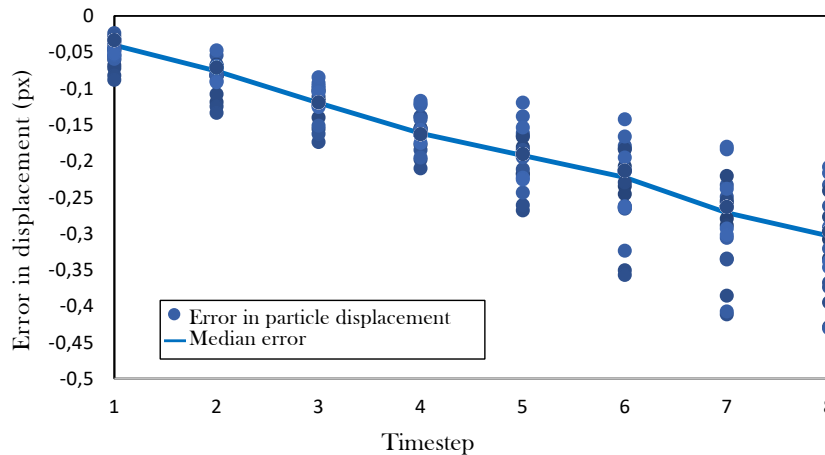
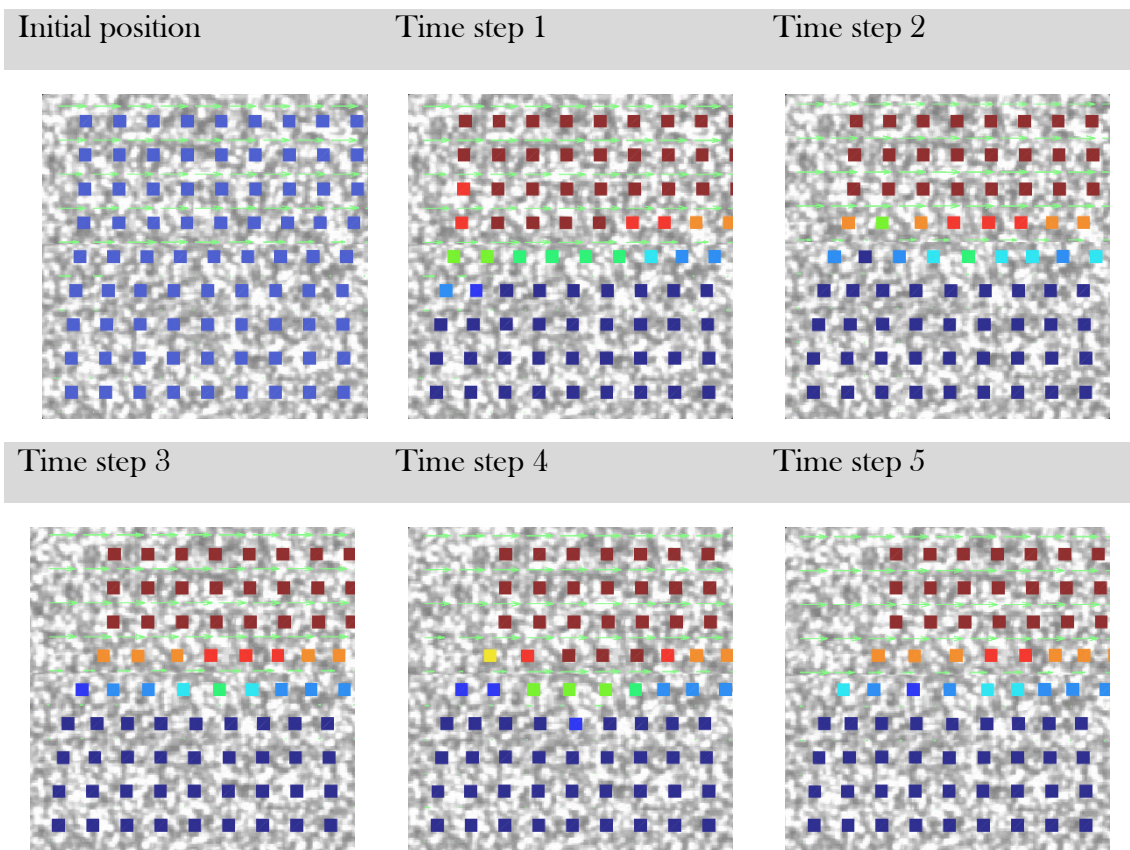


Figure 61. Error accumulated in the particle displacements. Case of synthetic images with linear displacement (1 numerical particle per element).

5.2.2.2 Horizontal shear.

In this case, the synthetic image is divided horizontally into two parts. The upper image part 10 pixels right per time step, while the lower image part remains static. The contact between the two image parts has zero thickness, the discretization in nodes transform the zero thickness into 1 element thickness. The analysis is focused on the errors on the shear band and the surrounding elements. The numerical analog (Section 5.2.1.2) indicate that the shear band would be ideally restricted to the size of one element.

Figure 62 shows the movement of the numerical particles; the colors display the instantaneous displacement for each time step. As expected, the displacement of the numerical particles of the upper block is 10, and the lower block is 0. The errors on the upper and lower numerical particles are not relevant for the purpose of this Section. The focus is on the numerical particles in the shear band. The particles that correspond to the shear band are in line 5, in the central part of the volume of analysis. The point that differs most notably from the numerical ideal is in the particles corresponding to the line immediately above and below those of the shear band (lines 4 and 6).



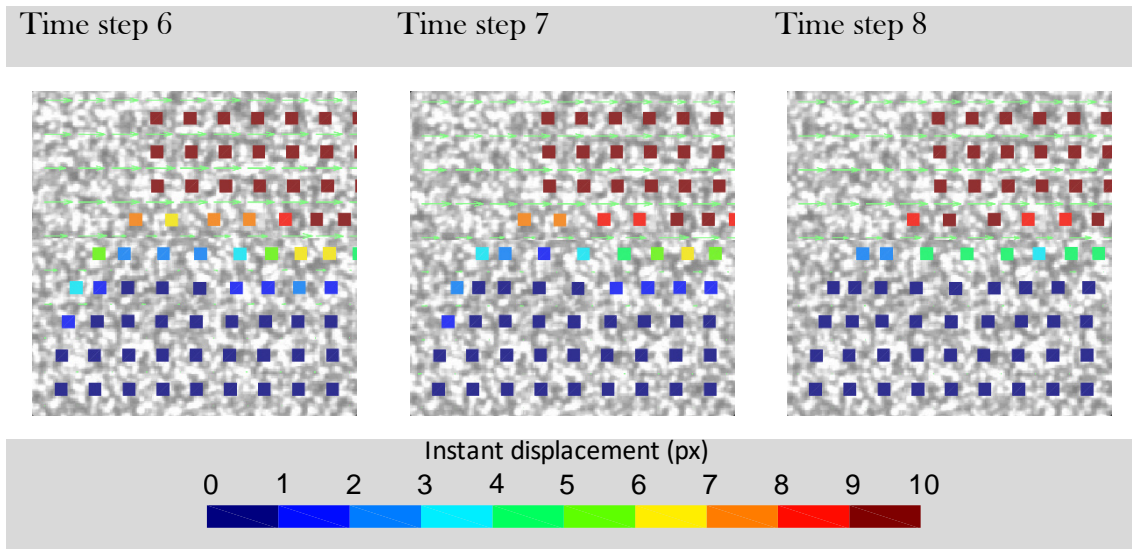


Figure 62. Numerical particle location and instantaneous displacement on the zero-thickness shear case with synthetic images.

The instantaneous displacements of all the particles in the area of influence of the shear band are analyzed in Figure 63. The orange particles correspond to the particles of line 4 (immediately above the shear band), the theoretical displacement of these particles would be 10 px. The green particles correspond to the particles of line 5 (shear band), the theoretical displacement of these particles would be 5 px. The blue particles correspond to the particles of line 6 (immediately below shear band), the theoretical displacement of these particles would be 0 px.

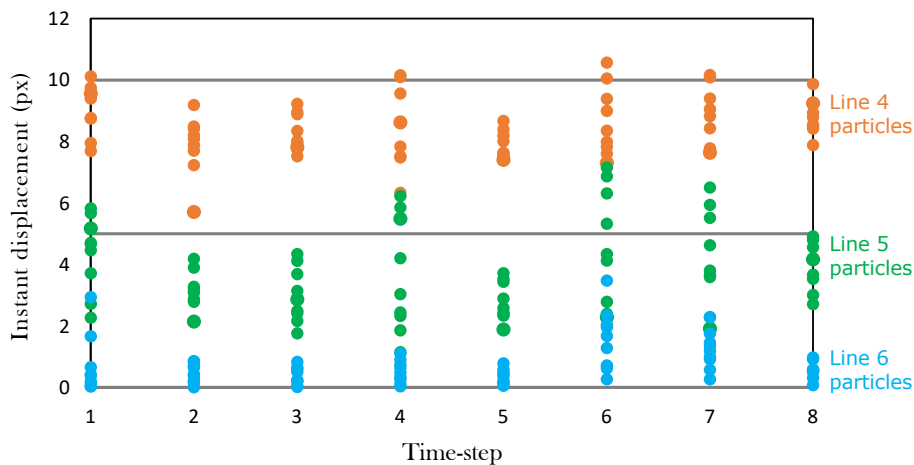


Figure 63. Instantaneous displacement graph of the zero-thickness shear case with synthetic images (1 numerical particle per element).

The errors in the displacements of these particles are two orders of magnitude higher than the errors evaluated in the previous Section 5.2.2.1 (Synthetic images - linear

displacement). The origin of these errors is no longer the intrinsic noise of the PIVlab but the small mismatches in the patch correlation of the areas near the shear band.

The image correlation of this case is performed analyzing images with a zero thickness shear band. Consequently, the patches that contain it might be cut into two parts. The high deformation of these patches makes cross-correlation near the shear band more complicated. This causes errors in the resulting displacement vectors. These errors might be small enough to go unnoticed or might be evident enough to be spotted (wild vectors). The positive point in the Eulerian Image Correlation programs is that the correction of these wild vectors is easy and do not require to rerun the analysis. The displacement in that point is then interpolated from the surrounding vectors. That interpolation is not perfect in the areas, like this case, where the changes are abrupt, because it causes a smooth on the data. These two types of errors, small and interpolated, causes the shear band to be 3 elements wide instead of 1 element wide.

This case of zero thickness shear band on synthetic image analysis exemplifies a classic error on the input data from Image Correlation programs. In real cases, this problem is not relevant on the soil-soil shear band, where the shear bands are not pure 0 thickness. Nevertheless, it represents what happens on the limits between soil and background. The patches on the limit between the soil and the background tend to contain parts of both elements. The soil moves while the background remains static, that creates a case similar to the zero thickness shear band analyzed on this Section. These errors might be plotted to the Numerical Particles that are in the soil limits, slowing them down.

5.2.2.3 Vertical compression

A case with constant vertical compression is analyzed to evaluate the precision in of the calculated volumetric strain. The compression imposed on the synthetic images was constant and homogeneous in all the domain. However, the results of the volumetric strain calculated by the PIV-NP contain heterogeneities (Figure 64a). The expected instantaneous volumetric strain per time step was -0.1 , but the results contain a range of values from -0.09 to -0.11 (Figure 64b). These errors on the calculation of the volumetric strains are caused by the intrinsic noise of the input data. The volumetric strain of a particle is calculated analyzing the displacements of the four reference node (Equation 11). Small deviations on the measured displacements have a notable effect on the direct comparison between nodes. The faster solution of this problem is to apply a smooth filter to the input data, but that might not be useful for all cases due to the loss of precision. The proper solution could be to calculate the volumetric strain analyzing a larger area of surrounding nodes.

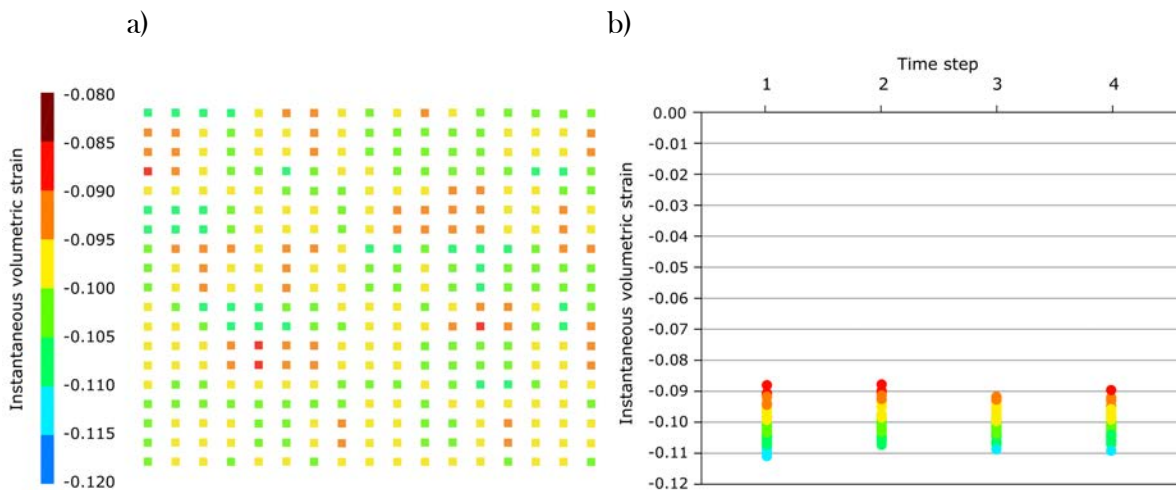


Figure 64. Vertical compression case analysis a) Numerical particle position and instantaneous volumetric strain at time step 4. b) Instantaneous volumetric strain of the numerical particles on each time step.

5.2.3 Real images

The real case is performed in the transparent tank described in Section 4.1. This case is a scaled landslide; in this Section, a reduced area of the slope is analyzed (Figure 65). The area selected contains three blue particles that are used to track the real position of three soil areas.

The analysis has been focused on the time steps of the experiment, where all the tree particles are involved in the displacement. The framerate of the camera used for the recording is 25 frames per second. The analysis uses only 1 frame per second; the reduction of frames is applied to increment the displacement per time step and facilitate the comparison between real and measured displacements.

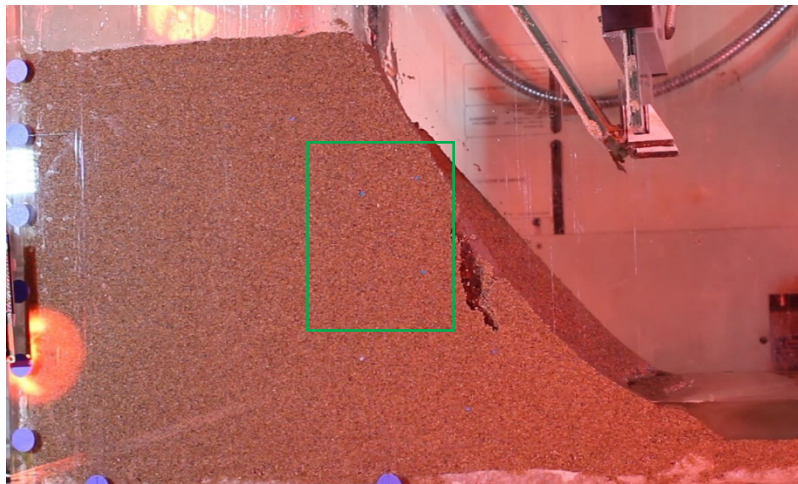


Figure 65. The general image of the real case evaluated. The analysis is performed inside the green square, where there are 3 blue particles.

The size of the analyzed area is 256x320 pixels. The size of patches used on the Eulerian Image Correlation is 16x16 pixels. The resulting input data is a regular rectangular grid of 17 x 21 vectors, with a space of 16 pixels between vectors. (Figure 66)

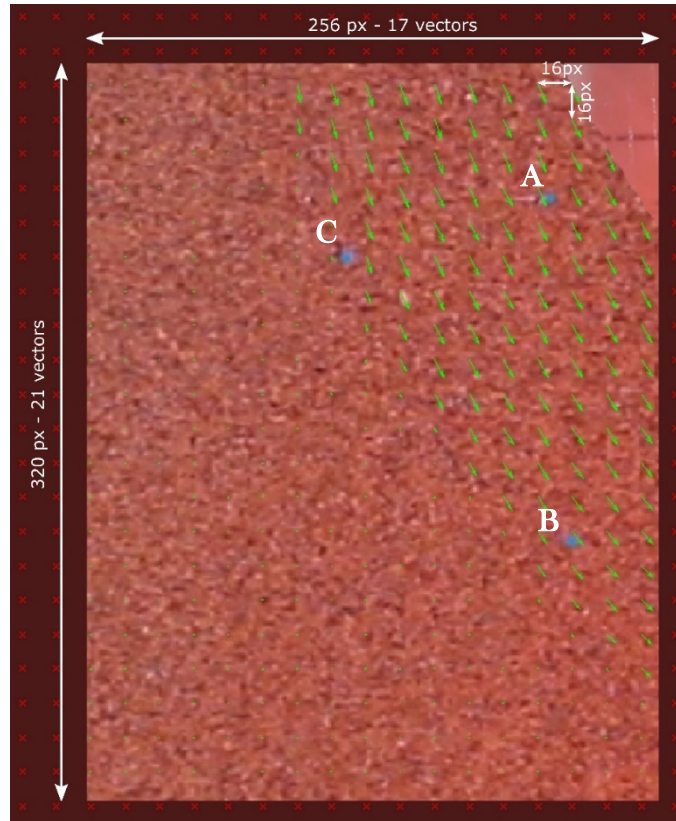


Figure 66. Grid of input data from PIVlab overlaid to the real image. The 3 blue particles are observable.

El PIV-NP uses as an input the PIVlab grid of displacement vectors that are calculated on invariable coordinates. The PIV-NP generates numerical particles in all the area enclosed by the vectors. The displacements and rest of the variables are calculated on all the particles. The evaluation is focused on the results of three numerical particles that correspond to the initial position of the blue particles.

Figure 67 shows the evolution of the location of the three blue particles measured directly in the real images. The location of the blue particles is compared with the position of the numerical particles generated by the PIV-NP. The graph expresses, qualitatively, the proper track of the location of the blue particles by the PIV-NP though the time steps. The coordinates of the graph axis are assembled in groups of 16 pixels to represent the fixed grid of input data. This illustrates how the particles change the element from one time step to the next one. This indeed means that the reference vectors that influence the numeric particle in a time step might be different from the vectors that this particle takes as a reference in the next time step. The tracking of the particles is well performed regardless of the movement of the particles through the grid elements.

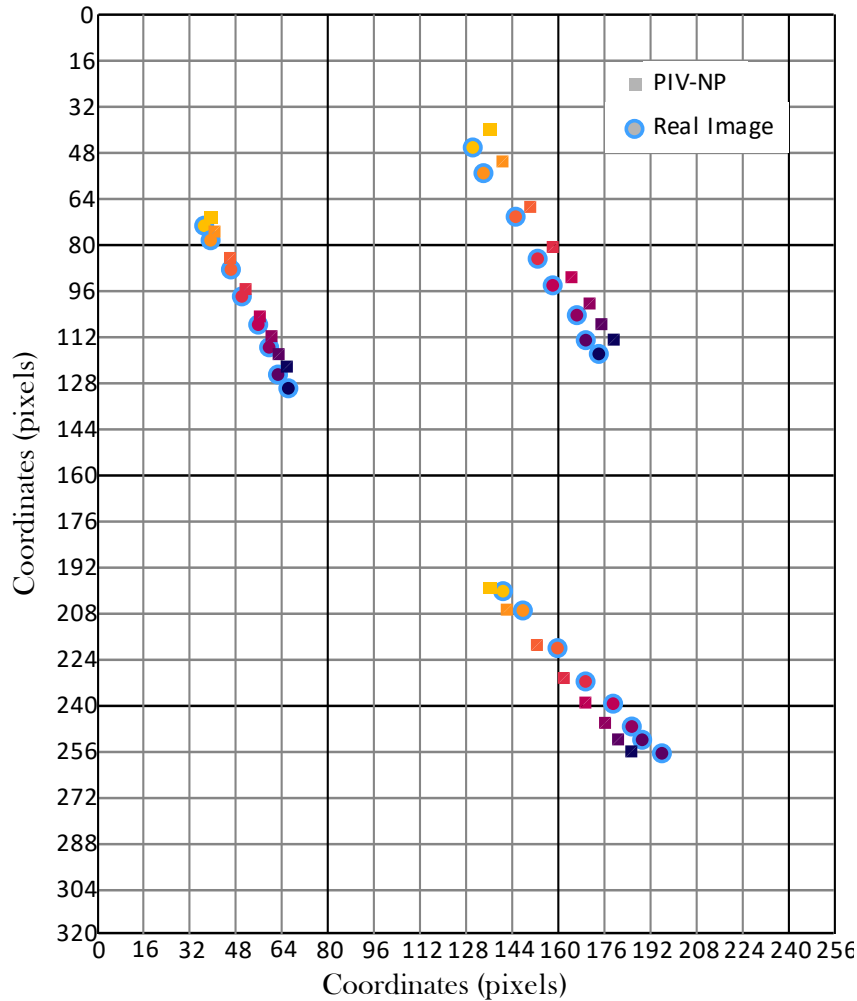


Figure 67. Evolution of the particle coordinates comparing the location in real images and the location of the numerical particle from PIV-NP.

The quantitative evaluation of the accuracy of particle tracking is performed. The displacement calculated by the PIV-NP is compared by the displacement calculated directly selecting the coordinates of the blue particles on the images.

Figure 68, Figure 69, and Figure 70 show that the accumulated displacement calculated by PIV-NP coincides with the real accumulated displacement in the three blue particles. Despite there being small discrepancies in the accumulated displacement in some time steps, these are not remarkable enough to deviate the track of the particle. The accumulated error showed part *b* of Figure 68, Figure 69 and Figure 70 is calculated by subtracting the accumulated displacement value calculated by PIV-NP from the real value. Therefore, a negative error indicates an underestimation of the displacement and vice versa.

The important conclusion of this graph is that accumulated errors do not increase with the passage of time. A weakness of the PIV-NP post-process is that if the input data were systematically higher (or smaller) than the real values, they would not be useful for long displacements, even though the input errors were within acceptable tolerances. Because with time, the accumulation of these errors would cause the numerical particles of PIV-NP to be detached from the real particles they represent, being governed by entirely different reference vectors.

Fortunately, accumulated error in Figure 68, Figure 69 and Figure 70 show that the input data from PIVlab does not have systematic error problems. The accumulated errors of the PIV-NP follow a line with a horizontal trend. The error in the cumulative displacement in particle B is taken as an example (Figure 69). At time 1 the error was overvaluation of 2 pixels, at time 2 this error is compensated with an undervaluation leaving an accumulated error of 0 pixels. At time 3 the error indicates an underestimation of -3 pixels, in the next time step the accumulated error is compensated giving an error of -2 pixels, and so on. This means that Eulerian image correlation code chosen as input data (PIVlab) tendency to underestimate the displacements (observed in 5.2.2.1 – Synthetic images), is not relevant analyzing real images. The noise errors on image correlation in real images are one order of magnitude greater than the observed underestimation. Therefore, the PIVlab data is suitable as an input for PIV-NP.

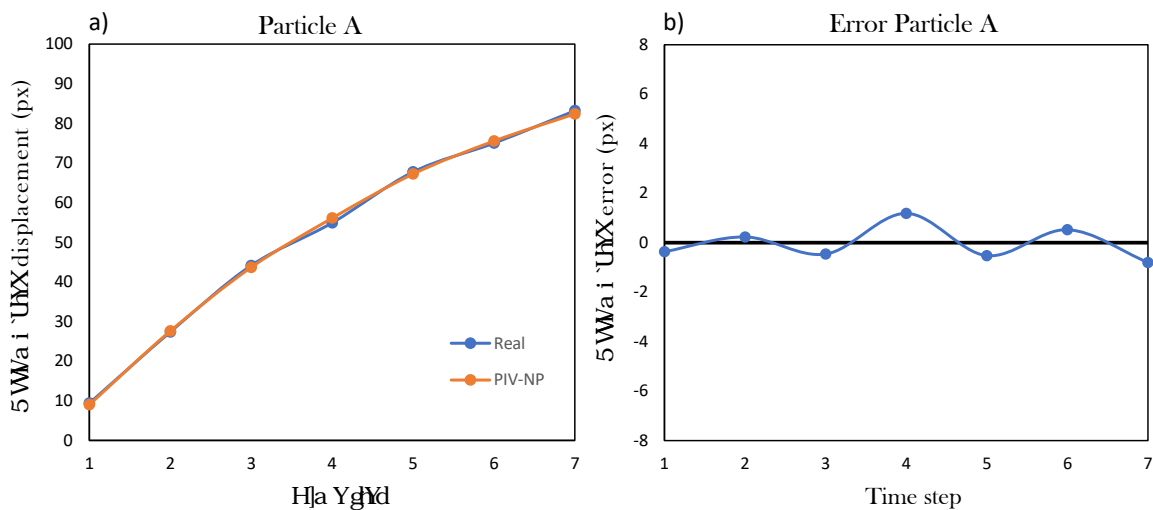


Figure 68. a) Accumulated displacement of the blue particle A and the closest numerical particle. b) Accumulated error on the numerical particle displacement.

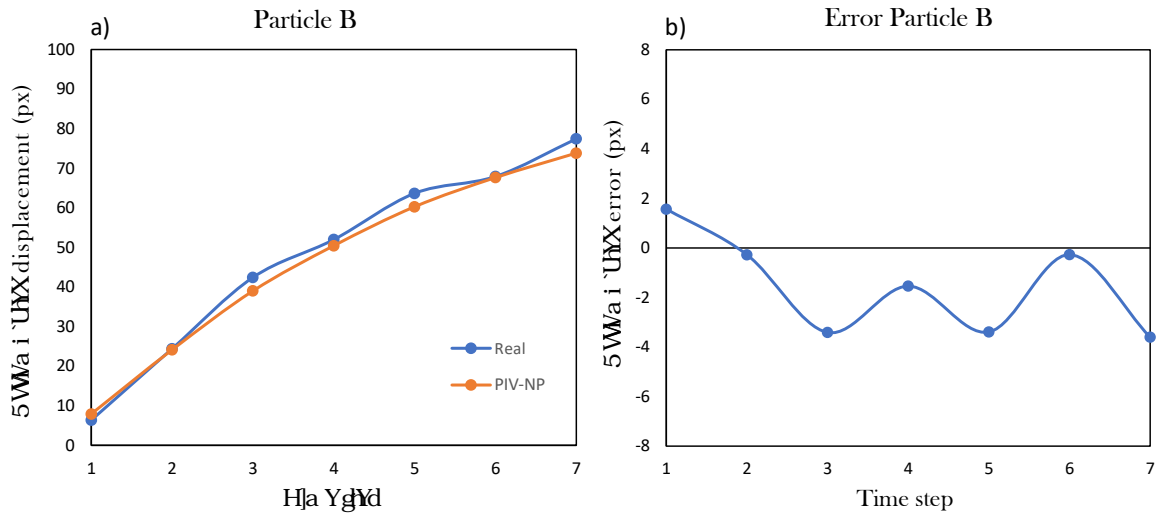


Figure 69. a) Accumulated displacement of the blue particle B and the closest numerical particle. b) Accumulated error on the numerical particle displacement.

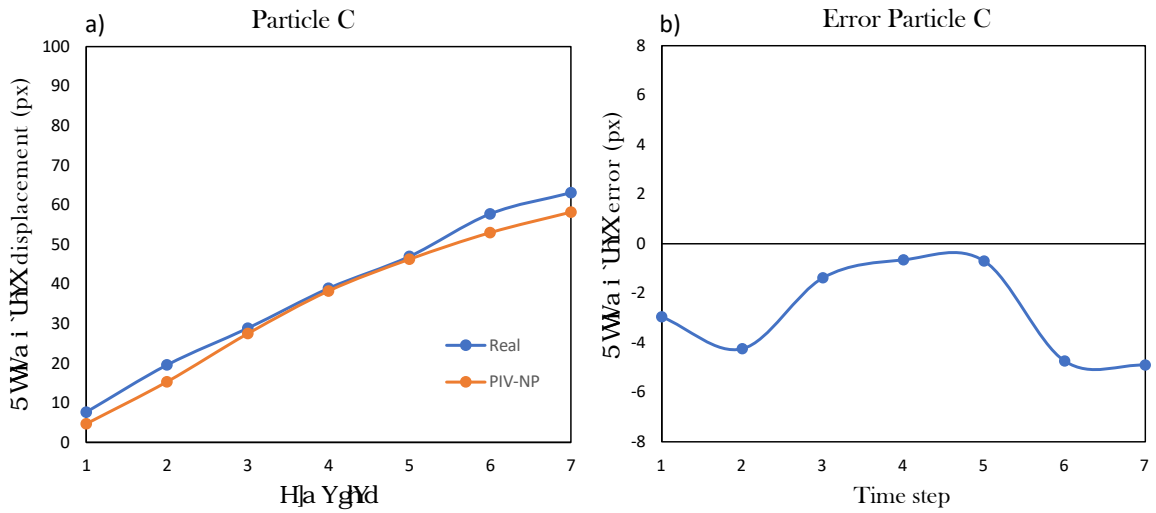


Figure 70. a) Accumulated displacement of the blue particle C and the closest numerical particle. b) Accumulated error on the numerical particle displacement.

5.3 PIV-NP analysis of experiments

PIV-NP is applied in a real laboratory experiment. The experiment consists of a rainfall induced landslide on a small scale unsaturated slope.

5.3.1 Experimental setup

The experiment was performed on a slope of sand placed on the methacrylate tank, described in Section 4.1. The tank length was limited by a glass guillotine inclined 60° . The initial slope dimensions were 250 mm high, 200 mm width, and 330mm long (Figure 71).

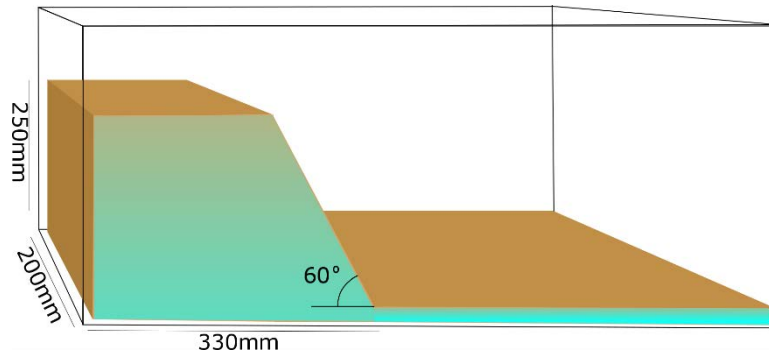


Figure 71. Initial dimensions of the slope.

The sand was placed by dry pluviation. The phreatic level was initially fixed on the base, by means of the injection system (Section 4.1) and water rose up by capillarity until reaching stable conditions. At certain time, the guillotine was removed, and the slope remained stable. The slope is then wetted by means of a regular matrix dip system (Figure 20) simulating rainfall. The loss of suction during wetting induced the slope failure which is analyzed by means of PIVlab and PIV-NP.

The soil used in the test is calcareous-siliceous fine sand from Castelldefels' beach (Catalonia, Spain). This soil is used as a reference soil in this Thesis. The geotechnical and hydraulic properties of Castelldefels' beach sand is detailed in the following sections (6.3.2 and 7.3.2).

The experiment was recorded with a digital reflex camera (Canon EOS M50) at 50 frames per second, and it lasts for just over a minute.

5.3.2 Input data and preliminary steps.

The Eulerian image correlation analysis was performed using the PIVlab. The size of the patches used is 8.9 x 8.9 mm. Therefore, the instantaneous displacement at each time step is measured on nodes forming a grid of regular rectangular elements of 78 x 43 nodes spaced 8.9 mm. For PIV-NP analysis, the elements located on the slope are filled by 1 numerical particle (Figure 72).

The information of some selected particles is bellow graphed for a better understanding of the landslide behavior using the PIV-NP possibilities.

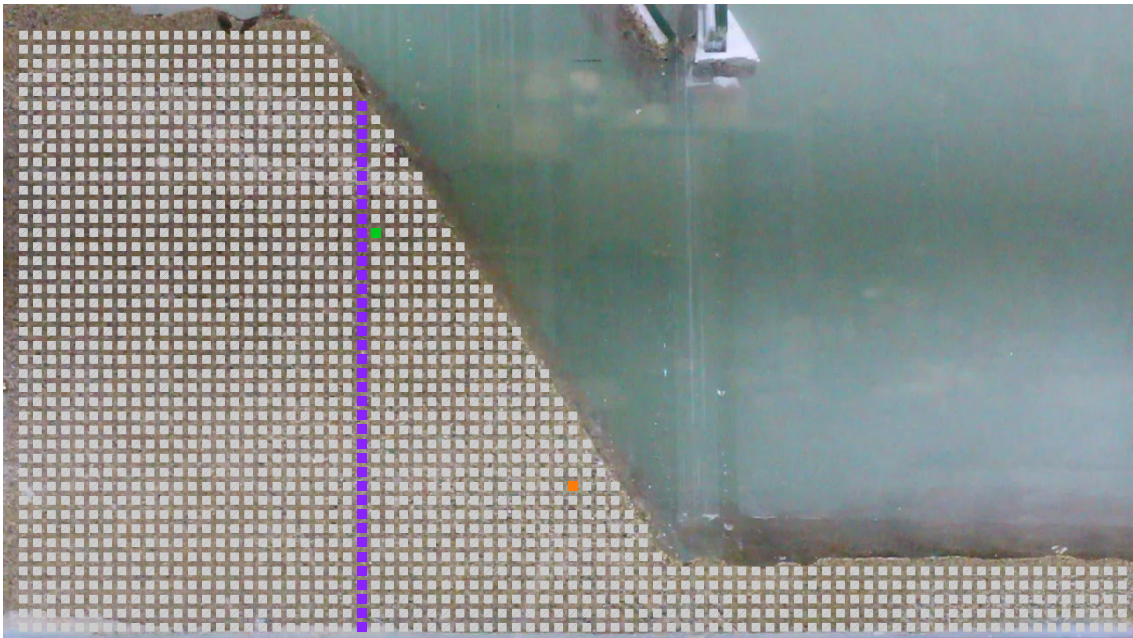


Figure 72. Initial numerical particle distribution. Highlighted particles (purple, green, orange) are analyzed more deeply.

The analysis of this case was particular because it had a long duration but with velocity peaks. The duration of the experiment was around 60s. Using 50 frames per second available, the volume of analyzed frames would be 3000 frames. In order to reduce the computational time and facilitate the visualization of the results, the Eulerian image correlation analysis was performed using 1 frame per second. This frequency (1fps) was enough to achieve a proper image correlation during most of the analysis.

However, there were some specific time steps with velocity peaks (20, 37, 50, 60s). The displacement occurred in 1 second was too large to correlate the patches accurately. That caused an accumulation of errors in the deformed area. This problem was solved using the main advantage that offers the Eulerian type of image correlation (explained in Section 2.3.1). The advantage is the independence of the results between time steps. The independency allows the modification of the results of one time step without affecting the posterior time steps results.

On this particular case, the problematic time steps were detected. A new analysis was performed just on this time steps, using 5 frames per second. A representative result of this analysis replaced the previous results of the problematic time step. Finally, the full correct results were used as the input data for the PIV-NP analysis.

5.3.3 Results

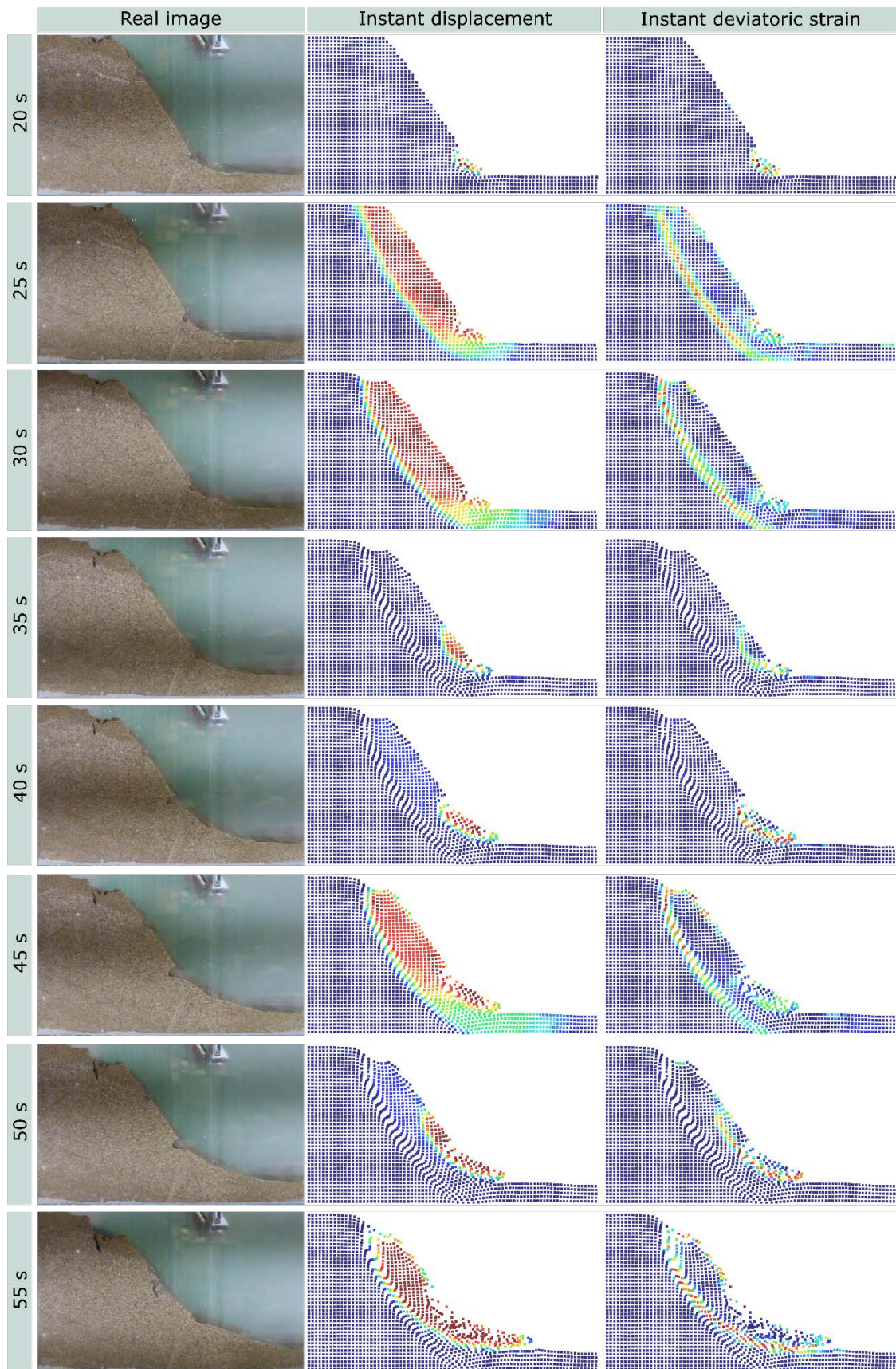


Figure 73. 2D visualization of the PIV-NP analysis of a landslide. Real image, instantaneous displacement, and instantaneous deviatoric strain.

Figure 73 is an overview of the full PIV-NP analysis of the landslide experiment. 8 time steps were selected to represent the displacement behavior. The first column shows the original frame that corresponds to the time step. The second and third columns show the instantaneous displacement and the instantaneous deviation strain, respectively. The 2D plots do not have a common legend for all time steps because the range of values is an order of magnitude different. The use of a common legend would hide most of the results. Unfortunately, it is impossible to display the legend for each plot in a readable way on a single page. Regardless, the graphs shown in Figure 73 allow a qualitative analysis, the legend in all the time steps follows the rainbow sequence, blue for the values close to 0 until red for the maximum values. The quantitative analysis would be performed using the linear graphs (Figure 74).

The PIV-NP enables to observe the landslide complex behavior and distinguish two different movements inside it. The analysis of the numerical particles combines the bi-dimensional mapping with linear graphs reveal the characteristics of each movement. Moreover, the correlation between them and their reactivations.

The landslide is defined by two movements that alternate successively: general landslide and failure of the slope base. This alternation of movements is directly observable in Figure 73. Figure 74 shows the evolution of the velocities of two selected numerical particles. The green particle, located initially in the upper third of the slope, exemplifies the behavior of the general landslide body. The orange particle, located in the lower third of the slope, exemplifies the behavior of the slope base. The exact location of these particles is shown in Figure 72.

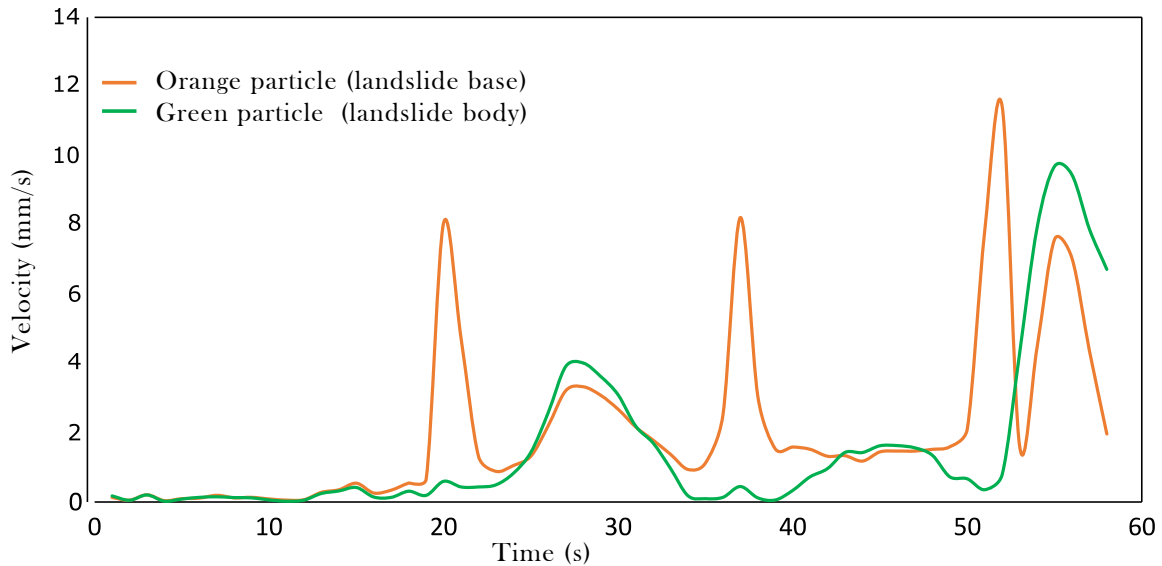


Figure 74. Comparison on the velocities of an NP in the landslide base with the velocity of an NP on the landslide body.

The general landslide occurs mainly in two episodes, between 23 – 33s and 43 – 48s. It is characterized by a rigid body movement involving the whole slope. The range of velocity is between 2 and 4 mm/s.

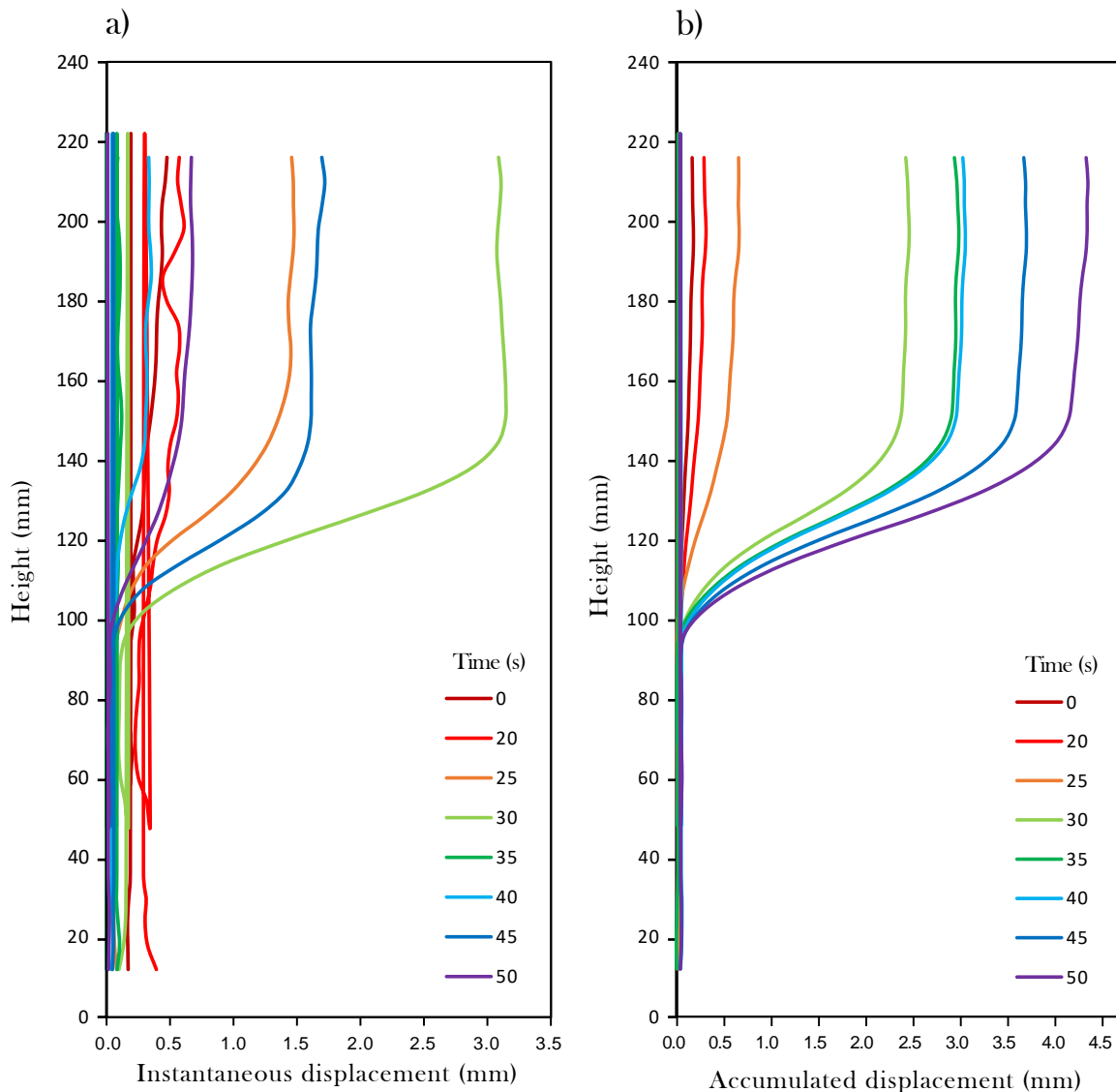
The base failure episodes occur at the time steps 20, 37, and 51s. The duration of these episodes is more restrained than in the general landslide. The movement is more chaotic and is focused on the slope base. The range of velocities is between 8 and 17 mm/s.

It is useful to be able to observe the 2D map of the state of the variables and compare it with a single NP evolution graph line. This comparison leads to infer a tight connection between the two movements. The alternation of movements follows this sequence: The base failure is the first to occur (20s). When this movement has stopped, the general landslide starts reaching a peak of velocity at 28s, after that, it slows down until it stops (37s). On that moment, the base failure reoccurs. After the base failure, the general landslide reactivates.

This comparison based on the linear graph (Figure 74) would lead to deduce that the base failure triggers the general landslide. However, the observation of the displacement and deviatoric strain maps (Figure 73) show that the shear surface of the general landslide is more profound than the base failure. Their respective shear surfaces do not interact until the last failure (55s).

The combined analysis of the results illustrates that the correlation between movements is not obvious. Figure 75 plots the evolution of the variables (instantaneous and accumulated displacement and deviatoric strain) in a line of numerical particles (purple in Figure 72). These figures exemplify the behavior of the general landslide.

The instantaneous and accumulated displacements (Figure 75 a-b) show that the body of the landslide moves as a rigid body. The displacements of the NP that correspond to the landslide are equal inside each time step. The instantaneous displacement graph highlights the time steps when the landslide is more active. On the time steps that the landslide is stopped, and on the stable NP, a certain level of error is observable on the instantaneous displacement graph. Nevertheless, these errors are negligible compared with the data, as in the accumulated displacement, the errors are not noticeable.



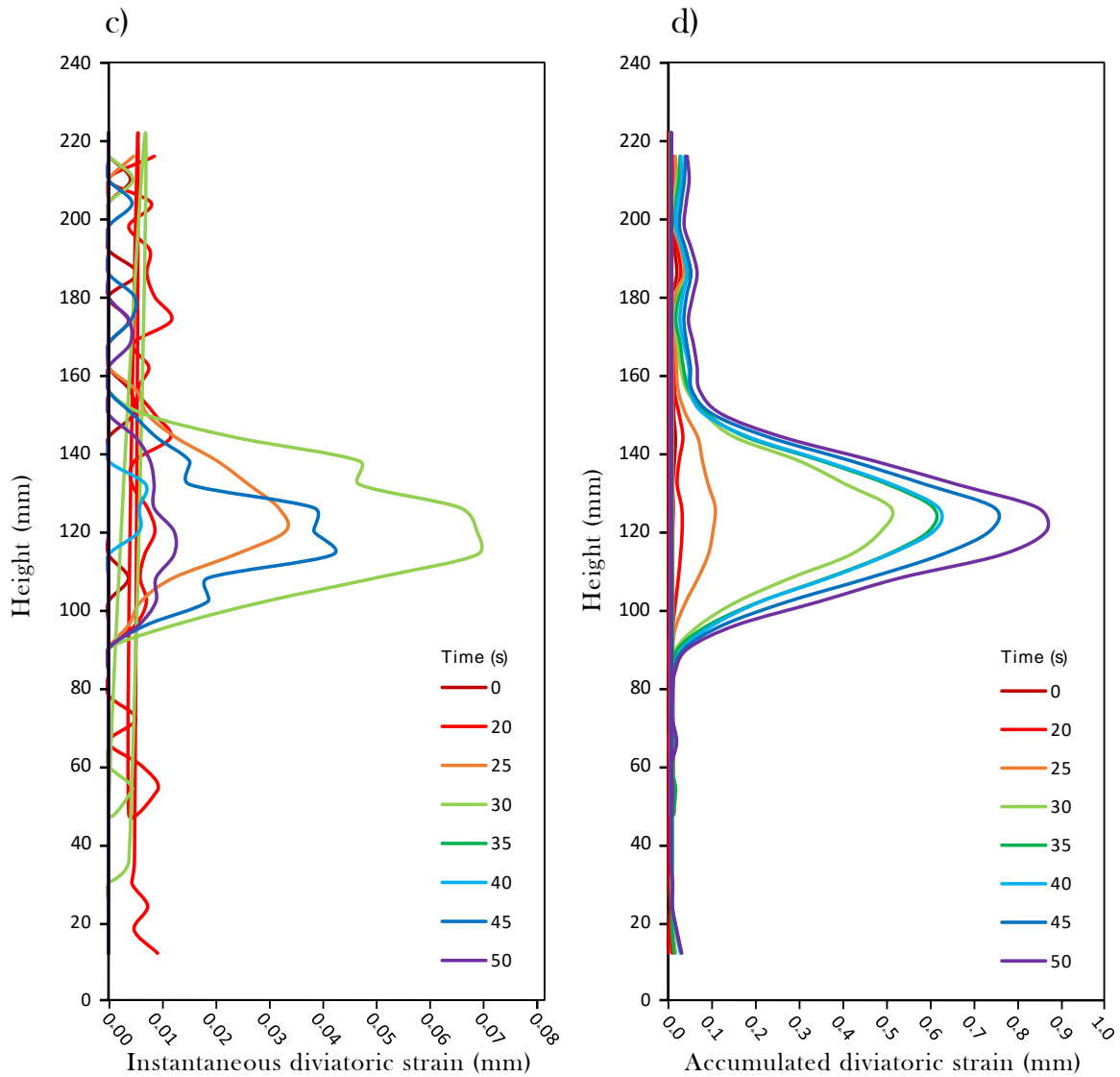


Figure 75. a) Instantaneous displacement b) Accumulated displacement c) Instantaneous deviatoric strain d) Accumulated deviatoric strain.

Figure 75c-d plots the instantaneous and accumulated deviatoric strains on the purple NP to exemplify the general landslide. On both graphs, the shear surface is clearly marked with a peak on 120 mm on this line of NP. The feature of PIV-NP to work with numerical particles, that moves with the soil that represents, enables the evaluation of the evolution of the state of the real soil particles. On this case, it is especially interesting to observe how the shear surface of the landslide coincides in all the episodes. Therefore, it is appropriate to name it a reactivation of the landslide.

5.4 Conclusions

The Particle Image Velocimetry - Numerical Particle (PIV-NP) is a post-process that combines the useful characteristics of the Eulerian and the Lagrangian scheme. The PIV-NP uses as an input the Eulerian Image Correlation results. The Eulerian Image Correlation results are structured as a fixed grid of spatial coordinates (x,y) with the displacements measured on them in each time step (u,v) . The PIV-NP applies the Material Point Method (MPM) concepts to map these displacements into Numerical Particles that move through the fixed grid. Each Numerical Particle represents a part of the analyzed soil surface.

The validation of PIV-NP was performed using 3 types of input data:

- Synthetic data: Input data manually written.
- Synthetic images: Input data from the image correlation analysis of artificially generated images.
- Real images: Input data from the image correlation analysis of natural soil images.

The main conclusions from the validation are:

- The PIV-NP correctly maps the displacements and does not introduce additional errors.
- The PIV-NP just requires defining the initial area of interest on the input data, which simplifies the user actions in the image correlation preprocess.
- The shear bands are complex areas to analyze due to the errors from the input data and the discretization, but interesting in terms of calculating the deviatoric strain.
- The PIVlab might be a good Eulerian Image Correlation software for the input data, because its errors do not systematically tend to over or lower estimate the displacements in soils.

The PIV-NP was used to analyze a case of a small scale landslide. It correctly plots the mobilized soil and shear bands. The sequence of reactivations of the landslide is properly analyzed using the PIV-NP features.

6

Chapter 6

Non-invasive surface measurement of the degree of saturation by ShortWave InfraRed images

A massive, continuous and non-invasive technique for measuring the degree of saturation in laboratory experiments by means of images is proposed. Soils become darker when they are wetted because the presence of water leads to a lower reflectance if compared with dryer states. The effect of the degree of saturation on the reflectance is especially high at certain wavelengths of the Short-Wave InfraRed (SWIR) spectrum (1400 -1550 nm and 1900 - 2000 nm). Therefore, the reflectance can be univocally correlated with the degree of saturation. Reflectance allows measuring the distribution of the degree of saturation and its evolution in time on planar surfaces of samples recorded by SWIR images.

The study presents the basis of the methodology and the procedure steps, including the calibration of the curve correlating reflectance and degree of saturation. The degree of saturation was measured in stationary and transitorily tests performed in a sandy soil column (20 cm wide and 40 cm high). The agreement of the image-based measurement of degree of saturation with direct measurements by means of standards sensors (which provide point data in the domain) highlights the capabilities of the proposed methodology.

The effect of the density of the soil is also discussed in Section 6.8.1. It was concluded that the density effect has a minor relevance. The degree of saturation was found to be the variable contributing to the reflectance for the analyzed soil densities.

6.1 Introduction

In the experimental field of unsaturated soils, it is of interest to measure the degree of saturation, water content and suction because they control their mechanical and hydraulic behavior (Vanapalli and Mohamed, 2007; Olivares *et al.*, 2009). The measurement of these inter-related variables is traditionally carried out by means of devices (tensiometers, hygrometers, capacitance sensors and dielectric sensors) that collect discrete data in localized volumes. The placement of these sensors at or near the region of interest has to be selected a priori. However, the region of interest to measure such variables is, in some cases, unknown at the beginning of the test. This is, for instance, the case of scaled tests of slope failures in unsaturated soils in which the position of the failure surface, where the value of the degree of saturation is of interest, cannot be specified at the beginning of the test.

As an alternative to sensors, other methods to evaluate the distribution of the degree of saturation or water content in soil have been explored. The Neutron radiography and tomography were proposed as a non-invasive measurement of the water content (Tumlinson *et al.*, 2008; Cheng *et al.*, 2012; Kim, Penumadu and Hussey, 2012; Kang *et al.*, 2014). It is based on the high neutron attenuation caused by the hydrogen of the water molecule compared to the interaction with the atoms of soil grains. This technique allows analyzing in 3D the entire sample and it is useful to determine the hydraulic properties of granular soils. However, it presents some limitations for being used in general laboratory experiments. The technique is restricted to small samples that are placed in front of a neutron's beam. The procedure is based on the analysis of the neutrons that crosses the sample; therefore, the neutron penetration limits the thickness of the sample. The main difficulty is to manage the neutron radiation and induced radioactivity hazard, which implies the need to perform the experiments in isolated capsules or chambers.

This Chapter presents a non-invasive and non-destructive technique for the measurement of the degree of saturation (S_r) of porous media in experimental tests by means of Short-Wave InfraRed (SWIR) image processing, with the aim of providing massive information on the spatial distribution of S_r and its evolution in time. The techniques described in this Chapter may help to perform comprehensive laboratory tests at a mid-scale which are useful to build benchmark boundary values problems to validate computational models.

6.2 Physical principles

The methodology presented in this paper is based on the difference of light reflection/absorbance between water and solid particles. Water is more absorbent of light than solid soil particles. This is the reason behind the fact that wet soil is less reflective (darker) than the same soil at identical conditions but drier. (David B Lobell and Asner, 2002; Knadel, 2012; Nolet *et al.*, 2014; Sadeghi, Scott B Jones and Philpot, 2015; Tian and Philpot, 2015) carried out specific tests using laboratory spectroscopy to analyze the effect of moisture on the reflectance of different soils. (Leu, 1977; Shuchman and Rea, 1981) evaluate other soil properties affecting the reflectance.

Given a soil (characterized by mineral composition, grain size distribution, packing density, surface roughness), the presence of the water surrounding the soil grains causes a change in scattering and absorption of the incident light. A comprehensive explanation of the effect of water on the light reflectance was given by (Nolet *et al.*, 2014) after describing briefly the theoretical background. Under dry conditions, the reflectance is controlled by the soil mineralogy and structure (Figure 76a). When some water is added to the soil (Figure 76b), water is held in the soil as adsorbed water films around the solid grains. At this condition, the optical path length in the water is close to zero and the decrease of spectral reflectance is almost solely due to scattering. As the water content increases (Figure 76c), water meniscus form bridges between grains, which increase the optical path length, resulting in an increase availability for the absorption of light by water. When the soil becomes fully saturated (Figure 76d) and the free water appears at the surface being evaluated, the optical path length in water is at its maximum and certain wavelengths may be completely absorbed (Hillel, 1998; David B. Lobell and Asner, 2002).

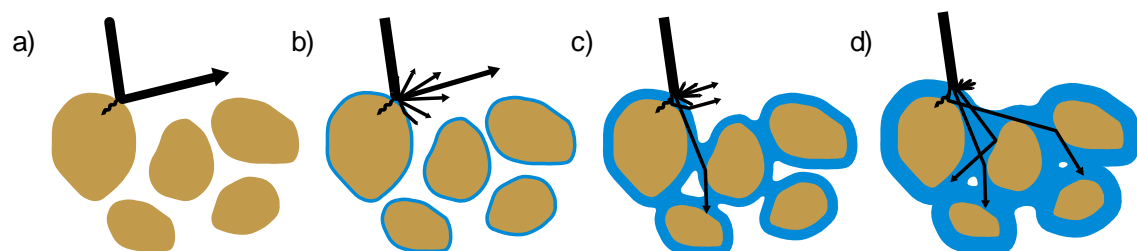
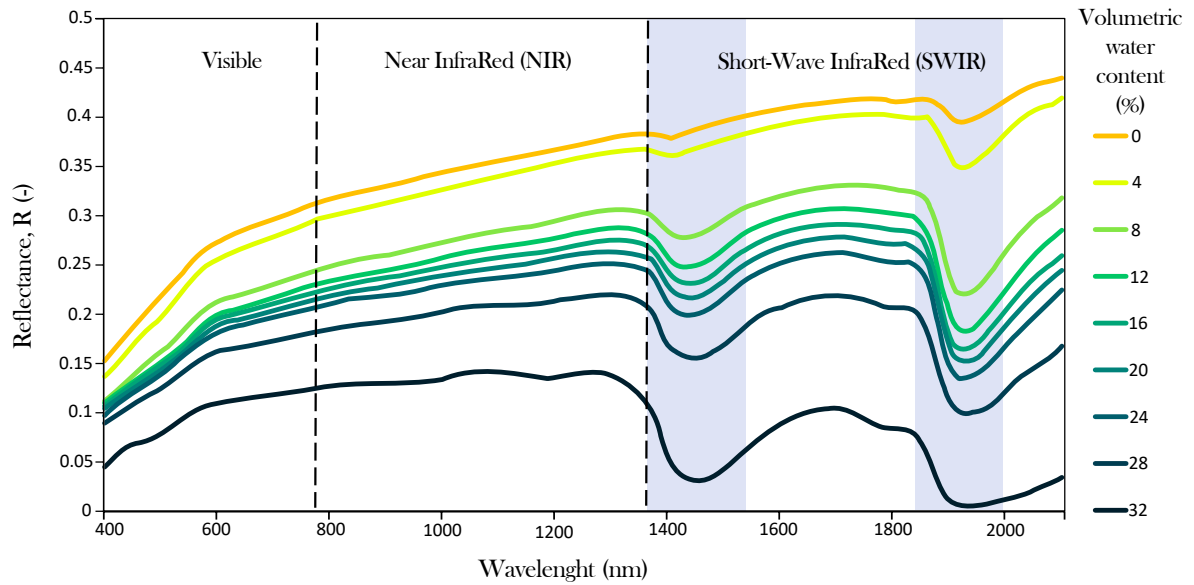


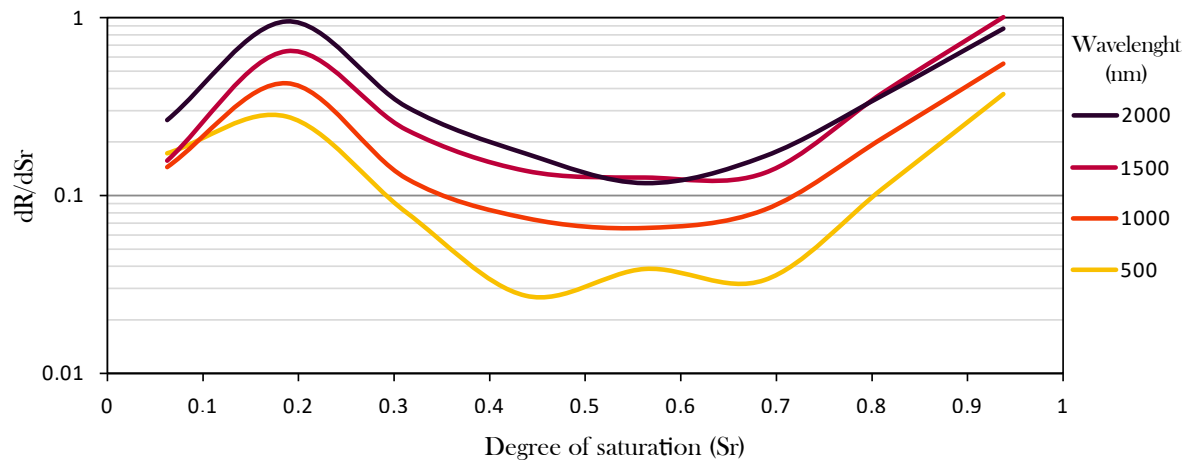
Figure 76 Effect of water content light absorbance. (a) Dry soil; (b) Adsorbed water films; (c) Capillary menisci between grains; (d) Saturated.

Given a soil, the magnitude of the absorbed light will change not only depending on the water content but also on the wavelength of the light (Knadel *et al.*, 2014; Nolet *et al.*, 2014; Sadeghi, Scott B. Jones and Philpot, 2015; Tian and Philpot, 2015). This is made evident in Figure 77a (Nolet *et al.*, 2014). The reflectance of sand at different values of the degree of saturation was measured in the laboratory by means of a wavelength full range (300-2500 nm) spectrometer. It was observed that, for a given wavelength, the reflectance decreased with the increasing amount of water. The magnitude of this variation depends on the wavelength (Figure 77b). With the aim of correlating the reflectance with the degree of saturation, it is convenient to select the wavelength range in which the reflectance is most sensitive to the degree of saturation. (Soranzo, Tamagnini and Wu, 2015) evaluated the degree of saturation in natural soils by means of the analysis of images taken at the visual spectrum. For the range of wavelengths of the visual spectrum, the effect of the degree of saturation on the reflectance is not enough to provide a proper precision in the correlation between reflectance and degree of saturation. To overcome this limitation of visual spectrum images, (Siemens, Peters and Take, 2013; Siemens, Take and Peters, 2014; Peters, Siemens and Take, 2017; Sills, Mumford and Siemens, 2017) use artificial transparent soils with the same reflection than the fluid used and a black background. Then, they are able to estimate the amount of air in the sample and, therefore, to calculate the degree of saturation.

For natural soils, and according to Figure 77, convenient wavelength ranges for correlating reflectance and degree of saturation are 1400 -1550 nm and 1900 - 2000 nm (shaded areas in Figure 77a).



(a)



(b)

Figure 77 Reflectometry of coastal beach sand (Nolet *et al.*, 2014). (a) Measured spectral reflectance of beach sand over a range of 350-2100 nm in samples with different values of degree of saturation. Shaded areas indicate the optimal range to evaluate the S_r measuring the reflected light. (b) Variation of reflectance with the degree of saturation calculated from the figure a) for four wavelengths (500, 1000, 1500 and 2000 nm).

The effect of changing soil saturation on the light reflectance has been evaluated in the literature for different soils (from coarse sand to silty loam). This information is collected in Figure 78. In all cases, the maximum difference between the reflectance for dry and saturated conditions is reached in the range of 1400 -1550 nm and 1900 - 2000 nm. This behavior is mainly controlled by the optical properties of the water, which exhibits an absorption peak for these two wavelength ranges.

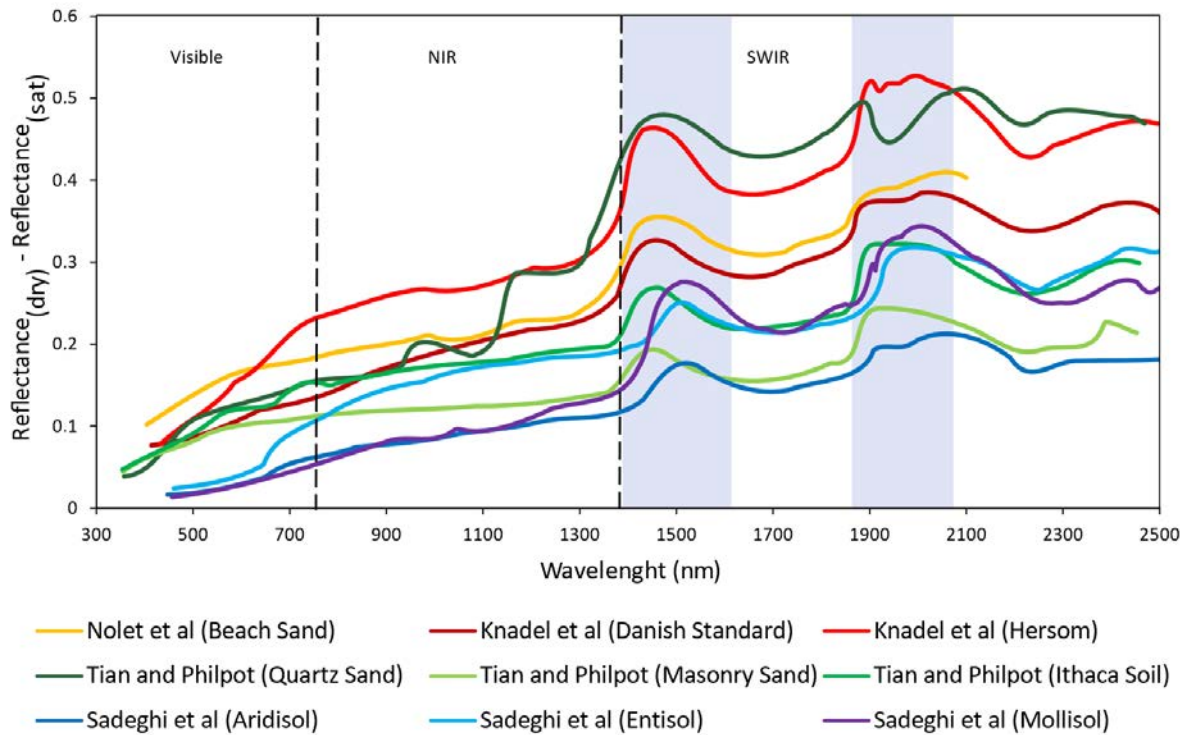


Figure 78 Variation, for different soils, of the difference between the reflectance measured at dry and saturated conditions for varying wavelengths of different soils. Shaded areas (1400 -1550 nm and 1900 - 2000 nm) corresponds to maximum differences.

Based on these data, this paper explores the possibility of assessing the degree of saturation of soil samples by means of the correlation between the reflectance of SWIR images (wavelength of 1400-1550 nm) and the degree of saturation. The chosen wavelength is determined by the available options of cameras between the budget. The aim of the method is to provide the distribution of the degree of saturation and its evolution in time of unsaturated samples under stationary and transient conditions. The method is first calibrated by means of prepared samples of calcareous-siliceous fine sand at different degrees of saturation. Results will be validated in an unsaturated soil column. Details of the procedure are indicated in the next Sections.

6.3 Experimental setup

The purpose of the test performed is to measure the degree of saturation of unsaturated soil surfaces by correlating the light reflectance with the degree of saturation. The procedure requires previous calibration carried out on samples with a known degree of saturation. Based on the spectrometry studies discussed above, the wavelength used in this work is 1500-1560 nm.

6.3.1 Camera

The unsaturated samples are captured by a Short-Wave InfraRed (SWIR) camera. Common SWIR cameras use the InGaAs sensor. This is a specialized and expensive technology. As an alternative, the common sensor used in digital cameras (CCD array charge-coupled device) can be used after a phosphor-coated treatment (which is significantly cheaper). In the experiments presented in this paper, the CamIR sensor from Scintacor is used. The camera should not have any gain or automatic image improvement to avoid additional pixel intensity changes not caused by the soil reflectivity. The sensor (Sony progressive scan interface interline transfer ICX445 1/3" Exview HAD CCDTM), after the phosphor treatment, has two spectral sensitivity peaks at 1512 and 1540 nm (Figure 79).

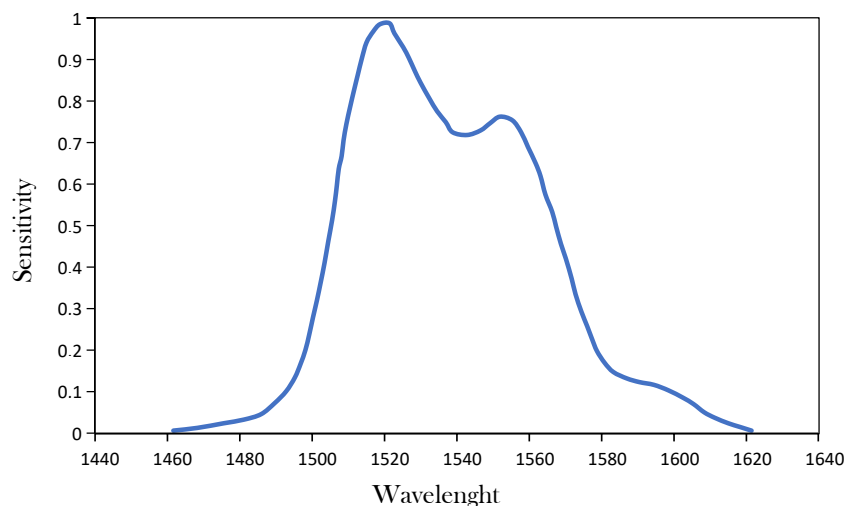


Figure 79 Sensitivity curve of the camera phosphor treated sensor.

Energy-efficient infrared lightbulbs of 175W are used as a light source. Other options that could be used are incandescent tungsten light bulbs (dismissed due to the low energy-efficiency) or Sunlight (dismissed due to the lack of intensity control). Normal LED or CFL lights cannot be used as a light source because they emit only in the visible spectrum.

The illumination must be constant throughout the experiment because the light reflected depends on the reflectivity index but also on the amount of incident light. Therefore, all the experiments of a set shall be performed with the same lightbulb arrangement and camera distance.

6.3.2 Material

The soil used in the test is calcareous-siliceous fine sand from Castelldefels' beach (Catalonia, Spain). The properties are summarized in Table 7. The soil-water retention curve (SWRC), under imbibition conditions, was measured by the gravimetric method in a segmented hanging column. The measured points (S_r , suction) are indicated in Figure 80 together with the estimated van Genuchten model (van Genuchten, 1980). (Values of the model parameters are indicated in Table 7).

Table 7 Geotechnical properties of Castelldefels' sand.

| Parameter | Units | |
|--|--|-------------------|
| Particle density | kg/m ³ | 2665 |
| | | min - max |
| Dry density | kg/m ³ | 1442 - 1795 |
| Porosity | | 0.459 - 0.326 |
| Particle size distribution | | |
| D10 | mm | 0.254 |
| D30 | mm | 0.3109 |
| D60 | mm | 0.3715 |
| Air-entry value | kPa | 0.7 |
| van Genuchten parameters: | $S_r = S_{r_r} + \frac{(S_{r_s} - S_{r_r})}{[1 + (\alpha h)^n]^m}$ | |
| α | | 0.07 |
| n | | 2.2 |
| m | | 0.545 |
| S_{r_s} | | 0.73 |
| S_{r_r} | | 0 |
| Saturated permeability at a porosity of 0.4 | m/s | $2 \cdot 10^{-4}$ |

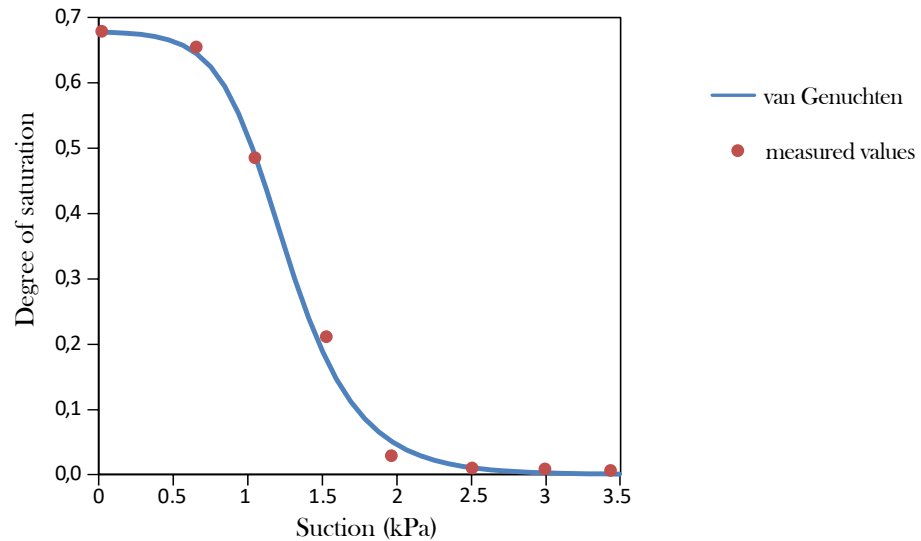


Figure 80 Measured values and calibrated water retention curve of Castelldefels' beach sand.

6.3.3 Measuring the reflectance (gray value)

The method requires the measurement of the reflectance in granular materials. The pixel intensity, which is a measure of the reflectance, is defined by means of the gray value (GV). It ranges from 0 (black color) to 255 (white color). Consider a homogeneous and unsaturated sample (150x250 mm) of Castelldefels' sand whose bottom is saturated, and the degree of saturation reduces with height in a situation of equilibrium. 0 shows digital images of this sample taken at visible light spectrum (Figure 81a) and at an infrared wavelength (SWIR) (Figure 81b). The varying degree of saturation results in a gradual color variation from the light color of the upper part of the sample to the darker color of the saturated bottom.

Due to the texture of the soil, the different colors of the sand grains and the phosphor-coated treatment to transform the visual sensor into a SWIR sensor, the image exhibits "salt-and-pepper" noise. This noise implies that the discrete information from each single pixel (in this case 1x1 mm) does not represent the general reflection of the surrounding area, which depends on the degree of saturation. Therefore, an analysis based on pixel intensity (Grey value: GV) cannot be correlated with the degree of saturation and a GV of a representative area for each pixel is required.

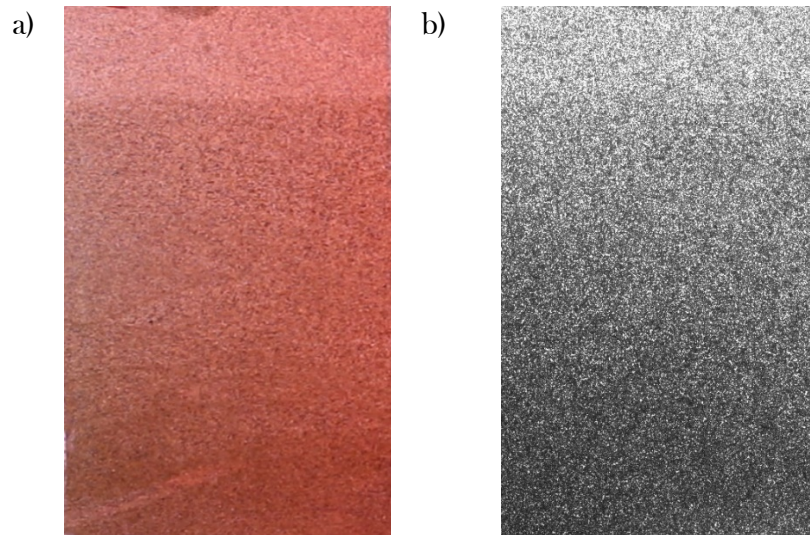


Figure 81 Images of an unsaturated column of Castelldevels beach sand in (a) the visible and (b) the SWIR spectra.

In order to wane the salt-and-pepper noise, the intensity of each pixel is calculated as a weighted average of the intensity of the pixels located in the vicinity of a given location by means of a Gaussian filter. The average gray value ($GV_{x_0y_0}$) associated with a pixel located at coordinates (x_0, y_0) is computed by means of the 2-dimensional Gaussian function centered on the pixel evaluated:

$$GV_{x_0y_0} = \sum GV_{xy} \frac{1}{2\pi\sigma^2} e^{-\frac{(x-x_0)^2+(y-y_0)^2}{2\sigma^2}}$$

Equation 15

where GV_{xy} is the gray value of a pixel located at coordinates (x,y) and σ is the standard deviation of the Gaussian function. The value of the standard deviation mainly depends on: the noise from the camera sensor, the grain size and the expected spatial gradient of the degree of saturation. Figure 82 shows the SWIR image of the sample after applying the Gaussian filter with a standard deviation of 20 pixels. In this example, each filtered PI



Figure 82 SWIR image after a Gaussian filter.

6.4 Calibration

The calibration procedure allows correlating the SWIR reflectance of soil samples with the degree of saturation. SWIR images of a set of samples of Castelldefels' sand having the same density and different water contents were analyzed. The calibration will provide a curve correlating the pixel intensity (GV) with the degree of saturation.

The samples were prepared in cylindrical containers, 7.1 cm of diameter and 3.6 cm high (Figure 83). The camera and two infrared lightbulbs were fixed in position. Zenithal images were taken with the SWIR camera. All the samples were placed under the fixed camera in the same place in order to maintain a constant intensity of incident light.

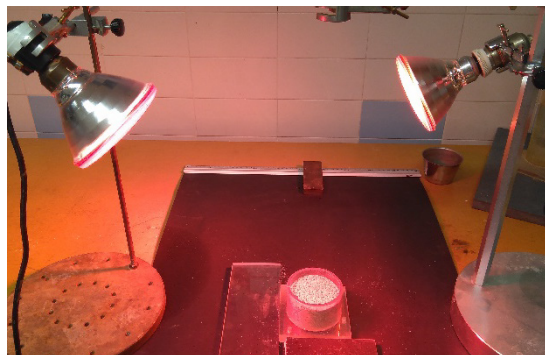
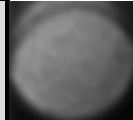
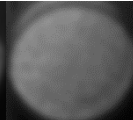
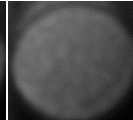
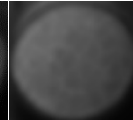
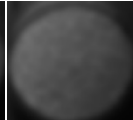
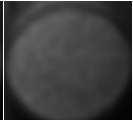

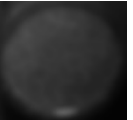


Figure 83 Experiment setup for calibration.

Non-invasive surface measurement of the degree of saturation by ShortWave InfraRed images

Eight samples compacted at 1390 kg/m^3 of dry density and different degrees of saturation (0, 0.75%, 2.5%, 5%, 10%, 15%, 20% and 25%) were evaluated. In order to reduce the salt-and-pepper noise, the intensity value of each sample is determined by means of a Gaussian average pixel intensity. 0 shows the SWIR images of the samples after applying the Gaussian filter (applying a standard deviation of 50 pixels) and the values of water content, degree of saturation and GV. Figure 84, based on Table 8, shows the curves correlating the degree of saturation and the gray value.

Table 8 SWIR images after Gaussian filter and parameters of the sample used in the calibration

| | | | | | | | | |
|---------------|---|---|---|---|---|--|---|---|
| Water content | 0 | 0.73 | 2.63 | 5.26 | 10.53 | 15.79 | 21.05 | 26.35 |
| Sr | 0 | 0.02 | 0.07 | 0.15 | 0.30 | 0.44 | 0.60 | 0.73 |
| SWIR image |  |  |  |  |  |  |  |  |
| GV | 119 | 92 | 86 | 83 | 78 | 71 | 64 | 54 |

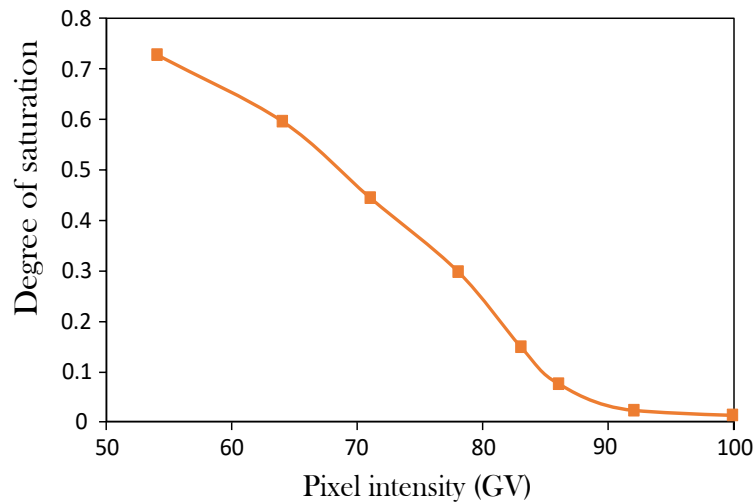


Figure 84 Correlation curve between the degree of saturation and gray value measured in samples.

The correlation curve of 0 depends not only on the type of soil, density and degree of saturation but also on the intensity of the incident light. It follows that this curve cannot be used to evaluate the degree of saturation of samples of the same soil from SWIR images taken under different light intensity because the light intensity changes the absolute value of the reflectance. However, the GV values, for a given light intensity, for the extreme cases of soil moisture (dry, $Sr = 0$, and fully saturated, $Sr = 1$) may be used to normalize the GV values (GV_{norm}) as follows:

$$GV_{norm} = \frac{GV - GV_{dry}}{GV_{sat} - GV_{dry}}$$

Where GV_{sat} and GV_{dry} are the gray value at saturated and dry condition ($Sr = 0$), respectively. Then the correlation Sr vs GV_{norm} becomes independent of the light intensity. Figure 85 shows the calibration curve for the samples analyzed.

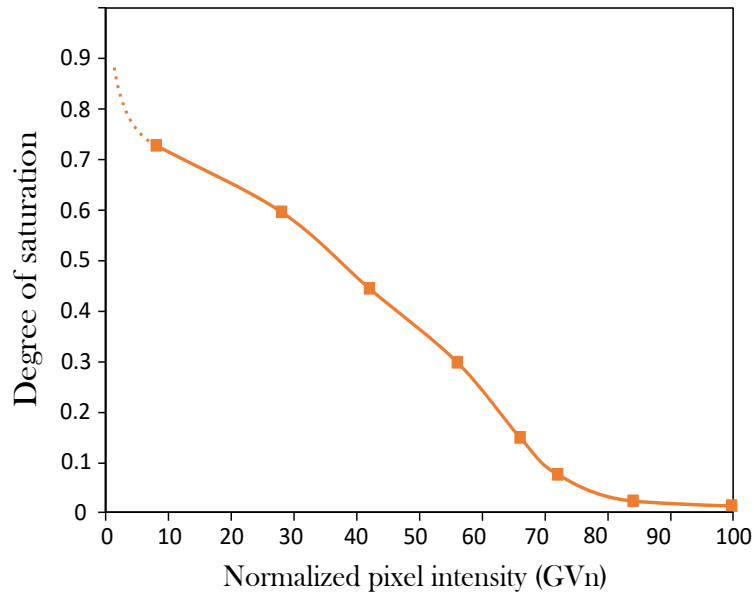


Figure 85 Calibration curve correlating normalized gray value and degree of saturation measured in samples.

6.5 Analysis

Once the calibration is achieved, this Section presents the steps to assess the degree of saturation based on SWIR images. The method can be applied to a sequence of images in order to evaluate not only the distribution of the degree of saturation at a certain time, but also its variation in time. The steps are described below and indicated in the flowchart of Figure 86 for a SWIR video recording. The analysis will be carried out for each extracted frame from the video images.

Steps

1. Record the laboratory experiment with the SWIR camera, and extract the frames from the video.
2. Each image is stored as a matrix where each position corresponds to the pixel intensity (GV) of every pixel.
3. The Gaussian filter is applied
4. The Point of Interest (POI) coordinates are selected or imported.
5. The area of interest is selected or imported.
6. The GV matrix is created storing the pixel intensity of the points of interest that are inside the area of interest.
7. The GV_n matrix is created, normalizing the values of the GV matrix.
- 8a. The degree of saturation and the water content of every point of interest is calculated from the GV_n matrix using the calibration curves.
- 8b. The calibration curves come from the calibration process performed once for each material. The curves provide the relationship between the normalized GV of the calibration images and their degree of saturation or water content.
9. Suction is calculated from the degree of saturation using the Water Retention Curve of the material.
10. The results can be plotted on contour graphs providing the spatial distribution of the variable of interest (degree of saturation water content, suction) at any time t (0). The histories of desirable variables may be built at any point of interest (0).

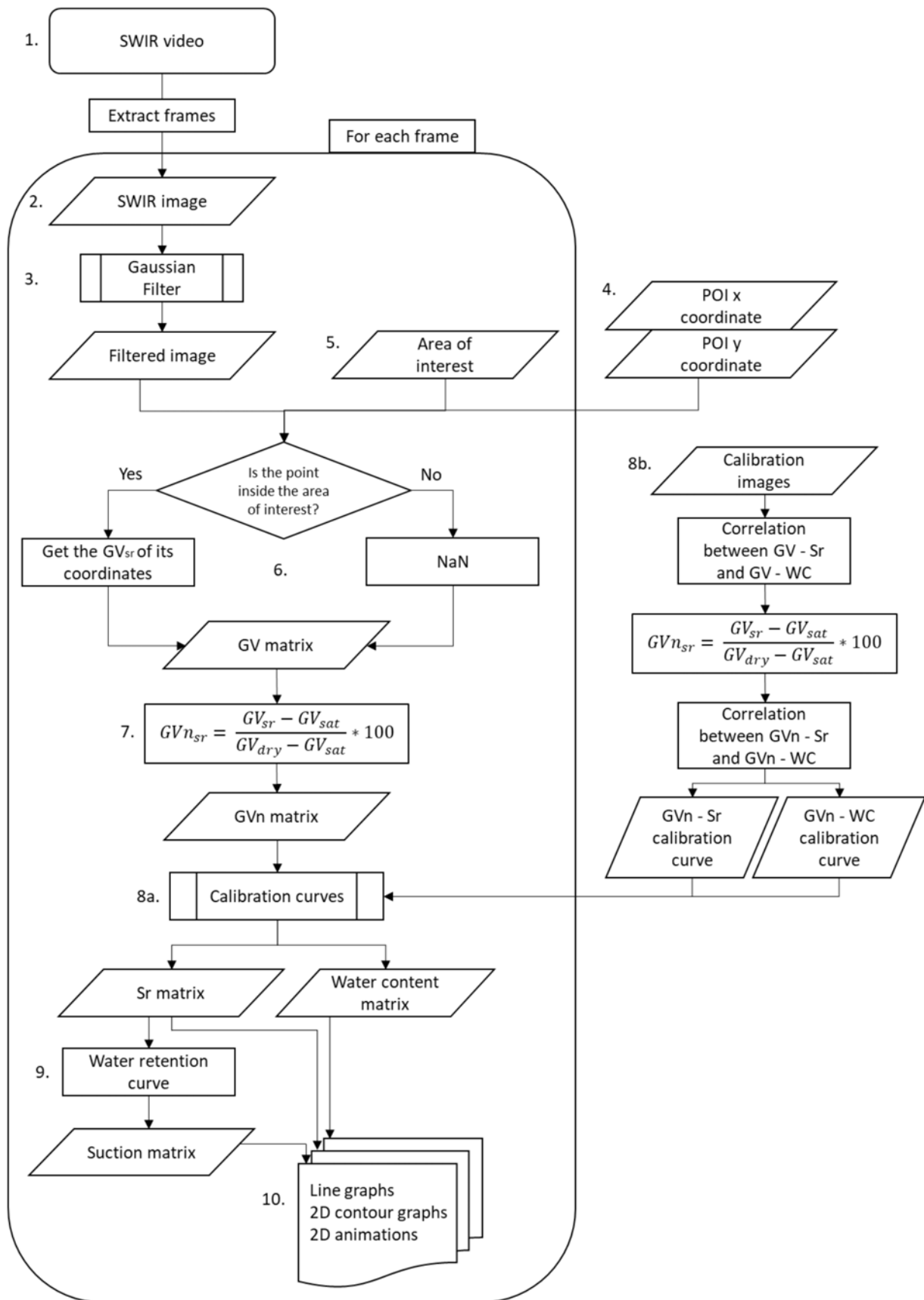


Figure 86 Flowchart of the technique algorithm to assess the saturation degree and suction from SWIR images.

6.6 Validation and evaluation

The method proposed is applied in this Section to measure the distribution of the degree of saturation (S_r) in a column of an unsaturated Castelldefels' sandy soil using the calibration curve of 0. The experiment is divided into two stages: (a) stationary stage after imposing the saturation of the bottom of the column; and (b) transient stage during a wetting process from the top of the column. In order to validate the method, the measurements of S_r based on SWIR images are compared with measures taken by means of conventional moisture sensors installed in the sample at different elevations.

6.6.1 Experimental setup

The experiment was performed on a column of sand placed on a Perspex transparent tank except for the frontal side that was made of glass to avoid scratches that could affect the quality of the images. The tank was 400 mm high, 1000 mm long (limited to 200mm by adding a glass wall) and 200 mm deep. The sand sample tested was a column with a square cross-sectional area, 200x200mm, and a height of 300 mm. (0). The tank base was filled with a 2 cm thick layer of gravel which was covered with a geotextile to avoid sand penetration into the gravel layer. The top was covered by a plastic film to minimize evaporation without affecting the atmospheric pressure. The sand was placed in the tank by dry pluviation and the density was controlled by weighting sequentially the amount of soil. The average density of the sample is 1500 kg/m³. Three capacitive soil moisture sensor (SEN0193) were installed at different heights: 60, 140 and 220 mm.

Two wetting situations (stages) were analyzed:

First stage: The bottom of the sample is saturated imposing a stable water level at the top of the gravel layer located in the bottom of the sample. The water rose up through the sand by capillarity until it reached the stationary condition. At this time, the lateral surface of the column was recorded by means of the SWIR camera and the degree of saturation was estimated by analyzing the image.

Second stage. The soil column is wetted from the top with a water flow applied, simulating rainfall, using a drip system with nozzles separated 10 mm. The vertical water infiltration process in time was recorded using the SWIR camera. The time evolution of the distribution of the degree of saturation on the sample face will be analyzed.



Figure 87 Experiment setup for validation

6.6.2 Results

First stage

Once the condition of saturation was fixed on the bottom of the sandy column, the water rose up progressively through the sand. Equilibrated and stable conditions were reached two weeks after the base saturation.

Figure 88 shows the distribution of the degree of saturation and water content at the stationary condition measured by means of the SWIR image, following the procedure presented before and the calibration curves of Figure 84.

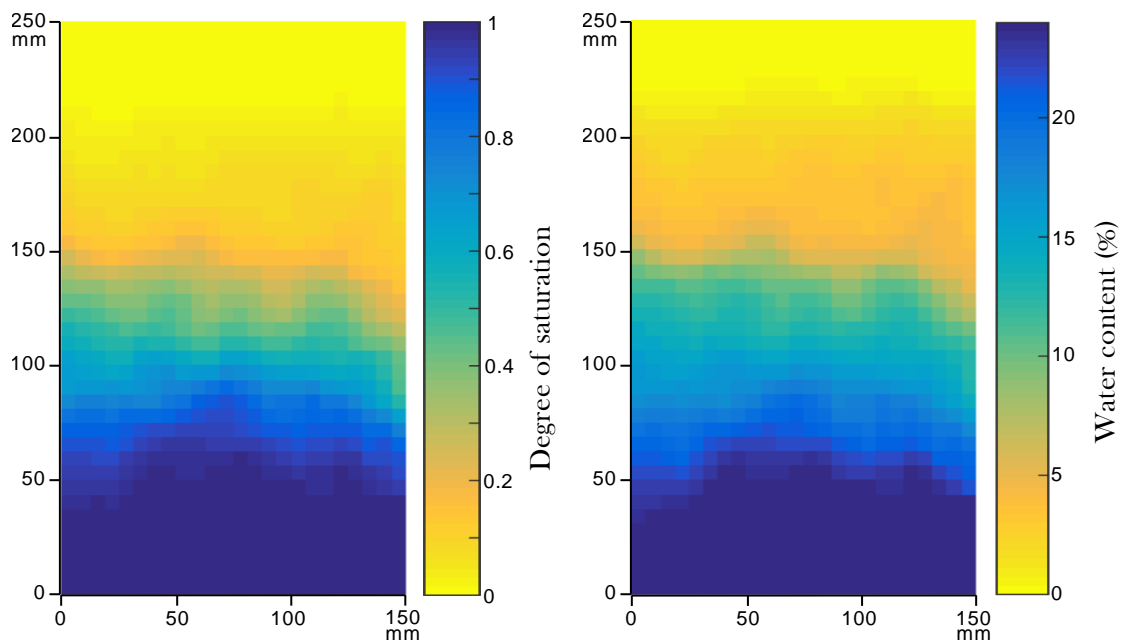


Figure 88 Values of (a) degree of saturation and (b) water content of the column measured by the SWIR image.

Several vertical profiles of the SWIR-measured degree of saturation are plotted in Figure 89. They are compared with the theoretical vertical profile computed by accepting a linear increase of the suction with height, applying the previously determined retention curve (approximated by the Van Genuchten expression, Figure 80). In addition, the values of the degree of saturation measured by moisture sensors are also indicated. The average dry density (1500 kg/m^3) was used to compute the water content from the degree of saturation measurements.

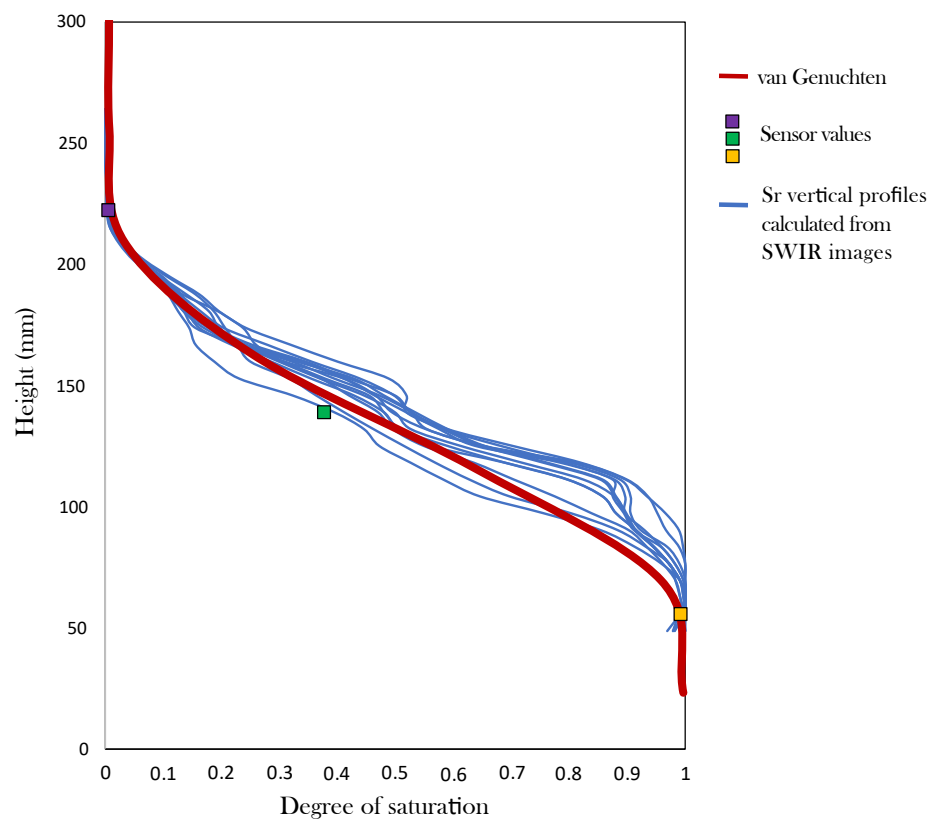


Figure 89 Comparison of vertical profiles of degree of saturation determined by SWIR images and values computed from equilibrium suction profile and the experimental water retention curve.

Second stage

The rainfall applied to the second stage of the experiment had an intensity of 0.6425 mm/s (equivalent to a flow rate of 0.0257 l/s on a 200x200 mm area). The infiltration process was recorded with a SWIR camera at 15 frames per second. However, only one image per second was selected to determine the degree of saturation. The time evolution of the SWIR-estimated degree of saturation is plotted in Figure 90.

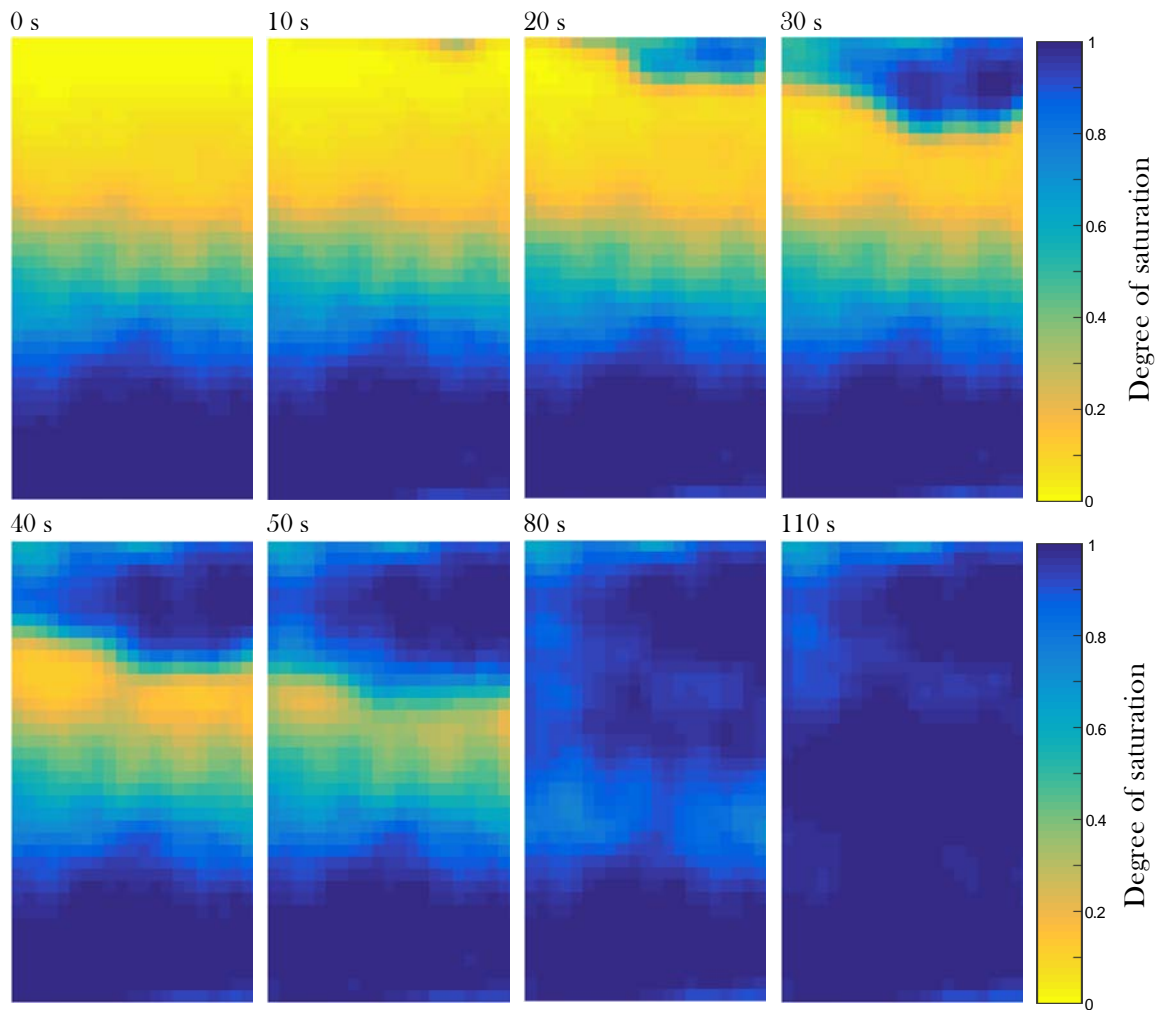


Figure 90 SWIR-measured degree of saturation at increasing time during the soil column wetting.

The measured values by means SWIR images and the values measured by moisture sensors are compared in Figure 91. The evolution of the Sr at three heights, by means of SWIR images, match well with the direct measurements by moisture sensors. The evolution of the descending waterfront is also well captured by the image analysis.

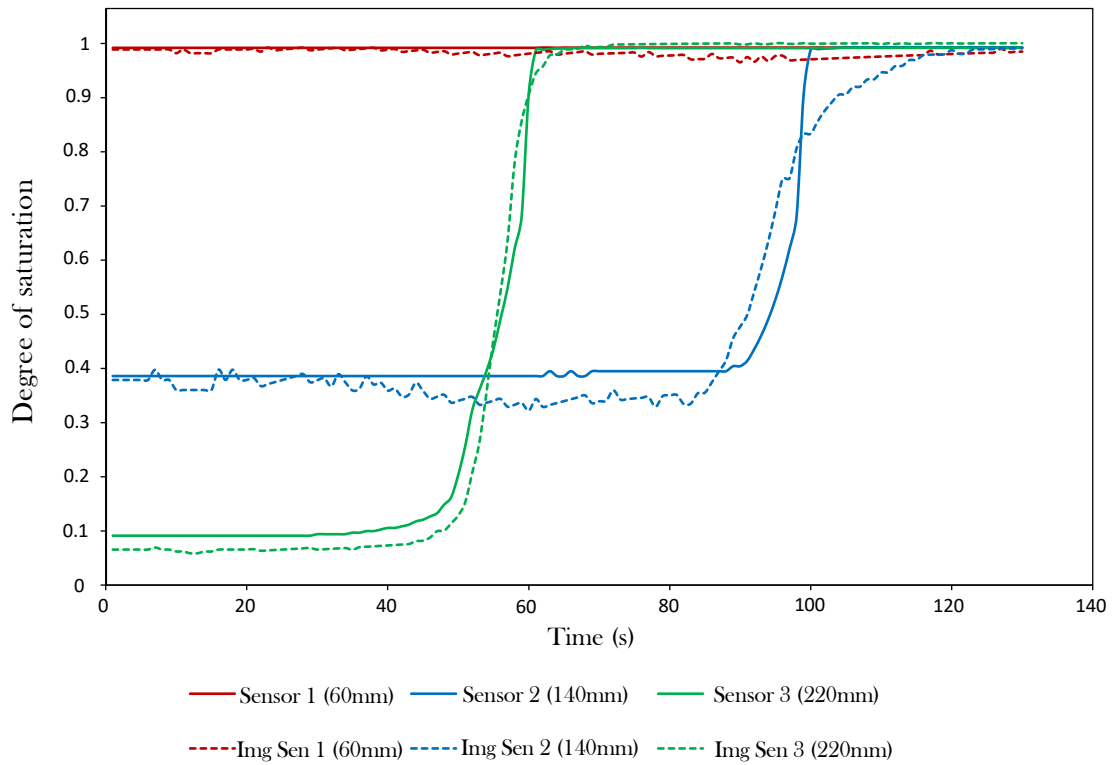


Figure 91 Comparison between the degree of saturation measured by SWIR images (dashed line) and by moisture sensors at three column heights (60 mm, 14 mm and 220 mm).

6.7 Numerical model

The experiment has been modeled using the finite element program Code_Bright (Olivella *et al.*, 1996). The model has used only hydraulic solving equations. The water retention curve used in the numerical simulation was the van Genuchten model (Equation 17 and Equation 18). The hydraulic properties of the sand introduced as the model parameters are described in Table 9.

Equation 17

$$S_e = \frac{S_l - S_{rl}}{S_{ls} - S_{rl}} = \left(1 + \left(\frac{P_g - P_l}{P} \right)^{\frac{1}{1-\lambda}} \right)^{-\lambda}$$

Equation 18

$$P = P_0 \frac{\sigma}{\sigma_0}$$

Table 9 Hydraulic properties of the Castelldefels' sand.

| Sign | Parameter | Value | Unit |
|-----------------|------------------------|--------|----------------|
| P ₀ | pore pressure | 0.0012 | MPa |
| σ ₀ | surface tension | 0.072 | N/m |
| λ | shape function | 0.8 | |
| S _{rl} | residual saturation | 0 | |
| S _{ls} | maximum saturation | 1 | |
| K ₀ | intrinsic permeability | 4e-11 | m ² |

The numerical water retention curve as a result of the parameters introduced in the van Genuchten equations is compared to the experimental curve measured on the laboratory (Figure 92).

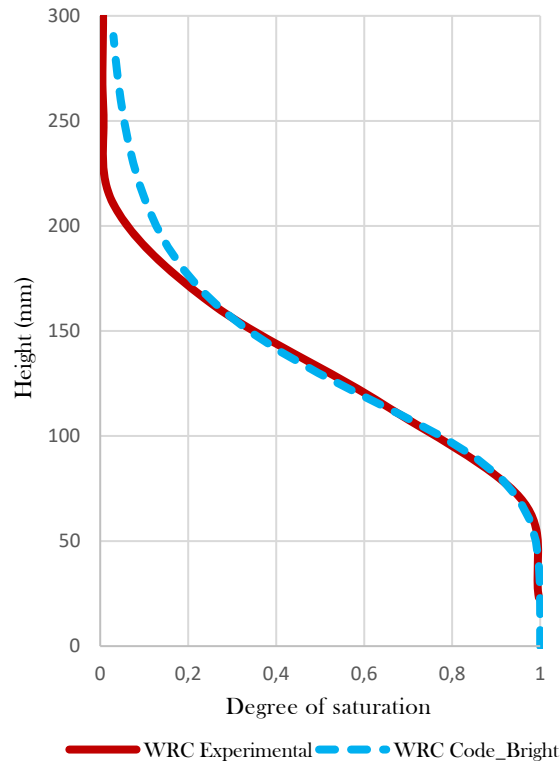


Figure 92 Comparison between the experimental and the numerical water retention curve.

The liquid phase relative permeability follows Equation 19, it is exposed to Figure 93 for better visualization. The permeability rises as it gets closer to the saturated level to take into account the reduction of pore volume due the collapse caused by the saturation.

Equation 19

$$k_{rl} = S_e^5$$

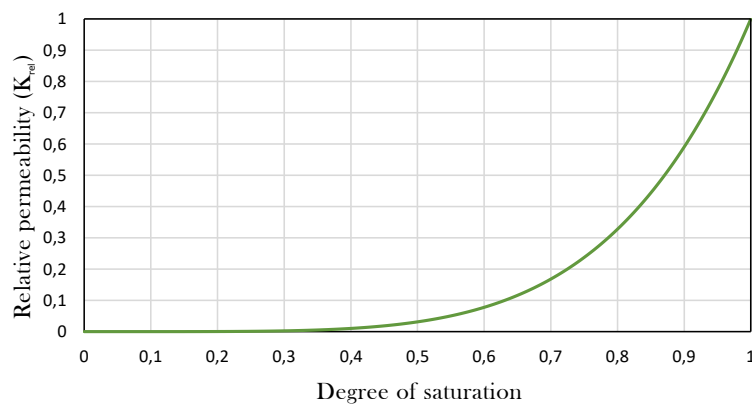


Figure 93 Degree of saturation effect on the liquid phase relative permeability

The time evolution of the SWIR-measured degree of saturation is compared to the results from the Code_Bright numerical simulation. Figure 95 shows the spatial distribution of the degree of saturation in certain moments comparing the measurements on SWIR images and the results from the numerical simulation. The descent of the waterfront follows the same general evolution. Nevertheless, the measurements on the images show the heterogeneities on the distribution of the degree of saturation. On the real experimental test on soils exist a certain level of imperfection that the numerical simulation does not represent. The opportunity to measure and map the spatial distribution of the degree of saturation enables to better understand the real behavior of the soil during the whole experiment, even when it does not match with the expectations.

The measured values by means SWIR images are compared to the values measured by moisture sensors and to the values calculated on the numerical simulation (Figure 94). The evolution of the S_r at three heights, by means of SWIR images, match the direct measurements by moisture sensors.

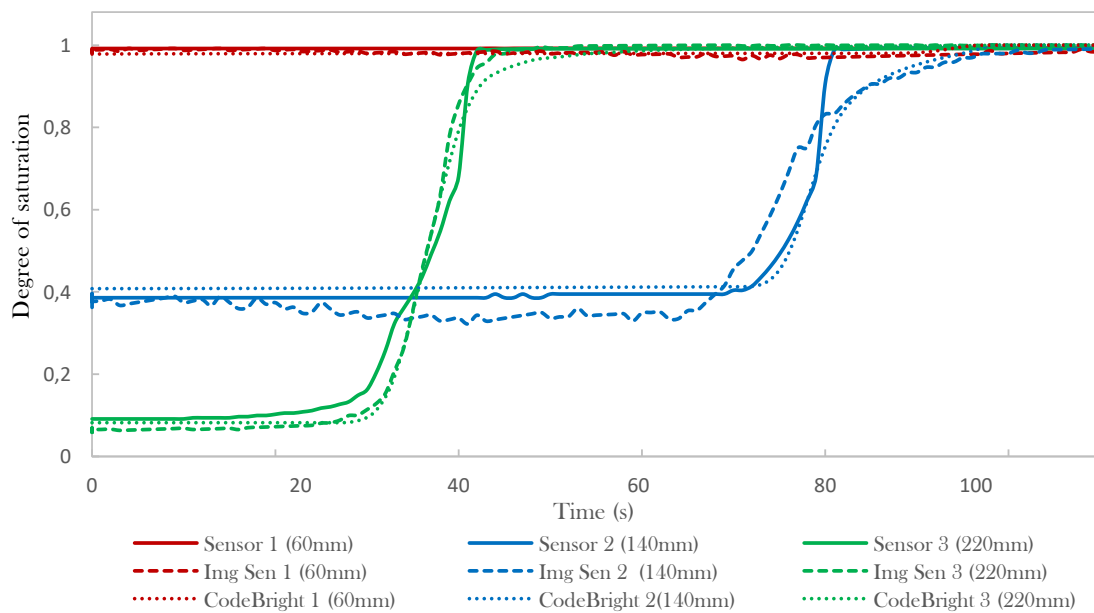


Figure 94 Comparison between the degree of saturation measured by SWIR images (dashed line), by moisture sensors (solid line), and calculated through numerical simulation (dotted line) at three column heights (60 mm, 14 mm and 220 mm).

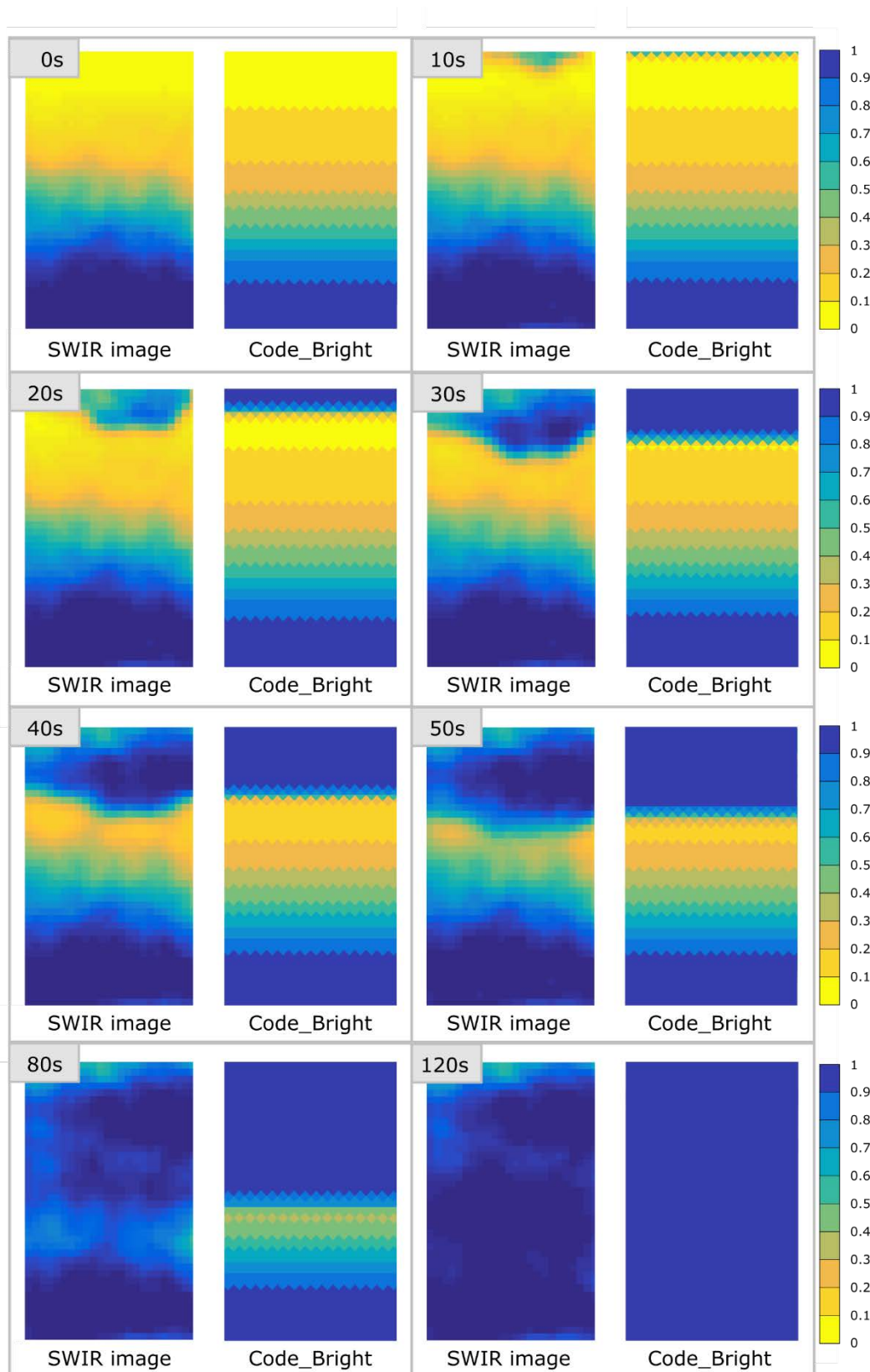


Figure 95 SWIR-measured degree of saturation compared to Code_Bright numerical simulation at increasing time during the soil column wetting.

6.8 Discussion

6.8.1 Effect of void ratio

An additional set of calibration experiments was performed to evaluate the effect of the variation of void ratio on the SWIR reflectance. It was important to know if reflectance was controlled by the soil degree of saturation or by water content. Three samples of sand were prepared assigning a certain value of water content to each one. The sand was placed in a metallic cylinder and the top base was covered by a glass. The bottom base of the cylinder had a piston to change the volume of the sample. In this way, the void ratio could be controlled. Reducing the void ratio, the degree of saturation increases maintaining constant the water content (Table 10).

Table 10 Degree of saturation of tested samples. For each water content, three different degrees of saturation are obtained by reducing the void ratio.

| | | Void ratio | | |
|---------------|------|------------|------|------|
| | | 0.70 | 0.82 | 1.08 |
| Water content | 7.1 | 0.28 | 0.24 | 0.18 |
| | 14.3 | 0.56 | 0.48 | 0.36 |
| | 22.9 | 0.90 | 0.77 | 0.58 |

For each of the cases presented in Table 10, a picture of the sample was taken with the SWIR camera. Table 11 shows the average pixel intensity (GV) measured on each sample surface. If the GV was constant regardless of changes in void ratio, the images were measuring water content. Otherwise, if the GV decreases as the void ratio increases, the images are actually measuring the degree of saturation.

Table 11 Average pixel intensity (GV) of each sample condition presented in Table 10.

| | | Void ratio | | |
|---------------|-------|------------|------|------|
| | | 0.70 | 0.82 | 1.08 |
| Water content | 7.14 | 171 | 174 | 177 |
| | 14.29 | 130 | 133 | 159 |
| | 22.86 | 106 | 109 | 139 |

The results plotted in Figure 96 show the correlation between the degree of saturation and Pixel intensity (GV). Note that the variation on degree of saturation of the curves is not determined by the water content alone. The void ratio is required. In fact, the plot shows that pixel intensity (GV) is essentially determined by degree of saturation. This is further illustrated in Figure 97, where water content is related to GV. For a given water content, GV may adopt a wide range of values, as the degree of saturation changes. It is concluded that the index of reflectance is determined by degree of saturation. Figure 96 (dotted line) shows the correlation between degree of saturation and GV values measured in the three samples tested. The correlation starts and ends in two fixed points: fully saturated and dry soil. The tests show that a unique (Sr, GV) relationship can be accepted.

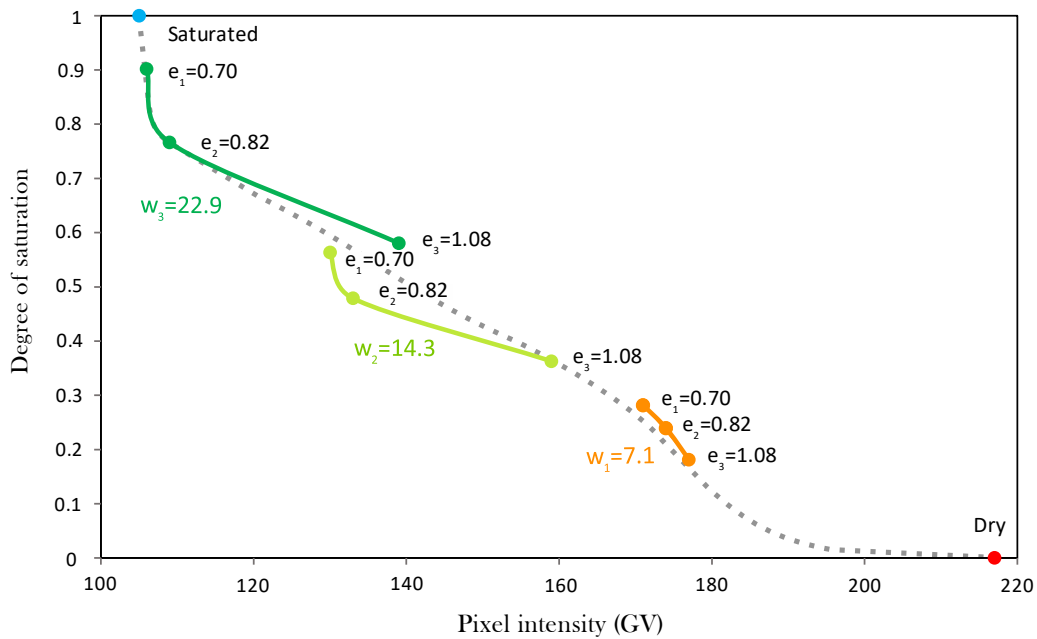


Figure 96 Effect of the void ratio on the reflectance of the soil for the different water contents (7.14, 14.29, 22.86). The pixel intensity for dry and saturated conditions is also plotted as a reference. The average trend is plotted as a dotted line.

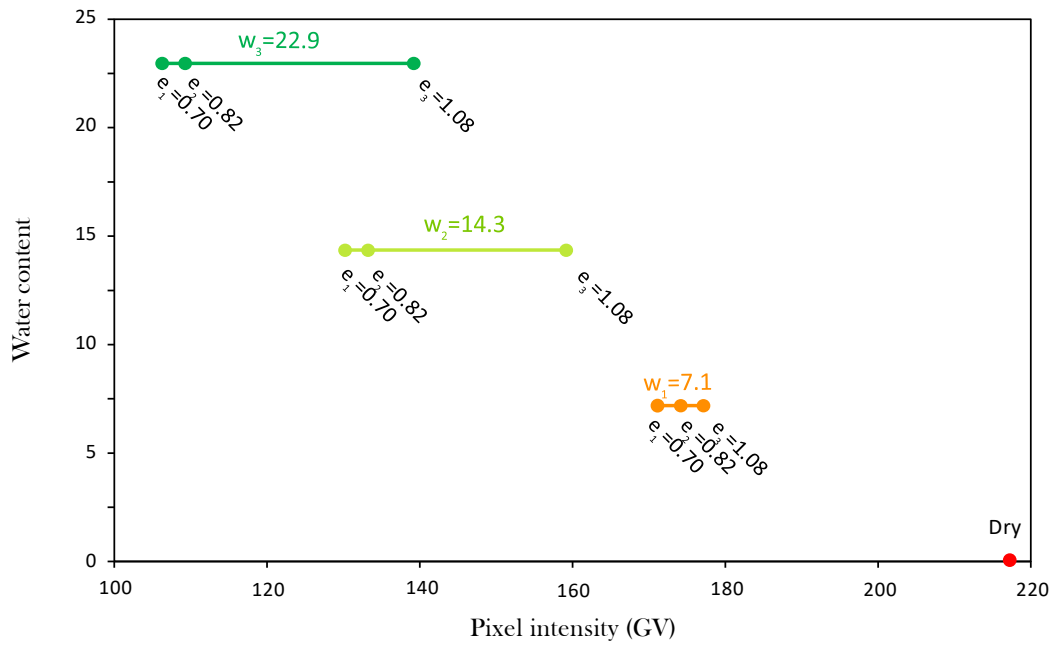


Figure 97 Variation of pixel intensity (GV) of samples having the same water content but different void ratio.

Figure 98 summarizes the normalized pixel intensity (GV) – degree of saturation curves for all the samples tested. The degree of saturation of the samples indicated was imposed by different procedures. The constant dry density (1390 kg/m^3) curve plotted (orange) was determined for the calibration procedure (Figure 85). The variation on the degree of saturation was imposed by increasing the water content. The second curve (blue), at a higher dry density (1470 kg/m^3), was determined following the same procedure. The three additional curves (yellow, lime, green) shown in the plot were just discussed in the previous section (Figure 96): the variation of degree of saturation was imposed by increasing the density (in the range $1290 - 1560 \text{ kg/m}^3$) at constant water content. There is some scatter in the plot, but it is clear that the degree of saturation is the dominant parameter explaining the soil reflectance for the tested densities.

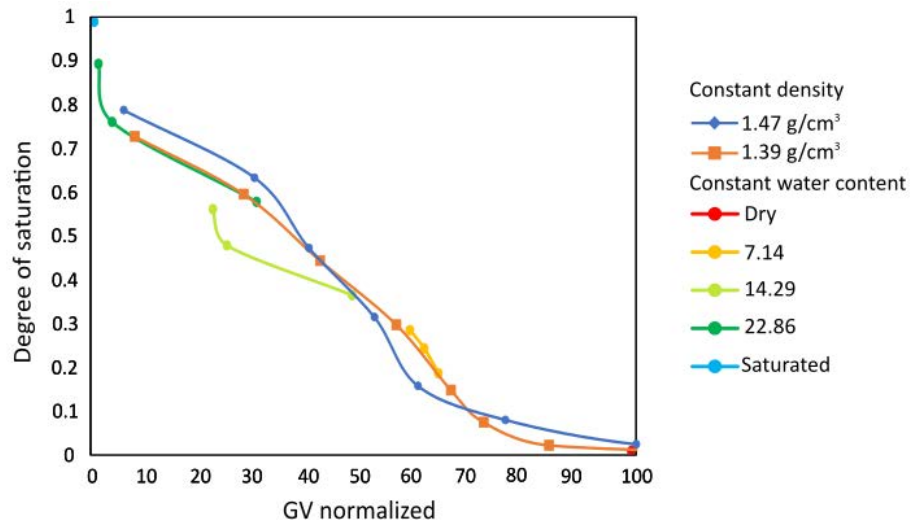


Figure 98 GV normalized - Sr plot of soil samples at constant water content (7.14, 14.29, 22.86) and varying void ratio. GV normalized - Sr plot of samples at constant density (1.47, 1.39 g/cm³) and varying water content.

6.8.2 Limitations of the method

Non-uniform incident light:

The method is based on the light reflected by the soil, but the reflection is dependent on the intensity of the incident light. In order to keep the incident light intensity stable through time, the arrangement of the light emitters can be fixed if the experiments are performed in the same location. In spite of having a stable light intensity through time, the intensity cannot be spatially homogeneous because the light comes from point sources (Figure 99). The intensity of light that reaches the experiment surface depends on the distance to the emitter. These factors force to normalize the calibration and the pixel intensity values from the images.

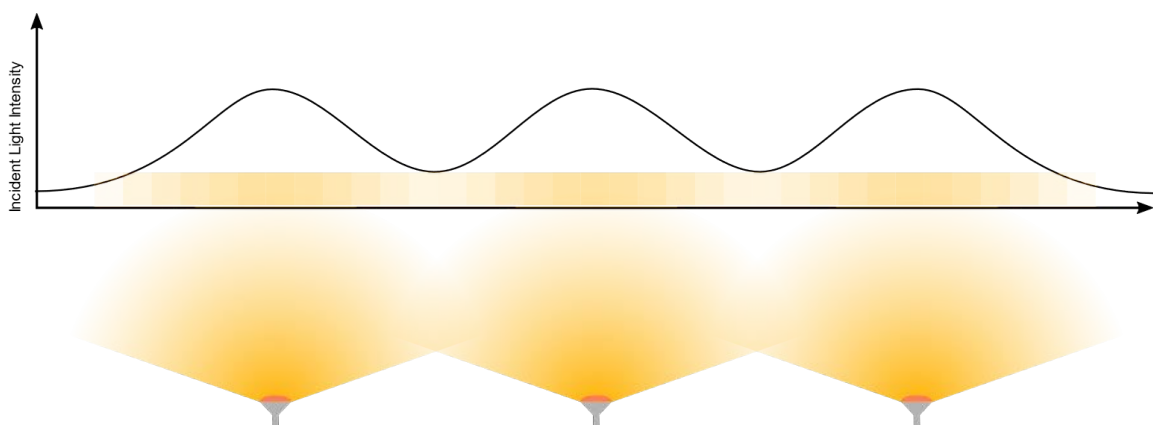


Figure 99 Example of the spatial non-uniformity of the light from 3 emitters when reaches a surface.

Image edges:

The images from the camera should be filtered, as discussed above (using a Gaussian filter) to attenuate the effect of the different grain mineralogy and the sensor noise. This filter makes the pixel intensity from the background interfere in the filtered values close to the edges. This effect should be taken into account when interpreting the results near the edge. The degree of saturation values close to the boundaries may appear higher than really are.

Surface measurements:

The penetration of the SWIR electromagnetic waves into the unsaturated soil is low, therefore the technique is only capable of assessing the degree of saturation of the surface of the soil samples tested.

6.9 Conclusions

This Chapter presents a method to measure the degree of saturation of unsaturated soil in laboratory experiments by means of the optical sensing of soil reflectance using short wave infrared (SWIR) images. The method accuracy relies on the differential spectral absorbance of water partially filling the soil pores. Among the analyzed range of light wavelengths, the SWIR spectrum is the most absorbent.

An affordable SWIR camera alternative to the most expensive InGaAs sensor cameras is proposed. The performance of the camera is judged to be sufficient for the purposes of determining the soil's degree of saturation. The testing arrangement of the camera and the light sources must be stable for a proper analysis.

SWIR images interpreted by a filtered and normalized gray value (GV) was shown to depend on the degree of saturation (and not on water content). An initial experimental calibration, for a given soil, is required to relate GV and degree of saturation. A benchmark experiment conducted on an unsaturated soil column in equilibrium with a saturated lower boundary (suction increases linearly with elevation above the base) allowed to compare the derived water retention curve with a direct determination by standard procedures. The agreement was very satisfactory (Figure 89).

In a second benchmark experiment, during a surface wetting (simulating rainfall) of the previous column, SWIR results, were compared with the readings of moisture sensors located in the column. Again, the correspondence was very good (Figure 91). These benchmarks indicate that the method may be as accurate as other known procedures based on "point" sensors. However, the main value of the method is its capability to capture two-dimensional fields of the evolving degree of saturation. This is a major advantage to design experiments to validate numerical models in boundary value problems.

7

Chapter 7

Measurement of the degree of saturation by SWIR images on soils in motion

This Chapter combines the two main techniques presented in this Thesis in an integrated methodology. The PIV-NP (Chapter 5) and measurements of the degree of saturation from SWIR images (Chapter 6). This Chapter contains the description of modifications on the PIV-NP algorithm to read, map, and store new information extracted from images. After a case of a rain-triggered collapse of an unsaturated soil column is analyzed, as an example of the combination of techniques into an integrated methodology.

7.1 Introduction

The methodology is structured based on the PIV-NP mapping procedure (Section 5.1). The procedure is equivalent to the mapping of displacement information from a Eulerian image correlation code (Section 2.3.1). The variable of interest, in this case, degree of saturation, is measured in the fixed node coordinates. Subsequently, the information from the nodes is transferred to the Numerical Particles using the same shape functions. Thus, the Numerical Particles store the evolution of the degree of saturation not in fixed coordinates but in each part of the soil in movement that represents. The fact that the numerical particles store the information of the evolution of multiple variables enables to compare and correlate the values of these variables in each instant of time. This might empower a more in-depth analysis of the experiments, finding possible causal relationships between the variables.

7.2 Algorithm

This Section presents the steps to combine the saturation degree data into the PIV-NP code. The PIV-NP base code has been described in Chapter 5. The base code does not require significant modifications. The evaluation of the degree of saturation on the coordinates of the nodes simplifies the transfer into the particles, through the same mapping technique used on the nodal displacement.

Some of the steps already explained in the Section 5.1 (PIV-NP description) are mentioned again to give coherence to the general explanation of the process. Others are encompassed in closed functions to simplify the description; in these cases, reference is made to the Section in which they are described in detail.

7.2.1 Steps

1. Read the coordinates of the nodes of the grid.

1.1 Transform the nodal coordinates from the visible image to the SWIR image.

2.1 Determine the position of the particles.

The initial particle position depends on the input data of the first time step. This procedure is explained in the preliminary steps of Section 5.1.3.

2.2. Identify the reference nodes of the particles.

3. Map the displacements from the nodes to the particles.

4. Calculate the derivative parameters.

The calculation of the accumulated displacement, velocity, acceleration, and strains is detailed in step 4 of Section 5.1.3.

5. Transform the coordinates of the nodes into the reference system of the SWIR image.

6. Measure the degree of saturation in the coordinates of the grid nodes.

The algorithm to measure the degree of saturation by means of SWIR images is described in the whole Section 6.5.

7. Map the degree of saturation of the from the nodes to the numerical particles.

The shape functions to map the degree of saturation are the same shape function used to map the instant displacement.

8. Update the particle position.

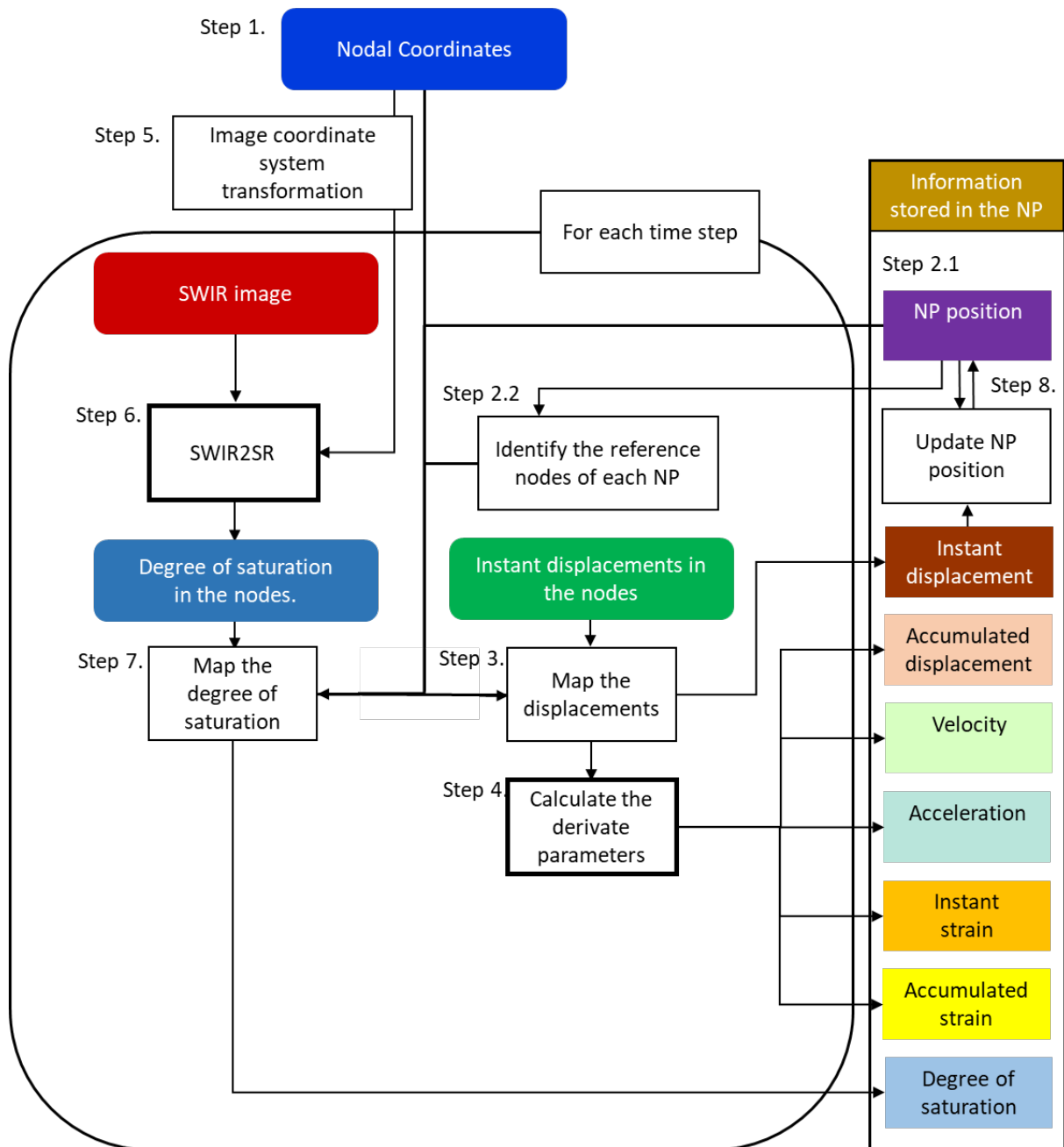


Figure 100 Flowchart of the combination of the PIV-NP with the degree of saturation measurements.

7.3 Validation and evaluation

A simple experiment is analyzed as a support for the presentation of the combination between the two techniques developed: PIV-NP and degree of saturation from SWIR images.

The experiment is a collapse of a soil column due to the change in the degree of saturation. It was performed in the tank described in Section 3.1; using the drip system to simulate rain on the top. The full experiment has been recorded with two different cameras.

7.3.1 Camera

Two different cameras have been used to measure the displacement and degree of saturation.

- The SWIR camera (CamIR - Scintacor), described in Section 6.4.1 has been used to measure the degree of saturation. Using the detailed calibration in Section 6.5.
- The camera in visible (Canon Eos50) has been used for the measurement of displacements.

Both cameras used its particular lighting source because the light recorded per each camera is on two distant spectral bands (visible and short wave infrared). The cameras and the lighting system were mounted on the structure described in Section 4.1. In this case, the use of two cameras is inevitable, despite the drawbacks that it causes.

The camera that records in the visible spectrum cannot be used to measure the degree of saturation since the absorption of light by water is not gradual. The reasons for using the SWIR spectrum are widely discussed in Section 6.2. On the other hand, the SWIR camera cannot be used for the measurement of displacements because the resolution and noise in the image do not allow the creation of patches (patch) that can be correlated from one image to the next.

Image coordinate system transformation.

The use of two cameras requires converting the coordinates of the nodes written on for the visible image into the coordinate system of the SWIR images. The transformation is done taking as reference the two of the blue dots adhered to the tank (4.1).

After a process of evaluation of different methods to find the parameters for the coordinate system transformation, it has been concluded that the most effective and reliable method is the use of two simple systems of equations (Equations 20).

Equations 20

$$\begin{cases} mulx \cdot x_1^{swir} + sumx = x_1^{vis} \\ mulx \cdot x_2^{swir} + sumx = x_2^{vis} \end{cases}$$

$$\begin{cases} muly \cdot y_1^{swir} + sumy = y_1^{vis} \\ muly \cdot y_2^{swir} + sumy = y_2^{vis} \end{cases}$$

7.3.2 Material

The experiment was performed on a column of sand placed on the methacrylate tank (Section 4.1). The tank length was limited to 240mm by adding a vertical glass wall. The sand sample tested was a column with a square cross-Sectional area, 240x200mm, and a height of 270 mm. (Figure 101). The top of the column was covered by a plastic grid to distribute the load but permitting the rain infiltration. The sand was placed in the tank by pluviation in unsaturated conditions, and the density was controlled by sequentially weighting the amount of soil placed. The average density of the sample is 1,5 g/cm³. Two capacitive soil moisture sensor (SEN0193) were installed at different heights: 60 and 140 mm.

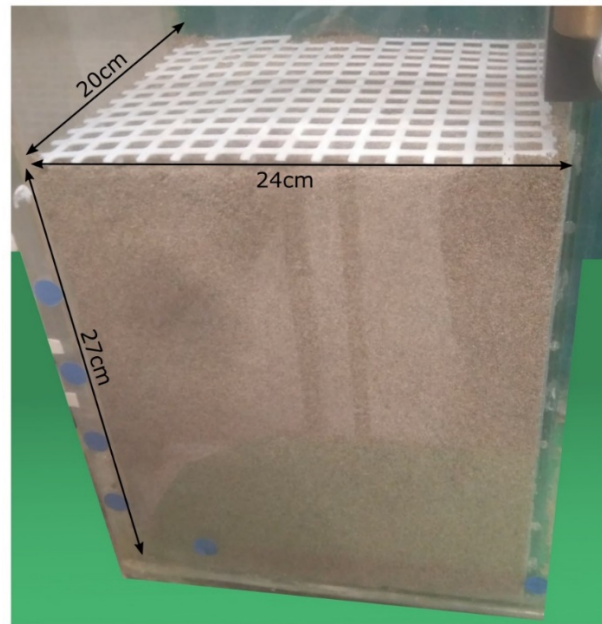


Figure 101 Experimental setup of the column before the load placement.

The soil used in the test is calcareous-siliceous fine sand from Castelldefels' beach (Catalonia, Spain). The same soil used in the previous Sections 5.3 and 6.3.2. The properties are summarized in Table 12.

Table 12 Geotechnical properties of Castelldefels' sand and initial conditions.

| Parameter | | Value | Units |
|--------------------------------------|-------------------------------------|--------|-------------------|
| Grains geomechanics parameters | Particle density | 2.665 | g/cm ³ |
| | Particle Elastic modulus | 73.0 | GPa |
| Soil geomechanics parameters | Dry density (initial) | 1.212 | g/cm ³ |
| | Porosity (initial) | 0.545 | |
| | Pores index (initial) | 1.199 | |
| | Angle of internal friction (dry) | 31.0 | |
| | Cohesion (dry) | 0.00 | |
| | Poisson modulus | 0.30 | |
| Particle size distribution | Soil elastic modulus | 10.0 | |
| | D10 | 0.254 | mm |
| | D30 | 0.3109 | mm |
| | D60 | 0.3715 | mm |

| | | | |
|--------------------------|--|-------------------|-----|
| Hydraulic parameters | Air-entry value | 0.70 | kPa |
| | Saturated permeability | $2 \cdot 10^{-4}$ | m/s |
| van Genuchten parameters | $S_r = S_{r_r} + \frac{(S_{r_s} - S_{r_r})}{[1 + (ah)^n]^m}$ | | |
| | α | 0.07 | |
| | n | 2.20 | |
| | m | 0.545 | |
| | S_{r_s} | 0.73 | |
| | S_{r_r} | 0.00 | |

The soil-water retention curve (SWRC), under imbibition conditions, was measured by the gravimetric method in a segmented hanging column. The measured points (S_r , suction) are indicated in Figure 102, together with the estimated van Genuchten model (van Genuchten, 1980). Values of the model parameters are indicated in Table 12.

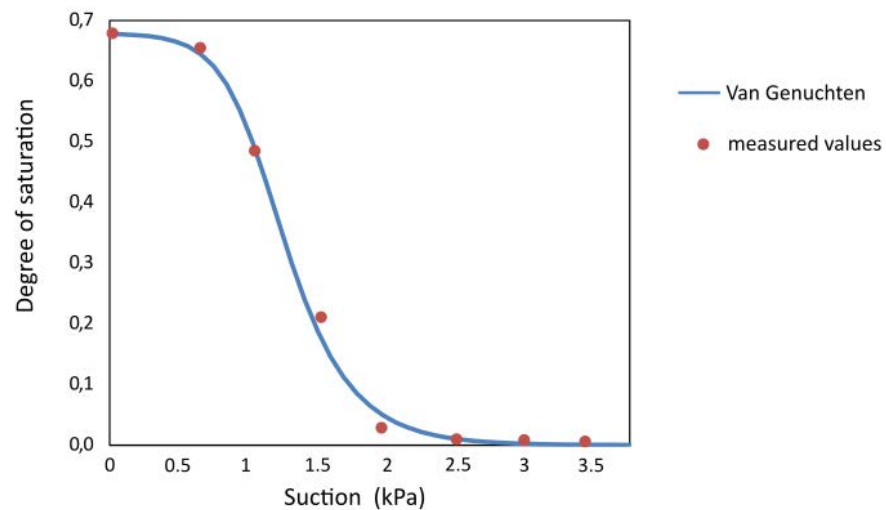


Figure 102. Measured values and calibrated water retention curve of Castelldefels' beach sand.

7.3.3 Results

The results from the integrated methodology are displayed in this section. The aim of the exposure the results is not the analysis of this particular case of collapse, but to present the multiple visualization options that the methodology offers: 2D (mapped), 1D (line of particles) or 0D (particle by particle). Each one of the visualization types is useful for different purposes. Bellow, examples of each type of visualization are displayed with the explanation of what type of information is providing.

The bidimensional visualization of the degree of saturation, accumulated displacement, and volumetric strain are exposed in Figure 104 and Figure 105. The legend of the data plotted in the figures is shown in Figure 103.

The bidimensional display of the degree of saturation shows that the saturation front is not entirely horizontal. This is due to the inherent heterogeneity of real cases, which is challenging to consider in numerical models. The degree of saturation tends to increase more rapidly in the right area of the soil column, as does accumulate displacement and volumetric strain. The saturation front has a thickness of 5-7 particles between the initial degree of saturation and fully saturated, which corresponds to a distance of around 5 cm.

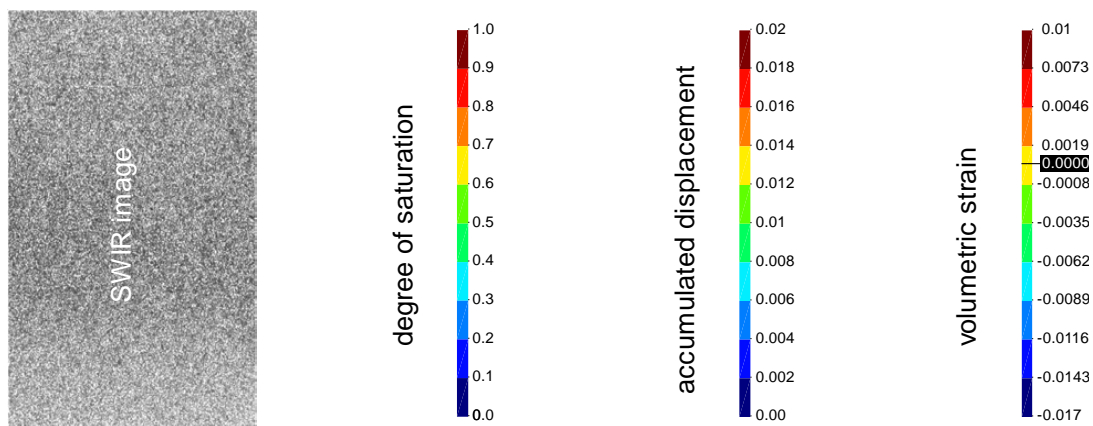


Figure 103 Legend of the data displayed in Figure 104, and Figure 105: Degree of saturation, accumulated displacement, and volumetric strain.

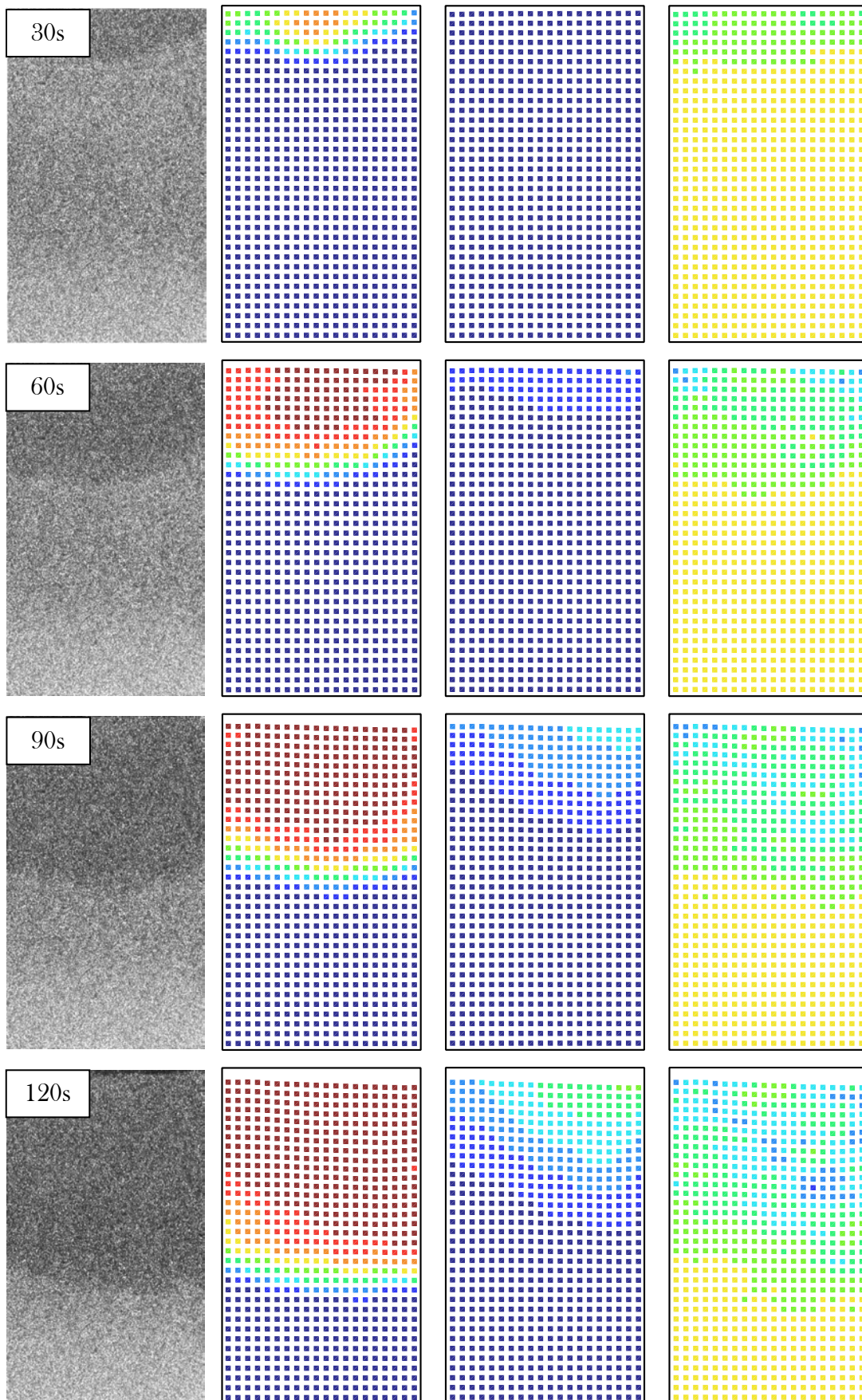


Figure 104 2D visualization of the column collapse experiment: Degree of saturation, accumulated displacement, and volumetric strain. Time steps: 30, 60, 90 and 120 seconds.

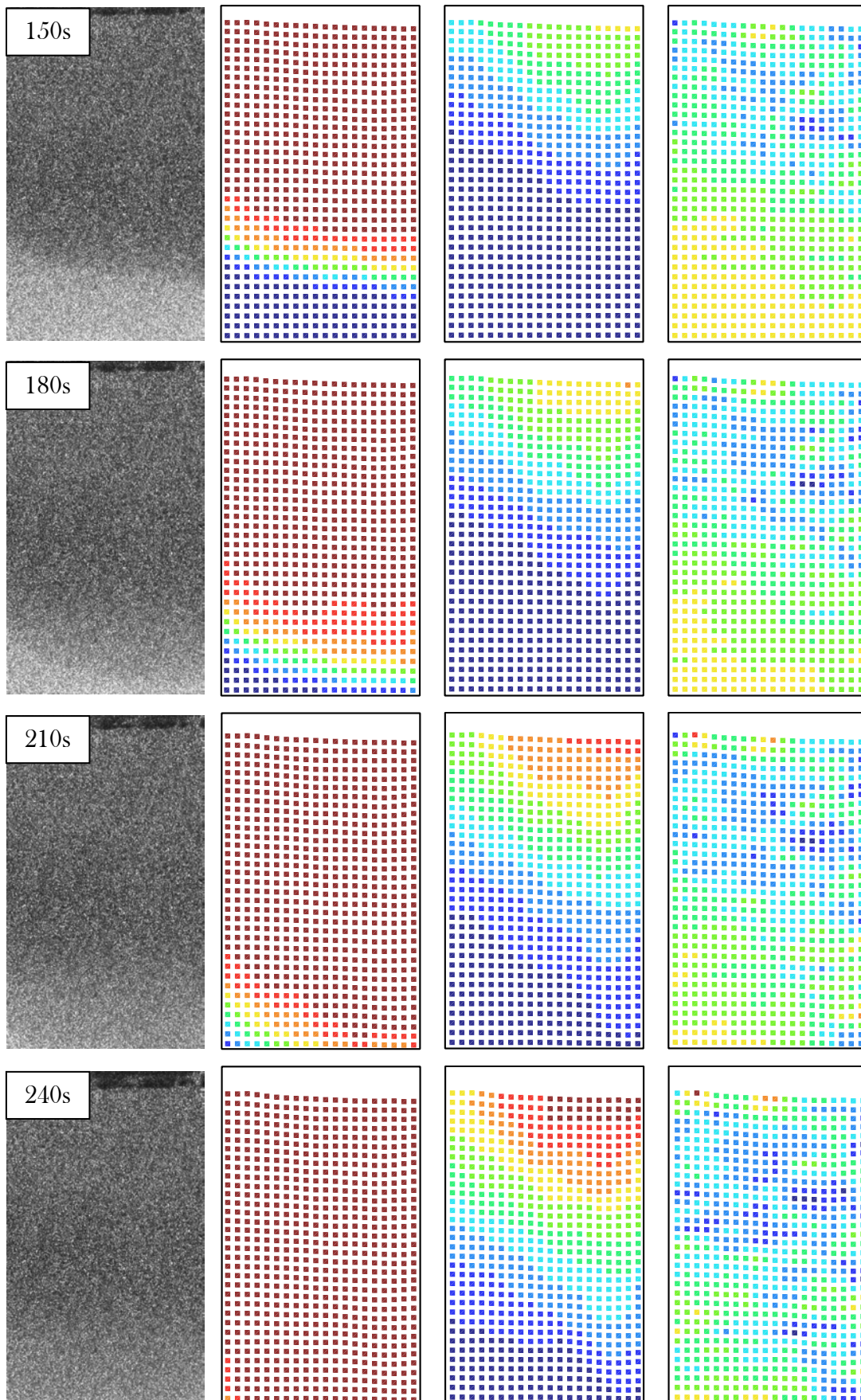


Figure 105 2D visualization of the column collapse experiment: Degree of saturation, accumulated displacement, and volumetric strain. Time steps: 150, 180, 210 and 240 seconds.

The correlation between these three values (degree of saturation, accumulated displacement and volumetric strain) is analyzed in more detail (Figure 107) in the column of particles highlighted in Figure 106. A line is plotted every 10 seconds to visualize the state of the variables depending on the height. The legend is plotted on the bottom of the figure.

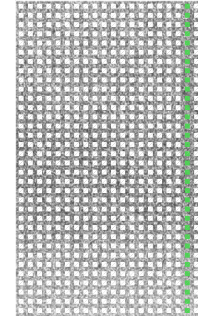


Figure 106 Column of particles analyzed .

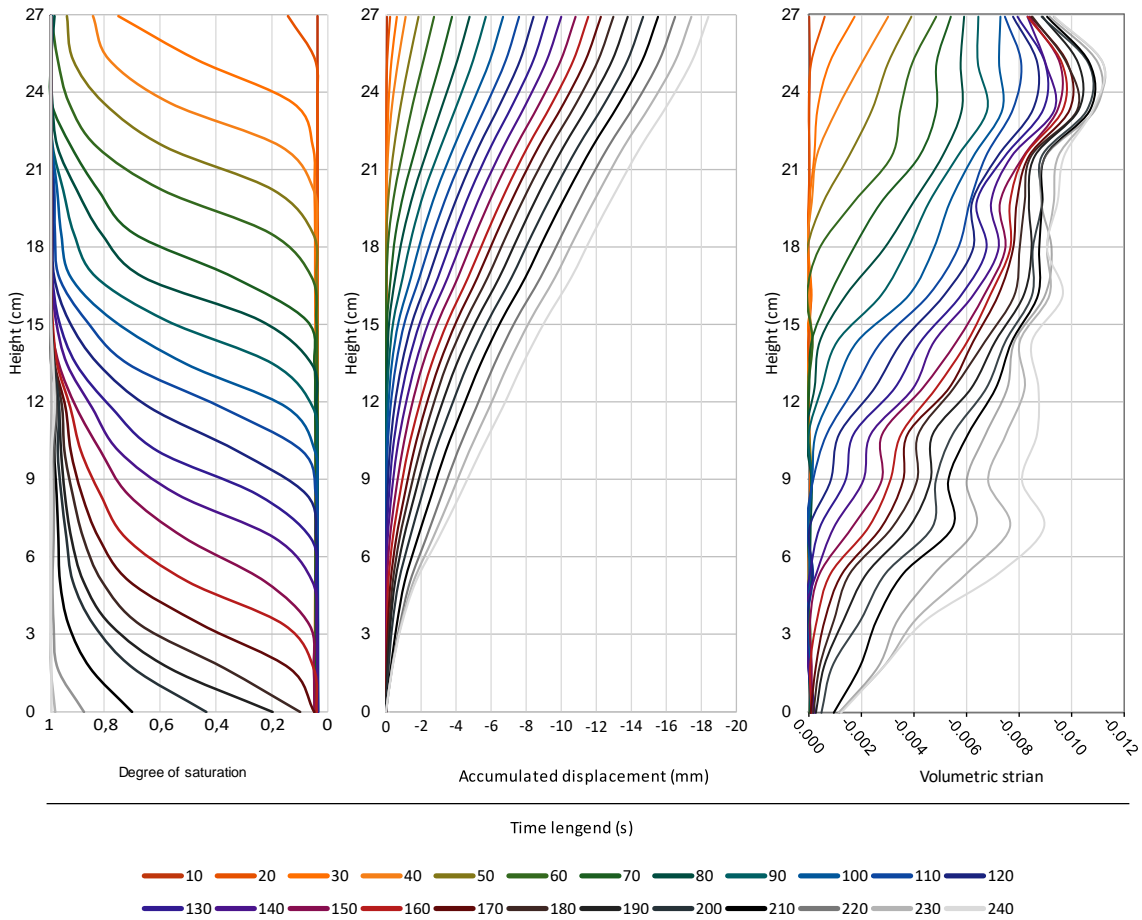


Figure 107 1D visualization of the column collapse experiment: Degree of saturation, accumulated displacement, and volumetric strain. Time steps from 0 to 240 seconds.

Figure 107 compares the evolution of the accumulated displacement and volumetric strain of each height with its degree of saturation value. The increase in the degree of saturation is equivalent to a reduction on the suction, following the line plotted in Figure 102. The reduction on the suction increases the effective stresses, which produces the collapse of the column.

The collapse occurs gradually, once the saturation degree mapped in a numerical particle starts increasing is when the particle registers a movement downwards, expressed as a negative displacement. The total displacement of each time recorded by the particles on the top of the column does not represent the displacement produced by the collapse of this area, but the accumulation of the displacements produced by the collapse of the bellow areas. That plot is useful to observe the general collapse behavior, but it complicates the analysis of the correlation between changes in the degree of saturation and collapse. The comparison with the volumetric strain in the same Figure 107 and the particle by particle analysis in Figure 109 are more useful to analyze this concert correlation.

The negative volumetric strain, as well as the negative displacement, express the collapse of the different heights of the column when the saturation front reaches that area. The reduction of the pore volume is initiated at the moment that the saturation degree starts increasing. From that point, the volume gradually decreases until it reaches a volumetric strain around -0.0008. That volumetric strain value might indicate the maximum reduction of pore volume produced uniquely by the changes on the suction on this case. However, a volumetric strain is registered, especially on the top particles, when the degree of saturation is already 1. That could be caused by the water flow or by changes in the water pore pressures.

Figure 109 displays the relation between the degree of saturation and velocity of displacement of four numerical particles highlighted in Figure 108. The particles analyzed represent the behavior at four different heights: 27 cm (red particle), 24 cm (blue particle), 16 cm (purple particle), and 10 cm (yellow particle).

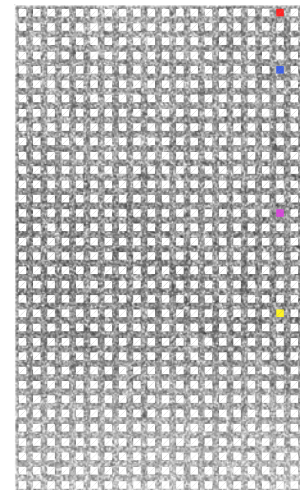


Figure 108 Particles analyzed individually

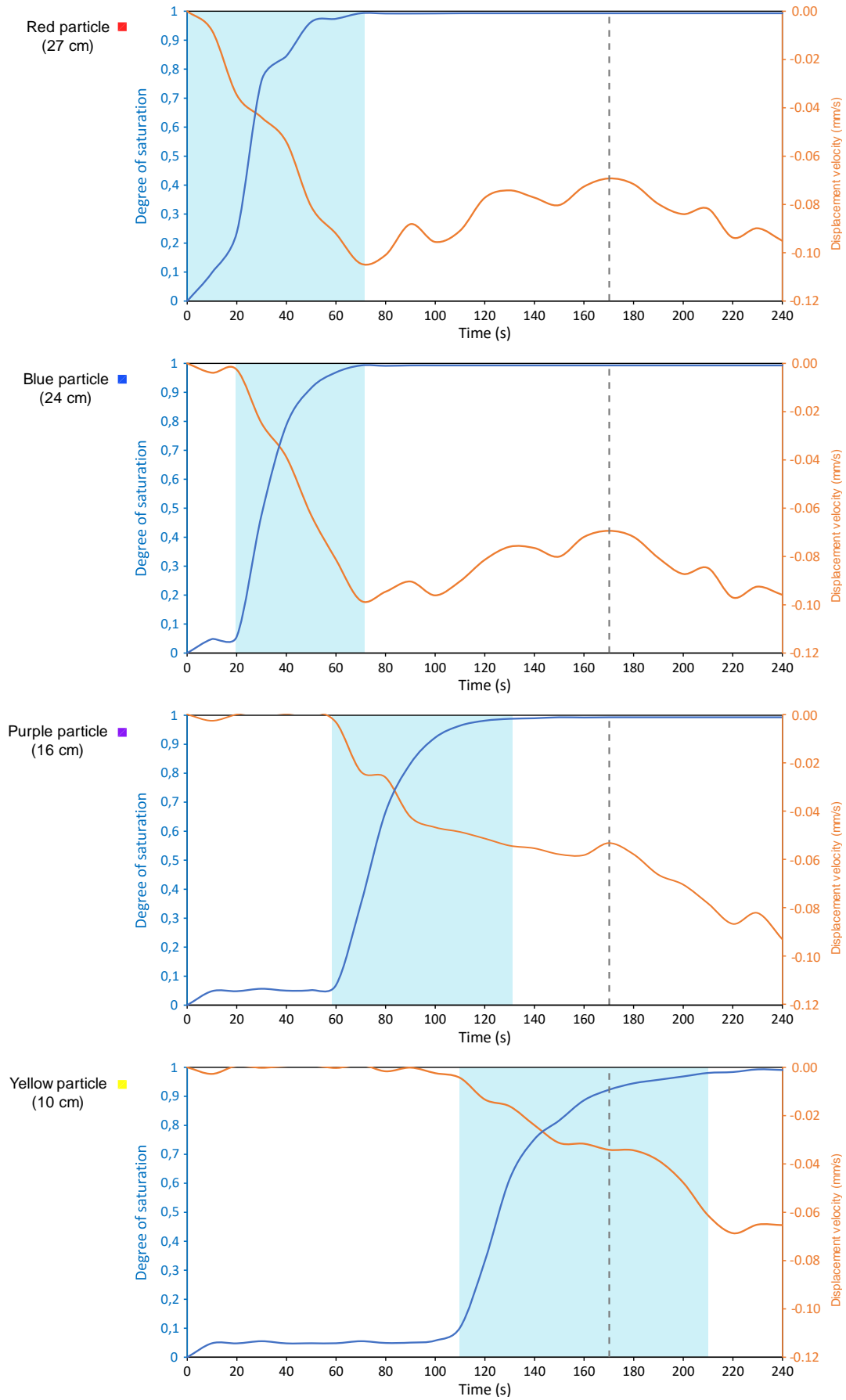


Figure 109 Particle by particle visualization of the column collapse experiment: Evolution of the accumulated displacement compared with the degree of saturation. Time from 0 to 240 seconds.

The initial analysis of Figure 109 is focused on the degree of saturation evolution. The degree of saturation of the red particle increases from the initial time because it is on the top of the column. The saturation front last 20 seconds to reach the area of the blue particle (3 cm below). Regardless of the difference in the wetting start, both particles reach the full saturation at the same moment, around 70 seconds after the start. This might be caused by irregularities in the surface flow that affect the standard degree of saturation evolution. Excluding then the red particle, the evolution of the degree of saturation of the three lower graphs (blue, purple, and yellow particles) follow the same tendency. When the saturation front reaches the area of a particle, the degree of saturation increases almost linearly until reaching the S_r 0.7. After that value, the evolution of the degree of saturation follows an exponential curve with an asymptote on the S_r 1. The duration of the full saturation process (shaded in blue) increases with the distance from the top. In the blue particle, 50 seconds pass from the saturation front arrival to the full saturation; in the purple particle, 70 seconds are required; and 10 seconds in yellow particle.

The analysis of the velocity of displacement (as a representation of the collapse) exposes a clear correlation with the degree of saturation. The behavior of the red and blue particles is similar. The downward displacement of the particles increases linearly with the degree of saturation during the wetting process. When the saturation degree is 1, the displacement velocity stabilizes in around 1mm/10s and starts to slow down until the second 170.

The acceleration of the particles purple and yellow is lower, corresponding to the lower saturation rate. On these particles, the displacement reaches the semi-stable velocity before the saturation is complete, approximately when the degree of saturation is 0.7.

In all the particles, after the second 170 (dashed line) the velocity of displacement increases again. That might be caused by the leak on the base of the column, that makes the water flow out when the saturation front reaches the base.

7.4 Conclusions

The property of the PIV-NP to combine the kinetic information with other information extracted from images (the degree of saturation in this case) opens a whole new option for the experimental analysis.

The use of the Numerical Particles storing all state values of each part of the soil facilitates the analysis at three different levels.

- **2D:** The mapping of a variable in all the points the experiment analyzed surface enables to observe the spatial tendencies (such as flow directions or displacement accumulation), but also the inherent heterogeneity of real cases, which is challenging to consider in numerical models.
- **1D:** The unidimensional graphs enable to observe the correlation between the evolution of different variables in a line of particles. This type of graphs permits to get an idea of the general evolution of a variable in a vertical, horizontal, or other direction lines, depending on the direction that better represents the experiment.
- **0D:** The particle by particle graphs are useful for quantitative analysis of the variables. This type of graphs enables the detailed correlation between variables, which facilitate to uncover possible cause-effect relation.

8

Chapter 8

Footprints in the beach - Analysis using PIV-NP and transparent soil

On this Chapter, the developed post-process Particle Image Velocimetry - Numerical Particles (PIV-NP) is combined with a mature technique to measure the degree of saturation by images in experiments with transparent soils.

The Chapter brings to light the high potential that the union of PIV-NP with another image technique has to profoundly analyze the experiments in the laboratory. This combination uncovers, in this case, the processes that occur walking along the seashore.

The investigations exposed in this Chapter were performed in the Queen's University and Royal Military College of Canada, under the supervision of prof. Andy Take and prof. Greg Siemens, during the stage in Kingston, Canada. The experiments were performed in conjunction with Meg McKellar Civil, engineer student from Queen's University.

8.1 Introduction

It is common to notice when walking on the beach close to the seashore that the wet sand around the foot dries as it steps on the sand (Figure 110). It might seem a bit contra intuitive for most people, applying pressure on a media should compact it, and more water should be expelled to the surface.



Figure 110 Dry circles appear around the feet when walking next to the sea. (source: Greg Siemens)

At the end of the XIX century, this contra intuitive fact intrigued the professor Osborne Reynolds. Reynolds uses this fact, among other experiments and observations to expose the theory of the dilatancy (Reynolds, 1885).

Dilatancy is the effect that produces an increase in the volume of a compacted dense granular media when it is sheared. The compact arrangement (distribution) of the grains are interlocking, therefore block the relative displacement between them. When the stress applied to the media forces this relative displacement, the space between the grains has to increase to overcome this interlocking arrangement. The increase of the pore volume and the fixed volume of the grains result in an increase in the total volume of the media (Figure 111).

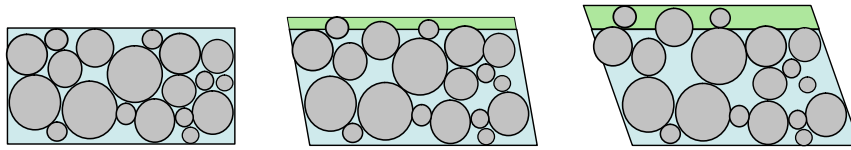


Figure 111 Schematic visualization of the dilatancy in the granular media.

The effect of the dilatancy is well-known in the soil mechanics, through the time multiple experimental and numerical articles were published regarding this topic (Bolton, 1986; Morrow and Byerlee, 1989; Stone and Wood, 1992; Chakraborty and Salgado, 2010; Pradhan, Tatsuoka and Sato, 2011; Wang *et al.*, 2017; Wu *et al.*, 2018).

In the particular case of the footprints effect, Geng *et al.* investigated the force patterns in granular media caused by local perturbation using photoelastic particles (Geng *et al.*, 2001).

This research was able to investigate beyond current knowledge thanks to the combination of modern developed techniques and high-tech tools. The combination uncovers the full process, observing the correlation between the variables: load, degree of saturation, strain, and velocity of displacement.

The main objective of this investigation is to visualize and understand the complete process of air entering into the soil as a result of the dilatation caused by a footstep. The concept of footstep is assimilated to a shallow foundation on a bearing capacity failure.

A set of shallow foundation experiments was performed in a metal tank with the main face made of laminated glass. The experiments were performed using transparent soil, varying the oil level to reproduce the entire transition from dry to submerged. The transparent soil enables to observe the air penetration into a completely saturated soil, and measure the degree of saturation at each point of the experiment using images. The experiments were recorded using an ultrahigh-speed camera at a frame rate of 500 fps with a resolution of 1280x800 px. The frequency and quality of these images enable to calculate the displacements using the eulerian method of image correlation, in brief events as the failures analyzed.

The displacement and degree of saturation data measured at fixed coordinates in the images are used as input data in the post process code PIV-NP. Through this code; the instant and accumulated values of displacement, velocity, deformation, and degree of saturation are obtained in numerical particles that move attached to the areas of soil which represent (described in Chapter 7). This arrangement of the data, combined with the data of punctual sensors allows a 2D exhaustive analysis of the entire failure process, observing the interrelationships between the different variables (Figure 112).

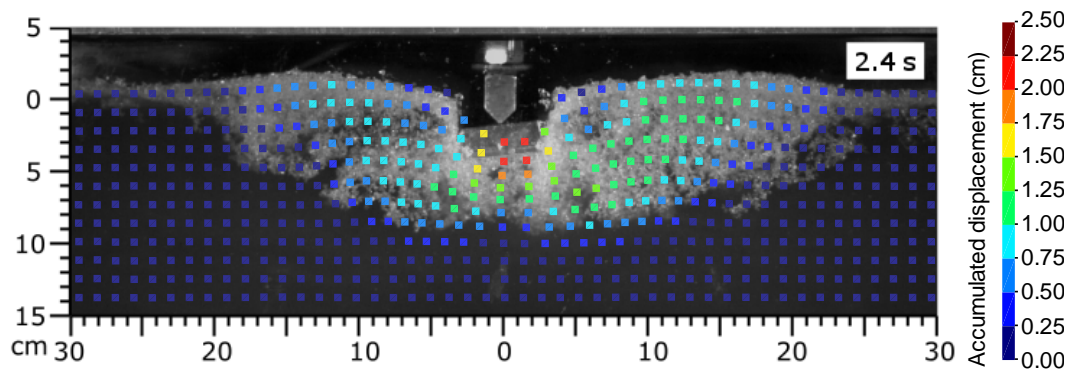


Figure 112 Frame of a shallow foundation experiment with visible air penetration. The numerical particles with the accumulated displacement information are overlapped.

8.2 Techniques description

8.2.1 Transparent soil

The soil used in this study was the artificial fused quartz sand (noncrystalline form of SiO_2) developed on the Royal Military College of Canada (Ezzein and Bathurst, 2011; Peters, Siemens and Take, 2011). The geotechnical properties of the artificial transparent sand displayed in

Table 13 and Figure 113 are extracted from these two articles, where a more extended geotechnical description can be found.

Table 13 Geotechnical properties of the artificial transparent coarse sand. Values extracted from (Ezzein and Bathurst, 2011; Peters, Siemens and Take, 2011).

| Parameter | Value | | Units |
|----------------------------|------------------|----------|-------------------|
| Grain density | 2300 | | kg/m ³ |
| Minimum dry density | 1050 | | kg/m ³ |
| Particle size distribution | | | |
| D ₁₀ | 0.75 | | mm |
| D ₃₀ | 1.16 | | mm |
| D ₆₀ | 1.75 | | mm |
| Coefficient of uniformity | 2.3 | | - |
| Coefficient of curvature | 1.0 | | - |
| Friction angle | Peak | Residual | |
| Dry | 43 | 36 | ° |
| Oil | 42 | 39 | ° |
| Saturated conductivity | 10 ⁻³ | | m/s |
| Refractive index | 1.459 | | - |

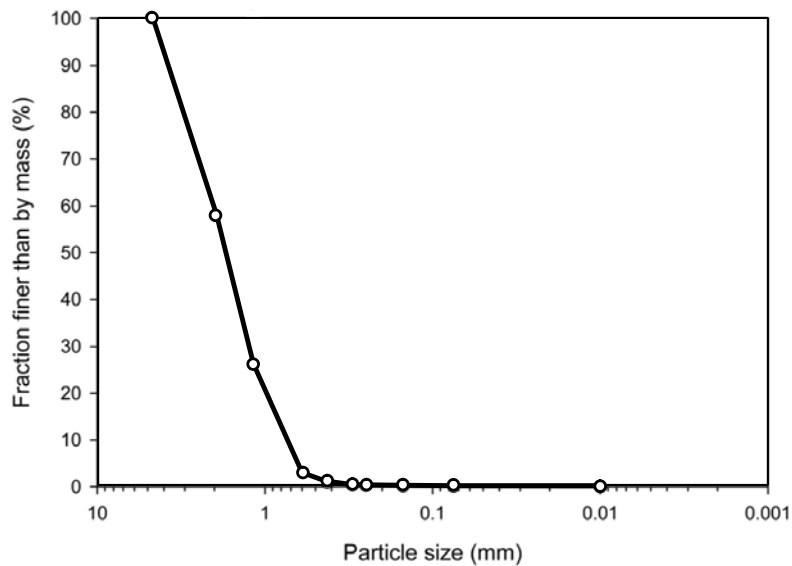


Figure 113 Particle size distribution for the coarse fused quartz soil (Ezzein and Bathurst, 2011).

The wetting fluid used is a mixture (1:1) of two mineral oils: Petro-Canada Krystol 40 and Life Brand baby oil (Siemens, Peters and Take, 2013; Siemens, Take and Peters, 2014). The refractive index of the oils is 1.451 and 1.464 respectively, the mixture of the oils has a resultant index of refraction of 1.46. The resultant oil mixture has a density of 830 kg/m³, an interfacial tension of 0.023 N/m, and a viscosity of 0.01 kg/m·s (Peters, Siemens and Take, 2011; Sills, Mumford and Siemens, 2017).

Degree of saturation measurement on transparent soils

The measurement of the degree of saturation in transparent soil is based on the mirror effect described in Section 2.3.1 Reflection and Refraction. The summary of the effect is that when the light changes from a medium with a refractive index to another medium with different refractive index, a fraction of the incident light is reflected instead of refracted. The amount of light reflected depends on the incident light, the angle of incidence, and the refractive indexes of the media.

On the case of transparent soil, the refractive index of the transparent soil and the refractive index of the oil mixture are 1.46 in both cases. Therefore, the refracted light is not affected by the change between these media; it behaves as the saturated soil was a homogeneous medium (Figure 114a). Elsewhere, the refractive index of air is 1. So, the light that travels through the unsaturated soil does not behave as it was homogeneous. When the light

crosses a bubble of air, it has to change twice the medium with different refractive index, resulting in a fraction of the incident light reflected (Figure 114b).

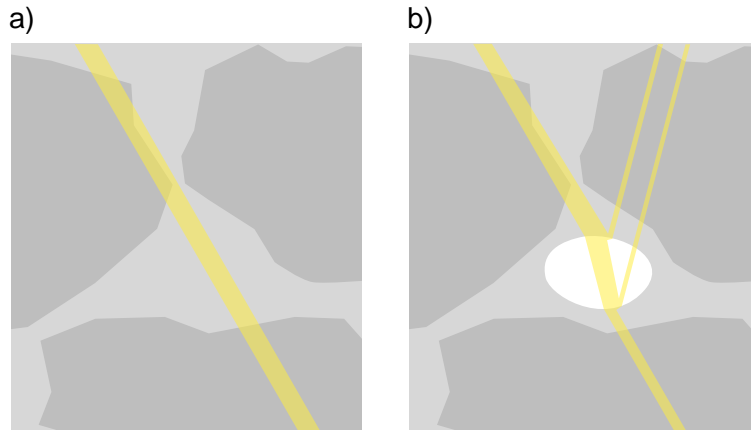


Figure 114 Ideal representation of the interaction of a beam of light with the transparent soil. a) Full saturated soil (soil + oil). b) Unsaturated soil with a bubble (soil + oil + air).

The reduction of the degree of saturation increases the surface of contact between media with different refractive index (oil-air, or soil-air). Following the effect described, more surface of contact results as a higher fraction of the incident light reflected.

On the experiments performed, the refracted light that reaches the back of the tank is absorbed by black paint. The reflected light is captured by the camera that is placed in front of the tank. Therefore, the intensity of the pixels of the image store the information of the amount of light reflected by each part of the soil.

The amount of reflected light depends on the amount of incident light, which implies the need for a normalization of the pixel intensity before the calculation of the degree of saturation. The normalization is performed using two reference images, full saturated (I_s) and dry (I_d). The intensity of each pixel of the image ($I(x, y)$) is normalized following Equation 21.

$$I_n(x, y) = \frac{I_d(x, y) - I(x, y)}{I_d(x, y) - I_s(x, y)} \quad \text{Equation 21}$$

The normalized pixel intensity is correlated to a degree of saturation using the improved calibration curve displayed in Figure 115 (Sills, Mumford and Siemens, 2017).

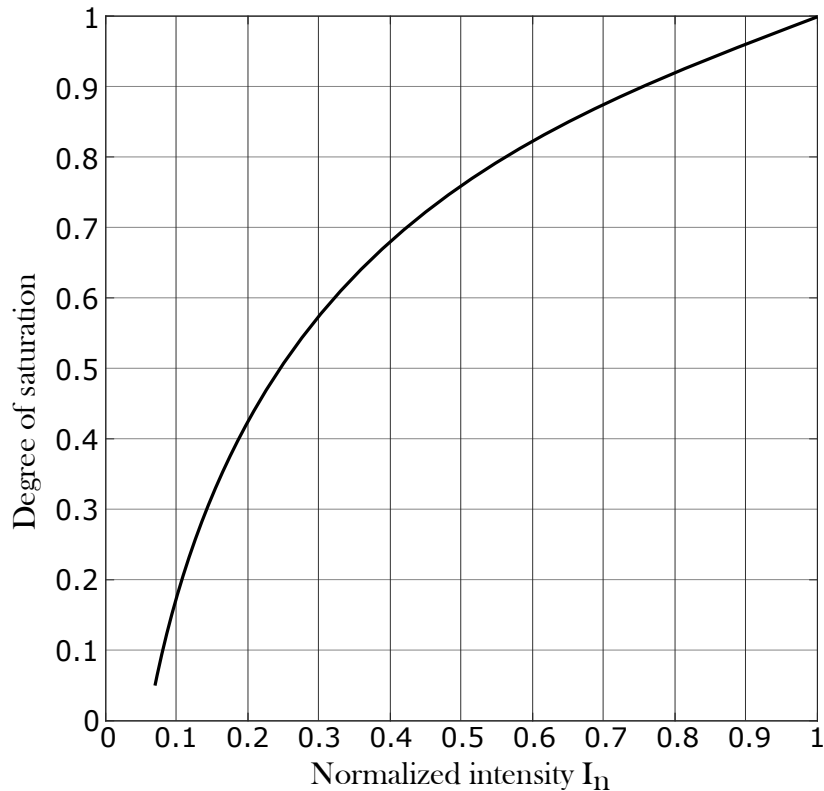


Figure 115 Calibration curve for transparent soils. Saturation - normalized pixel intensity relationship. (Sills, Mumford and Siemens, 2017).

8.2.2 PIV-NP in transparent soils measurements

The Particle Image Velocimetry - Numerical Particles is a post-process that uses the Eulerian PIV results to get the evolution of the values in each part of the soil. Besides getting the evolution of the velocity and displacement, also calculates the acceleration, instant and accumulated volumetric and deviatoric strains. The PIV-NP description and validation are presented in Chapter 5.

The degree of saturation calculated on fixed coordinates using the methodology explained in Section 8.2.1 is set as input data in the PIV-NP. Chapter 7 presents the procedure to include the degree of saturation data into the PIV-NP post-process.

8.3 Experimental setup

8.3.1 Ultrahigh-speed camera and lighting.

The camera used to record the experiments was a Phantom v2512 (Figure 116). The expected velocity of the failures required an ultra-high-speed camera. The three camera parameters that are critical to record useful images for a proper image correlation: image resolution, frame rate, and exposure time.

The **image resolution** must have enough quality to be able to divide the image into representative patches that can be traced in the next image. On this case the image resolution was 1280x800 px.

The **frame rate** must be high enough to ensure that the distance between the original patch location (in image 1) and the displaced patch location (in image 2) is restrained; and to ensure that the displaced patch is not deformed that becomes unrecognizable. On this case the frame rate was 500 frames per second.

The **exposure time** must be short enough to consider that the image represents an instant of time. It is important to avoid that a punctual grain appears as a line in the image because it captured its displacement. These lines difficult the traceability of the patches. On this case the exposure time was 20 μ s.



Figure 116 The ultrahigh-speed camera Phantom V2512.

The Phantom v2512 comfortably accomplishes the requirements of the experiments. The ultra-high-speed camera has an internal dynamic RAM memory to avoid the speed limit due the automatic transference of data into the computer. The internal memory defines the amount of time that can be stored depending on the image resolution and the frame rate.

In this case the maximum time that can be stored is 20 seconds, which is enough to include the ultimate failure but not enough to store the full experiment. For this type of cases where the interesting event occurs in an indeterminate time inside the experiment, the camera offers the option of circular buffer recording.

The explanation of circular buffer recording is based on the description extracted from the Phantom high-speed website (Vision Research, 2019):

"In the circular buffer or loop recording, the camera is continuously recording images into its internal memory. When it gets to the end of memory, it cycles back to the beginning and continues recording, constantly overwriting itself. This loop is performed until the camera is triggered."

On the experiments of this investigation, the camera is set to store the 90% of the recorded movie be what happens prior to the trigger and 10% after the trigger. So, the trigger needs to be manually activated right after the ultimate failure occurs.

The high-speed camera requires a special light source. The light source must provide a high intense incident light which ensures that the reflected light captured per exposure time (20 μ s) is enough for a clear image. The light source must be continuous to avoid the flickering effect. Most of the LED sources emit pulses of light at 100 - 120 Hz (pulses per second), which seems continuous for a human vision 60 fps but is insufficient the high speed recording 500 fps.

The light source arrangement and camera distance were the same through all the experiments to maintain the incident light constant (Figure 117).



Figure 117 Light source and camera location respect to the tank.

8.3.2 Tank, pneumatic load system and sensors

The experiments were performed in a steel tank with the main wall made with 1.5cm thick laminated glass. The tank dimensions are 89 cm wide x 30.5 cm long x 25 depth. The reference dots are attached to the glass wall perimeter at intervals of 5 cm.

At the upper center of the tank, the shallow foundation device is installed. The device is controlled by a pneumatic loading system that increases air pressure of a piston. The piston applies the load by means of a metallic piece on the center of the footing of 5 x 25 cm.

The punctual parameters of the experiment are measured by sensors controlled simultaneously by the data acquisition software. The load applied by the piston is measured with a load cell screwed to the piston rod. The vertical displacement of the footing is measured by an LVDT installed on the piece (b). Oil pressures inside the tank are measured by a PPT located 14 cm below the soil surface.

8.3.3 Experiment performance

The footprint in the beach was assimilated to the bearing capacity failure test using a small footing. Multiple experiments were performed to analyze the behavior of the soil, varying the initial conditions. However, the whole experiments are performed following the same procedure.

The transparent soil is placed in the tank by dry pluviation, and the density is controlled by weighting sequentially the amount of soil placed. The complexity of the soil placement is reaching the degree of saturation of 1 in the soil from the base to the requested oil level. The main issue is the air trapped in bubbles between the grains. A 3 cm layer of oil is maintained in the soil surface, while the dry pluviation of soil grains is slowly executed. By this procedure, the amount of bubbles trapped is highly reduced. In the cases that some bubbles remain trapped, the soil is deaired by manually stirring the soil until the bubbles flow freely to the surface.

During the soil placement, the ppt sensor is installed inside the soil at 14 cm below the soil surface. Once the soil is placed inside the tank with the requested initial oil level, the footing is installed on the soil surface, ensuring its horizontality with a level. On the center of the footing, the piston of the pneumatic cylinder is placed, with the LVDT on it.

When the experiment is ready to start, the data acquisition software is initiated, the lights are turned on, and the camera is set on the recording loop. The air from the compressor is injected inside the pneumatic cylinder in a constant flow creating a regular increase of the load applied on the footing. Right after the bearing capacity failure occurs, the camera trigger is pressed, so the camera stores just the failure. Whereas, the sensors record the full experiment.

8.4 Results on three representative cases

Multiple shallow foundation failure for bearing capacity tests were performed to represent the different distances to the seashore varying the oil level.

In this Section, three cases are analyzed in detail to exemplify the three archetypal situations considering the relative position of the oil level respect to the soil surface (Figure 118). The cases are displayed ordered by its complexity.

1. Dry case: Represents a point distant to the shoreline. The oil level is deep enough to affect the soil around the surface.

2. Submerged case: Represents a point inside the sea. The oil level is high enough to ensure that the air does not interact with the soil.

3. Saturated case: Represents a point in the shoreline at the moment when a wave has left. The oil level is exactly at the level of the soil surface.

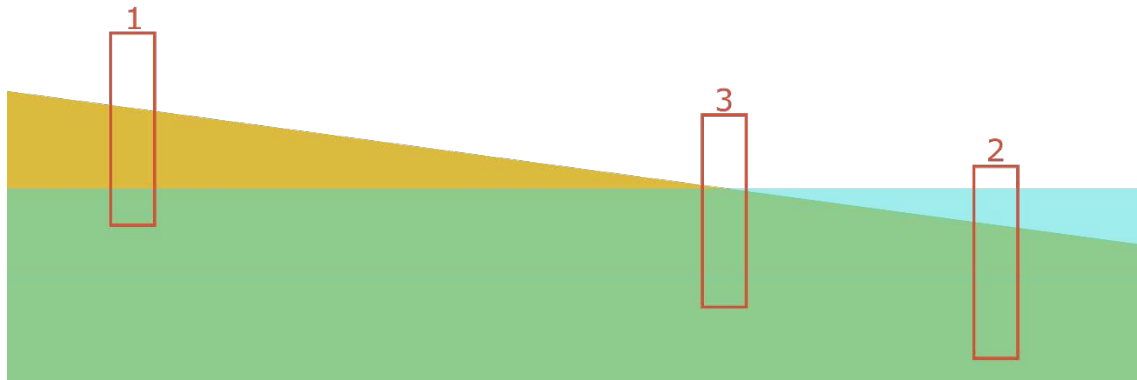


Figure 118 Points of the 3 cases exposed in this part. 1) Dry 2) Submerged 3) Saturated.

8.4.1 Dry case

The dry case represents the cases where the oil level is distant to the potential area of affectation in the shallow foundation general failure Figure 119.



Figure 119 Steps on the dry area of the beach (Salento, Italy).

The degree of saturation in the soil is the residual oil content that remains attached to the particles. The effect of the residual oil content is considered negligible for the mechanisms evaluated in this Chapter. This assumption had to be made because the oil does not evaporate, the procedure to dry the soil is by gravity, letting the oil flow away. That procedure leaves an oil film attached to the soil grains.

Figure 120 plot the evolution of the footing settlement with the regular increment of the load applied. Three micro-failures occur before the general failure (20, 50, 100 kg).

The image analysis focuses on the ultimate failure that occurs after applying a load of 150 kg. The images of the micro-failures are not available because of the limitation on the internal memory of the high-speed camera.

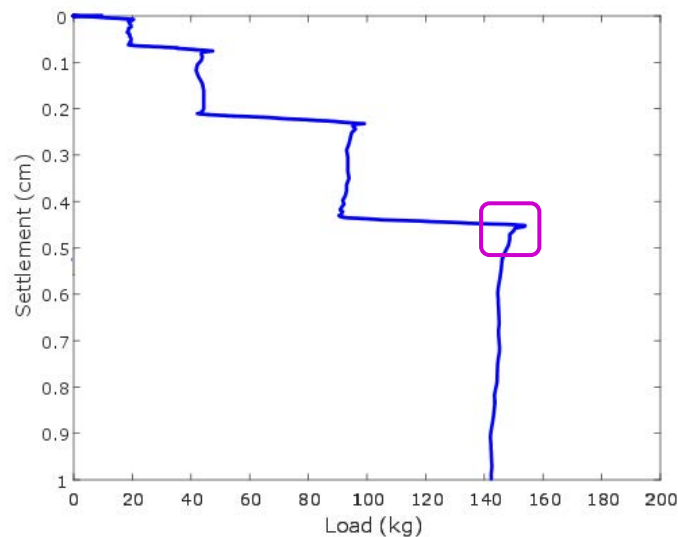


Figure 120 Load vs. settlement during the whole dry experiment. There are different micro-failures before the ultimate failure occurs. The analysis is based on that ultimate failure marked on purple.

The images were extracted from the highspeed camera video, accurately selecting the moment of the ultimate failure. The high number of frames stored on the highspeed video implies the decision of the number of frames per second needed to properly analyze the case.

Figure 121 shows the image before the ultimate failure. The image is a zoomed to the area of interest for better visualization. The soil is white as it reflexes most of the incident light. However, the granular texture is noticeable for the image correlation analysis.

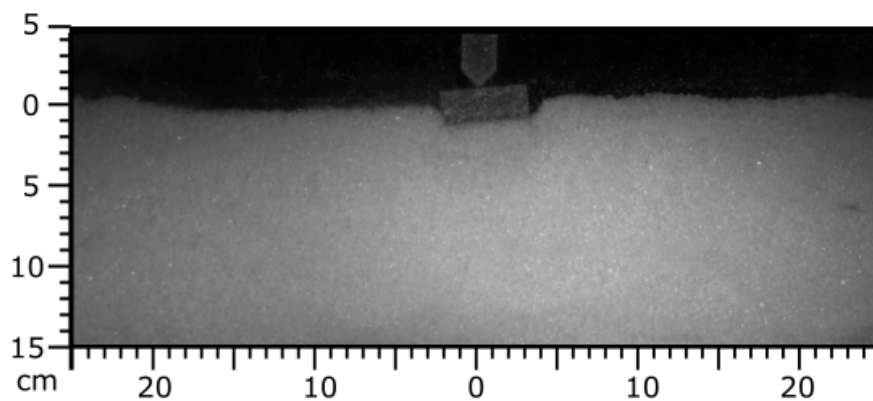


Figure 121 Image before the ultimate failure. This condition is defined as the initial situation of the image analysis.

Figure 122 shows the displacement vectors measured by the Eulerian image correlation analysis. These displacements are measured on fixed coordinates and are the input data for the PIV-NP analysis.

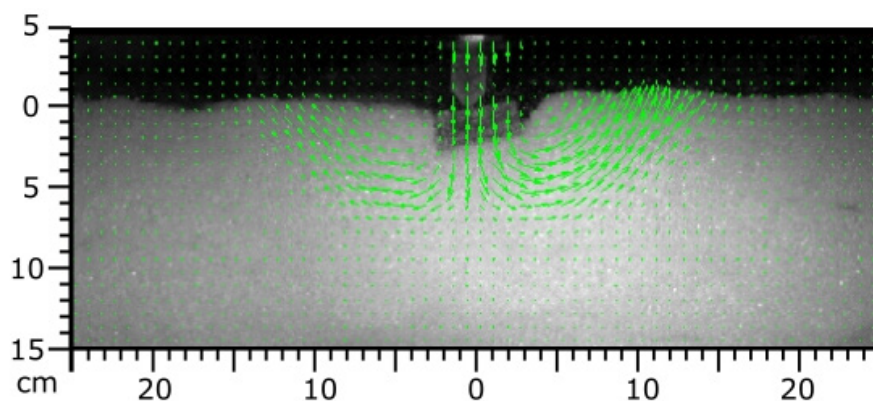


Figure 122 Vectors of displacement calculated by PIV in the moment of the failure.

The results are analyzed using PIV-NP. Each numerical particle stores and calculates the values of the parameters corresponding to part of the soil that represents. Figure 123 plots the numerical particles at the end of the ultimate failure. The colors represent the displacement accumulated on each NP. The evolution of the variables of a line of particles (highlighted in pink) is analyzed below.

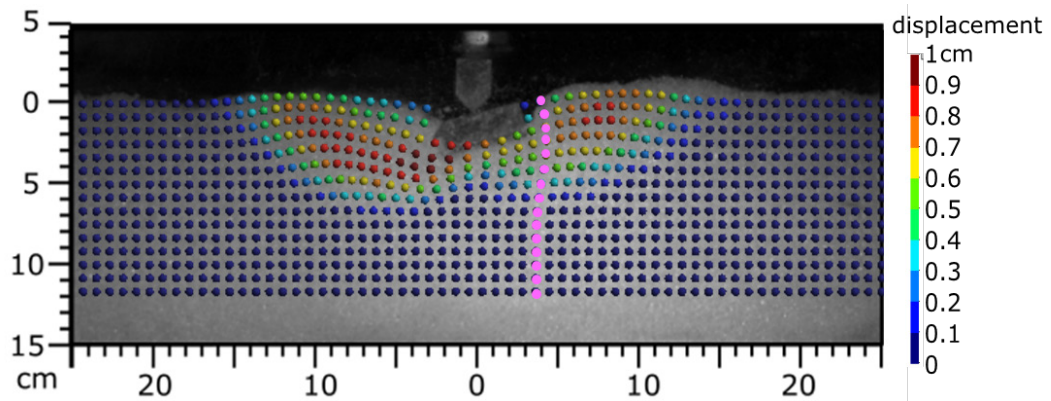


Figure 123 Total displacement on the particles generated by PIV-NP in the dry case. The evolution of the line of particles marked on pink is plotted in Figure 125.

The behavior of the soil is expected on the general failure on shallow foundations. The failure mechanism has the geometry of the ideal general failure from the literature (Figure 124).

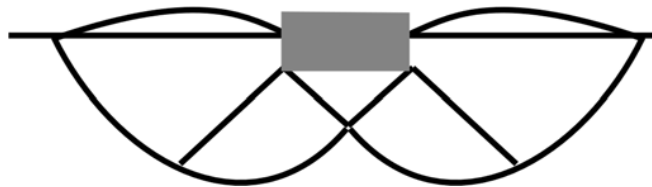


Figure 124 Theoretical general failure mechanism.

The displacement and volumetric strain evolution of the line of particles marked on pink are plotted in Figure 125. The accumulated displacement is higher on the particles in the middle of the mobilized area, that occurs due to the rotational movement of each side of the failure. The relative displacement between the soil grains causes a volumetric strain in the whole mobilized area. The volumetric strain is not located on a single shear surface. The whole mobilized area is sheared, causing a generalized increment of the pore volume.

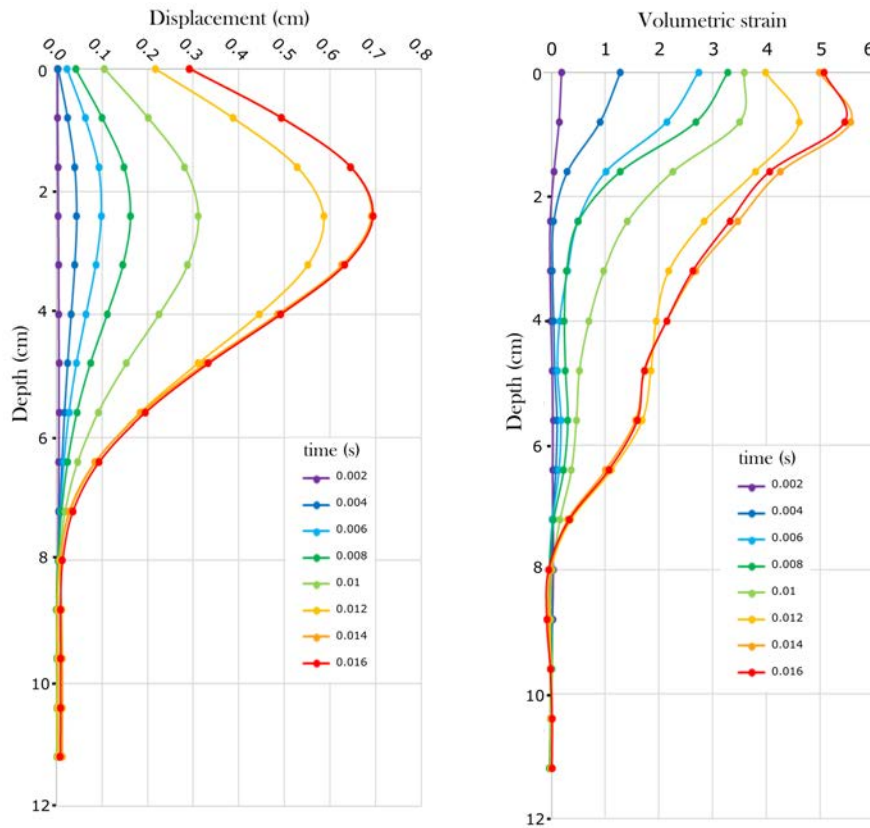


Figure 125 Evolution of the displacement and volumetric strain of the particles along the vertical profile indicated in pink in Figure 123.

Figure 126 plots the velocity of the particles compared with the settlement measured on the footing. The graph shows that the ultimate failure duration is less than 0.015 seconds. The evolution of the speed has a single peak after 0.01 seconds.

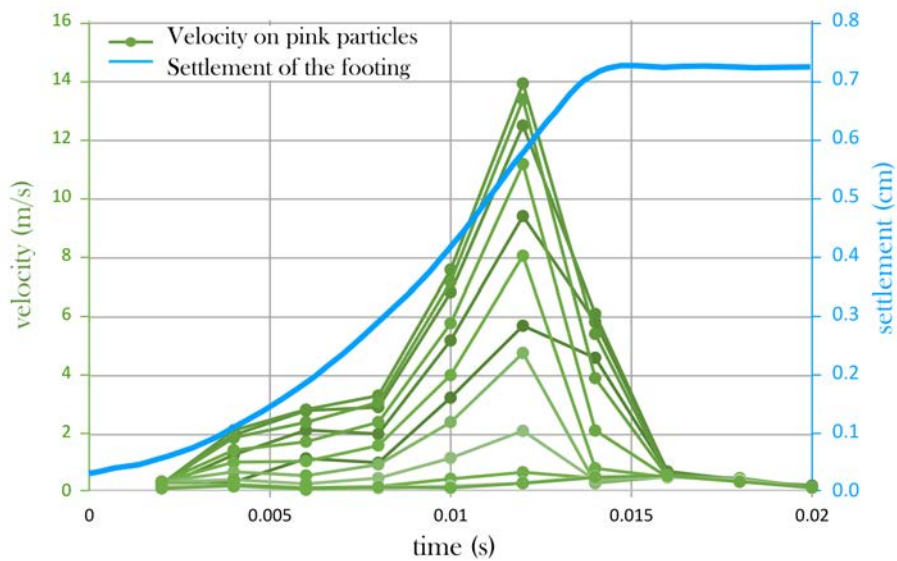


Figure 126 Correlation between the settlement of the footing measured by the LVDT and the velocity of the particles measured by PIV-NP.

8.4.2 Submerged case

The submerged case represents the cases where the oil level is higher than the soil surface. The distance between the oil level and the soil surface is 20mm. The volume of free oil on the top of the soil ensures that the air is not penetrating into the soil (Figure 127).



Figure 127 Steps on the submerged area of the beach (Salento, Italy).

Figure 128 plots the evolution of the footing settlement with the regular increment of the load applied. Two micro-failures occur before the general failure (40, 70 kg). The image analysis focuses on the ultimate failure that occurs after applying a load of 130 kg. The load-settlement path is similar to the previous dry case. The soil resistance to the failure of both cases is on the same range.

However, the duration of the ultimate failure on this case (2.5 s) is an order of magnitude longer than the dry case (0.15 s). Unfortunately, the failure of the submerged case presented (Figure 129) is not symmetrical as the dry case (Figure 123). The tendency of the footing to tilt is a common issue in general failure mechanisms (Figure 124). That reduces the bearing capacity measured by the test, compared with its symmetrical related test. This effect is widely described in Section 8.5.2.

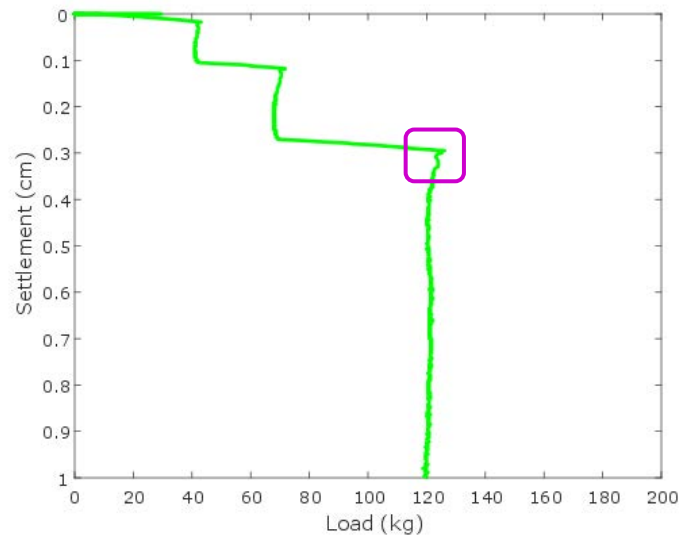


Figure 128 Load vs. settlement during the whole submerged experiment. There are different micro-failures before the ultimate failure occurs. The analysis is based on that ultimate failure marked on purple.

Figure 129 plots the numerical particles generated by the PIV-NP at the end of the ultimate failure. The colors represent the displacement accumulated on each NP.

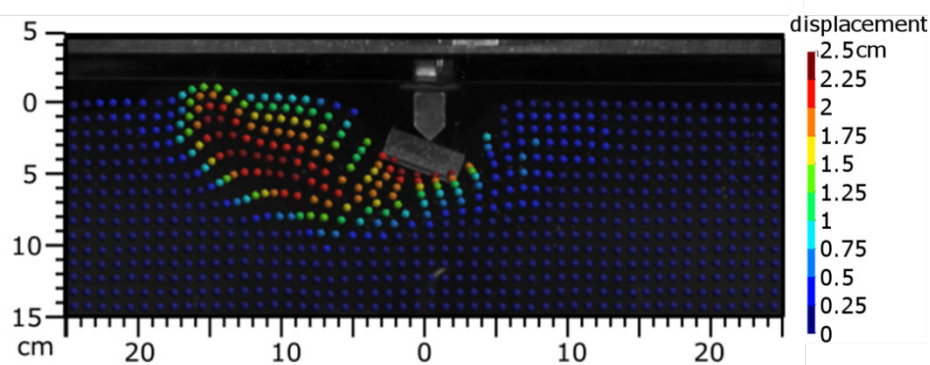


Figure 129 Total displacement on the particles generated by PIV-NP in the submerged case.

Figure 130 displays the data from the PPT and LVDT sensors during the ultimate failure. The PPT is located 14 cm below the soil surface. Figure 129 shows that the maximum depth of mobilized soil is 10 cm below the surface; therefore, the PPT is located in the undisturbed soil.

However, the pressure head measured by the PPT (Figure 130) indicates a drop in the oil pressure correlated to the failure. The reason for this reduction on the oil pressure in the undisturbed soil derives from the positive volumetric strain observed in Figure 125. The

oil in the soil surrounding the mobilized area (as well as the free oil on the top) flows to fill the extra pore volume created by the effect of the dilatancy.

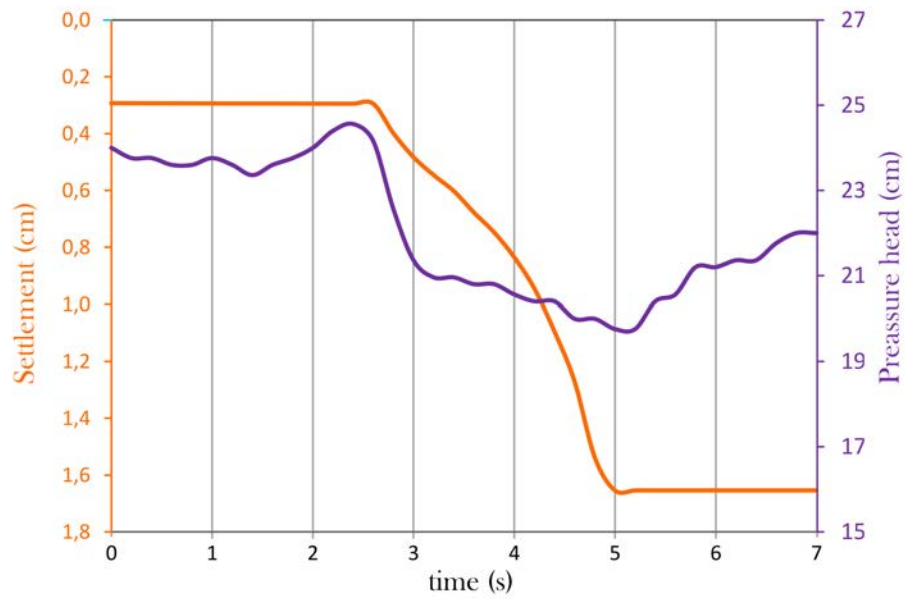


Figure 130 Effect of the failure in the pressure measured by the ppt correlated with the settlement of the footing.

8.4.3 Saturated case

The saturated case represents the footprints close to the seashore, where the effect that this Chapter analyzes is more outstanding. The wave movement creates, for every cycle, an area saturated with the oil level at the soil surface. The area that appears when the wave leaves is compacted and fully deaired. The steps on this area originate a dry circle around the foot (Figure 131). This is the case that is aimed to represent in this Section. As described in the Section 8.3.3 the deaired soil is demanding to reproduce on the experiment; in nature the same wave motion deair the soil by itself.



Figure 131 Steps on the saturated area created by the wave movement (Salento, Italy).

Figure 120 plot the evolution of the footing settlement with the regular increment of the load applied. Two micro-failures occur before the general failure (120, 260 kg).

The image analysis focuses on the ultimate failure that occurs after applying a load of 400 kg.

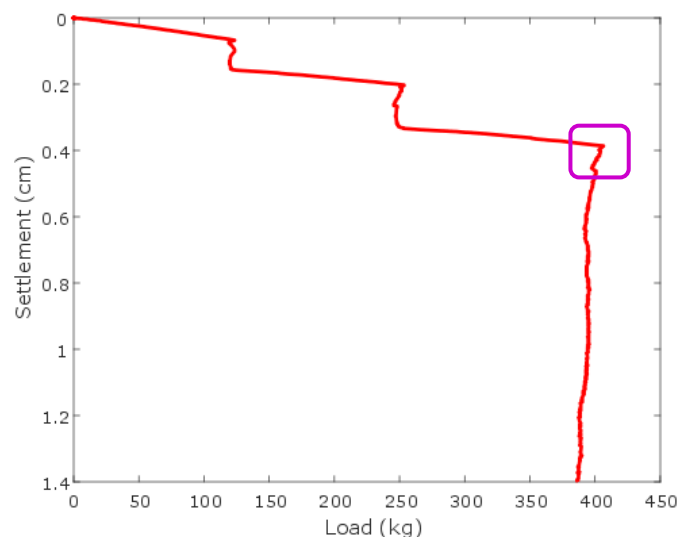


Figure 132 Load vs. settlement during the whole experiment. The analysis is based on that ultimate failure marked on purple.

Figure 133 shows the saturated soil before the failure compared with the soil with the air in the pores after the failure. The entrance of air in the soil describes the same pattern as the theoretical general failure mechanism exposed in Figure 124. The duration of the ultimate failure on this case (2.4 s) is similar to the submerged case (2.5 s), and an order of magnitude longer than the dry case (0.15 s).

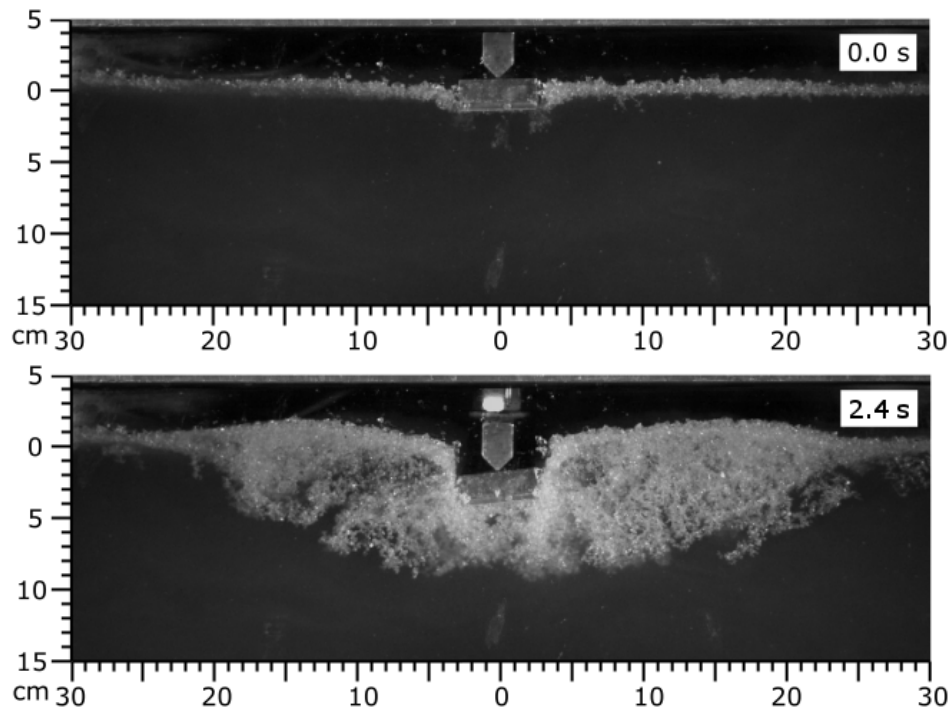


Figure 133 Initial and final frames of the ultimate failure in the saturated case.

The analysis of this case is described in three different stages. The first stage is a 2D analysis to observe the air penetration compared to the distribution of the velocity from the particles of the PIV-NP. The second stage is a 1D analysis. A line of particles is selected to explain the evolution of the accumulated displacement, velocity, volumetric strain, and degree of saturation. The third stage, four representative particles are selected for a better understanding of the relation between the degree of saturation and velocity of deformation.

First stage – 2D analysis

Figure 134 shows the full process of the ultimate failure. A reference of the soil state is presented every 0.4 s. The left column displays the unaltered frames to visualize air penetration into the soil. The right column displays the velocity of displacement of all the

numerical particles from PIV-NP. A step by step analysis of the ultimate failure process is presented below in Figure 134.

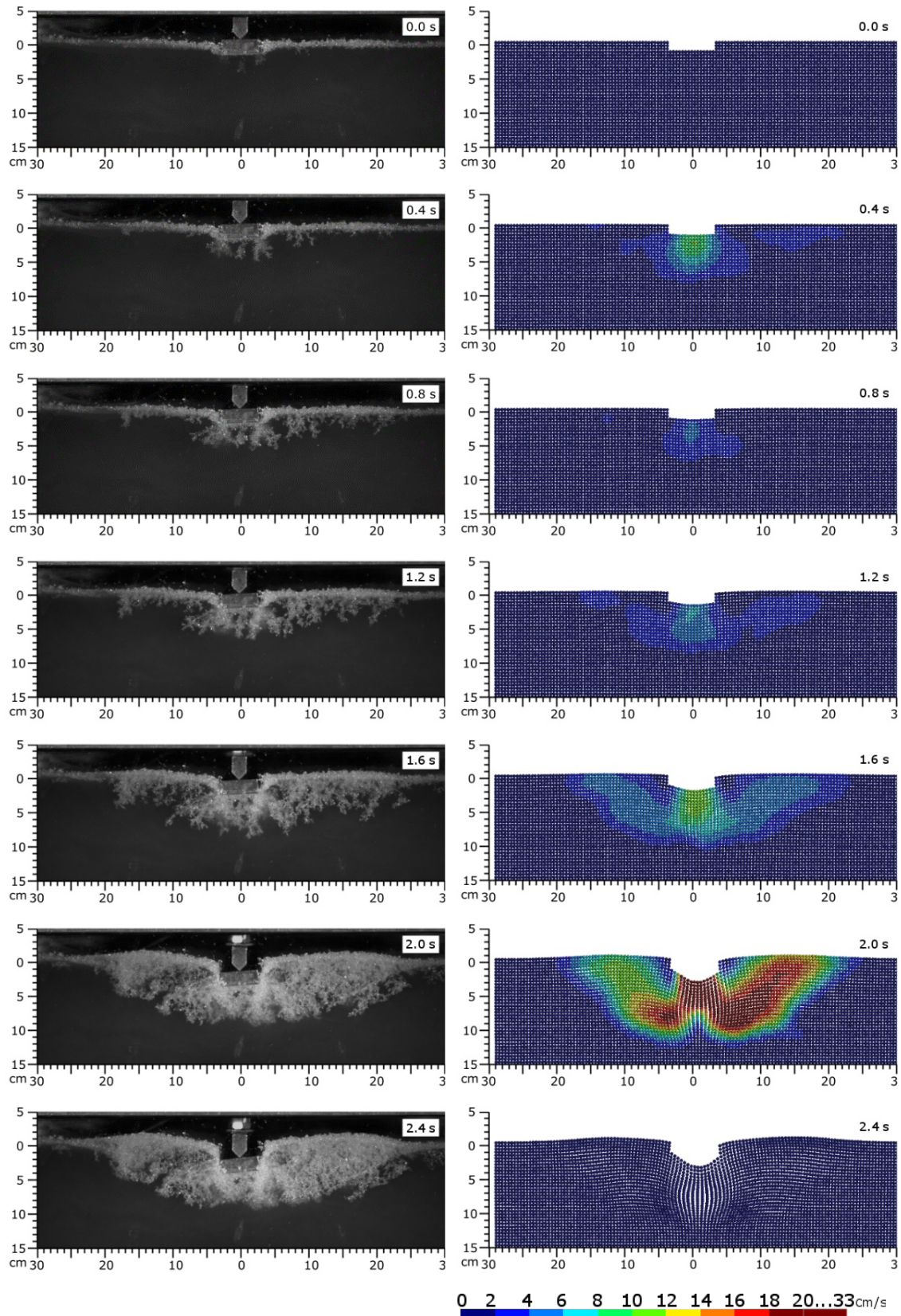


Figure 134 Evolution of the ultimate failure in the saturated case. a) Real image b) Numerical particles position and their velocity of displacement.

The instant before the ultimate failure is considered the 0.0s time, to facilitate the description of the failure steps. At this moment, the air has almost not penetrated, there are some imperceptible air bubbles near the footing, remaining from the previous small failures. At this moment, the particles are static.

At the instant 0.4s, a punching shear failure occurs. The deformations are concentrated in the area immediately below the footing. At this moment, the air begins to penetrate inside the deformed zone. During the time between moments 0.8-1.2s, the soil deformation velocity is low, less than 4cm/s. However, the air penetrates into the soil occupying the deformation zone. At the instant 1.4s, the air has penetrated almost the entire deformation zone. At this moment, the velocity of deformation of the soil begins to accelerate. At the instant 2.0s, when the air extends throughout the deformation zone, the velocity of deformation reaches its peak of 33cm/s. After the failure, at 2.4s, the particles are static again. The air that has penetrated remains trapped inside the soil. However, on the peripheric zone of the air penetration, the oil starts refilling the unsaturated pores.

According to the observed behavior, an explanation of the process can be concluded. During the failure, the volume of pores needs to increase to permit the grain displacement, following the dilatancy theory. On the dry case, the air in the pores can expand to fill the extra pore volume. On the in the saturated case, this extra pore volume is filled, decreasing the oil pressure on the deformed zone and surroundings. In the saturated case, the oil pressure between the grains and the surrounding oil is not enough to fill an increase of volume produced by a failure.

Therefore, in order to deform the soil needs to suck the air from the surface inside. But the surface tension of the oil creates a resistance to air penetration. This resistance occurs during all the air penetration in each space between grains. Right after the first punching failure what occurs is that the soil enters into an unstable stage of iterations of small deformations and air penetration: The soil slightly dilatates which suck some air inside, then the air that has penetrated permits to dilate a bit more. Unlikely the oil, the air inside the pores can expand. Therefore, as much air is inside the soil pores easier, the soil can dilate. General failure is a mechanism that involves the full deformed zone. For instance, the peak of the failure velocity occurs when the penetrated air reaches the entire zone of failure. This explanation is endorsed by the punctual analysis in Stage 3.

Second stage – 1D analysis

The PIV-NP property of calculating all the variables in the same numerical particles that move attached to the soil is used in the second stage of analysis to compare the evolution of multiple variables with time and depth. A column of numerical particles, initially vertical, is selected to analyze the evolution of the accumulated displacement, velocity, volumetric strain, and degree of saturation (Figure 135).

The particles from the PIV-NP exposed in Figure 135 are generated with an initial distribution of one particle per element. While the particles exposed in the right column of Figure 134 are generated with an initial distribution of four particles per element. This difference in the initial density of particles is for better visualization of the 2D analysis and better manageability of the data in 1D and 0D analysis.

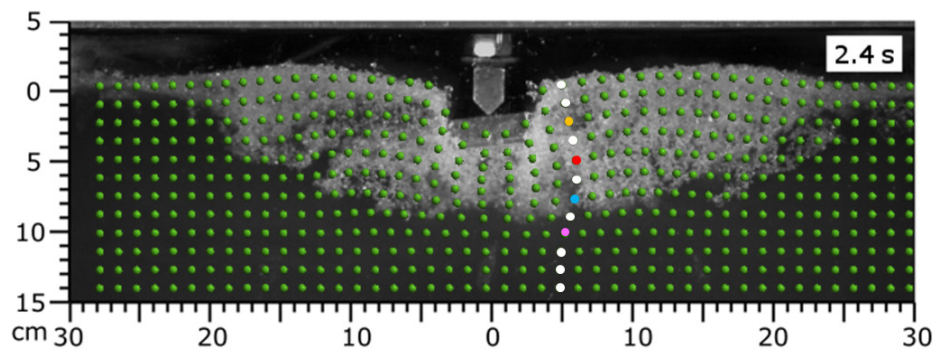


Figure 135 Image after the failure and with the particles generated by PIV-NP superposed. The line of particles marked is selected to evaluate the evolution of their status. The particles marked in colors will be evaluated individually.

The evolution of accumulated displacement and velocity are plotted in Figure 136. The displacement graph shows the movement as a general failure, where all the displacement lines have a similar shape that involves all the deformed zone. The accumulated displacement lines are more spaced with the time, which indicates an acceleration. That is confirmed by the velocity graph, where velocity increases with the time.

The evolution of the velocity shows that despite the failure involves the full zone of deformation, the peak of velocity gets deeper by the time. During the period from 0.2 to 1.2, the velocity peak is around 4 cm deep. During the period from 1.4 to 1.8, the velocity peak is around 6 cm deep. During the period from 2.0 to 2.2, the velocity peak is around 8 cm deep. This evolution of the velocity is related to the air in the pores.

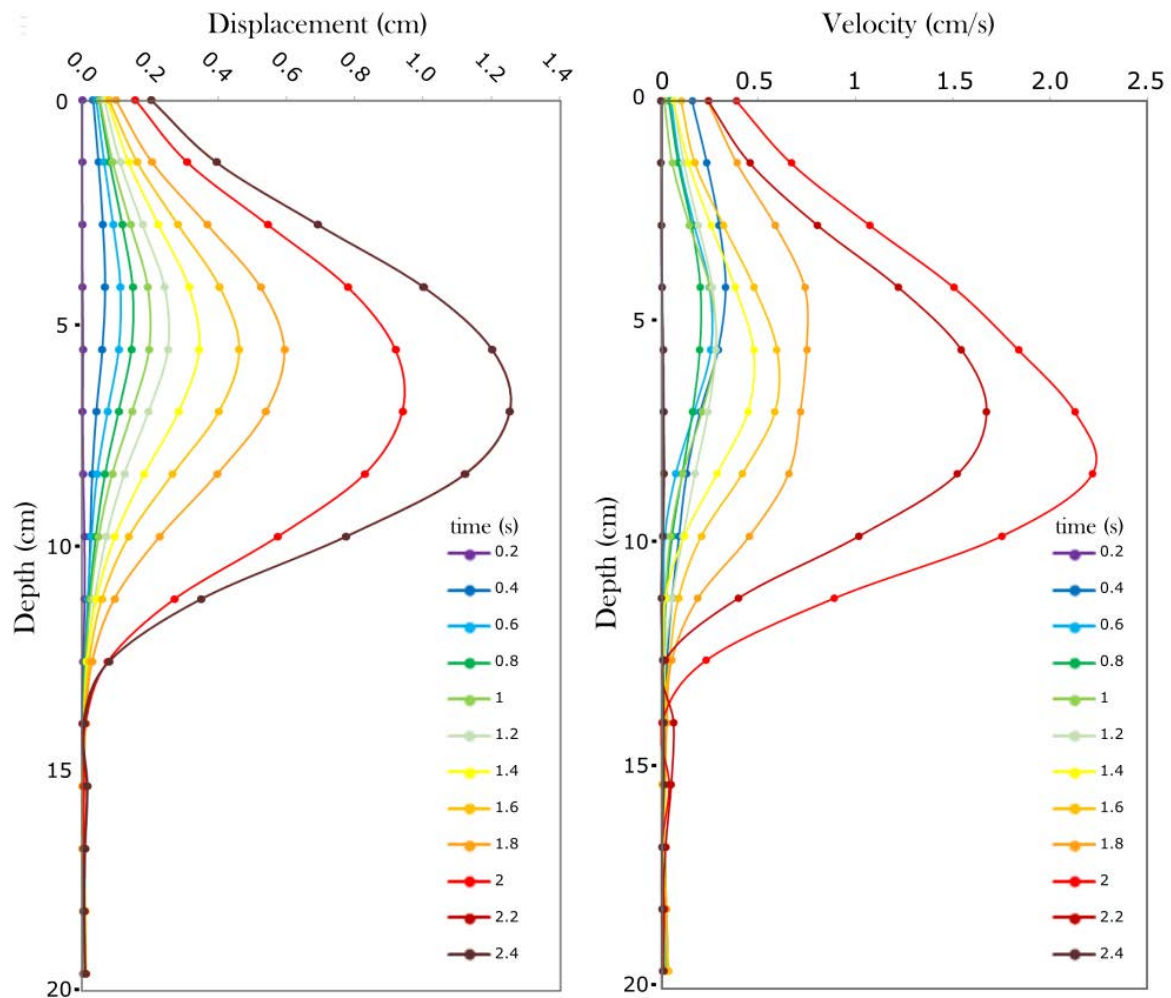


Figure 136 Evolution of the accumulated displacement and instant velocity of the line of particles selected in Figure 135.

Figure 137 compares the evolution of the volumetric strain with the degree of saturation in the column of particles. The volumetric strain and the degree of saturation follow approximately the same path. On the depth between 10 and 12 cm, the volumetric strain is difficult to discern from the intrinsic noise. On that depth, the degree of saturation remains around 1, which means that the air did not penetrate there. The displacement graph indicates that there is movement of the soil in that depth, but the extra pore volume might be compensated by the surrounding oil.

The evolution of the degree of saturation indicates that while the air is penetrating deeply, the percentage of the pore volume filled with air in the upper zones also increases. The increment of the percentage of air respect the oil is caused by more air penetration, but also by the expansion of the air that already has penetrated.

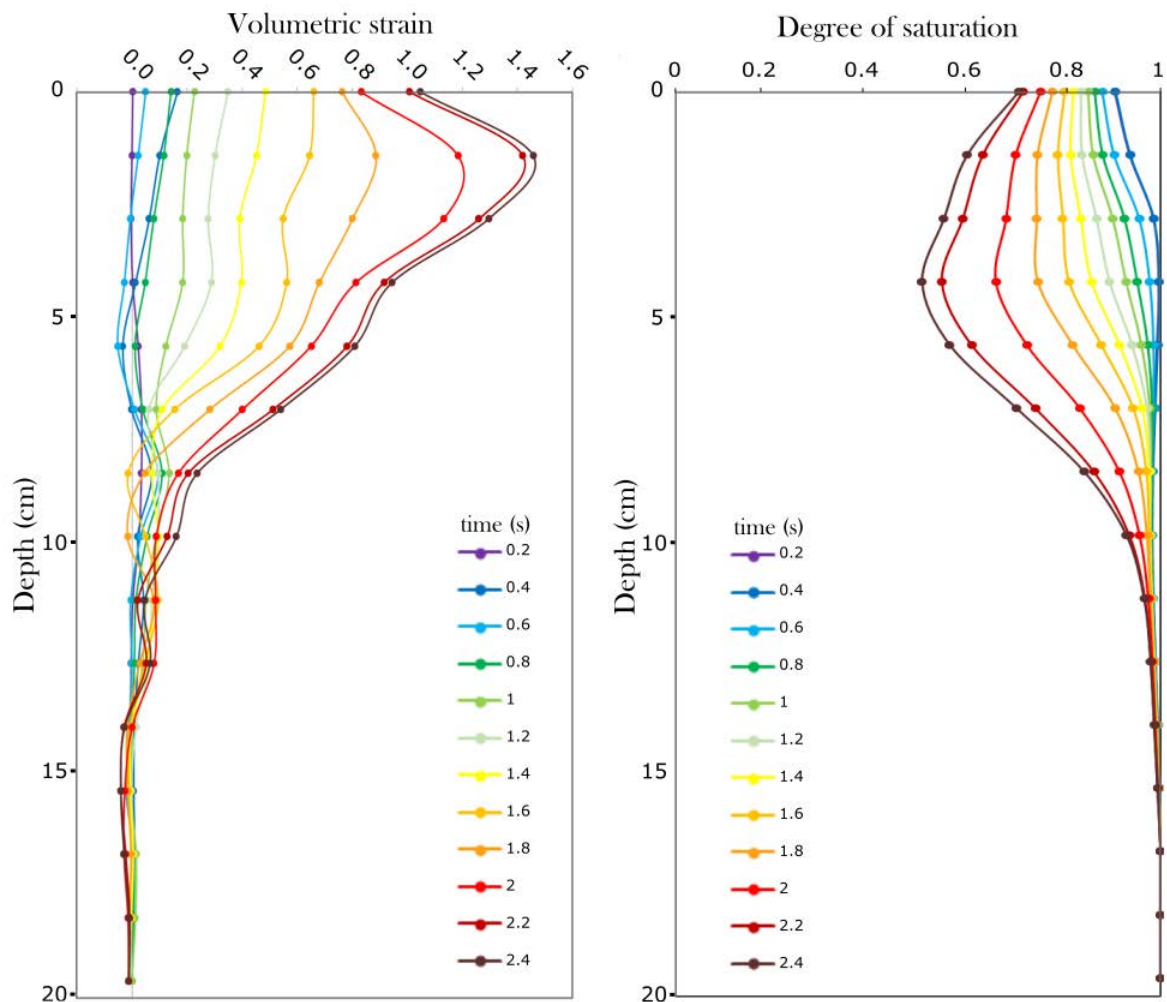


Figure 137 Evolution of the volumetric strain and the degree of saturation the line of particles selected in Figure 135.

Third stage – Punctual analysis

The punctual analysis is based on the individual examination of four reference particles. The particles are marked in color in Figure 135. Each particle is representative of a depth: **Orange particle**: - 2.5 cm. **Red particle**: - 5.0 cm. **Blue particle**: - 7.5 cm. **Pink particle**: - 10 cm.

Also, the punctual data from the sensors is evaluated and correlated in this stage. The load applied on the footing measured by the load cell, and the oil pressure at -14 cm measured by the ppt sensor. The analysis of the variables in individual particles facilitates the discovery of the relation between different variables of the soil status.

The definition of two events inside the ultimate failure is presented in Figure 138. The graph compares the load applied to the footing with the velocity on the orange particle located close to the footing. The punching shear failure (marked in green) occurs between the second 0.2 and 0.6 (which corresponds to the blue lines in Figure 136 and Figure 137). This failure causes a drop in the load applied on the footing of 10Kg. The general failure (marked in red) occurs between the second 1.8 and 2.4 (which corresponds to the red lines in Figure 136 and Figure 137). This failure causes a drop in the load applied on the footing of 140Kg.

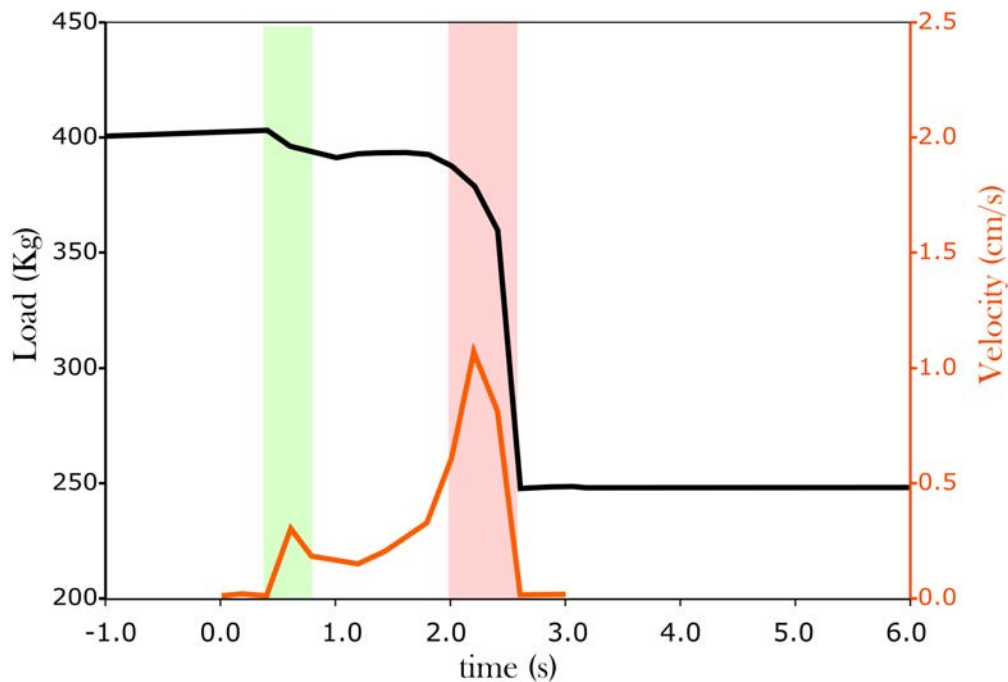


Figure 138 Evolution of the load applied on the footing (measured by the load cell) and the velocity on the particle orange. The two peaks of failure are marked: punching failure (green) and general failure (red).

Figure 139 plots the evolution of the velocity of displacement compared to the degree of saturation on the reference particles colored in Figure 135.

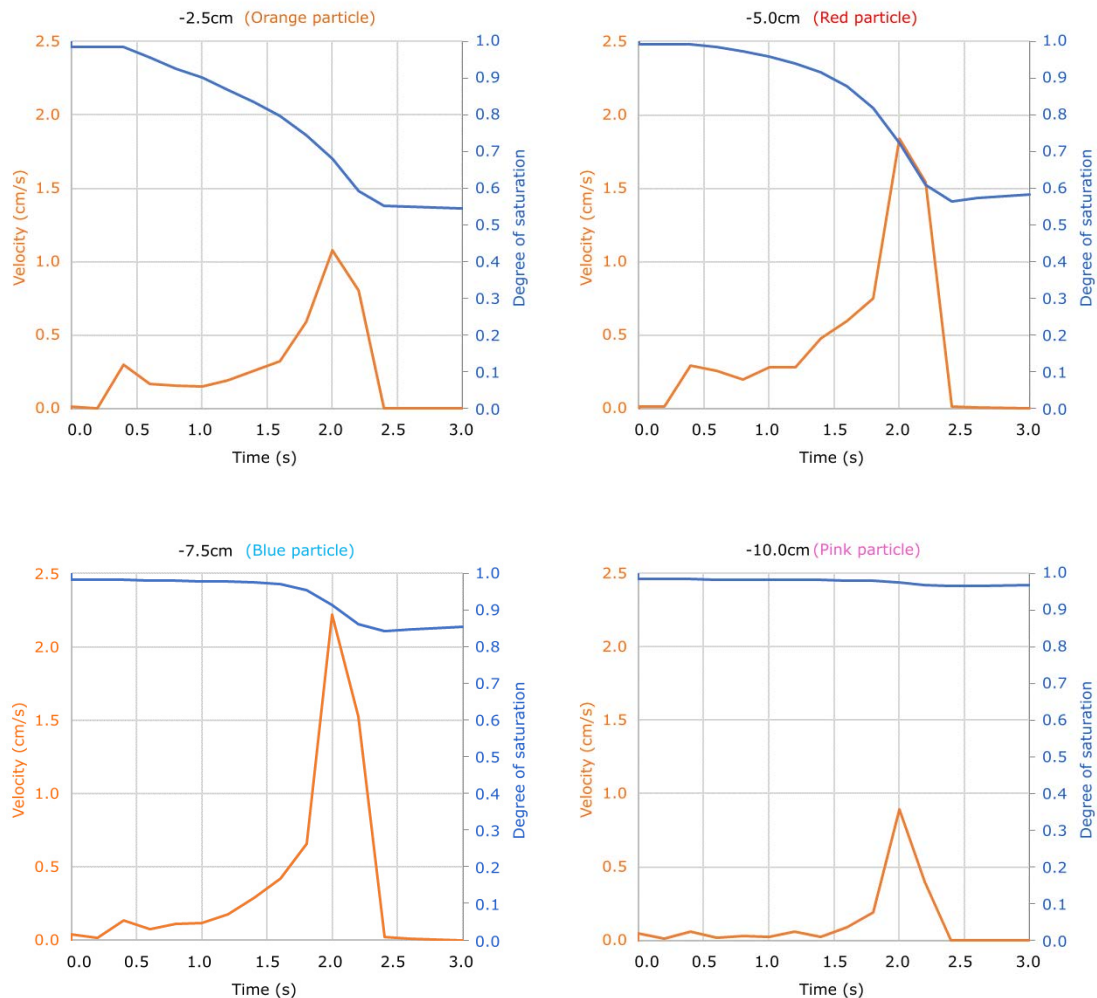


Figure 139 Evolution of the velocity and degree of saturation in the particles at -2.5, -5.0, -7.5, and -10.0 cm.

The punching failure affects mainly the particles on the upper part of the soil. The peak on the velocity at 0.4s it can be observed on the particles at -2.5 and -5.0 cm; while it is almost absent on the lower part of the soil. After the punching failure, the velocity of deformation restrains to 0.1 cm/s. The velocity starts to increase gradually as the degree of saturation reduces. This acceleration reaches its maximum at the 2.0s; then the general failure is able to mobilize the soil on the full failure mechanism. On that point, the general failure mobilizes part of the soil that the air has not penetrated yet. The degree of saturation on the particle at -7.5 cm decreases practically when the general failure occurs. At -10 cm, the soil is mobilized despite the air do not penetrate that deep.

Figure 140 plots the velocity of the particles depending on its degree of saturation during the interval of time from 0.8 to 2.0s. These graphs are created for better visualization of the relation between these two variables during the acceleration of general failure. The particles chosen for the graphs are the superior particles, where the relation is more prominent.

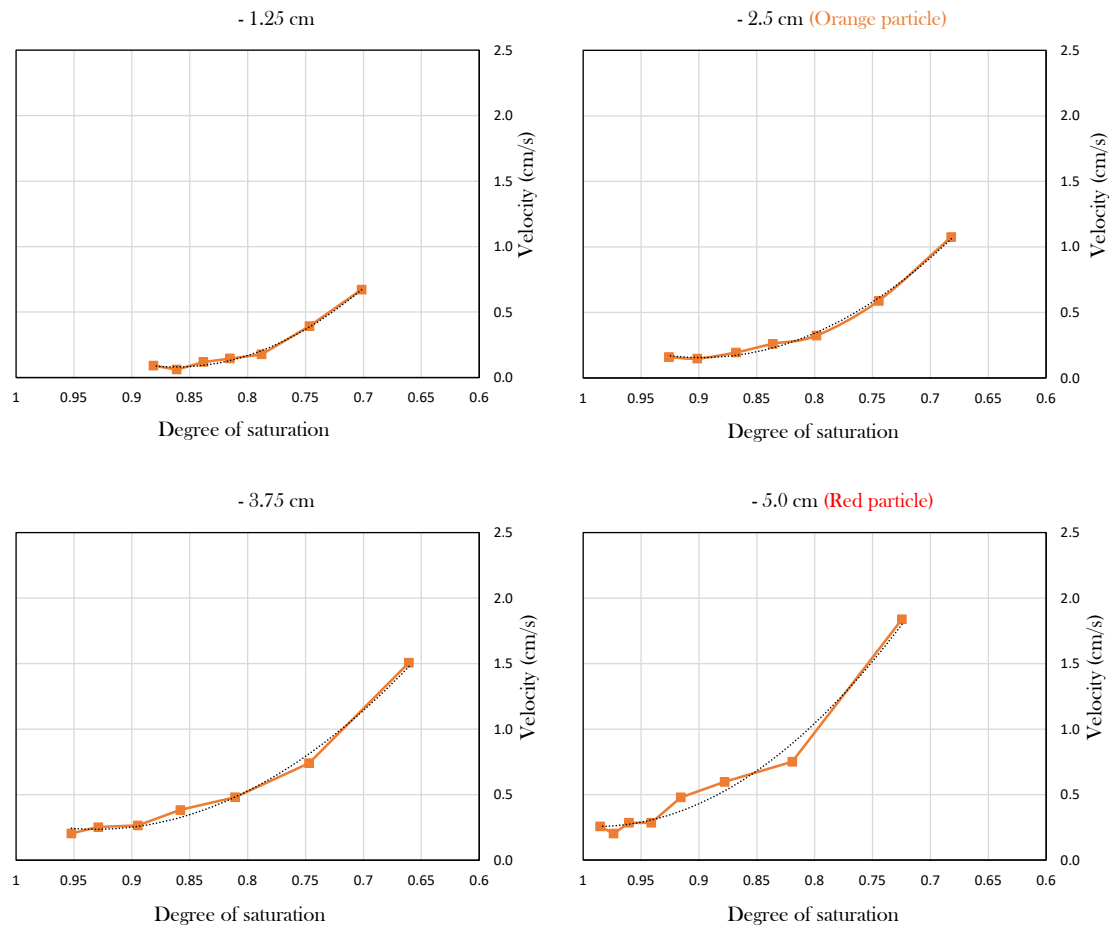


Figure 140 Velocity depending on the degree of saturation of the particles at -1.25, -2.5, -3.75, and -5.0 cm.

The graphs uncover a relationship between the degree of saturation and the velocity, which agrees with the hypothesis suggested in the 2D analysis. The velocity increases as the degree of saturation decreases following a polynomial equation of second degree in all the particles (Equations 22). The coefficient of correlation (R) in all the cases is over 0.99.

Equations 22

$$v_{-1.25} = 23,045 Sr_{-1.25}^2 - 39,714 Sr_{-1.25} + 17,191$$

$$v_{-2.50} = 19,442 Sr_{-2.5}^2 - 34,912 Sr_{-2.50} + 15,829$$

$$v_{-3.75} = 16,988 Sr_{-3.75}^2 - 31,635 Sr_{-3.75} + 14,964$$

$$v_{-5.00} = 22,153 Sr_{-5.00}^2 - 43,797 Sr_{-5.00} + 21,903$$

Following the previous conclusive explanation, the reason behind the quadratic relationship between the degree of saturation and the velocity of deformation is the air facility to expand. The air that penetrates is not just filling the extra pore volume required at this moment, it will expand to fulfill the extra pore volume to continue with the failure. Therefore, more air in the pores implies fewer restrictions to the increase of volumetric strain necessary for the relative displacement between the grains.

Post-failure behavior

The post-failure behavior of oil is analyzed in Figure 141. The graph plots the degree of saturation of the blue particle (-7.5cm) and the pressure measured by the PPT sensor outside the mobilized zone (-14 cm). The time is extended but takes the same reference instant used for all the analysis. The time comprises from -1.0s until 6.0s, the two failure peaks defined in Figure 138 are marked as a reference.

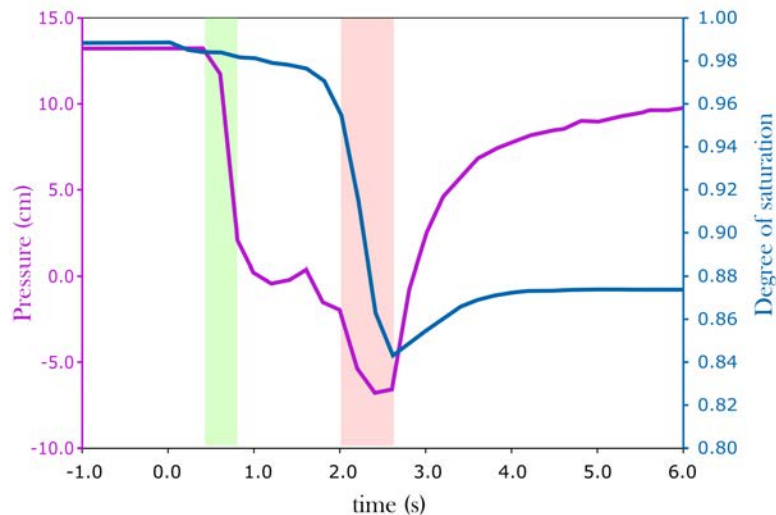


Figure 141 Evolution the degree of saturation in the particle at -7.5 cm and the pressure measured by the PPT at -14 cm. The two peaks of failure are marked: punching failure (green) and general failure (red).

After the general failure, the oil flows to achieve a new stable state. The oil from areas unaffected by the failure flows to the mobilized area and its surroundings. It can be observed on the degree of saturation in the particle at -7.5cm, that increases from 0.84 to 0.88 after the big failure (2.6 -4.0 s). The pressure measured by the ppt (placed at -14cm) recovers from the negative pressure to a head pressure of 10cm.

The degree of saturation and pressures on the affected area are lower than the initial values because part of the air gets trapped between the soil grains.

8.5 The effect of the phreatic level on the bearing capacity.

The summary of the three cases analyzed in the previous section (Table 14 and Figure 142) bring up to the forefront the effect of the oil level on the behavior of the soil with a surface load.

Focusing on the bearing capacity of the soil, a large difference is observed in the maximum load reached in the saturated case compared to the other two cases.

Table 14 Summary of the three representative cases: dry, saturated, and submerged.

| | Dry | Saturated | Submerged |
|-----------------------|--------|-----------|-----------|
| Duration of the event | 0.02s | 2.4s | 2.5s |
| Maximum load | 150 kg | 400 kg | 110 kg |
| Maximum velocity | 20 m/s | 0.02 m/s | 0.016 m/s |

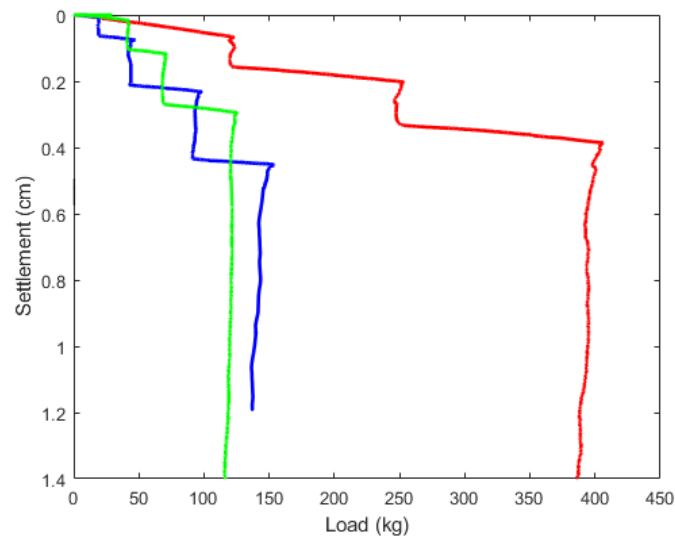


Figure 142 The Load vs. settlement graph of the three cases: dry (blue), saturated (red), and submerged (green).

The effect of the oil level on the bearing capacity is evaluated, analyzing the same shallow foundation experiment varying the oil level distance respect to the soil surface. The experiments are performed to cover the full transition from dry to submerged (Figure 143). Experiments with similar oil levels are also performed to evaluate the variation of the results.

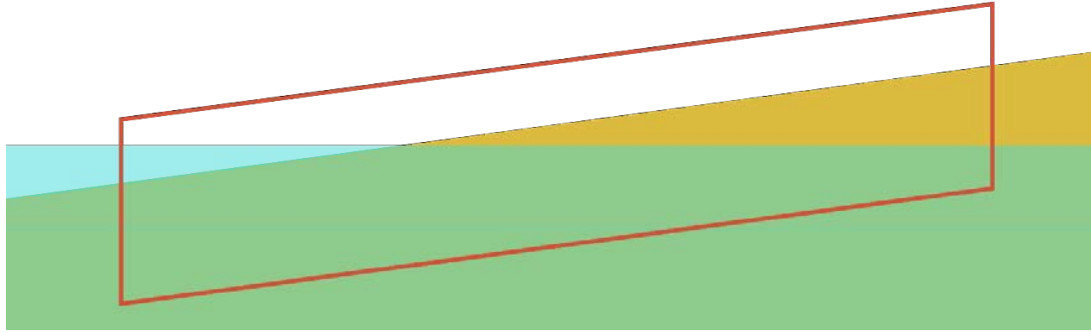


Figure 143 The points analyzed in this part cover the whole transition from submerged to dry.

8.5.1 Difficulties on the comparison of the shallow foundation experiments

Observing the results of all the experiments of shallow foundation conducted on the coarse sand, it is clear that the distance between the soil surface and the oil level plays an important role on the bearing capacity of the soil (Figure 144). However, the analysis of the bearing capacity in shallow foundation test implies a variability on the results (Ingra and Baecher, 1983; Das, 2017). This noise on the results complicates the definition of a pattern on the effect of the phreatic level.

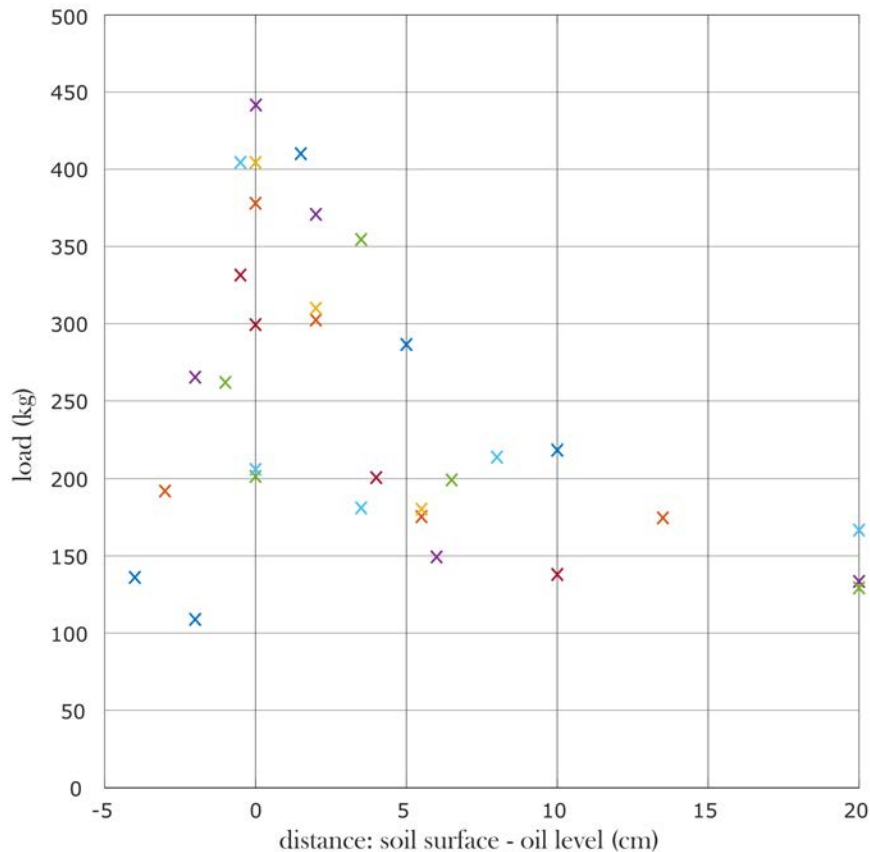


Figure 144 Last failure load of all the experiments performed with coarse sand.

8.5.2 Effect of the inclination and eccentricity

The effect of the inclination and eccentricity on the bearing capacity in shallow foundation tests is described in the literature (Meyerhof and Hanna, 1978; Loukidis, Chakraborty and Salgado, 2008; Ganesh, Khuntia and Sahoo, 2017). The general failure that occurs in this shallow foundation test tends to tilt the footing, which implies an unsymmetrical failure and a reduction on the ultimate bearing capacity.

During the footing placement on the soil surface and the piston placement on the footing some imperceptible misplacements might occur:

- Inclination: The footing might not be perfectly horizontal and have a small degree of inclination.
- Eccentricity: The load might not be applied in the exact center of the footing.

Generally, in the experiments, there are small failures before the ultimate failure. These small failures tend to increment inclination of the footing and the deviation of the load application point. For that reason, the inclination and deviation of the footing right before the ultimate failure are measured to discard the cases where the inclination or/and deviation were too high.

The bearing capacity equations defined by Terzaghi (Terzaghi, 1943), were modified to include the effect of inclination and eccentricity (Ingra and Baecher, 1983).

Equation 23 is the Terzaghi ultimate bearing capacity equation simplified for a shallow foundation in cohesionless soil, with the two correction factors of eccentricity (E_γ) and inclination (I_γ). The key parameters of each correction factor are presented in Equation 24 and Equation 25 using the reference measures from Figure 145.

Equation 23

$$q_\gamma = \frac{1}{2} \gamma B N_\gamma E_\gamma I_\gamma$$

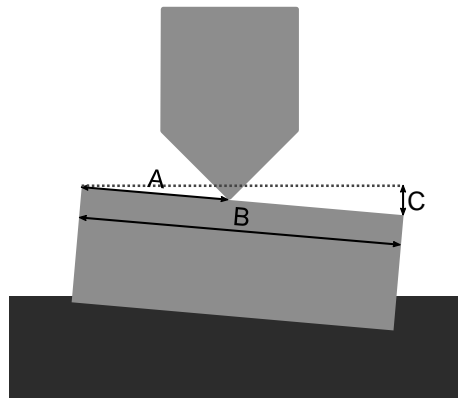


Figure 145 Measures to determine the parameters of deviation and inclination before the ultimate failure.

Equation 24

$$Eccentricity = \left| \frac{A - (B/2)}{B} \right|$$

Equation 25

$$Inclination = \frac{C}{B}$$

The two parameters presented in Equation 24 and Equation 25 are used to define the tolerance in eccentricity and inclination. The values of eccentricity and inclination of all the shallow foundation test performed are calculated.

Figure 146 plots the eccentricity value of each test respect to the distance between the soil surface and the oil surface. Each experiment is represented by a circle. The tolerance for the eccentricity is set at 0.03, and it is marked by the green area. The test which the eccentricity of the load application respect to the center is higher than 0.003 (outside the green area) are not considered for the analysis of the phreatic level effect.

Figure 147 plots the inclination value of each test respect to the distance between the soil surface and oil surface. Each experiment is represented by a triangle. The tolerance for the inclination is set at 0.04, and it is marked by the green area. The test which the inclination of the footing respect to the horizontal is higher than 0.04 (outside the green area) are not considered for the analysis of the phreatic level effect.

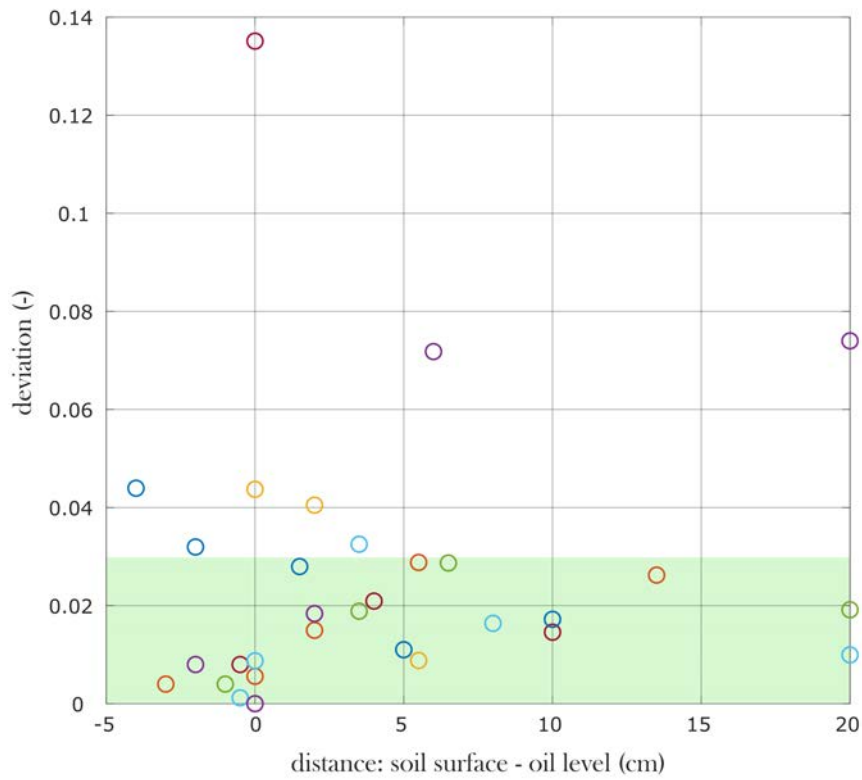


Figure 146 The eccentricity of the footing on the shallow foundation test. The limit of tolerance was set at 0.03 of deviation.

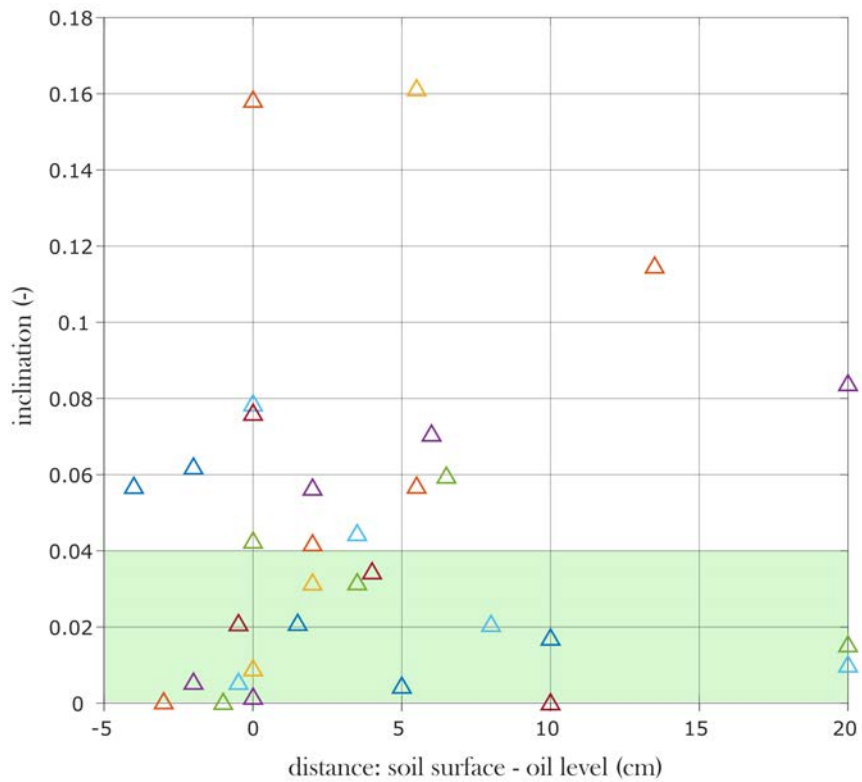


Figure 147 Inclination of the footing on the shallow foundation test. The limit of tolerance was set at 0.04 of inclination.

Figure 148 plots the ultimate bearing capacity versus the distance between the soil surface and the oil level of the test that its inclination and eccentricity are under the tolerance. The graph shows a peak on ultimate bearing capacity when the oil level is at the soil surface, which is the saturated case analyzed in Section 8.4.3.

On the submerged side of the peak, the bearing capacity decreases abruptly. The transition between the saturated case (0 cm) and the full submerged case (-3 cm) include the cases where the layer of oil is thin and insufficient to fulfill the volumetric strain, so the air needs to penetrate into the soil creating an extra bearing capacity.

On the drier side of the peak, the bearing capacity decreases inversely with the distance between the soil surface and the oil level. On this transition, the size of the potential mobilized area that would be below the oil level reduces as the oil level is more distant to the soil surface. Therefore, the volume of air that needs to penetrate to fill the volumetric strain reduces with the distance, and so the bearing capacity. Until the oil level is far enough from the soil surface that the full mobilized area is dry, from that point, the bearing capacity is independent of the oil level.

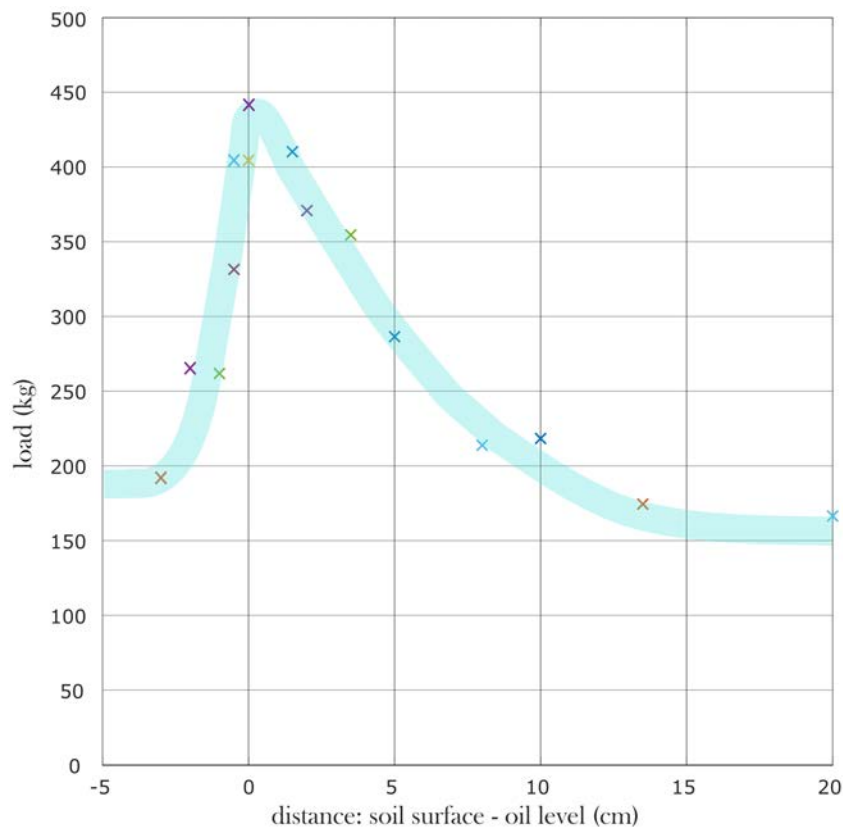


Figure 148 Relation between load and phreatic level using the data from the experiments with inclination and deviation under the tolerance.

8.6 Conclusions

The methodology exposed in Chapter 7 is applied using the technique to measure the degree of saturation in transparent soils developed in the Royal Military College of Canada and the Queen's University. The technique is based on the mirror effect explained in Chapter 2.

The methodology was applied to study the dry footprints: dry circles that appear around the foot when it steps on the saturated sand close to the seashore. The dry footprints effect is caused by the dilatancy of the sand. The footprint was assimilated to a shallow foundation on a bearing capacity failure. Multiple experiments were performed varying the oil level respect to the soil surface.

Three archetypal situations were studied in deep: dry, submerged, and saturated cases. The conclusions extracted from them are:

- In all cases, there are small failures before the ultimate failure. The load required for the ultimate failure in dry and submerged cases is similar. The load required in the saturated case is three times higher.
- There is a positive volumetric strain in the mobilized area of the soil (dilatancy). In the dry case, the soil dilatates freely, because the inter pore air can expand. In the submerged case the oil cannot expand, so the oil from the surrounding areas flows to fill the extra pore volume required to dilate.
- In the saturated case the soil cannot dilate (not enough surrounding oil to fill the extra pore volume), requires the air from the surface to penetrate into the saturated soil to fill the extra pore volume required to dilate. The surface tension of the oil creates a resistance to air penetration that causes of the higher load required to fail.

The methodology feature to correlate different variables enables to deduce an explanation: There is a quadratic relationship between the velocity of failure and the degree of saturation. This correlation describes the evolution of the small deformation and the air penetration required to occur. The air ability to expand causes the acceleration of the failure mechanism.

The results of all analyzed cases were used to find the relation between the maximum load before the ultimate failure and the oil level distance to the soil surface.

9

Chapter 9

Conclusions and future work

The aim of this Chapter is to present the main conclusions of the research. The conclusions respond to the general and specific objectives exposed in Chapter 1. Finally, some future research lines to continue the investigations of this Thesis are suggested.

9.1 Final conclusions and contributions

This Thesis presents an image analysis methodology specially focused on the analysis of the soil experiments and suitable for large displacements. The methodology comprises primary two different techniques: the PIV-NP for displacement and movement-related variables and the analysis of SWIR images for the degree of saturation measurement.

The PIV-NP is a powerful post-process that combines the advantages of the Eulerian image correlation with the advantages of the Lagrangian arrangement of the results. The Eulerian advantages are based on the PIV-NP input data. The input data are the results of an image correlation method with a eulerian scheme (such as Particle Image Velocimetry). That type of image correlation method analyses each pair of images independently, which gives total freedom to modify and correct the errors that might occur. The lagrangian advantages are based on the PIV-NP data transformation. The Eulerian independent results are converted into a Lagrangian scheme which accumulates the evolution of the results in numerical particles that move attached to the soil. This scheme is more appropriated for the analysis of the historical dependent soil behavior.

The transformation from Eulerian to Lagrangian scheme enables to calculate new variables: velocity, acceleration, and strains. Moreover, the accumulation of the results in numerical particles enables to calculate historical dependent variables: accumulated displacements and strains.

The set of tests used to validate the PIV-NP was useful to detect and correct some problems of the post-process. The actual state of the PIV-NP is robust and flexible to be used to analyze different type of experiments and especially suitable for large displacement analysis. However, the limitations of the post-process, mainly regarded to the quality of the input data, are also pointed to be considered.

The technique to measure the degree of saturation using SWIR images is a powerful tool to be used in laboratory experiments with natural soils. It is non-invasive technique to obtain massive data of the degree of saturation evolution and distribution of the soil surface. The selected range of wavelength of the light spectrum (1400 -1550 nm) is especially sensitive to the changes on the degree of saturation. A calibration analysis performed in two soil samples, varying their degree of saturation was used to obtain the calibration curve. The calibration was completed performing an analysis in soil samples with fixed water content and varying the density, the analysis concludes that the measured variable is the degree of saturation and not the water content. The technique was applied to a real case of rainfall on a soil column. The measures were compared with data got by means of conventional moisture sensors and with the results of a numerical model. The agreement between the results indicates proper accuracy of the measures.

This technique is ideal for validating models because the result comparison can be performed throughout all the surface. The analysis of the spatial distribution is also interesting to evaluate heterogeneities and preference flow direction in unsaturated soils. The technique can be used in any laboratory following the specified steps: calibration using a set of soil sample images at different degree of saturation, normalization using dry and saturated images of the soil in the experiment, and assessment using the algorithm procedure described. It is a relatively affordable technique due to the use of a modified CDD camera with a phosphor-coated treatment and does not require modifications on the apparatus were the experiments are performed.

Both techniques were integrated into a single methodology to combine image analysis results. The methodology, that uses the framework of the PIV-NP, stores all the results in the numerical particles that represent a portion of the soil surface. The integration of both techniques was applied to a simple case of a column collapse caused by changes in the degree of saturation. It was proved useful for a combined analysis of the different variables.

The methodology also was used combining the PIV-NP with measurements of the degree of saturation in transparent soils, a technique developed in Canada (Royal Military College of Canada and Queen's University). The integrated analysis of the image analysis results was useful to understand the soil behavior that originates the dry footprints effect when walking close to the seashore. A correlation between the air penetration into the soil and the velocity of failure was possible to be uncovered thanks to the coupled analysis of both variables measured.

The integrated methodology also presents a useful variety of options to display the results. The results accumulated in the set of numerical particles can be read and plotted at different dimensions: surface (2D), line (1D), or particle (0D). Each dimension provides a different point of view of the behavior and is useful for different purposes. Bidimensional contour plot (2D) enables to observe the spatial tendencies (such as flow directions or displacement accumulation), but also the inherent heterogeneity of real cases, which is challenging to consider in numerical models. Linear graph display (1D) enables to observe the correlation between the evolution of different variables in a line of particles. This type of graphs permits to get an idea of the general evolution of a variable in the direction that better represents the experiment. One particle evolution graph (0D) is useful for quantitative analysis of the variables in the points of interest. This type of graphs enables the detailed correlation between variables, which facilitate to uncover possible cause-effect relation.

It can be finally concluded that the image analysis methodology presented, formed by the techniques developed, would be a useful tool to enhance the volume and quality of the information extracted from the soil experiments. The methodology is ready to be exported to other laboratories, and its flexibility would make it useful for diverse purposes. The methodology might serve as a base to extend the knowledge generated from the experimental laboratory branch.

9.2 Future work

The main objective in the short term is to validate the developed techniques and methodology to other materials and evaluate their range of application.

The PIV-NP technique has already been proven robust. However, some of the post-process weaknesses (expressed in Section 5.2) could be improved in future versions of the code. The underestimation of the displacement of external particles in the limit between the moving soil and the static background. The noise in the volumetric strain originated in the intrinsic input data noise.

The technique of measuring the degree of saturation by SWIR images was validated in safety conditions, where its performance was not evaluated to its limit. Therefore, to detect and quantify its limitations in general cases, the technique requires a more extensive set of real cases tests. Complex cases, as landslides with large total displacement, are on the list of validation test. This Thesis work was performed using an affordable adaptation of a visual camera to record SWIR images; it would be optimal to use an InGaAs camera which would reduce the noise problems and increase the accuracy.

On the medium term, the integration of the other image analysis techniques into the methodology developed would be useful. For instance, the use of thermal infrared images to measure the temperature and assess the thermal diffusivity (Kodikara, Rajeev and Rhoden, 2011) or the use of polarized light and photoelastic plastics to measure and observe the stress paths in granular materials (Daniels, Kollmer and Puckett, 2017) could be interesting to enhance the opportunities of variable correlation.

On the long term, it would be appealing the export to the methodology to combine the results of image analysis to other fields of science. An application where the analyzed surfaces suffer displacements or deformations combined with other changes on their properties. The methodology might be useful for remote sensing using satellite images, the material testing or even the microbiology.

Bibliography

- Adrian, R. J. (1991) Particle-Imaging Techniques for Experimental Fluid Mechanics, *Annual Review of Fluid Mechanics*. Annual Reviews 4139 El Camino Way, P.O. Box 10139, Palo Alto, CA 94303-0139, USA , 23(1), pp. 261–304.
- Ahlborn, F. (1896) Über die Bedeutung der Heterozerkie und ähnlicher unsymmetrischer Schwanzformen schwimmender Wirbeltiere für die Ortsbewegung, *Z. wiss. Zool*, 61(1).
- Aloisio, G. and Di Felice, F. (2006) PIV analysis around the Bilge Keel of a Ship Model in Free Roll Decay, in *XIV Convegno Nazionale A.I.V.E.L.A.* Rome, Italy.
- Alonso, E. E., Pinyol, N. M. and Yerro, A. (2014) Mathematical Modelling of Slopes, *Procedia Earth and Planetary Science*. Elsevier, 9, pp. 64–73.
- Alvarado Bueno, M. (2018) *Landslide motion assessment including thermal interaction : an MPM approach*. Universitat Politècnica de Catalunya.
- Amarasinghe, R. S. (2013) *Macro-scale direct shear device for studying the large displacement shear strength of soil-structure interfaces under very low effective stresses*. University of British Columbia.
- Azad, K. (2017) *Colorized Math Equations - Better Explained*.
- Baker, R. S. and Hillel, D. (1990) Laboratory Tests of a Theory of Fingering during Infiltration into Layered Soils, *Soil Science Society of America Journal*. Soil Science Society of America, 54(1), p. 20.
- Banzi, M. and Shiloh, M. (2014) *Getting started with Arduino: the open source electronics prototyping platform*. Maker Media, Inc.
- Barragán, H. (2004) *Wiring: Prototyping physical interaction design*. Interaction Design Institute of Ivrea, Italy.
- De Beer, E. E. (1963) The Scale Effect in the Transposition of the Results of Deep-sounding Tests on the Ultimate Bearing Capacity of Piles and Caisson Foundations, *Géotechnique*, 13(1), pp. 39–75.
- Berger, C. *et al.* (2010) Rill development and soil erosion: a laboratory study of slope and rainfall intensity, *Earth Surface Processes and Landforms*. John Wiley & Sons, Ltd, 35(12), pp. 1456–1467.
- Blaber, J., Adair, B. and Antoniou, A. (2015) Ncorr: Open-Source 2D Digital Image Correlation Matlab Software, *Experimental Mechanics*. Springer US, 55(6), pp. 1105–

- 1122.
- Bohr, N., Kramers, H. A. and Slater, J. C. (1924) The quantum theory of radiation, *The London, Edinburgh, and Dublin Philosophical Magazine and Journal of Science*. Taylor & Francis Group, 47(281), pp. 785–802.
- Bolton, M. D. (1986) The strength and dilatancy of sands, *Géotechnique*. Thomas Telford Ltd, 36(1), pp. 65–78.
- Chakraborty, T. and Salgado, R. (2010) Dilatancy and Shear Strength of Sand at Low Confining Pressures, *Journal of Geotechnical and Geoenvironmental Engineering*, 136(3), pp. 527–532.
- Cheng, C. L. *et al.* (2012) Average Soil Water Retention Curves Measured by Neutron Radiography, *Soil Science Society of America Journal*. The Soil Science Society of America, Inc., 76(4), p. 1184.
- Christensen, K. and Adrian, R. (2002) Measurement of instantaneous Eulerian acceleration fields by particle image accelerometry: method and accuracy, *Experiments in Fluids*. Springer-Verlag, 33(6), pp. 759–769.
- Cleland, C. E. (2001) Historical science, experimental science, and the scientific method, *Geology*. GeoScienceWorld, 29(11), p. 987.
- Daniels, K. E., Kollmer, J. E. and Puckett, J. G. (2017) Photoelastic force measurements in granular materials, *Review of Scientific Instruments*. AIP Publishing LLC , 88(5), p. 051808.
- Das, B. M. (2017) *Shallow Foundations*. Third edition. | Boca Raton : CRC Press, 2017.: CRC Press.
- Descartes, R. (1637) *Discours de la méthode*. Edited by E. Gilson. Librairie J. Vrin.
- DFRobot (2018) *Temperature and humidity sensors.*, *DFRobot Shanghai*.
- Dimitrova, T. L. and Weis, A. (2008) The wave-particle duality of light: A demonstration experiment, *American Journal of Physics*. American Association of Physics Teachers, 76(2), pp. 137–142.
- Dirac, P. A. M. (1927) The Quantum Theory of the Emission and Absorption of Radiation, *Proceedings of the Royal Society A: Mathematical, Physical and Engineering Sciences*. The Royal Society London, 114(767), pp. 243–265.
- Einstein, A. (1905) Concerning an heuristic point of view toward the emission and transformation of light, *Annalen Phys.*, 17, pp. 132–148.
- Elkateb, T., Chalaturnyk, R. and Robertson, P. K. (2003) An overview of soil heterogeneity: quantification and implications on geotechnical field problems, *Canadian*

- Geotechnical Journal*. NRC Research Press Ottawa, Canada , 40(1), pp. 1-15.
- Ezzein, F. M. and Bathurst, R. J. (2011) A Transparent Sand for Geotechnical Laboratory Modeling, *Geotechnical Testing Journal*. ASTM International, 34(6), p. 103808.
- Flammer, J. (Josef), Mozaffarieh, M. and Bebie, H. (2013) *Basic sciences in ophthalmology : physics and chemistry*. Springer.
- Fresnel, A. (1818) *Memoir on the Diffraction of Light, The Wave Theory of Light: Memoirs by Huygens, Young and Fresnel*. Woodstock, GA: American Book Company.
- Ganesh, R., Khuntia, S. and Sahoo, J. P. (2017) Bearing Capacity of Shallow Strip Foundations in Sand under Eccentric and Oblique Loads, *International Journal of Geomechanics*, 17(4), p. 06016028.
- Garnier, J. *et al.* (2007) Catalogue of scaling laws and similitude questions in geotechnical centrifuge modelling.
- Geng, J. *et al.* (2001) Footprints in Sand: The Response of a Granular Material to Local Perturbations, *Physical Review Letters*. American Physical Society, 87(3), p. 035506.
- van Genuchten, M. T. (1980) A Closed-form Equation for Predicting the Hydraulic Conductivity of Unsaturated Soils¹, *Soil Science Society of America Journal*, 44(5), p. 892.
- van Genuchten, M. T. and Parker, J. C. (1984) Boundary Conditions for Displacement Experiments through Short Laboratory Soil Columns¹, *Soil Science Society of America Journal*. Soil Science Society of America, 48(4), p. 703.
- Germaine, J. T. and Germaine, A. V. (2009) *Geotechnical laboratory measurements for engineers*. John Wiley & Sons.
- Gui, L. and Merzkirch, W. (2000) A comparative study of the MQD method and several correlation-based PIV evaluation algorithms, *Experiments in Fluids*. Springer-Verlag, 28(1), pp. 36-44.
- Hertz, H. (1888) On the finite velocity of propagation of electromagnetic actions, *Electric Waves*, 34, p. 551.
- Hillel, D. (1998) *Environmental soil physics*. San Diego, CA: Elsevier.
- Hinsch, K. D. (1995) Three-dimensional particle velocimetry, *Measurement Science and Technology*. IOP Publishing, 6(6), pp. 742-753.
- Huygens, C. (1678) *Treatise on Light*.
- Ingra, T. S. and Baecher, G. B. (1983) Uncertainty in Bearing Capacity of Sands, *Journal of Geotechnical Engineering*, 109(7), pp. 899-914.

- Kähler, C. J., Scharnowski, S. and Cierpka, C. (2012) On the resolution limit of digital particle image velocimetry, *Experiments in Fluids*. Springer-Verlag, 52(6), pp. 1629–1639.
- Kang, M. *et al.* (2014) Multiple pixel-scale soil water retention curves quantified by neutron radiography, *Advances in Water Resources*. Elsevier, 65, pp. 1–8.
- Kerle, N. (2013) Electromagnetic Radiation (EMR), in. Springer, Dordrecht, pp. 250–250.
- Kim, F. H., Penumadu, D. and Hussey, D. S. (2012) Water Distribution Variation in Partially Saturated Granular Materials Using Neutron Imaging, *Journal of Geotechnical and Geoenvironmental Engineering*, 138(2), pp. 147–154.
- Knadel, M. (2012) The Effects of Moisture Conditions—From Wet to Hyper dry—On Visible Near-Infrared Spectra of Danish Reference Soils, *Soil Science Society of America Journal*, 78.2, pp. 422–433.
- Knadel, M. *et al.* (2014) The Effects of Moisture Conditions—From Wet to Hyper dry—On Visible Near-Infrared Spectra of Danish Reference Soils, *Soil Science Society of America Journal*. The Soil Science Society of America, Inc., 78(2), p. 422.
- Kodikara, J., Rajeev, P. and Rhoden, N. J. (2011) Determination of thermal diffusivity of soil using infrared thermal imaging, *Canadian Geotechnical Journal*. NRC Research Press , 48(8), pp. 1295–1302.
- Lauterborn, W. and Vogel, A. (1984) Modern Optical Techniques in Fluid Mechanics, *Annual Review of Fluid Mechanics*. Annual Reviews 4139 El Camino Way, P.O. Box 10139, Palo Alto, CA 94303-0139, USA , 16(1), pp. 223–244.
- Leu, D. J. (1977) Visible and near – infrared reflectance of beach sands: A study on the spectral reflectance/ grain size relationship, *Remote Sensing of Environment*. Elsevier, 6(3), pp. 169–182.
- Likos, W. J. *et al.* (2010) Modified direct shear apparatus for unsaturated sands at low suction and stress, *Geotechnical Testing Journal*, 33(4).
- Lings, M. L. and Dietz, M. S. (2004) An improved direct shear apparatus for sand, *Géotechnique*. Thomas Telford Ltd, 54(4), pp. 245–256.
- Lobell, David B and Asner, G. P. (2002) Moisture Effects on Soil Reflectance, *Soil Science Society of America Journal*, 66(3), pp. 722–727.
- Lobell, David B. and Asner, G. P. (2002) Moisture Effects on Soil Reflectance, *Soil Science Society of America Journal*. Soil Science Society, 66(3), p. 722.
- Loukidis, D., Chakraborty, T. and Salgado, R. (2008) Bearing capacity of strip footings on purely frictional soil under eccentric and inclined loads, *Canadian Geotechnical*

- Journal*, 45(6), pp. 768-787.
- Marey, E.-J. (1874) *Animal mechanism: a treatise on terrestrial and aërial locomotion.*, *Animal mechanism: a treatise on terrestrial and aërial locomotion*. London: Henry S. King and Company.
- Matheson, G. D. (1989) The collection and use of field discontinuity data in rock slope design, *Quarterly Journal of Engineering Geology and Hydrogeology*. Geological Society of London, 22(1), pp. 19-30.
- Maxwell, J. C. (1868) XXVI. On a method of making a direct comparison of electrostatic with electro-magnetic force; with a note on the electromagnetic theory of light, *Philosophical Transactions of the Royal Society of London*. The Royal Society London, 158, pp. 643-657.
- Meyerhof, G. G. and Hanna, A. M. (1978) Ultimate bearing capacity of foundations on layered soils under inclined load, *Canadian Geotechnical Journal*. NRC Research Press Ottawa, Canada, 15(4), pp. 565-572.
- Meynart, R. (1983) Instantaneous velocity field measurements in unsteady gas flow by speckle velocimetry, *Applied optics*, 22(4), pp. 535-540.
- Moriwaki, H. *et al.* (2004) Failure processes in a full-scale landslide experiment using a rainfall simulator, *Landslides*. Springer-Verlag, 1(4), pp. 277-288.
- Morrow, C. A. and Byerlee, J. D. (1989) Experimental studies of compaction and dilatancy during frictional sliding on faults containing gouge, *Journal of Structural Geology*. Pergamon, 11(7), pp. 815-825.
- Murray, C. A., Take, W. A. and Hout, N. A. (2015) Measurement of vertical and longitudinal rail displacements using digital image correlation, *Canadian Geotechnical Journal*. NRC Research Press, 52(2), pp. 141-155.
- Newton, I. (1730) *Opticks: A Treatise of the Reflections, Refractions, Inflections and Colours of Light*. Dover Publications.
- Nolet, C. *et al.* (2014) Measuring and Modeling the Effect of Surface Moisture on the Spectral Reflectance of Coastal Beach Sand, *PLoS ONE*. Edited by V. Magar. Public Library of Science, 9(11), p. e112151.
- Ochiai, H., Sammori, T. and Okada, Y. (2007) Landslide Experiments on Artificial and Natural Slopes, in *Progress in Landslide Science*. Berlin, Heidelberg: Springer Berlin Heidelberg, pp. 209-226.
- Olivares, L. *et al.* (2009) An Instrumented Flume to Investigate the Mechanics of Rainfall-Induced Landslides in Unsaturated Granular Soils, *Geotechnical Testing Journal*.

- ASTM International, 32(2), p. 101366.
- Olivella, S. *et al.* (1996) Numerical formulation for a simulator (CODE_BRIGHT) for the coupled analysis of saline media, *Engineering Computations*. MCB UP Ltd, 13(7), pp. 87-112.
- Pan, B. *et al.* (2009) Two-dimensional digital image correlation for in-plane displacement and strain measurement: a review, *Measurement Science and Technology*. IOP Publishing, 20(6), p. 062001.
- Peters, S. B., Siemens, G. and Take, W. A. (2011) Characterization of Transparent Soil for Unsaturated Applications, *Geotechnical Testing Journal*. ASTM International, 34(5), p. 103580.
- Peters, S. B., Siemens, G. and Take, W. A. (2017) Characterization of Transparent Soil for Unsaturated Applications, 34(5), pp. 1-12.
- Peters, W. H. and Ranson, W. F. (1982) Digital Imaging Techniques In Experimental Stress Analysis, *Optical Engineering*. International Society for Optics and Photonics, 21(3), p. 213427.
- Pinyol, N. M. *et al.* (2018) Thermal effects in landslide mobility, *Géotechnique*. Thomas Telford, 68(6), pp. 528-545.
- Planck, M. (1914) *The theory of heat radiation*. Dover Publications.
- Pradhan, T. B. S., Tatsuoka, F. and Sato, Y. (2011) Experimental stress-dilatancy relations of sand subjected to cyclic loading., *Soils and foundations*. The Japanese Geotechnical Society, 29(1), pp. 45-64.
- Prandtl, L. (1953) *Essentials of fluid dynamics : with applications to hydraulics, aeronautics, meteorology and other subjects*. London: Blackie and Son.
- Purwana, Y. M. *et al.* (2012) Experimental Studies of Suction-Monitored Direct Shear Apparatus on Perth Poorly Graded Sand, in *Proceedings of the International Conference on Advances in Geotechnical Engineering*. Perth: Curtin University, Department of Civil Engineering, p. 1114.
- Raffel, M. *et al.* (2018) *Particle image velocimetry : a practical guide*.
- Rechenmacher, A. L. and Finno, R. J. (2004) Digital Image Correlation to Evaluate Shear Banding in Dilative Sands, *Geotechnical Testing Journal*. ASTM International, 27(1), pp. 13-22.
- Reynolds, O. (1885) On the dilatancy of media composed of rigid particles in contact. With experimental illustrations., *The London, Edinburgh, and Dublin Philosophical Magazine and Journal of Science*. Taylor & Francis Group, 20(127), pp. 469-481.

- Riffle, S. (2011) *#AltDevBlogADay*.
- Sadeghi, M., Jones, Scott B. and Philpot, W. D. (2015) A linear physically-based model for remote sensing of soil moisture using short wave infrared bands, *Remote Sensing of Environment*. Elsevier, 164, pp. 66-76.
- Sadeghi, M., Jones, Scott B and Philpot, W. D. (2015) Remote Sensing of Environment A linear physically-based model for remote sensing of soil moisture using short wave infrared bands, *Remote Sensing of Environment*. Elsevier Inc., 164, pp. 66-76.
- Sadek, S., Iskander, M. G. and Liu, J. (2003) Accuracy of Digital Image Correlation for Measuring Deformations in Transparent Media, *Journal of Computing in Civil Engineering*, 17(2), pp. 88-96.
- Shuchman, R. A. and Rea, D. K. (1981) Determination of beach sand parameters using remotely sensed aircraft reflectance data, *Remote Sensing of Environment*. Elsevier, 11, pp. 295-310.
- Siemens, G. A., Peters, S. B. and Take, W. A. (2013) Comparison of confined and unconfined infiltration in transparent porous media, 49(February 2012), pp. 851-863.
- Siemens, G. A., Take, W. A. and Peters, S. B. (2014) Physical and numerical modeling of infiltration including consideration of the pore-air phase 1, 1487(October), pp. 1475-1487.
- Sills, L.-A. K., Mumford, K. G. and Siemens, G. A. (2017) Quantification of Fluid Saturations in Transparent Porous Media, *Vadose Zone Journal*. GeoScienceWorld, 16(2), p. 0.
- Snell, W. (1621) *Cyclometricus*.
- Soranzo, E., Tamagnini, R. and Wu, W. (2015) Face stability of shallow tunnels in partially saturated soil: centrifuge testing and numerical analysis, *Géotechnique*. Thomas Telford Ltd, 65(6), pp. 454-467.
- Stanier, S. A. *et al.* (2016) Improved image-based deformation measurement for geotechnical applications, *Canadian Geotechnical Journal*. NRC Research Press, 53(5), pp. 727-739.
- Stone, K. J. L. and Wood, D. M. (1992) Effects of dilatancy and particle size observed in model tests on sand., *Soils and foundations*. The Japanese Geotechnical Society, 32(4), pp. 43-57.
- Sulsky, D., Chen, Z. and Schreyer, H. L. (1994) A particle method for history-dependent materials, *Computer Methods in Applied Mechanics and Engineering*. North-Holland, 118(1-2), pp. 179-196.

- Sutton, M. *et al.* (1983) Determination of displacements using an improved digital correlation method, *Image and Vision Computing*. Elsevier, 1(3), pp. 133–139.
- Terzaghi, K. (1943) *Theoretical Soil Mechanics*. New York, NY: JohnWiley & Sons.
- Thielicke, W. and Buma, A. (Anita G. J. (2014) *The flapping flight of birds : analysis and application*. [S.n.].
- Thielicke, W. and Stamhuis, E. J. (2014) PIVlab – Towards User-friendly , Affordable and Accurate Digital Particle Image Velocimetry in MATLAB.
- Tian, J. and Philpot, W. D. (2015) Relationship between surface soil water content , evaporation rate , and water absorption band depths in SWIR re f l ectance spectra, *Remote Sensing of Environment*. Elsevier Inc., 169, pp. 280–289.
- Tumlinson, L. G. *et al.* (2008) Thermal Neutron Computed Tomography of Soil Water and Plant Roots, *Soil Science Society of America Journal*. Soil Science Society, 72(5), p. 1234.
- Vanapalli, S. K. and Mohamed, F. M. O. (2007) Bearing Capacity of Model Footings in Unsaturated Soils, in *Experimental Unsaturated Soil Mechanics*. Berlin, Heidelberg: Springer Berlin Heidelberg, pp. 483–493.
- Vision Research (2019) *Phantom high speed*.
- Wang, C. *et al.* (2017) Dilatancy and compaction effects on the submerged granular column collapse, *Physics of Fluids*. AIP Publishing LLC, 29(10), p. 103307.
- Weisskopf, V. F. (1968) How Light Interacts with Matter, *Scientific American*. Scientific American, a division of Nature America, Inc., pp. 60–71.
- Westerweel, J. (1997) Fundamentals of digital particle image velocimetry, *Measurement Science and Technology*. IOP Publishing, 8(12), pp. 1379–1392.
- White, D. J., Take, W. A. and Bolton, M. D. (2003) Soil deformation measurement using particle image velocimetry (PIV) and photogrammetry, *Géotechnique*, 53(7), pp. 619–631.
- Wozniak, B. and Dera, J. (2006) *Light Absorption in Sea Water*. New York, NY: Springer New York.
- Wu, J. *et al.* (2018) Experimental investigation on dilatancy behavior of water-saturated sandstone, *International Journal of Mining Science and Technology*. Elsevier, 28(2), pp. 323–329.
- Yerro, A., Alonso, E. E. and Pinyol, N. M. (2015) The material point method for unsaturated soils, *Géotechnique*. Thomas Telford, 65(3), pp. 201–217.
- Yerro Colom, A. (2015) *MPM modelling of landslides in brittle and unsaturated soils*.

Universitat Politècnica de Catalunya.

Yoneyama, S. and Murasawa, G. (2009) Digital image correlation, *Experimental Mechanics*, 207.

Young, T. (1802) II. The Bakerian Lecture. On the theory of light and colours, *Philosophical Transactions of the Royal Society of London*. The Royal Society London, 92, pp. 12-48.

List of figures

| | |
|--|----|
| Figure 1. Example of a generic image analysis focused on one single node. The patch is defined on the picture A (blue square). The location of the patch is found on picture B inside the searching area (red dashed square). The original location and the new location of the patch are connected by a green vector to represent the measured displacement. .. | 12 |
| Figure 2. Eulerian image correlation | 14 |
| Figure 3. Lagrangian Image Correlation | 17 |
| Figure 4. Example of the electromagnetic wave. | 21 |
| Figure 5. Electromagnetic spectrum. | 23 |
| Figure 6. a) Ideal representation of the absorption of the light. b)Whitewashed house example. | 25 |
| Figure 7. a) Ideal representation of the diffuse reflection of the light. b) Green leaf example. | 26 |
| Figure 8. a) Ideal representation of the scattering of the light. b) Blue sky example..... | 27 |
| Figure 9. a) Ideal representation the specular reflection of the light. b) Metallic surface example. | 27 |
| Figure 10. a) Ideal representation of the refraction of the light. b) Spoon in a glass of water example. | 28 |
| Figure 11. Effect of the refraction on a beam of light. α and β are the angles of the rays with respect to the surface normal. (based on the figure from the book Basic Sciences in Ophthalmology (Flammer, Mozaffarieh and Bebie, 2013). | 29 |
| Figure 12. Mirror effect on the calm water of the Charleston lake, Canada. | 30 |
| Figure 13. Refraction and reflection of a beam of light in the air-water interface. | 31 |
| Figure 14. Vibration modes of the water molecule. | 33 |
| Figure 15. Coefficient of light absorption by water depending on the light wavelength (visible, NIR and SWIR). Based on the figure form the book Light absorption in seawater (Wozniak and Dera, 2006). | 34 |
| Figure 16. Overview of the tank from the main face. | 36 |
| Figure 17 Dimensions of the thank. | 36 |
| Figure 18 Lower water injection system, at the initial moment of injection. | 37 |
| Figure 19. Modified lower and lateral water injection system. | 37 |
| Figure 20. Upper water system. | 38 |
| Figure 21 Guillotine with the system to fix the initial angle. | 38 |

| | |
|--|----|
| Figure 22 Humidifier adapted to the thank..... | 39 |
| Figure 23 Illumination and camera holding structure. | 39 |
| Figure 24. Instructions to connect the SEN0193 moisture sensor to an Arduino shield (DFRobot, 2018)..... | 40 |
| Figure 25. Disposition of 3 sensors for the calibration. The disposition recreates the thank arrangement to consider possible interferences between the sensors and the effect of the rubber plug..... | 41 |
| Figure 26. Calibration curve of the SEN0193 moisture sensors. | 42 |
| Figure 27. Frontal view of the designed direct shear apparatus for low-stress tests..... | 44 |
| Figure 28. Posterior view of the designed direct shear apparatus for low-stress tests..... | 44 |
| Figure 29. Expanded view of the direct shear apparatus pieces. | 45 |
| Figure 30. Half slice of the apparatus. The arrange between the shear box, and the holding structure is visible..... | 48 |
| Figure 31. Design plan - lateral view. The linear guides and sliding blocks engagements are visible..... | 49 |
| Figure 32. Deign plan - frontal view. The arc to hold the vertical LVDT is visible. | 49 |
| Figure 33. Interior view of the direct shear apparatus with a soil sample inside. The vertical load system is visible. | 50 |
| Figure 34. Interior view of the apparatus without soil sample, vertical load system nor sintered filter. | 51 |
| Figure 35. Design plan - parallel cut. The attachment pieces for the motor and the load cell are visible..... | 52 |
| Figure 36. Graphical representation of the MPM scheme used by PIV-NP..... | 56 |
| Figure 37 Visual representation of the input data from Eulerian Image Correlation analysis for one time step. | 57 |
| Figure 38 Flowchart of the PIV-NP..... | 58 |
| Figure 39 Visual representation of the preliminary step i..... | 59 |
| Figure 40 Visual representation of the preliminary step ii..... | 60 |
| Figure 41 Visual representation of the preliminary step iii. a) 1 numerical particle per element. b) 4 numerical particles per element. | 60 |
| Figure 42 Visual representation of step 1. | 61 |
| Figure 43 Visual representation of step 2. | 61 |
| Figure 44 Visual representation of step 3. | 62 |
| Figure 45 Visual representation of step 5. | 64 |

Figure 46. Numerical Particle location on the linear displacement case with synthetic data.67

Figure 47. Instantaneous displacement of the numerical particles. Case of synthetic data with linear displacement.68

Figure 48. Accumulated displacement of the numerical particles. Case of synthetic data with linear displacement.68

Figure 49. Numerical Particle location and instantaneous displacement on the horizontal shear case with synthetic data. The numerical particles can be grouped in three zones depending on its instantaneous displacement: upper block (red particles = 10 px/time step), shear band (green particles = 5 px/time step), and lower block (blue particles = 0 px/time step).70

Figure 50. Instantaneous displacement of the numerical particles. Case of synthetic data with horizontal shear band (1 numerical particle per element).71

Figure 51. Instantaneous displacement of the numerical particles. Case of synthetic data with horizontal shear band (4 numerical particles per element).71

Figure 52. Numerical Particle location and instantaneous displacement. a) Shear band one element thickness. b) Shear band five elements thickness.72

Figure 53. Instantaneous displacement of the numerical particles. Case of synthetic data with horizontal shear band.73

Figure 54. Numerical Particle location on the oblique shear case with synthetic data. A line of NP is highlighted in red, blue, and purple to be analyzed in Figure 55.75

Figure 55. Instantaneous displacement graph of a line of particles normal to the shear band. Case of synthetic data with oblique shear band (1 numerical particle per element).76

Figure 56. Instantaneous displacement graph of a line of particles perpendicular to the shear band. Case of synthetic data with oblique shear band (4 numerical particles per element).76

Figure 57. Vertical line of particles with an oblique shear band input data. a) Numerical particle location at time steps 0, 10, and 20. b) Instantaneous displacement graph of the colored particles (24 time steps).77

Figure 58. Numerical Particle location and instantaneous displacement on the linear displacement case with synthetic images.79

Figure 59. Instantaneous displacement (x,y) of the particles respect to the correct expected displacement. Case of synthetic images with linear displacement (1 numerical particle per element).80

Figure 60. Total instantaneous displacement of the particles respect to the correct expected total displacement. Case of synthetic images with linear displacement (1 numerical particle per element)..... 81

Figure 61. Error accumulated in the particle displacements. Case of synthetic images with linear displacement (1 numerical particle per element). 81

Figure 62. Numerical particle location and instantaneous displacement on the zero-thickness shear case with synthetic images..... 83

Figure 63. Instantaneous displacement graph of the zero-thickness shear case with synthetic images (1 numerical particle per element)..... 83

Figure 64. Vertical compression case analysis a) Numerical particle position and instantaneous volumetric strain at time step 4. b) Instantaneous volumetric strain of the numerical particles on each time step..... 85

Figure 65. The general image of the real case evaluated. The analysis is performed inside the green square, where there are 3 blue particles..... 86

Figure 66. Grid of input data from PIVlab overlaid to the real image. The 3 blue particles are observable. 87

Figure 67. Evolution of the particle coordinates comparing the location in real images and the location of the numerical particle from PIV-NP. 88

Figure 68. a) Accumulated displacement of the blue particle A and the closest numerical particle. b) Accumulated error on the numerical particle displacement. 89

Figure 69. a) Accumulated displacement of the blue particle B and the closest numerical particle. b) Accumulated error on the numerical particle displacement. 90

Figure 70. a) Accumulated displacement of the blue particle C and the closest numerical particle. b) Accumulated error on the numerical particle displacement. 90

Figure 71. Initial dimensions of the slope..... 91

Figure 72. Initial numerical particle distribution. Highlighted particles (purple, green, orange) are analyzed more deeply. 92

Figure 73. 2D visualization of the PIV-NP analysis of a landslide. Real image, instantaneous displacement, and instantaneous deviatoric strain. 94

Figure 74. Comparison on the velocities of an NP in the landslide base with the velocity of an NP on the landslide body. 96

Figure 75. a) Instantaneous displacement b) Accumulated displacement c) Instantaneous deviatoric strain d) Accumulated deviatoric strain..... 98

Figure 76 Effect of water content light absorbance. (a) Dry soil; (b) Adsorbed water films; (c) Capillary menisci between grains; (d) Saturated. 102

Figure 77 Reflectometry of coastal beach sand (Nolet *et al.*, 2014). (a) Measured spectral reflectance of beach sand over a range of 350-2100 nm in samples with different values of degree of saturation. Shaded areas indicate the optimal range to evaluate the Sr measuring the reflected light. (b) Variation of reflectance with the degree of saturation calculated from the figure a) for four wavelengths (500, 1000, 1500 and 2000 nm)..... 104

Figure 78 Variation, for different soils, of the difference between the reflectance measured at dry and saturated conditions for varying wavelengths of different soils. Shaded areas (1400 -1550 nm and 1900 - 2000 nm) corresponds to maximum differences. 105

Figure 79 Sensitivity curve of the camera phosphor treated sensor. 106

Figure 80 Measured values and calibrated water retention curve of Castelldefels' beach sand. 108

Figure 81 Images of an unsaturated column of Castelldefels beach sand in (a) the visible and (b) the SWIR spectra. 109

Figure 82 SWIR image after a Gaussian filter. 110

Figure 83 Experiment setup for calibration. 110

Figure 84 Correlation curve between the degree of saturation and gray value measured in samples..... 111

Figure 85 Calibration curve correlating normalized gray value and degree of saturation measured in samples..... 112

Figure 86 Flowchart of the technique algorithm to assess the saturation degree and suction from SWIR images. 114

Figure 87 Experiment setup for validation 116

Figure 88 Values of (a) degree of saturation and (b) water content of the column measured by the SWIR image..... 117

Figure 89 Comparison of vertical profiles of degree of saturation determined by SWIR images and values computed from equilibrium suction profile and the experimental water retention curve. 118

Figure 90 SWIR-measured degree of saturation at increasing time during the soil column wetting. 119

Figure 91 Comparison between the degree of saturation measured by SWIR images (dashed line) and by moisture sensors at three column heights (60 mm, 14 mm and 220 mm). 120

Figure 92 Comparison between the experimental and the numerical water retention curve. 122

Figure 93 Degree of saturation effect on the liquid phase relative permeability 122

Figure 94 Comparison between the degree of saturation measured by SWIR images (dashed line), by moisture sensors (solid line), and calculated through numerical simulation (dotted line) at three column heights (60 mm, 14 mm and 220 mm. 123

Figure 95 SWIR-measured degree of saturation compared to Code_Bright numerical simulation at increasing time during the soil column wetting. 124

Figure 96 Effect of the void ratio on the reflectance of the soil for the different water contents (7.14, 14.29, 22.86). The pixel intensity for dry and saturated conditions is also plotted as a reference. The average trend is plotted as a dotted line..... 126

Figure 97 Variation of pixel intensity (GV) of samples having the same water content but different void ratio..... 127

Figure 98 GV normalized - Sr plot of soil samples at constant water content (7.14, 14.29, 22.86) and varying void ratio. GV normalized - Sr plot of samples at constant density (1.47, 1.39 g/cm³) and varying water content..... 128

Figure 99 Example of the spatial non-uniformity of the light from 3 emitters when reaches a surface. 128

Figure 100 Flowchart of the combination of the PIV-NP with the degree of saturation measurements. 133

Figure 101 Experimental setup of the column before the load placement. 136

Figure 102. Measured values and calibrated water retention curve of Castelldefels' beach sand. 137

Figure 103 Legend of the data displayed in Figure 104, and Figure 105: Degree of saturation, accumulated displacement, and volumetric strain. 138

Figure 104 2D visualization of the column collapse experiment: Degree of saturation, accumulated displacement, and volumetric strain. Time steps: 30, 60, 90 and 120 seconds. 139

Figure 105 2D visualization of the column collapse experiment: Degree of saturation, accumulated displacement, and volumetric strain. Time steps: 150, 180, 210 and 240 seconds..... 140

Figure 106 Column of particles analyzed 141

Figure 107 1D visualization of the column collapse experiment: Degree of saturation, accumulated displacement, and volumetric strain. Time steps from 0 to 240 seconds.. 141

Figure 108 Particles analyzed individually 142

Figure 109 Particle by particle visualization of the column collapse experiment: Evolution of the accumulated displacement compared with the degree of saturation. Time from 0 to 240 seconds..... 143

Figure 110 Dry circles appear around the feet when walking next to the sea. (source: Greg Siemens)..... 147

Figure 111 Schematic visualization of the dilatancy in the granular media. 148

Figure 112 Frame of a shallow foundation experiment with visible air penetration. The numerical particles with the accumulated displacement information are overlapped. ... 149

Figure 113 Particle size distribution for the coarse fused quartz soil (Ezzein and Bathurst, 2011). 151

Figure 114 Ideal representation of the interaction of a beam of light with the transparent soil. a) Full saturated soil (soil + oil). b) Unsaturated soil with a bubble (soil + oil + air).152

Figure 115 Calibration curve for transparent soils. Saturation - normalized pixel intensity relationship. (Sills, Mumford and Siemens, 2017). 153

Figure 116 The ultrahigh-speed camera Phantom V2512. 154

Figure 117 Light source and camera location respect to the tank. 156

Figure 118 Points of the 3 cases exposed in this part. 1) Dry 2) Submerged 3) Saturated. 158

Figure 119 Steps on the dry area of the beach (Salento, Italy)..... 159

Figure 120 Load vs. settlement during the whole dry experiment. There are different micro-failures before the ultimate failure occurs. The analysis is based on that ultimate failure marked on purple. 159

Figure 121 Image before the ultimate failure. This condition is defined as the initial situation of the image analysis. 160

Figure 122 Vectors of displacement calculated by PIV in the moment of the failure..... 160

Figure 123 Total displacement on the particles generated by PIV-NP in the dry case. The evolution of the line of particles marked on pink is plotted in Figure 125. 161

Figure 124 Theoretical general failure mechanism. 161

Figure 125 Evolution of the displacement and volumetric strain of the particles along the vertical profile indicated in pink in Figure 123..... 162

Figure 126 Correlation between the settlement of the footing measured by the LVDT and the velocity of the particles measured by PIV-NP. 162

Figure 127 Steps on the submerged area of the beach (Salento, Italy)..... 163

Figure 128 Load vs. settlement during the whole submerged experiment. There are different micro-failures before the ultimate failure occurs. The analysis is based on that ultimate failure marked on purple..... 164

Figure 129 Total displacement on the particles generated by PIV-NP in the submerged case..... 164

Figure 130 Effect of the failure in the pressure measured by the ppt correlated with the settlement of the footing. 165

Figure 131 Steps on the saturated area created by the wave movement (Salento, Italy).166

Figure 132 Load vs. settlement during the whole experiment. The analysis is based on that ultimate failure marked on purple..... 166

Figure 133 Initial and final frames of the ultimate failure in the saturated case..... 167

Figure 134 Evolution of the ultimate failure in the saturated case. a) Real image b) Numerical particles position and their velocity of displacement. 168

Figure 135 Image after the failure and with the particles generated by PIV-NP superposed. The line of particles marked is selected to evaluate the evolution of their status. The particles marked in colors will be evaluated individually..... 170

Figure 136 Evolution of the accumulated displacement and instant velocity of the line of particles selected in Figure 135. 171

Figure 137 Evolution of the volumetric strain and the degree of saturation the line of particles selected in Figure 135. 172

Figure 138 Evolution of the load applied on the footing (measured by the load cell) and the velocity on the particle orange. The two peaks of failure are marked: punching failure (green) and general failure (red)..... 173

Figure 139 Evolution of the velocity and degree of saturation in the particles at -2.5, -5.0, -7.5, and -10.0 cm..... 174

Figure 140 Velocity depending on the degree of saturation of the particles at -1.25, -2.5, -3.75, and -5.0 cm..... 175

Figure 141 Evolution the degree of saturation in the particle at -7.5 cm and the pressure measured by the PPT at -14 cm. The two peaks of failure are marked: punching failure (green) and general failure (red)..... 177

Figure 142 The Load vs. settlement graph of the three cases: dry (blue), saturated (red), and submerged (green). 178

Figure 143 The points analyzed in this part cover the whole transition form submerged to dry. 179

Figure 144 Last failure load of all the experiments performed with coarse sand..... 179

Figure 145 Measures to determine the parameters of deviation and inclination before the ultimate failure. 181

Figure 146 The eccentricity of the footing on the shallow foundation test. The limit of tolerance was set at 0.03 of deviation..... 182

Figure 147 Inclination of the footing on the shallow foundation test. The limit of tolerance was set at 0.04 of inclination. 182

Figure 148 Relation between load and phreatic level using the data from the experiments with inclination and deviation under the tolerance..... 183

List of tables

| | |
|--|-----|
| Table 1: Coordinates of the reference and compared patches in the Eulerian approach. | 14 |
| Table 2: Coordinates of the reference and compared patches in the Lagrangian approach. | 17 |
| Table 3: Bands of the wavelength with light absorbance by water, beside the correspondent vibrational state of the excited water molecule. | 33 |
| Table 4 Polyacetal physical properties..... | 46 |
| Table 5 Sintered metal sheet properties..... | 51 |
| Table 6 Example of the structure of the input data from Eulerian Image Correlation analysis for one time step for PIV-NP. | 57 |
| Table 7 Geotechnical properties of Castelldefels' sand. | 107 |
| Table 8 SWIR images after Gaussian filter and parameters of the sample used in the calibration..... | 111 |
| Table 9 Hydraulic properties of the Castelldefels' sand..... | 121 |
| Table 10 Degree of saturation of tested samples. For each water content, three different degrees of saturation are obtained by reducing the void ratio. | 125 |
| Table 11 Average pixel intensity (GV) of each sample condition presented in Table 10. | 125 |
| Table 12 Geotechnical properties of Castelldefels' sand and initial conditions..... | 136 |
| Table 13 Geotechnical properties of the artificial transparent coarse sand. Values extracted from (Ezzein and Bathurst, 2011; Peters, Siemens and Take, 2011)..... | 150 |
| Table 14 Summary of the three representative cases: dry, saturated, and submerged.... | 178 |

The question is not what you look at,
but what you see.

Henry David Thoreau.